University of Glasgow

Clough, Emily Heather (2023) *Investigating mechanisms and indicators of sensitivity to replication stress-targeting therapies in glioblastoma.* PhD thesis.

https://theses.gla.ac.uk/83598/

Copyright and moral rights for this work are retained by the author

A copy can be downloaded for personal non-commercial research or study, without prior permission or charge

This work cannot be reproduced or quoted extensively from without first obtaining permission in writing from the author

The content must not be changed in any way or sold commercially in any format or medium without the formal permission of the author

When referring to this work, full bibliographic details including the author, title, awarding institution and date of the thesis must be given

Enlighten: Theses
https://theses.gla.ac.uk/
research-enlighten@glasgow.ac.uk

Investigating mechanisms and indicators of sensitivity to replication stress-targeting therapies in glioblastoma.

Emily Heather Clough

BSc (Hons), MSc

Submitted in fulfilment of the requirements for the Degree of PhD

School of Cancer Sciences
College of Medical, Veterinary and Life Sciences
University of Glasgow

December 2022

Abstract

Introduction

Evidence suggests a subpopulation of treatment resistant glioblastoma (GBM) cancer stem cells (GSCs) is responsible for tumour recurrence, an almost universally deadly characteristic of this cancer of extreme unmet need. Current treatments fail to eradicate GSCs and novel GSC targeting therapies are a clinical priority. Elevated DNA replication stress (RS) in GSCs has been described, leading to constitutive DNA damage response activation and treatment resistance and targeting RS with combined ATR and PARP inhibition (CAiPi) has provided potent GSC cytotoxicity. Nevertheless, there are a relative lack of studies investigating the underlying mechanisms of response to CAiPi in GBM and a lack of robust transcriptional signatures or genomic biomarkers correlated with CAiPi response in GSCs.

Aims

This thesis aims to investigate RS as a targetable vulnerability of GSCs. It aims to achieve this by studying the mechanisms of sensitivity to inhibition of the RS response to inform transcriptional indicators of sensitivity. Lastly, it aims to investigate the feasibility of this therapeutic strategy in a preclinical model.

Methods

Paired GSC-enriched and GSC-depleted, differentiated ('bulk') populations, derived from resected GBM specimens, were maintained in serum-free, stem-enriching conditions or differentiating conditions respectively. WGS and RNAseq were utilised to characterise the genomic and transcriptomic landscape of the cell line panel. Responses to CAiPi were assessed by clonogenic and cell viability assays and validated in a CD133 sorted population by neurosphere assay. Replication dynamics in paired GSC and bulk cells were investigated by a DNA fibre assay. Dysregulated S phase was analysed by quantification of 53BP1 nuclear bodies (53BP1NB), indicative of under-replication of the genome, and quantification of re-replicating cells by flow cytometry. Chromosomal instability was interrogated by quantification of chromatin bridges and micronuclei. Novel

mechanistic discoveries prevalent in GSCs with potent CAiPi-sensitivity were used to curate a transcriptional marker of sensitivity for interrogation in GBM cell lines and in published clinical datasets. Lastly the feasibility of CAiPi was investigated in an *in vivo* preclinical model, assessing tolerability and tumour penetration.

Results

CAiPi was potently cytotoxic to a population of GSCs but highly heterogenous responses to CAiPi were observed across a panel of seven paired GSCs and bulk cells. Sensitivity was not predicted by elevated RS in GSCs or any previously defined biomarkers of RS or CAiPi sensitivity. Differential sensitivity was exploited for further investigations which identified transcriptional dysregulation of DNA replication, specifically in a CAiPi-responsive GSC line. Subsequent analysis of DNA replication identified PARPi-induced increase in origin firing, associated with PARP trapping. GSCs with this origin firing phenotype also exhibited an increase in both under-replicated DNA and re-replication in response to CAiPi, with an increase in chromosomal aberrations and instability.

A curated transcriptional signature, based on mechanistic discoveries in CAiPi-sensitive GSCs, predicted GSC sensitivity and identified populations of GBM patients with poor survival who may respond to CAiPi treatment. *In vivo* studies demonstrated murine blood brain barrier (BBB) penetration of a PARPi and an ATRi with minimal toxicity, however optimal dosing and scheduling remains a challenge.

Conclusions

We propose that CAiPi-sensitivity is marked by loss of replication coordination leading to chromosomal damage as cells move through S phase. Additionally, we propose a model whereby under-replication and re-replication can occur due to spatial and temporal uncoupling during S phase. Targeting RS via CAiPi represents a promising therapeutic strategy for selectively targeting recurrence driving GSCs to improve clinical outcomes in GBM.

Table of Contents

List of Tables

List of Figures

Posters and abstracts

Clough, E. *et al.* (2020) 'Investigating mechanisms and biomarkers of replication stress-targeting therapies in glioblastoma', *Oral Presentation at the Scottish Radiotherapy Research Forum Annual Meeting, 12th March 2020, Stirling, UK.*

Clough, E. *et al.* (2021) 'Excessive new origin firing underlies selective glioma stem cell cytotoxicity induced by replication stress response inhibition', *Poster Presentation at the 1st International Electronic Conference on Cancers Meeting, 1-3rd February 2021, virtual meeting.*

Clough, E. *et al.* (2021) 'Excessive new origin firing underlies selective glioma stem cell cytotoxicity induced by replication stress response inhibition', *Poster Presentation at the 14th Annual International PhD Student Cancer Conference, 16-18th June 2021, virtual meeting hosted by the CRUK Beatson Institute, Glasgow, UK.*

Clough, E. *et al.* (2021) 'Excessive new origin firing underlies selective glioma stem cell cytotoxicity induced by replication stress response inhibition', *Oral Presentation at the British Neuro-Oncology Society Annual Meeting, 8-9th July 2021, virtual meeting.*

Clough, E. *et al.* (2021) 'Targeting replication stress response for glioma stem cell specific cytotoxicity', *Poster Presentation at the Society for Neuro-Oncology Annual Meeting, 18-21st November 2021, Boston USA.* Awarded a Top Poster Award.

Clough, E. *et al.* (2022) 'Targeting replication stress response for glioma stem cell specific cytotoxicity', *Poster Presentation at the British Neuro-Oncology Society Annual Meeting, 22-24th June 2022, Liverpool UK.* Awarded a Best Poster Presentation: Basic Science Award

Acknowledgements

Firstly, I'd like to thank my primary supervisor, Dr Ross Carruthers, who has been a massive source of support and knowledge over the last four years. I really appreciate all the time and effort, for pushing me out of my comfort zone and without complaint being bombarded with drafts, corrections and questions in the last couple of months. I'd also like to thank my other supervisors for all their input, expertise and mentorship; Dr Patricia Roxburgh and Dr Ros Glasspool especially in the beginning of my PhD, Professor Anthony Chalmers for being an invaluable source of knowledge and Dr Mark O'Connor of AstraZeneca, where I sadly was unable to fulfil the placement due to COVID but provided guidance from afar. I'd also like to thank the University of Glasgow, University of Edinburgh, Medical Research Council and AstraZeneca for accepting me onto the programme and funding this project.

The help of so many was invaluable during my time as part of M12 (and M33 and M19). I can't thank Karen enough; I have learned so much from her (I don't know how I'll manage in a different lab without her magic book of everything) and coffee was always a welcome break. Thank you to Sarah for being a great support during the last year, it was a joy to have you in the group and if you fancy catching a flight to France again let me know. A special thanks goes to Mark, for answering endless queries on ImageJ, R, WGS (the list goes on). Thank you to Suzanne who showed me the ropes in my first few months at the Wolfson Wohl. Lastly, I'd like to acknowledge everyone who has provided support, knowledge and coffee breaks over the last four years: Katrina, Karin, Nati, Jo, Conchita, Sandy, Sid, Rodrigo and Dave.

Doing a PhD during a global pandemic was never going to be easy, and there are so many I couldn't have done it without. Thanks first to my parents, who let me crash with them in 2020 and then again while writing up. Writing up would have been a much bigger struggle if it wasn't for all their cooking, coffee and cocktails. Thanks to Alex, George and Rudi for being the best board game buddies while I'm at home, and to George for letting me crash on my sofa in my flat. Thank you to Zoë for buying a house with a spare room just for me and being an alright egg, Sophie and Nina F for taking me on trips around Scotland at a minute's notice, Nina P and Bethan for supplying the tequila and gin, and to

Jack, Fraser, Lorne and Andrew for the Saturday night zoom quizzes in lockdown. Lastly, I'd like to thank everyone I've met and friends I've made along the way during my nine years at the University of Glasgow, who have given me guidance, advice and support.

Author's Declaration

I declare that I am the sole author of this thesis. The work recorded in this thesis is my own and the research described herein was carried out by me unless otherwise stated or acknowledged. No part of this thesis has been submitted for consideration for another degree at the University of Glasgow or any other institution.

Emily Clough

December 2022

List of abbreviations

53BP1	p53 binding protein 1
53BP1NB	53BP1 nuclear bodies
9-1-1	RAD9-HUS1-RAD1
a-KG	α-ketoglutarate
AML	Acute myeloid leukaemia
ATM	Ataxia telangiectasia mutated
ATR	Ataxia telangiectasia and Rad3-related
ATRi	ATR inhibitor
ATRIP	ATR-interacting protein
ATRX	Alpha thalassemia/mental retardation syndrome X-linked
B/P	Brain/plasma
BBB	Blood brain barrier
BCA	Bicinchoninic acid
BCRP	Breast cancer resistance protein
BER	Base excision repair
bFGF	Basic fibroblast growth factor
BID	Twice daily
BIR	Break-induced replication
BLM	Bloom's syndrome RecQ like helicase
BRCA1	Breast cancer gene 1
BRCA2	Breast cancer gene 2
BrdU	Bromodeoxyuridine
BSA	Bovine serum albumin
BWA	Burrows-wheeler aligner
CAiPi	Combined ATR and PARP inhibition
CARM1	Coactivator Associated Arginine Methyltransferase 1
CCNE1	Cyclin E1
CDC25	Cell division cycle 25
CDC45	Cell division cycle 45
CDC6	Cell division cycle 6
CDI	Coefficient of drug interactions
CDK	Cyclin-dependent kinases
CDK1	Cyclin-dependent kinase 1
CDKN2A	Cyclin dependent kinase inhibitor 2A
CDT1	Chromatin Licensing and DNA Replication Factor 1
CENP-F	Centromere protein F
CFS	Common fragile sites
CGGA	Chinese Glioma Genome Atlas
CHK1	Checkpoint kinase 1
CI	Confidence interval
CldU	Chloro-deoxyuridine
CMG	CDC45, MCM, GINS
cnetplot	Category network plot
CNS	Central nervous system
CNV	Copy number variation
CoxPH	Cox proportional-hazards

CSC	Cancer stem cells
DAPI	4′,6-diamidino-2-phenylindole
DDK	Dbf4-dependent kinase
DDR	DNA damage response
DDW	Double distilled water
DEG	Differentially expressed gene
DEL	Deletion
DFS	Double fork stalling
DMS	Dimethyl sulfate
DMSO	Dimethyl sulfoxide
DNA-PK	DNA-dependent protein kinase
dNTP	Deoxynucleotide triphosphate
DSB	Double strand breaks
ECL	Enhanced chemiluminescent
ECM	Extracellular matrix
EdU	5-Ethynyl-2′-deoxyuridine
EGF	Epidermal growth factor
EGFR	Epidermal growth factor receptor
emapplot	Enrichment map plot
EME1	Essential meiotic endonuclease 1
ERCC1	Excision repair cross complementation group 1
ES	Enrichment score
FACS	Fluorescence-activated cell sorting
FANC	Fanconi anaemia group
FCS	Foetal calf serum
FSC	Forward scatter
FS-UFB	Fragile site ultra-fine bridge
GBM	Glioblastoma
GO	Gene ontology
GSC	Glioblastoma CSC
GSEA	Gene set enrichment analysis
GSVA	Gene set variation analysis
H_2O_2	hydrogen peroxide
HCl	Hydrochloric acid
HR	Homologous recombination
HRD	HR-deficient
HRP	Horse-radish peroxidase
HRR	HR repair genes
HU	Hydroxyurea
IDH	Isocitrate dehydrogenase
IdU	Iodo-deoxyuridine
InDel	Insertion / deletion
INS	Insertion
IR	Irradiation
iRFP	Near-infrared fluorescent protein
KEGG	Kyoto Encyclopedia of Genes and Genomes
LDA	Limiting dilution assay
LFC	Log fold change
MCM	Minichromosome maintenance

MGMT	O^6-methylguanine-DNA methyltransferase
MiDAS	Mitotic DNA synthesis
MLL	Mixed lineage leukaemia
MMS	Methyl methanesulphonate
MS	Mass spectrometry
MTD	Maximum tolerated doses
mTOR	Mechanistic Target of Rapamycin Kinase
MTT	Thiazolyl Blue Tetrazolium Bromide
MUS81	MMS ultraviolet-sensitive gene clone 81
NAD	Nicotinamide adenine dinucleotide
NADPH	Reduced nicotinamide adenine dinucleotide phosphate
NER	Nucleotide excision repair
NHEJ	Non-homologous end joining
NSC	Neural stem cells
NSCLC	Non-small cell lung cancer
OCT4	Octamer-binding transcription factor 4
OLIG2	Oligodendrocyte transcription factor 2
ORC	Origin recognition complex
ORR	Objective response rate
OS	Overall survival
PAR	Poly(ADP-ribose)
PARG	Poly(ADP-Ribose) Glycohydrolase
PARP	poly(ADP-ribose) polymerase
PARPi	PARP inhibitor
PBS	Phosphate buffered saline solution
PCA	Principal component analysis
PC	Principal component
PCNA	Proliferating cell nuclear antigen
PDX	Patient-derived xenograft
PD	Pharmacodynamic
PEG 400	Polyethylene glycol 400
PFA	Paraformaldehyde
PFS	Progression free survival
P-gp	P-glycoprotein
PI	Propidium iodide
PI3K	Phosphoinositide 3-kinases
PIKK	Phosphatidylinositol 3-kinase-related kinases
PK	Pharmacokinetic
PLK1	Polo-like kinase 1
POLD3	DNA polymerase Delta 3
pre-IC	Pre-initiation complex
pre-RC	Pre-replication complex
PROM1	Prominin1
PTEN	Phosphatase and tensin homolog
RECQ1	ATP-dependent DNA helicase Q1
RIF1	Replication Timing Regulatory Factor 1
RNAseq	RNA sequencing
ROS	Reactive oxygen species
RPA	Replication protein A

RS	Replication stress
RT	Radiotherapy
SARRP	Small Animal Radiation Research Platform
SCLC	Small cell lung cancer
SD	Standard deviation
SDS	Sodium dodecyl sulphate
SEM	Standard error of the mean
siRNA	small interfering RNA
SLFN11	Schlafen 11
SMARCAL1	SWI/SNF-related matrix-associated actin-dependent regulator of chromatin subfamily A-like protein 1
SNP	Single nucleotide polymorphism
SOX2	SRY-box 2
SSB	Single strand break
SSC	Side scatter
ssDNA	Single stranded DNA
SV	Structural variant
T/P	Tumour/plasma
TBS	Tris-buffered saline
TBST	TBS-TWEEN
TBST-M	TBST with 5% Marvel
TCGA	The Cancer Genome Atlas
TERT	Telomerase reverse transcriptase
TGFβ	Transforming growth factor beta
TGFα	Transforming growth factor alpha
TMZ	Temozolomide
TOP1	DNA topoisomerase 1
TOPBP1	DNA topoisomerase 2-binding protein 1
TP53	Tumour protein p53
UFB	Ultrafine bridge
UR-DNA	Under-replicated DNA
VLG	Very large genes
WCC	White cell count
WGS	Whole genome sequencing
WHO	World Health Organisation
WT	Wildtype
γH2AX	γH2A histone family, member X

Chapter 1 Introduction

1.1 Introduction

Glioblastoma (GBM) is the most common and devastating primary brain tumour in adults. Current treatment involves surgical resection where possible, followed by radiotherapy (RT), concurrent temozolomide (TMZ) chemotherapy and a six-month adjuvant course of TMZ. Despite aggressive treatment, recurrence and disease progression is inevitable, with a median survival of only 14.6 months (Stupp et al., 2009). There is a need to identify therapies that can improve debilitating symptoms, increase the efficacy of current treatment modalities and improve survival.

The greatest advancement in standard of care for GBM came with the addition of the alkylating agent TMZ to RT, which increased the two-year survival rate to 26.5%, compared to 10.4% with RT alone (Stupp et al., 2005). However, it had a much more modest effect on median survival. The addition of TMZ to standard of care in 2005 remains the only significant advancement of GBM treatment and survival rates, despite extensive research and clinical trials. GBM remains a deadly cancer of extreme unmet need. High levels of treatment resistance drive recurrence and disease progression. This clinical behaviour has been associated with the presence of highly radiation resistant cancer stem cells (CSC) (Bao et al., 2006). New therapies are being investigated for their capacity to target and sensitize this recurrent population of cells.

1.2 Glioblastoma characteristics

1.2.1 MGMT methylation

To date, the biomarker with most clinical utility in GBM is methylation of the MGMT (O^6-methylguanine-DNA methyltransferase) promoter (Hegi et al., 2005). MGMT acts to remove cytotoxic O^6-alkylguanine lesions which are a lethal bioproduct of alkylating TMZ chemotherapy. However, methylation of the CpG islands in the promoter, which is present in about 45% of GBM tumours, silences the gene and sensitises GBM to the chemotherapy (Hegi et al., 2005, Watts et al., 1997). A greater and significant survival benefit from the addition of TMZ to RT was seen in patients with MGMT promoter methylation, increasing median

survival from 15.3 months to 21.7 months (Hegi et al., 2005). In patients without MGMT promoter methylation, there was a smaller and statistically insignificant difference in survival when TMZ was added to RT. There are contrasting reports of MGMT methylation status also being a prognostic biomarker for RT (Criniere et al., 2007, Rivera et al., 2010), but overall, MGMT promoter methylation status is an important biomarker of treatment response, and consequently is often used for patient stratification in clinical trials. However, as with many biomarkers there are limitations, including the fact that some tumours with unmethylated MGMT promoters do respond to TMZ and some with methylated MGMT promoters can exhibit poor responses and survival.

1.2.2 IDH mutational status

Mutations in IDH1 (isocitrate dehydrogenase 1), associated with glioma, were first identified in 2008 by analysis of 105 GBM tumour samples which found a point mutation resulting in a R132 amino acid substitution in 12% of patients (Parsons et al., 2008). Mutations in IDH2, also associated with glioma, are found at R172 but are much less frequent than IDH1 mutations (Yan et al., 2009). IDH1 and IDH2 are involved in glucose metabolism, catalysing the production of α-ketoglutarate (α-KG) and reduced nicotinamide adenine dinucleotide phosphate (NADPH), which function in the response to oxidative stress. IDH mutations were initially of interest as they were most prevalent in younger GBM patients and associated with a 16-month median survival benefit (Parsons et al., 2008, Yan et al., 2009). IDH mutations were found to be highly prevalent in low grade glioma and in secondary GBM (73%) but not in primary GBM (3.7%), which highlights the tendency for IDH-mutant low-grade gliomas to recur as a secondary GBM (Nobusawa et al., 2009). Primary GBMs with an IDH mutation had similar clinical and genetic profiles to secondary GBM, leading Nobusawa et al to postulate that they may arise from rapidly progressing low-grade gliomas that go undiagnosed and are therefore actually secondary GBM (Nobusawa et al., 2009). Classification of GBM by the World Health Organisation (WHO) had been as either IDH wildtype (WT) or IDH mutant until the recent reclassification in 2021, which stated that all GBM are IDH WT and any previously defined IDH mutant GBMs are now ‘IDH mutant astrocytoma’ (Louis et al., 2021).

1.2.3 GBM genomic landscape

GBM is characterised by both intratumoral and intertumoral heterogeneity. PTEN (phosphatase and tensin homolog), TP53 (tumour protein p53), TERT (telomerase reverse transcriptase), EGFR (epidermal growth factor receptor) and CDKN2A (cyclin dependent kinase inhibitor 2A) have been reported as the most frequently mutated or altered genes in GBM (Sakthikumar et al., 2020, Parsons et al., 2008, Brennan et al., 2013). Parsons et al found CDKN2A was the most frequently altered, with homozygous deletions found in 50% of patients (Parsons et al., 2008), which predicted worse survival in IDH WT GBM (Ma et al., 2020). They also found point mutations in TP53 (35%), EGFR (14%) and PTEN (26%), amplifications of EGFR (23%) and homozygous deletions in TP53 (5%) and PTEN (5%). Whole genome sequencing of GBM by Sakthikumar et al identified TP53, EGFR and PTEN as the only "significantly mutated genes", which were genes that contained more clinically significant variants than expected by chance (Sakthikumar et al., 2020). EGFR amplification is associated with a more aggressive GBM phenotype (Xu et al., 2017), as well as being identified as an early event in GBM progression, alongside CDKN2A copy number alterations (Sottoriva et al., 2013). TP53 and PTEN mutations in GBM are not prognostic but may be more crucial for initiation or progression (Rich et al., 2005), with aberrations in both associated with later malignant events in a study of tumour evolution (Sottoriva et al., 2013).

Extensive characterisation of GBM mutations in recent years has led to identification of some frequently altered but also defining GBM mutations. Historically, CNS tumour diagnosis and grading was based exclusively on histology, however, several molecular markers now add prognostic information which is incorporated into the WHO classification of CNS tumours. The WHO classification of GBM, a grade IV glioma, has recently been updated in 2021. Previously, GBM was categorised as either IDH mutant or wildtype but since 2021 any IDH mutant GBM have been reclassified as astrocytomas, in keeping with them being less aggressive and infrequently found in primary GBM (Nobusawa et al., 2009). Now GBM is only IDH wildtype, the most aggressive CNS tumour. Additionally, several molecular markers have been added as grading biomarkers; a histologically "lower grade" glioma could be classified as GBM if an IDH WT diffuse astrocytic glioma is accompanied with one or more of TERT promoter

mutation, EGFR amplification and +7/-10 copy number changes (Louis et al., 2021).

1.2.4 Glioblastoma subtypes

Another GBM stratification method is by transcriptomic subtype. There have been several transcriptomic signatures proposed for subtyping, with 'mesenchymal' and 'proneural' subtypes most frequently discussed, and 'classical', 'neural' and 'proliferative' variably described. Verhaak et al were the first to describe a transcriptional subtype signature in 2010 to classify GBM as either proneural, neural, classical or mesenchymal (Verhaak et al., 2010). However, an updated transcriptional subtype signature which categorised GBM as proneural, classical or mesenchymal has since been described (Wang et al., 2018). Wang et al aimed to identify GBM-specific gene expression, excluding gene expression from any tumour micro-environment and non-malignant cells, by comparing patient samples to matched cell cultures, sequencing single cells and comparing core versus margin samples. They found no association with the previously described neural subtype suggesting this was non-tumour specific and in keeping with the neural subtype's relationship to the tumour margin (Wang et al., 2018, Gill et al., 2014). They also investigated the survival outcomes of the three subtypes. High levels of intratumour heterogeneity were evident in these data with more than one subtype often present within a single tumour (Patel et al., 2014, Sottoriva et al., 2013) which resulted in no significant differences in survival between subtypes. However, analysis of only patients with the lowest heterogeneity found a median survival of 11.5, 14.7 and 17.0 months for mesenchymal, classical and proneural respectively (Wang et al., 2018).

Subtypes have shown limited utility in treatment stratification despite differential survival probabilities and distinct molecular biomarkers of GBM subtypes (Phillips et al., 2006, Verhaak et al., 2010). Park et al more recently identified subtype-specific alterations associated with prognosis which they proposed should be further investigated as therapeutic targets (Park et al., 2019). However, they do acknowledge the challenges that have prevented more targeted therapies to have clinical success in GBM thus far, namely high levels of subtype and molecular heterogeneity and complex pathway activation. In addition, the ability of tumour cells to shift subtypes (Tang et al., 2021) and

molecular alterations after recurrence (Neilsen et al., 2019, Schafer et al., 2019) are likely factors in the failure of targeted therapies in GBM so far. To date, *MGMT* promoter methylation remains the only biomarker with clinical utility in GBM.

1.3 Glioblastoma cancer stem cells

The CSC theory proposes that cells within tumours are hierarchical, with a cellular organisation similar to that of normal tissue. CSCs sit at the apex of this tumoural society with increasing differentiation seen in CSC progeny. Although comparable to normal tissue organisation, the tumoural hierarchy is likely more chaotic and probably demonstrates a greater degree of plasticity (Rich, 2016). Glioblastoma CSC (GSCs) have been well characterised and are important clinically as they are highly treatment resistant and their persistence after standard of care drives recurrent disease, an almost universal feature of GBM. The defining features of GSCs are a capacity for self-renewal, unlimited proliferative potential and the ability to initiate tumours upon secondary transplantation *in vivo*. An important feature of GSCs is not only tumour initiation *in vivo* but also to have the capacity to recapitulate the heterogeneity of the parental tumour upon intracranial injection, which is the strictest functional assay for defining GSCs. Other defining features include differentiation along multiple lineages and expression of GSC markers (Lathia et al., 2015).

Below GSCs in the hierarchical ‘pyramid’ of GBM are relatively more differentiated cancer cells that lack the self-renewal, proliferative and tumorigenic capacities of GSCs. Despite these cells lacking the ability to drive tumour growth alone, they do make up most of the tumour bulk and are herein entitled ‘bulk’ cells. Bulk cells are still important clinically since they drive symptomatic disease due to making up the majority of the tumour volume. However, a key focus for GBM research is targeting treatment resistant, recurrence driving GSCs.

1.3.1 GSC definition

There has been differing nomenclature used for the cells at the top of the tumoural cellular hierarchy. Tumour-initiating, tumour-propagating and cancer stem/stem-like cells have all been used to describe this population of cells, however they all differ slightly in their functional characteristics. The first two describe cells with an ability to initiate or propagate tumours upon secondary transplantation, whereas the more restrictive CSC definition is used to define cells that generate heterogeneous tumours that contain cells with varying degrees of self-renewal capacities (Lathia et al., 2015). Therefore, CSCs, or GSCs in relation to GBM, is the most frequently used and most informative term.

The GBM cell-of-origin is often debated, and despite the role of GSCs in tumour-initiation and their overlapping characteristics, neural stem cells (NSC) are not necessarily the cell-of-origin. In fact, there are several different cell types that have been proposed as the cell of origin from studies which have utilised genetic inactivation of tumour suppressors such as TP53 or overexpression of TGFα (transforming growth factor alpha), including oligodendrocyte precursor cells (Liu et al., 2011), NSCs (Zhu et al., 2005) and mature astrocytes that have regressed to a progenitor-like state (Dufour et al., 2009). Some studies have shown a correlation between these GBM cell-of-origin models and a specific GBM subtype, suggesting that there are potentially different cells-of-origin that dictate GBM subtype and phenotype (Alcantara Llaguno et al., 2015, Liu et al., 2011).

There are also arguments and evidence to suggest that GBM cancer cells exhibit intrinsic plasticity and exist as a transcriptional cellular state rather than a specific cellular population, driven by tumour microenvironment and cellular interactions. Some studies have found GBM cancer cells that did not express GSC markers have GSC-like phenotypes such as tumorigenicity, self-renewal and indefinite proliferation (Wang et al., 2008, Dirkse et al., 2019). Additionally, a study of single cell RNA-seq from five primary GBMs found a continuous gradient of GSC-associated gene expression, rather than distinct populations. Studies have shown evidence of the microenvironment-induced adaption by GSCs, including to hypoxic conditions and in complex *in vivo* microenvironments (Dirkse et al., 2019). There are theories that tumour cells that exist in a plastic

state can drive treatment resistance as cells with pre-existing resistance are selected for and can be adapted towards under therapeutic pressures. However, studies of both radiotherapy (Bao et al., 2006) and chemotherapy (Dirkse et al., 2019) showed limited shifts in cellular state as a mechanism of resistance so if true it is likely treatment-specific. These studies add to the ever-evolving concept and complexity of GSCs.

1.3.2 Evidence for GSCs

The debate surrounding the CSC theory has been recent but a hierarchical structure for cancer was first proposed almost two hundred years ago. As early as the 1800s, it was proposed that cancer was initiated from remnants of embryonic tissues and the morphological heterogeneity of tumour cells was observed using light microscopy. Identification and isolation of CSCs was first described almost three decades ago in haematopoietic malignancies. A study in 1994 identified a proliferative population of cells that had the capacity to initiate acute myeloid leukaemia (AML) (Lapidot et al., 1994). Further characterisation of this population of AML-initiating cells in 1997 described a cellular hierarchy driven by these tumour initiating cells with differentiating, proliferative and self-renewal capacities (Bonnet and Dick, 1997), in keeping with the present-day definition and understanding of CSCs.

Isolation of CSCs in solid malignancies began in the early 2000s, with Singh et al the first to describe a brain tumour-initiating population of cells in 2003 (Singh et al., 2003). They isolated brain tumour cells from paediatric brain malignancies and through a limiting dilution assay (LDA) they found between 0.3-25.1% of isolated cells formed primary spheres. These spheres were non-adherent, proliferative and expressed nestin and CD133, known NSC markers, but did not express markers of differentiation. They also showed the self-renewal capacities of these cells, as when dissociated they formed secondary tumour spheres, and their self-renewal capacities correlated with tumour grade. Lastly, they displayed evidence of recapitulation of parental tumour, as dissociated spheres grown in differentiating, adherent conditions resulted in cells preferentially expressing markers correlating to the original tumour phenotype (Singh et al., 2003). Singh et al went on to show that this tumour-initiating population of cells were capable of initiating tumours *in vivo* (Singh et

al., 2004). They isolated $CD133^+$ cells from a range of human brain tumours including GBM and found that as few as 100 $CD133^+$ cells injected intracranially into NOD-SCID mice could produce a tumour that was phenotypically similar to the original tumour, whereas up to 100,000 $CD133^-$ cells were not able to initiate a tumour *in vivo*. At a similar time, Galli et al also investigated a tumour-initiating stem cell, with a focus on GBM (Galli et al., 2004). They disaggregated GBM tumours and cultured cells in serum-free conditions with growth factors, and found all tumours formed neurospheres at rates of 0.5-31.0%. *In vitro* validation of these cells as GSCs found that half of their GBM specimens established long-term cultures indicative of sustained proliferation, they showed multipotency through generation of neurons, astrocytes and oligodendrocyte-like cells and all could generate secondary clonal spheres. *In vivo* analysis showed 100% uptake of tumours by intracranial injection. Additionally, despite tumour generation being much slower than commercial GBM cell line U87, the tumours showed a marked resemblance to GBM tissue patterns (necrosis, vascular proliferation, infiltration) whereas U87 tumours showed no GBM-specific features (Galli et al., 2004). They also demonstrated the ability of these cells to generate tumours by serial transplantation. These studies supported the CSC theory in solid tumours, and since the identification and isolation of GSCs, most studies have focused and utilised this population of cells for more phenotypically accurate *in vivo* models.

1.3.3 Models of GSCs

GSCs are exclusively cultured under serum-free conditions, based on the long-established knowledge that serum results in terminal differentiation of NSCs *in vitro*. In addition, optimal conditions for maintenance of undifferentiated NSCs includes culturing with the supplements epidermal growth factor (EGF) and basic fibroblast growth factor (bFGF). Lee et al established how critical these conditions were for GSCs to closely match the primary tumour genotype and phenotype (Lee et al., 2006a). The maintenance of GSCs under serum-free conditions with the addition of EGF and bFGF is almost universally accepted and utilised as a medium, but additional supplements and additives remain subjective and lack standardisation (Zhang et al., 2020). Isogenic bulk cells, which are derived from the same parental primary GBM cell line as their paired

GSCs, can be cultured and maintained in medium containing foetal calf serum (FCS) to promote differentiation.

As discussed previously, isolation and identification of GSCs depends upon the key characteristics of CSCs, namely self-renewal, maintained proliferation and ability to recapitulate parental tumours *in vivo*. The gold standard assay for assessing tumour-initiating cells within a population is the *in vivo* LDA. An LDA aims to identify the frequency of active cells. Serial cell dilutions of both CSC and differentiated tumour cells are injected into immunocompromised mouse models and assessed for the formation of tumours. Through statistical analysis and comparisons of tumour initiation between CSCs and differentiated cells, a CSC frequency can be estimated (Hu and Smyth, 2009). It also assumes a single-hit hypothesis, critical for the CSC theory, whereby a single cell is sufficient or responsible for tumour-initiation as opposed to multiple cells together. It is a very time-consuming assay, with several cell dilutions required including dilutions that result in both positive and negative responses, and has therefore not been utilised very often in solid tumours, often being replaced by an *in vitro* sphere-formation LDA (O'Brien et al., 2010).

Sphere formation assays are utilised extensively in stem cell research as it can assess self-renewal, proliferation and differentiation. Sphere forming assays were first used to identify NSCs. Reynolds et al plated dissociated adult mouse brains in adherent conditions, and observed a small proliferative population, initially adherent but subsequently detaching and forming spheres (Reynolds and Weiss, 1992). These spheres were positive for nestin, a previously described embryonic brain stem cell marker, and formed secondary spheres when disaggregated. The removal of EGF prevented further proliferation and transfer to an adherent surface resulted in differentiation to neurons and glial cells (Reynolds and Weiss, 1992). This was the first evidence of multipotent brain stem cells and the utility of sphere-forming assays.

Since the discovery of GSCs and the utility and ease of the neurosphere formation assay, it has become commonplace in GSC research, however there are some limitations and considerations. There is evidence that not all neurospheres are formed from GSCs. Transit-amplifying cells are rapidly dividing secondary precursors which generate neuroblasts but have been shown to form

neurospheres due to being EGF-responsive (Pastrana et al., 2009, Doetsch et al., 2002). It therefore has been criticised as a uniquely GSC-specific detection method, and may be better described as evaluating the potential of a cell to have the characteristics of and behave as a GSC in an *in vitro* environment (Pastrana et al., 2011). Additionally, careful consideration needs to be taken when determining cell density, since an absolute requirement for neurosphere classification is its derivation from a single cell. A cell density too high can result in cell aggregation and therefore would not be truly clonal. For defining GSC potential via neurosphere assay, ideally one cell per well is plated, however a low cell density per well can be used for assessing proliferation or survival with the caveat that likely not all spheres are clonal.

Neurosphere assays can be used for assessing cytotoxicity of drugs that target GSCs. However, comparisons of GSCs and their adherent paired tumour bulk cells are often carried out. Therefore, there has been a desire to establish an adherent GSC model. Adherent GSC conditions can be established through the introduction of an extracellular matrix (ECM) to culturing flasks and plastics. Pollard et al sought to investigate the applicability of adherent GSCs, as they also postulated that it would address the aforementioned limitations of neurospheres, namely progenitor cell growth in suspension, clonal aggregates and additionally the non-uniform access to growth factors which can drive differentiation (Pollard et al., 2009). They demonstrated successful derivation of adherent GSCs from malignant GBM, at rates higher than found for derivation of spheres, that displayed GSC characteristics and initiated tumours *in vivo*. Concurrently, Al-Mayhani et al found improved efficiency of GSC derivation from tumours by sphere formation and subsequent growth as a monolayer (Fael Al-Mayhani et al., 2009). The GSCs grown as a monolayer were able to form tumours *in vivo*, with invasive properties and genotypes similar to that of the parental GBM tumour, validating this model for GSC enrichment. This presented a different GSC culture methodology, with advantages for drug screening and comparisons to adherent cell lines.

1.3.4 GSC markers

As has been touched on briefly, there are markers for GSCs utilised for characterisation and isolation, however there are many limitations. The most

frequently used GSC marker is the cell surface marker CD133. CD133 is a five transmembrane protein first identified as a marker of haematological stem cells (Miraglia et al., 1997) which is encoded by the Prominin 1 (PROM1) gene. A few years later it was used to identify self-renewing and pluripotent central nervous system (CNS) stem cells (Uchida et al., 2000), and a few years after that $CD133^+$ cells were identified in GBM that initiated tumours *in vivo* (Singh et al., 2004, Yuan et al., 2004). Despite initial promise and its widespread use as a GSC marker, many studies since have found both $CD133^-$ cells with GSC properties and identified GBM populations with no $CD133^+$ cells, as will be detailed below.

Beier et al were the first to describe a $CD133^-$ GSC population. They identified classical $CD133^+$ non-adherent neurospheres with multipotent and tumorigenic properties, however they also identified a subset of $CD133^-$ neurospheres, that also had GSC properties (Beier et al., 2007). These spheres had self-renewal and pluripotent capabilities and initiated tumours *in vivo*, whereas $CD133^-$ cells derived from $CD133^+$ neurospheres did not. They proposed that these $CD133^-$ sphere-forming cells represent a subset of GSCs, distinct from $CD133^+$ GSCs in terms of molecular, genetic and growth profiles (Beier et al., 2007). Several other studies also presented similar results showing the *in vivo* tumorigenicity of $CD133^-$ cells (Joo et al., 2008, Ogden et al., 2008, Fael Al-Mayhani et al., 2009, Son et al., 2009). Additionally, there are varying reports on how many tumour cells express CD133. Looking at dissociated tumours, Son et al reported 50% of tumours had no CD133 detectable by fluorescence-activated cell sorting (FACS) analysis (Son et al., 2009), whereas by a similar method Brescia et al detected $CD133^+$ cells in all dissociated tumours, albeit 50% of these had <1% $CD133^+$ cells (Brescia et al., 2013). Reporting of CD133 tumour positivity by other studies have set a cut off at 3% (Beier et al., 2007, Joo et al., 2008) and at 2% (Ogden et al., 2008), so there may be inconsistencies in reporting of absolute CD133 positivity. The potential absence of CD133 expression in some GBM tumours and the presence of GSC-like $CD133^-$ cells raises doubts on CD133 as a universally suitable GSC marker.

Other markers of GSCs have been proposed and analysed. The next most frequently discussed marker is nestin. Nestin is an intermediate filament protein and is a known marker of NSCs, important for their self-renewal capacities (Park

et al., 2010). Several early studies showed a correlation between nestin and undifferentiated patient derived neurospheres (Tunici et al., 2004, Hemmati et al., 2003) but despite its proposal as a GSC marker, subsequent studies have shown varying results. Lu et al showed rat-derived GBM clones with high nestin formed tumours significantly faster than low nestin expression (Lu et al., 2011), and Jin et al found nestin$^-$ cells formed smaller neurospheres than nestin$^+$ cells (Jin et al., 2013). However, the reliability of sphere size and speed of tumour growth as a measure of stemness has been questioned. Additionally, nestin$^+$ cells only formed spheres at a rate of 43% (Jin et al., 2013) and conversely, nestin$^-$ cells formed tumours *in vivo* with 80% uptake (Prestegarden et al., 2010) which raises questions about nestin's validity to solely identify GSCs. Nestin likely correlates with GSC populations, as Matsuda et al showed knockdown of nestin suppressed stemness in glioma cells by a sphere-forming assay (Matsuda et al., 2015), however like CD133 it may be identifying only a subpopulation of GSCs.

A whole host of other markers of GSCs have been proposed and studied. SOX2 (SRY-box 2) was detected in tumour-derived neurospheres, both differentiated and undifferentiated (Hemmati et al., 2003) but was found to be crucial for maintaining stemness and tumorigenicity in CD133$^+$ GSCs (Song et al., 2016). Other proposed GSC markers include NANOG (Niu et al., 2011, Ben-Porath et al., 2008), CD15 (Son et al., 2009), OLIG2 (oligodendrocyte transcription factor 2) (Ligon et al., 2007), CD44 (Liu et al., 2006) and OCT4 (octamer-binding transcription factor 4) (Ben-Porath et al., 2008). Due to the large array of proposed markers and varying reliability, identification of a universally applicable marker remains a challenge. Individual markers may be informative but cannot be conclusively linked to GSC phenotype on their own. A panel of markers, or potentially different markers identifying different subtypes of GSCs, may be the best strategy. Until then, CD133 remains the most utilised and well characterised GSC marker.

1.3.5 Clinical relevance of GSCs

The interest in GSCs and the desire to identify this subpopulation of GBM tumour cells is due to their treatment resistance and the self-renewal capacities driving tumour recurrence, a frequent and almost universally deadly occurrence. Recurrent GBM has been associated with an increase in CD133 positivity when

compared to paired primary GBM tumours (Liu et al., 2006), supporting the role of GSCs in resisting therapies and driving recurrence. There is also evidence of a correlation between GSCs and survival. Zeppernick et al studied 95 gliomas, of which 42 were GBM, and they found that the proportion of $CD133^+$ cells was a significant prognostic factor for adverse progression free survival (PFS) and overall survival (OS), independent of grade or extent of resection (Zeppernick et al., 2008). Pallini et al found similar results in 44 GBM patients treated with resection, where adverse PFS and OS correlated with both *in vitro* generation of neurospheres and >2% $CD133^+$ cells (Pallini et al., 2008). Metellus et al found high CD133 mRNA expression also correlated with adverse PFS and OS independently of resection or MGMT status (Metellus et al., 2011).

Eramo et al showed enhanced chemoresistance in undifferentiated primary GBM spheres that also recovered and proliferated at higher rates after removal of chemotherapy, in keeping with the treatment-resistant features of GSCs driving recurrence (Eramo et al., 2006). However, GSC sensitivity was compared to Jurkat cells, erythrocytes and chemosensitive tumorigenic small cell lung cancer (SCLC) stem cells, which was a limitation to this analysis as it did not provide evidence of differential sensitivities within GBM subpopulations. Shortly after, Liu et al made comparisons on CD133 sorted GBM cells, and consistently found enhanced chemoresistance in $CD133^+$ cells, including to TMZ (Liu et al., 2006).

Enhanced radioresistance of GSCs was first presented by Bao et al who showed irradiation (IR) enriched a $CD133^+$ subpopulation relative to untreated cultures and in a xenograft model (Bao et al., 2006). They found IR did not enrich for $CD133^+$ cells in a $CD133^-$ population, indicative of survival and enrichment of a $CD133^+$ population as opposed to a change in differentiation status of cells. Investigations into the mechanisms of $CD133^+$ cell radioresistance found preferential IR-induced activation of DNA damage checkpoints via Western blot of key repair factors, leading to more efficient DNA repair assessed by comet assay and subsequent cell survival (Bao et al., 2006). Ahmed et al also observed increased radioresistance in GSCs in comparison to paired bulk cells by clonogenic assay and similarly observed upregulated and activated DNA damage response (DDR) factors in GSCs in response to IR (Ahmed et al., 2015). This supported the work by Bao et al and confirmed cell cycle activation and

enhanced DNA repair in GSCs. Further mechanistic studies into the radioresistance of GSCs by Carruthers et al found that this increase in DDR activation was driven by increased replication stress (RS) in GSCs (Carruthers et al., 2018). They found $CD133^+$ GSCs had reduced replication fork speeds and increased stalled forks in comparison to $CD133^-$ cells, indicative of increased RS. They further confirmed this theory by inducing exogenous RS, which generated radioresistance in $CD133^-$ cells. The theory of increased RS being a targetable vulnerability of GSCs by Carruthers et al is the underpinning work for the rest of this thesis. RS and targeting RS will be reviewed in the rest of this chapter.

1.4 Replication stress

1.4.1 Definition

Varying definitions for RS have been used but the most frequently utilised is any process in the cell leading to problems during replication and slowing or stalling of replication forks. However, this may not encompass all types of RS, such as re-replication or aberrant origin firing, which will be discussed within this thesis. Throughout S phase there are numerous sources of stress the cell must deal with, which are often exacerbated during perturbed S phase, for example in cancerous cells. The cell has mechanisms of responding to RS, primarily through the apical kinase ataxia telangiectasia and Rad3-related protein (ATR), which helps the cell successfully complete DNA replication under stress to avoid DNA damage, genomic instability and cell death.

1.4.2 DNA replication coordination

DNA replication is a tightly coordinated cellular process, requiring duplication of the genome only once per cell cycle. If cells enter mitosis before completion of replication or following inappropriate re-replication of DNA, faithful chromosome segregation is interrupted causing genomic instability in daughter cells that can result in cell death or malignant cell growth. This regulation is coordinated through firing of replication origins, as reviewed at length by Boos and Ferreira (Boos and Ferreira, 2019). The mechanisms and key factors involved in origin firing are illustrated in Figure 1.1. Replication initiation occurs after successive origin licensing and origin firing/activation. In G1 phase, origin

recognition complexes (ORC) bind to replication origin sites interspersed throughout the genome. Origin licensing occurs at these sites, whereby Chromatin Licensing and DNA Replication Factor 1 (CDT1) and Cell Division Cycle 6 (CDC6) facilitate loading of the minichromosome maintenance (MCM) helicase to ORC. In this state, the MCM complex is an inactive helicase and known as the pre-replication complex (pre-RC). Origin firing of licensed origins requires high levels of cyclin-dependent kinases (CDK) and Dbf4-dependent kinase (DDK), which increase as cells move into S phase which ensures the temporal location of active replication during S phase. The levels of CDK and DDK also work to prevent re-licensing of origins in S phase. Several replication factors bind to the complex, forming the pre-initiation complex (pre-IC), including the GINS four subunit complex, cell division cycle 45 (CDC45) and polymerase. An origins fires or becomes activated after conversion of the pre-IC into two active helicases, made up of the CMG complex (CDC45, MCM, GINS), that move away from the origin bidirectionally to form two replication forks.

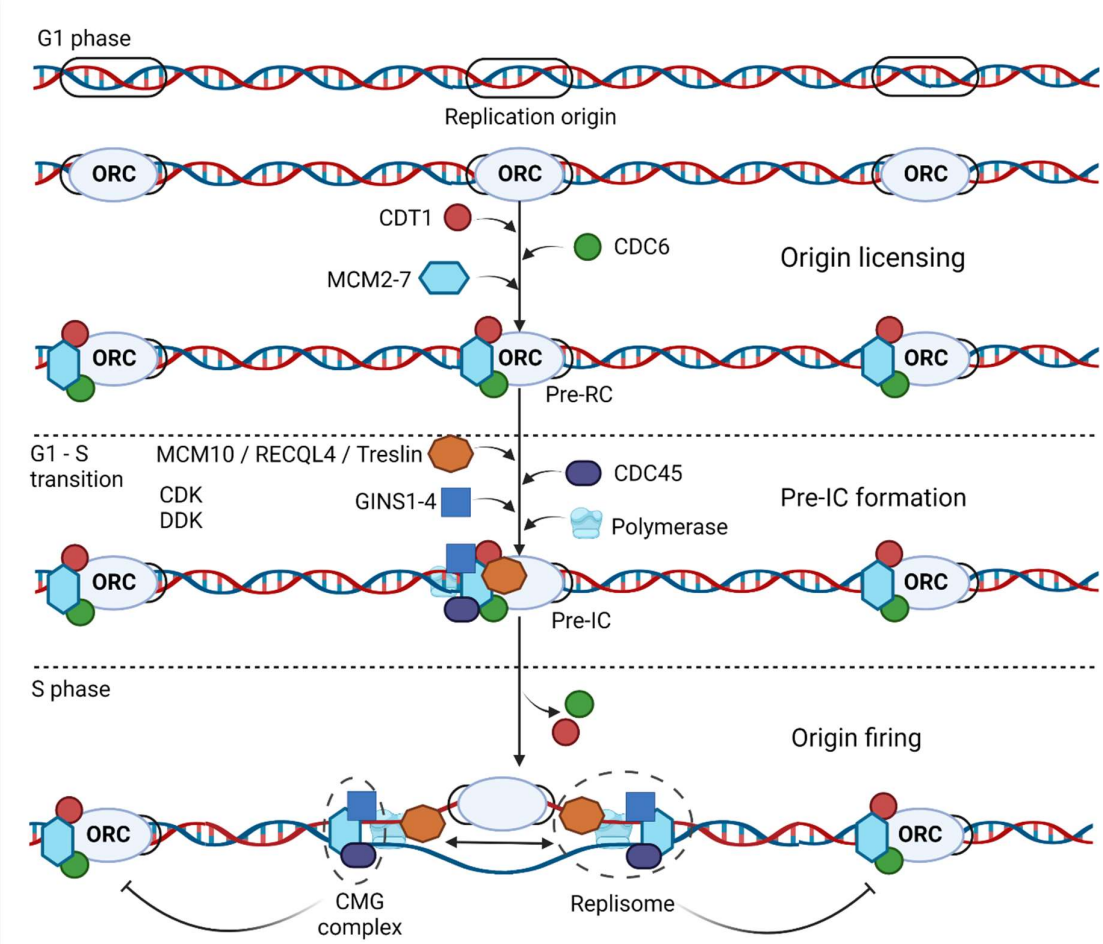

Figure 1.1. Origin firing mechanisms. In G1 phase origins of replication are licensed by binding of ORC and loading of MCM hexamer via CDT1 and CDC6 to form a pre-RC, which are interspersed throughout the genome. Licensed origins are activated as they move from G1 into S phase, due to increased levels of CDK and DDK which allows recruitment of several replication factors to form a pre-IC. Origins fire in S phase, where several factors dissociate and a replisome is formed of a CMG helicase and polymerase, which move away from the origin bidirectionally. Licensed origins in the vicinity of an active origin remain dormant unless required due to fork stalling. Created with BioRender.

It is estimated between one fifth and one third of all licensed origins fire during an unperturbed cell cycle (Cayrou et al., 2011, Fragkos et al., 2015), with the remaining origins remaining dormant. The number of active origins inversely influences replication fork velocity, and fork velocity can be adjusted to fully replicate the genome (Conti et al., 2007, Zhong et al., 2013). Several pre-RCs form a replicative unit or replicon, within which only one pre-RC is activated (Cayrou et al., 2011). The exact mechanisms are unknown, but adjacent origins to an active fork within a replication unit are repressed and remain dormant. In addition, dormant origins will normally be inactivated if their DNA is replicated by a fork in the vicinity. However, if this does not occur, for example if there is no fired origin nearby or when there is a stalled fork, dormant origins can fire to

help complete replication later in S phase. It is hypothesised that excess origins are licensed by MCM loading to provide backup capacity during RS, with dormant origins firing in the vicinity of stalled forks to aid in successful genome duplication (Ge et al., 2007, Ibarra et al., 2008, Woodward et al., 2006).

In addition, not all origins fire at the same time, with origins categorised as 'early', 'mid' and 'late' in respect to S phase. There are several theories as to how origins are temporally organised. Das et al showed that multiple MCM hexamers are loaded at each site and particular origins can be activated early in S phase by an increase in MCM loading (Das et al., 2015). They proposed that these origins fire early purely by an increased chance in origin activation correlating with MCM hexamers loading, and that early origins are identified due to a higher affinity for ORC binding (Das and Rhind, 2016). It has also been suggested that limited replication factors spreads origin firing throughout S phase, after a couple of studies showed overexpression of replication factors shifted late origins to early S phase (Mantiero et al., 2011, Tanaka et al., 2011), however this theory lacks a mechanistic explanation for preferential early and late firing by specific origins. It has also been proposed that nucleosome organisation may be important for replication timing, with more open chromatin associated with early origins (Soriano et al., 2014). Studies have also proposed Forkhead transcription factors (Knott et al., 2012) and histone acetylation (Vogelauer et al., 2002) as critical for origin firing timing. The exact mechanisms of replication timing and if any, all or some of these hypotheses play a part is yet to be fully determined. However, it is known that origins fire co-ordinately to achieve accuracy, speed and to balance consumption and distribution of replication machinery.

1.4.3 Causes of replication stress

There are many causes of RS, with the key sources of RS illustrated in Figure 1.2. For an in-depth review see Zeman and Cimprich (Zeman and Cimprich, 2014). Unrepaired DNA lesions, nicks, gaps and stretches of single stranded DNA (ssDNA) are some of the most frequently described sources of RS, and conversely can also be markers of RS. Some of these gaps in the DNA are naturally occurring DNA repair intermediates that can act as a replication barrier as persistent unrepaired DNA lesions frequently hinder replication fork progression. There are

many endogenous and exogenous sources of these DNA lesions, an in-depth review of which is beyond the scope of this thesis, but includes chemotherapy and RT, UV light and by-products of cellular metabolism. In addition, there are several hard-to-replicate regions of DNA that present challenges to replication machinery. These include repetitive DNA, secondary DNA structures such as hairpins and G-quadruplexes which are four-stranded DNA structures formed of GC-rich DNA (Hansel-Hertsch et al., 2017) and R-loops which are structures formed of RNA:DNA hybrids (Gan et al., 2011). Also, exhaustion of replicative factors has been shown to be a source of RS, most notably nucleotide supply. Anglana et al showed numerous cellular responses to a depletion of nucleotides, including slowed replication forks and increased active origin density (Anglana et al., 2003). Furthermore, work by Bester et al linked nucleotide supply not only to RS but also to oncogenesis, after the introduction of exogenous nucleotides rescued RS, RS-associated DNA damage and also decreased oncogene-induced transformation of cells (Bester et al., 2011). This led them to propose that uncoordinated nucleotide production fails to support normal replication and leads to subsequent oncogenic genome instability. Excess and unscheduled origin firing has been proposed as a source of nucleotide shortage (Beck et al., 2012).

Another proposed source of RS and genomic instability is collisions between replication and transcription machinery. In eukaryotes the existence of these collisions is still somewhat debated since replication is confined to S phase and transcription is largely restricted to cell cycle phases absent of ongoing replication (Wansink et al., 1994). However, evidence in support of collisions in eukaryotes include replication fork “pausing” at highly transcribed RNA polymerase II genes in *Saccharomyces cerevisiae* which was transcription dependent (Azvolinsky et al., 2009) and loss of DNA topoisomerase I (TOP1), which relaxes DNA supercoiling during replication, increased fork stalling due to R-loop formation during transcription (Tuduri et al., 2009). Probably most convincing was work by Helmrich et al which showed that long genes (>800kb) take more than one cell cycle to transcribe and also replicate late in S phase, making collisions almost inevitable (Helmrich et al., 2011). They found that these collisions resulted in formation of R-loops and caused DNA damage hot spots at common fragile sites (CFS).

CFS are chromosomal regions identified due to their propensity for RS-induced double strand breaks (DSB). CFS are sites of profound instability, driving chromosomal rearrangements in cancer and can be identified as breaks or gaps on chromosomes after induction of RS via aphidicolin. There are many hypotheses for CFS fragility, including their location within large genes which are transcriptionally active (Helmrich et al., 2011, Smith et al., 2006, Wilson et al., 2015), insufficient origins so a limited ability to rescue stalled forks (Letessier et al., 2011) and their replication late in S phase (Le Beau et al., 1998). Interestingly, replication fork speed was not reduced through CFS, suggesting there are no physical barriers resulting in their fragility (Letessier et al., 2011). It is believed that their fragility arises after entry into mitosis due to incomplete replication (Chan et al., 2009).

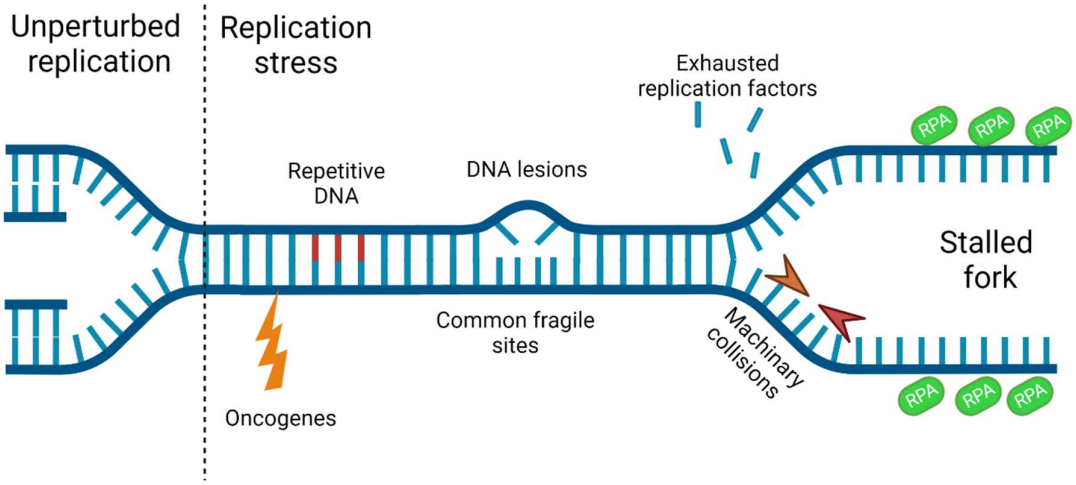

Figure 1.2. Causes of replication stress. In unperturbed S phase, replication forks and duplication of DNA can be carried out without problem. A stalled fork can occur due to RS which leads to long stretches of ssDNA bound by RPA. Sources of this stress include hard to replicate regions such as repetitive DNA and secondary structures, DNA lesions and CFS. Fork stalling can also occur due to collisions of transcription and replication machinery and due to exhausted replication factors like nucleotides. RS can also be induced by oncogenic activities. Created with BioRender.

Lastly, an increase in origin firing could be an indicator of relicensing of origins during the same cell cycle. Re-licensing and firing of forks, leading to replication of regions of the genome already duplicated is called re-replication, leading to genomic instability. As discussed in 1.4.2, through orchestrated activities of many replication factors and levels of CDK and DDK, licensing of pre-RC is tightly regulated to G1 phase, however if this regulation is lost it can lead to re-licensing and re-replication, as illustrated in Figure 1.3. Re-replication is associated with slower DNA synthesis, fork stalling, ssDNA and DSBs

(Archambault et al., 2005, Davidson et al., 2006, Fu et al., 2021). In addition, many studies have shown dysregulation of re-replication associated proteins in cancers, for example overexpression of CDT1 and CDC6 was linked to oncogenesis (Arentson et al., 2002, Gonzalez et al., 2006, Lau et al., 2007, Xouri et al., 2004).

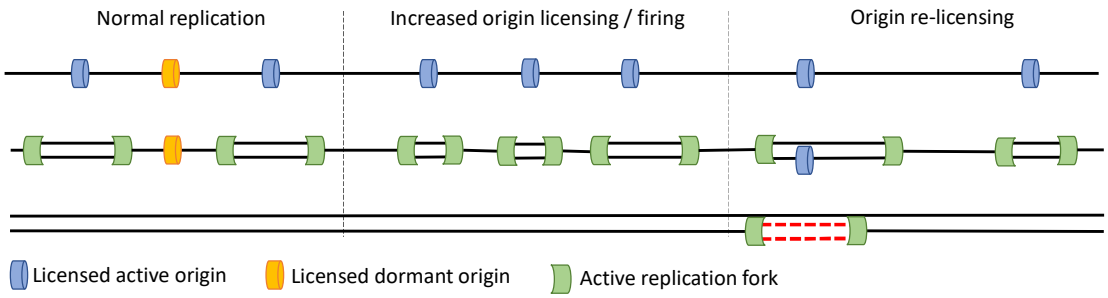

Figure 1.3. Re-replication by origin re-licensing. Tightly regulated origin firing leads to successful replication of the genome, only once per cell cycle. An increase of origin licensing and/or origin firing can lead to an increase in active forks, which can have detrimental effects on the cell in terms of replication/transcription machinery collisions and replication factor exhaustion but should ultimately lead to no re-replication as replication terminates as forks converge. Re-licensing of origins that have already fired early in S phase leads to replication of DNA already duplicated, and therefore areas of re-replication, as shown in red.

1.4.4 Consequences of replication stress

Prolonged and unresolved RS can have many detrimental effects on the cell, including fork collapse and under-replication of DNA, all potential sources of DNA damage and genomic instability. Fork collapse can lead to the formation of a DSB. The first reports of DSBs induced by stalled replication forks was by Michel et al, who observed the phenomenon in *E. coli* after identification of replication-dependent linearisation of circular DNA (Michel et al., 1997). Furthermore, a frequently used exogenous inducer of RS, hydroxyurea (HU) which depletes cellular deoxynucleotide triphosphate (dNTP) pools to stall forks, induced DSB (Hanada et al., 2007, Lundin et al., 2002). DSBs induced at stalled forks are dependent on the endonuclease methyl methanesulphonate (MMS) and the MMS ultraviolet-sensitive gene clone 81 (MUS81) and essential meiotic endonuclease 1 (EME1) complex (MUS81-EME1 complex) (Hanada et al., 2007). Hypotheses for how a collapsed fork forms a DSB include intentional DSB induction by the MUS81-EME1 complex to bypass irreversible stalled forks and initiate repair pathways, or persistent ssDNA in the vicinity of a stalled fork is susceptible to breakage (Lopes et al., 2006).

RS is frequently associated with aberrant origin firing and under-replication of the genome. Under-replicated DNA (UR-DNA) is frequently measured by p53 binding protein 1 (53BP1) nuclear bodies (53BP1NB), which were first identified by two corresponding studies in 2011 (Harrigan et al., 2011, Lukas et al., 2011). Lukas et al found that 53BP1NBs were induced by DNA damage or chromosomal aberrations, they increased with RS, were present primarily in G1 phase and produced symmetrical 53BP1NB numbers and patterns in daughter cells (Lukas et al., 2011). They hypothesised that under-replication of chromosomes could encompass and explain all these features. They proposed that UR-DNA bypassed G2 checkpoints and formed nuclear bodies sequestered by 53BP1, and the loci were converted to DNA lesions during mitosis. By ChIP-qPCR they found that 53BP1 was enriched at known CFS, confirming a link between UR-DNA and RS. Harrigan et al similarly observed RS-induced incomplete DNA synthesis in S phase resulting in the formation of nuclear sub-compartments in the subsequent G1 phase, marked by 53BP1 (Harrigan et al., 2011). These were the first investigations into the fate of under-replicated genomic loci and description of 53BP1NB as a marker of UR-DNA.

The effect of RS on genomic stability has been characterised, including through structures such as chromatin bridges, micronuclei and ultrafine bridges (UFBs). Chromatin bridges, also known as bulky or anaphase bridges, occur when sister chromatids fail to segregate during mitosis. If RS is unresolved, cells with UR-DNA can enter mitosis leading to aberrancies including chromatin bridges. Chan et al proposed that RS-induced chromatin bridging occurs after inefficient resolution of replication intermediates at hard to replicate regions such as CFS (Chan et al., 2009). Studies by Naim et al have implicated the endonucleases ERCC1 (Excision repair cross complementation group 1) and MUS81-EME1 complex in processing of UR-DNA at CFSs, since their depletion resulted in chromatin bridges and accumulation of DNA damage (Naim et al., 2013). Chromatin bridges can be visualised by conventional staining of DNA and confocal microscopy, hence often being described as “bulky”. Conversely, UFBs cannot be identified by staining of DNA and were only identified in 2007 after investigations of chromosome segregation found ultrafine DNA bridges which did not stain for conventional DNA markers but did for BLM (Bloom’s syndrome RecQ like helicase) (Chan et al., 2007). Mutations in BLM cause Bloom’s syndrome

which is associated with cancer predisposition and chromosomal instability. Subsequent studies have found that a subset of UFBs are prevalent at CFS due to sister chromatids at these hard to replicate loci being interlinked by replication intermediates, and they can be induced by RS (Chan et al., 2009). These were subsequently called ‘fragile site-UFB’ (FS-UFB). Other described UFBs include telomere- and centromere-UFBs, also both genomic regions with inherent replication difficulties (Liu et al., 2014).

Micronuclei are extranuclear bodies containing damaged chromosome fragments or whole chromosomes that were unsuccessfully incorporated into the main nuclei during mitosis. A nuclear membrane forms around the excluded chromosome or fragments, leaving small nuclear bodies which can be identified by confocal microscopy. They can be utilised to assess genotoxic events, genetic damage and chromosomal instability. There are several accepted mechanisms by which whole or fragmented chromosomes become separated. Centromere and spindle apparatus failure leading to a lagging chromosome during anaphase has long been accepted as a mechanism of micronuclei formation, but there has been further development into factors affecting their formation. Unrepaired DNA damage leading to acentric chromosome fragments has been linked to micronuclei, often associated with DNA replication and repair factors including DNA-damage response mediator protein TOPBP1 (DNA topoisomerase 2-binding protein 1) (Leimbacher et al., 2019), PrimPol (primase and DNA directed polymerase) (Bailey et al., 2019) and chromatin remodeler ATRX (alpha thalassemia/mental retardation syndrome X-linked), which is associated with CFS stability (Pladevall-Morera et al., 2019). Xu et al showed that RS induced the formation of micronuclei that stained positively with DNA damage marker γH2AX (γH2A histone family, member X) (Xu et al., 2011). Further mechanistic studies into the effects of mild RS on chromosomal instability by Wilhelm et al proposed that RS leads to premature centriole maturation and subsequent premature disengagement, causing transient multipolar spindles, lagging chromosomes and micronuclei (Wilhelm et al., 2019). Lastly, it has been proposed that resolution of chromatin bridges leads to fragmented chromosomes and subsequent micronuclei formation (Hoffelder et al., 2004).

1.4.5 Replication stress response

Since RS can have such detrimental effects on the cell, in terms of DNA damage, genomic stability and cell fate, it is critical that the cell has effective response mechanisms to deal with the source of the stress and subsequently restart stalled replication forks to complete replication. The key responder to RS is the ATR kinase, which acts to stabilise stalled forks, suppress late origin firing and activate cell cycle checkpoints to allow the cell time and resources to resolve the stress. For a comprehensive review of ATR's activities see Saldivar et al (Saldivar et al., 2017). ATR is a phosphoinositide 3-kinase-related (PIKK) protein kinase, which shares sequence and functional homology to ataxia telangiectasia mutated (ATM) and DNA-dependent protein kinase (DNA-PK), both involved in the DDR primarily via response to DSBs. Homozygous loss of ATR, but not ATM or DNA-PK, leads to embryonic lethality, highlighting how critical this RS response is for cell and for *in vivo* survival (Brown and Baltimore, 2000, de Klein et al., 2000).

A summary of the response of ATR to RS is illustrated in Figure 1.4. The ssDNA generated at a stalled fork which is bound by replication protein A (RPA) acts as a signalling platform for ATR-interacting protein (ATRIP), an obligate binding protein which signals to ATR and forms an ATR-ATRIP complex (Zou and Elledge, 2003). It has been shown that the length of ssDNA induced is critical for ATR activation (MacDougall et al., 2007), which explains why other activities of RPA loading on ssDNA does not activate ATR, such as ssDNA induced at ongoing replication forks. A checkpoint clamp containing RAD9-HUS1-RAD1 (9-1-1) is then recruited independently of ATR-ATRIP along with TOPBP1, which activates ATR (Kumagai et al., 2006, Lee et al., 2007) and a resulting signalling cascade via phosphorylation of ATR's downstream effectors, primarily checkpoint kinase 1 (Chk1) (Liu et al., 2000). Responses to a stalled fork include acting locally to stabilise, repair and restart the fork and acting globally to suppress late origin firing to preserve resources and to halt cell cycle progression to ensure successful genome duplication before entry into mitosis. Conversely to suppression of global origin firing, activation of dormant origins in the vicinity of the stalled fork takes place as a mechanism to overcome un-replicated regions. Accordingly, MCM proteins have been shown to be targets of phosphorylation by ATR (Cortez et al., 2004).

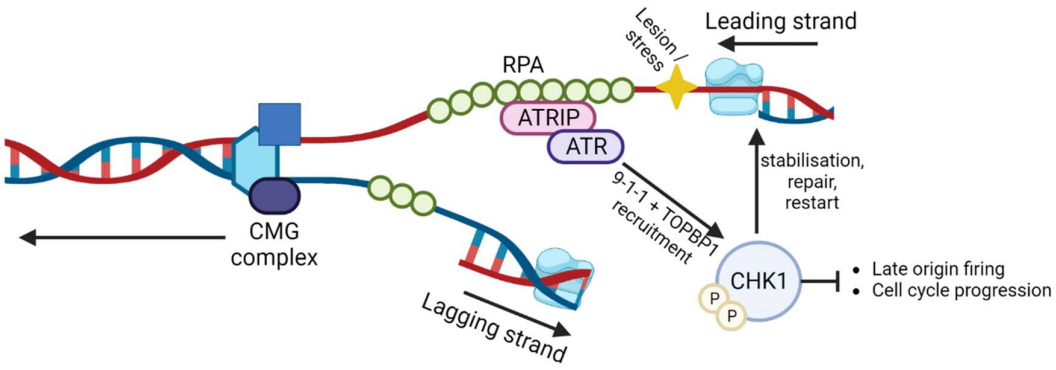

Figure 1.4. ATR response to replication stress. RS causes a fork to stall or slow, which leads to stalled polymerases, while the CMG helicase continues to unwind DNA leaving behind stretches of ssDNA bound by RPA. In this example, the lagging strand is ongoing, whereas the leading strand has stalled in the face of a lesion or stressor. This results in longer stretches of ssDNA which signals the ATRIP-ATR complex, and recruitment of the 9-1-1 complex and TOPBP1 allows for phosphorylation of Chk1. Responses to activated ATR include local activities on the stalled fork such as stabilisation, repair and restart and globally acting to suppress late origin firing and cell cycle progression. Created with BioRender.

A key response to RS by ATR is inhibition of cell cycle progression. ATR acts on the intra S phase checkpoint and the G2/M checkpoint, independently of p53 which has critical checkpoint functions elsewhere in the cell cycle. The intra S phase checkpoint functions to slow DNA replication in the face of RS by controlling origin firing and replication fork speed. ATR, via phosphorylated Chk1, acts to block G2/M cell cycle progression via the target substrate CDC25 (cell division cycle 25) phosphatase. In unperturbed cell cycles, CDC25 phosphatases dephosphorylate Cdk1 (cyclin dependent kinase 1) which in turn phosphorylates and inactivates Wee1, all of which allows entry into mitosis. Activated ATR works to block this commitment to mitosis by phosphorylation of CDC25 phosphatases.

To control global origin firing, activated ATR prevents Cdc45 loading at replication origins, believed to be via down-regulating CDK and DDK or via ATR-dependent phosphorylation of the histone MLL (mixed lineage leukaemia) (Liu et al., 2010). How ATR acts to both supress global origin firing but activate local origins remains enigmatic. As reviewed by Yekezare et al, there are several proposed models for this phenomenon but no consensus (Yekezare et al., 2013). These include a “passive” model whereby a delay to global suppression allows local dormant origins to fire or a model whereby origins within a local cluster may have passed a critical step in activation which global suppression cannot

overcome. However, no studies have determined if any of the proposed models are accurate.

There are several mechanisms that have been proposed for fork rescue and/or restart, based on studies of helicase, nuclease and homologous recombination (HR) factors, as illustrated in Figure 1.5 (Petermann and Helleday, 2010). If these fail or the stress cannot be resolved, the stalled fork can collapse and become inactivated either via replisome dissociation or generation of a DSB. Many methods of fork rescue do not resolve the lesion, rather work around it. These include activation of dormant origins (Ge et al., 2007, Woodward et al., 2006), repriming of replisome machinery past the lesion leaving a ssDNA gap which collapses into a DSB and is repaired by HR (Elvers et al., 2011) and the use of lesion bypass pathways whereby the replicative polymerase is replaced with a translesion synthesis polymerase (Mailand et al., 2013). Lastly, fork remodelling via fork reversal to form a 'chicken foot' structure can allow for fork restart by providing a sister chromatid as a template. Replication fork reversal involves turning a three-way junction at the replication fork to a four-way junction by regression and annealing of the two newly replicated strands. It has been proposed that a transient DSB can form at reversed forks, which are more amenable to DNA repair than stalled forks and replication intermediates, to allow replication to continue (Hanada et al., 2007, Shimura et al., 2008). A detailed review of replication fork restart mechanisms can be found by Petermann and Helleday (Petermann and Helleday, 2010). ATR is critical for prevention of fork collapse. This was shown via its interactions with SMARCAL1 (SWI/SNF-related matrix-associated actin-dependent regulator of chromatin subfamily A-like protein 1) which is involved in fork remodelling for repair and restart (Betous et al., 2012), and regulation of these activities relied on phosphorylation by ATR to prevent collapse (Couch et al., 2013).

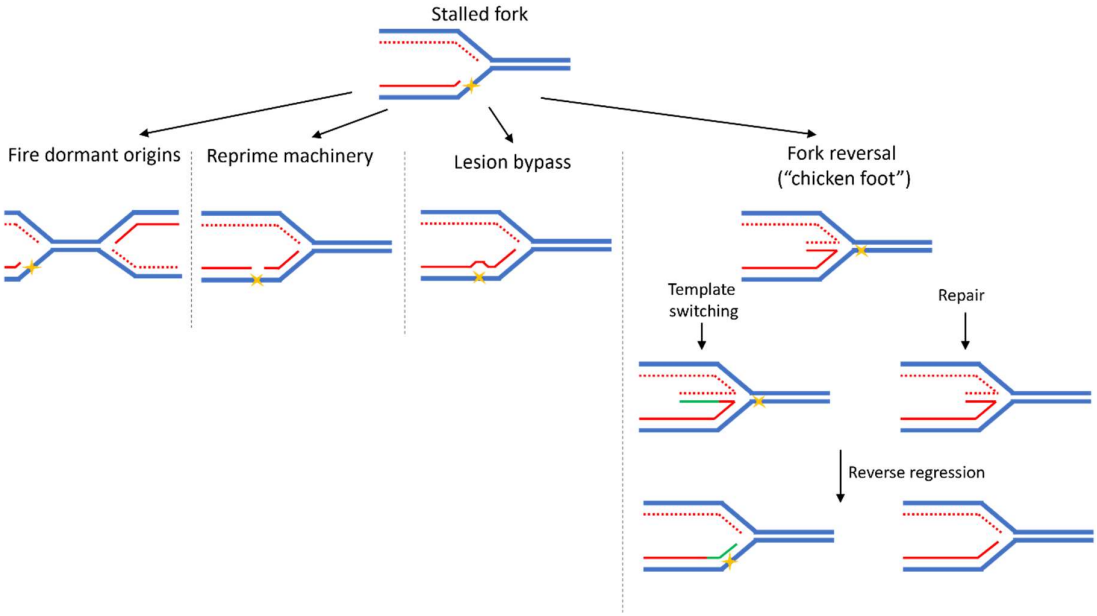

Figure 1.5. Stalled fork rescue mechanisms. Dormant origins can fire in the vicinity of a stalled fork to complete replication. Repriming of replication machinery past the lesion can allow for the fork to carry on replicating, however this results in a gap in the DNA which needs resolved, potentially by forming a DSB. There are also polymerases, called translesion synthesis polymerase, whose activities can allow replication over the lesion, although this does not resolve the problem. Lastly, a stalled fork can be remodelled by fork reversal to form a chicken foot structure. This can allow for sister chromatid template switching, known as a Holliday junction, to continue replication and subsequent resolution of the reversed fork. If the lesion is repaired the fork can be reversed again, however the chicken foot structures are believed to be susceptible to nuclease attack and may be a source of fork collapse.

In addition to these well-established roles of ATR in the RS response, Casper et al showed that ATR was critical for CFS stability (Casper et al., 2002), in keeping with ATR's role in the RS response and CFS sensitivity to RS. ATR is also critical for the prevention of re-replication via S phase checkpoint activation. Re-replication induces ssDNA, which Liu et al hypothesised served as a signal for ATR activation since loss of ATR induced more re-replication (Liu et al., 2007). Furthermore, studies have linked the ATR-mediated Fanconi anaemia pathway in responding to re-replication and subsequent G2/M checkpoint activation (Zhu and Dutta, 2006). Overall, ATR is implicated in numerous responses to RS during S phase to ensure faithful genomic duplication and stability.

A more recently discovered post-replicative response to RS-induced UR-DNA, outwith ATR, is mitotic DNA synthesis (MiDAS). With the knowledge that replication occurs late in S phase at CFSs, Minocherhomji et al sought to further characterise when DNA synthesis occurs in CFSs by inducing RS through low dose aphidicolin and assessing incorporation of the thymidine analogue EdU (5-Ethynyl-2′-deoxyuridine) (Minocherhomji et al., 2015). They found that 40% of

mitotic cells contained EdU foci, 80% of which co-localised with CFS markers and chromosome breaks. Their work highlighted the existence of MiDAS at CFSs in response to RS and explored the role of MiDAS in counteracting potentially lethal chromosome mis-segregation, primarily at chromosomes 3 and 16 which contain CFS most prone to form lesions. Recent high-resolution mapping has further linked RS-induced MiDAS with CFS, which remain largely un-replicated even in late S phase before MiDAS compensates to help complete successful DNA synthesis (Ji et al., 2020, Macheret et al., 2020). MiDAS is interesting as it has been hypothesised to be in a balance with 53BP1NB in response to UR-DNA. Inhibition of MiDAS factors have increased the numbers of 53BP1NB (Bertolin et al., 2020, Minocherhomji et al., 2015). Additionally, it has been suggested that increased UR-DNA could saturate MiDAS capabilities and induce 53BP1NB (Bertolin et al., 2020). Alternatively, since 53BP1NB are present in unperturbed cells but MiDAS is minimal, there could be preferential detection and resolution via 53BP1NB until RS reaches a threshold requiring more wide-spread resolution. This could be due to differing repair accuracies between the two mechanisms (Bertolin et al., 2020).

Figure 1.6 outlines the proposed response to UR-DNA at CFS and the consequences of incomplete UR-DNA resolution by MiDAS, and highlights the key genes involved. FANCD2 (Fanconi anaemia group) and FANCI dimers bind to the site of UR-DNA that has progressed into mitosis, forming a crosslink between sister chromatids in the form of a UFB (Chan et al., 2009). Work on chromosomal mapping of sites of MiDAS by Macheret et al found that the main role of MiDAS is to complete replication of the genome, with MiDAS mapping to all known CFS (Macheret et al., 2020). Minocherhomji et al explored the critical role of several factors on MiDAS (Minocherhomji et al., 2015). The MUS81-EME1 nuclease complex is known to promote CFS expression (Ying et al., 2013), and in keeping with that they found that loss of either complex factor inhibited MiDAS, assessed by EdU incorporation in mitotic cells. Additionally, loss of SLX4 which acts as a scaffold for MUS81-EME1 (Wyatt et al., 2013) lead to reduced MiDAS at CFS, CFS expression and recruitment of MUS81 to CFS (Minocherhomji et al., 2015).

Minocherhomji et al also discovered depletion of POLD3 (DNA polymerase Delta 3), a subunit of DNA polymerase δ which associated with mitotic chromatin after

RS, inhibited MiDAS at CFS (Minocherhomji et al., 2015). Overall, they proposed a model whereby SLX4 attracts MUS81-EME1 to cleave stalled forks and promote POLD3-dependent MiDAS. Following on from this work, Bhowmick et al hypothesised that the requirement for POLD3 in MiDAS suggested a potential role of a break-induced replication (BIR)-like process (Bhowmick et al., 2016). They therefore investigated HR factors and found only RAD52 was required for MiDAS following RS, while BRCA2 (Breast Cancer gene 2) and RAD51 were dispensable (Bhowmick et al., 2016). RAD52 was required for MUS81 and POLD3 recruitment in mitosis. They proposed that MiDAS was dependent on RAD52-mediated microhomology-driven BIR activities by D-loop formation.

Underpinning all of this work is evidence that MiDAS promotes chromosomal stability after RS-induced UR-DNA. Several studies have linked FANC proteins and BLM to chromosomal stability. Naim and Rosselli reported that FANCD2 localisation to RS-induced chromatid gaps limited aneuploidy and chromosomal instability in daughter cells, and together with BLM prevented the formation of micronuclei (Naim and Rosselli, 2009). Furthermore, BLM deficient cells display chromosomal instability, evidenced by chromatid gaps, micronuclei, increased FANCD2-associated UFBs and chromatin bridges (Chan et al., 2009, Chan et al., 2007). Chan et al provide evidence that BLM was required for FS-UFB resolution, not formation (Chan et al., 2009). Furthermore, they showed that a high proportion of micronuclei in BLM-deficient cells contained CFS DNA, consistent with unresolved FS-UFB leading to chromosomal breakage. Lastly, Minocherhomji et al provided evidence of increased FANCD2-associated UFB and 53BP1NB after SLX4 loss and proposed that the MUS81-EME1-POLD3 axis works to minimise chromosome mis-segregation and non-disjunction (Minocherhomji et al., 2015).

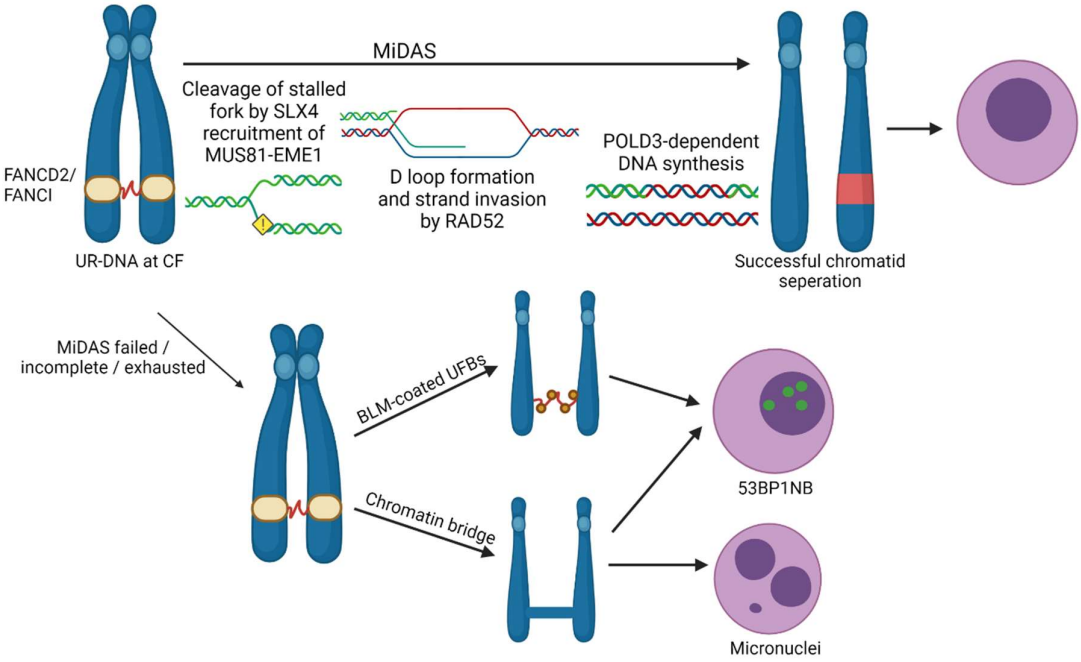

Figure 1.6. Response to UR-DNA at CFS by MiDAS. UR-DNA at CFS leads to sister chromatid bridging via FS-UFB, coated with BLM and marked by FANCD2 and FANCI dimers. Through a BIR-like process, SLX4 recruits the cleavage caspase MUS81-EME1 complex to sites of UR-DNA. This is resolved by RAD52-mediated microhomology-driven BIR activities and subsequent POLD3-dependent DNA synthesis to lead to MiDAS-associated successful completion of DNS synthesis and subsequent chromosomal stability. Loss of this process leads to persistent and increased BLM-coated FS-UFBs and bulky chromatin bridges, and subsequent chromosomal instability measured by chromosomal mis-segregation, 53BP1NB and micronuclei. Created with BioRender.

1.4.6 PARP and the replication stress response

Another more recently discovered factor of the RS response is poly(ADP-ribose) polymerase (PARP), via activities on the replication fork. The PARP family is made up of 17 proteins and is involved in many cellular processes including DNA repair and genomic integrity, chromatin remodelling, apoptosis and the stress response. PARP1 is the most well characterised member of the PARP family of enzymes. PARP1 has a critical function in the detection and repair of single strand breaks (SSB) via base excision repair (BER) but has also been shown to be involved in many other DDR pathways including nucleotide excision repair (NER), classical and alternative non-homologous end joining (NHEJ), HR and DNA mismatch repair. A full review of PARP's involvement in the DDR can be found by Chaudhuri and Nussenzweig (Ray Chaudhuri and Nussenzweig, 2017).

PARP activities are summarised in Figure 1.7. The recruitment of PARP1 to sites of damage is one of the earliest events in the DDR. Once activated PARP1 catalyses the post-translational polymerisation of ADP-ribose units (PAR) from

NAD^+ (nicotinamide adenine dinucleotide), which results in the attachment of chained PAR polymers to target proteins, termed PARylation. PARylation can occur at sites of DNA, target proteins and on PARP1 itself, known as auto-PARylation. Critically, the rapid degradation of PAR is crucial for PARP1 release from DNA and efficient DNA repair via steric hinderance of auto-PARylation (Zahradka and Ebisuzaki, 1982) and PAR-degrading enzymes such as Poly(ADP-Ribose) Glycohydrolase (PARG) (Uchida et al., 1993). PAR chains act as a scaffold for DDR proteins, resulting in their recruitment to sites of damage for repair (Altmeyer et al., 2015). PARP1 accounts for an estimated 90% of PARylation, but PARP2 and PARP3 also have known roles in the DDR (Beck et al., 2014). PARP1 and PARP2 have overlapping roles in the DDR and combined loss was embryonic lethal suggesting redundancy between the two enzymes (Hanzlikova et al., 2017, Menissier de Murcia et al., 2003).

More recently PARP's role in the RS response has been identified. Involvement of PARP in replication has long been implicated, having been found to be activated at newly replicated chromatin (Anachkova et al., 1989) and being described as part of the DNA "synthesome" by Simbulan-Rosenthal et al. They found that PARP1 co-purified with polymerases, helicases, topoisomerases, proliferating cell nuclear antigen (PCNA) and RPA by a series of centrifugation and chromatography steps (Simbulan-Rosenthal et al., 1996) and 15 of the 40 described replication complex proteins were PARylated (Simbulan-Rosenthal et al., 1999). Lastly, PARP1 was shown to be critical for recruitment of PCNA and TOP1 to the replication complex and for expression of polymerase α, primase and RPA (Simbulan-Rosenthal et al., 1998).

In terms of the RS response, PARP1 has been linked to replication fork speeds, fork reversal and restart, and PARylation at stalled forks. The first studies of PARP1 in the RS response was by Yang et al, who showed that cells depleted of PARP1 were hypersensitive to RS-inducing HU and displayed slow reactivation of stalled forks suggesting a role in fork restart (Yang et al., 2004). Subsequently, Bryant et al showed a connection between PARP1 and the RS response after they showed that PARP1 binds to stalled replication forks, signalled via gaps as small as four nucleotides in the DNA, resulting in PARylation and critical for cell survival during RS (Bryant et al., 2009). They also found that fork stalling was

independent of PARP activity, however replication elongation post RS was delayed with loss of PARP, also suggesting a critical role of PARP in resuming replication at stalled forks. Further investigations of the mechanisms of effective fork restart by Bryant et al found it co-localised with Mre-11 to promote fork restart via limited resection of the forks to allow for HR-mediated restart (Bryant et al., 2009). Analysis of protein abundance of replication fork machinery found PARP1 was present at normal and stalled forks but at similar levels at both fork types, whereas PARG was decreased at stalled forks, leading to the hypothesis that the increase in RS-induced PARylation could be due to reduced PARG activities as opposed to PARP1 (Dungrawala et al., 2015).

Studies have also shown a critical role of PARP1 in effective fork reversal, either by promoting fork reversal or stabilisation once in that state, which limited DSB formation and maintained genomic stability (Ray Chaudhuri et al., 2012, Zellweger et al., 2015). Mechanistically, Berti et al showed that PARP1 exerted its effects on replication fork restart via ATP-dependent DNA helicase Q1 (RECQ1) (Berti et al., 2013). They found that binding of PARylated PARP to RECQ1 inhibited its helicase activities and prevented unscheduled replication fork restart. Loss of PARP1 resulted in RECQ1-mediated fork restart under RS conditions and it has been hypothesised that this could lead to replication fork collapse and DSB as aberrantly restarted forks encounter unrepaired lesions (Berti et al., 2013).

Lastly, PARP1 has roles in regulating fork progression under RS conditions, with loss of PARP1 resulting in loss of slowed replication forks, which is a cellular mechanism to deal with DNA damage and RS (Ray Chaudhuri et al., 2012, Sugimura et al., 2008, Zellweger et al., 2015). PARP1-mediated fork progression has also been linked to RECQ1, suggesting a link between fork restart and fork progression activities via PARP1 (Zellweger et al., 2015). More recently, Genois et al showed a critical role of Coactivator Associated Arginine Methyltransferase 1 (CARM1) in these PARP1 activities, CARM1 promoted PARP1 association and PARylation at replication forks via enhanced binding (Genois et al., 2021). Loss of CARM1 reduced fork reversal and sped up replication forks, which was dependant on both RECQ1 and RAD18 which have roles in translesion synthesis. Lastly, Maya-Mendoza et al showed that loss of PARP not only prevented slowing

of forks upon RS but also resulted in replication fork acceleration (Maya-Mendoza et al., 2018). They proposed that PARylation acts as a suppressor of fork speed and a sensor of RS. Overall, these studies suggest PARP has critical roles in S phase, not only in the detection and restart of stalled forks but also maintaining fork speed to prevent RS in unperturbed S phase.

1.4.7 Replication stress and cancer

The most common human disease associated with RS is cancer, with some researchers suggesting RS be considered a 'hallmark' of cancer (Macheret and Halazonetis, 2015). In cancer, increased RS is inherently linked to oncogenes. Over 20 oncogenes have been implicated in inducing RS in cancer cells (Kotsantis et al., 2018). Importantly, oncogene-induced RS is believed to be one of the earliest drivers of genomic instability and tumorigenesis (Bartkova et al., 2005, Bartkova et al., 2006, Gorgoulis et al., 2005). Many oncogene activities that lead to RS are those previously discussed within this thesis, namely dysregulated origin firing (Di Micco et al., 2006, Dominguez-Sola et al., 2007), replication-transcription collisions (Jones et al., 2013), premature mitotic entry (Liu et al., 1995, Ohtsubo et al., 1995) and aberrant nucleotide metabolism. In addition, CFS are preferentially targeted by oncogene-induced RS (Tsantoulis et al., 2008). This almost universal phenomenon of increased RS in cancer has led many people to hypothesise that this provides a vulnerability of cancer cells. Cancer cells could be selectively targeted by inhibiting the cellular pathways that allow cancer cells to not only survive but also thrive with elevated RS, as evidenced by Carruthers et al who showed increased RS in GSCs drove radioresistance and cell survival via elevated DDR (Carruthers et al., 2018).

1.5 Therapeutic targeting of replication stress

RS is a major source of genomic instability in cancer. Genomic instability in cancer cells needs to be finely balanced as it drives tumorigenesis via increased mutational load but too much instability can be toxic to cells. Therefore, targeting the RS response is an appealing therapeutic strategy.

1.5.1 Inhibition of ATR

Before the advent of selective inhibitors of ATR, Murga et al showed the therapeutic potential of targeting ATR in a mouse model of Seckel syndrome, which is characterised by severe deficiency in ATR (Murga et al., 2009). They found that no tumours formed in their ATR-deficient model, even in the absence of p53, suggesting ATR loss is tumour suppressive. Development of inhibitors of ATR have long been hindered by the activities of ATR being restrained primarily to S phase, resulting in false positives from inhibitors that target cell cycle arrest and also due to high active site homology to other PIKKs including ATM and DNA-PKs. Historically, high dose caffeine was used to inhibit ATR, but this only induced a weak and non-selective inhibition (Sarkaria et al., 1999).

There were several developments of ATR inhibitors in 2011. Toledo et al developed a system whereby ATR was activated throughout the cell cycle and in the absence of DNA damage, overcoming previous problems with S phase specific activities (Toledo et al., 2008). This allowed them to screen 623 compounds for their ability to inhibit ATR *in vitro* (Toledo et al., 2011). These compounds were previously identified for their activities on phosphoinositide 3-kinases (PI3Ks) which have sequence similarities to PIKKs. Through this screen they identified two compounds which exhibited almost 100% inhibition of pan-nuclear phosphorylation of H2AX at 100nM, which they described as ATR-dependent. Both compounds abrogated cell cycle checkpoints, induced micronuclei and fragmented nuclei after IR but further analysis found they also acted on some PI3Ks.

The first discovery of a potent and selective ATR inhibitor (ATRi) was by Charrier et al, who screened a panel of novel inhibitors of ATR (Charrier et al., 2011). One of these inhibitors showed a >600-fold selectivity over related PIKKs, with an IC_{50} as low as 0.42μM. They demonstrated high potency of this ATRi as a single agent in an ATM-deficient cancer line, which also showed synergy with both IR and the chemotherapy cisplatin, whereas in normal fibroblasts the compound had no effect alone and combined effects were much reduced (Charrier et al., 2011). Further characterisation of one of these compounds, subsequently named VE821, was carried out by Reaper et al (Reaper et al., 2011). They also observed synergy with cisplatin exclusively in cancer cell lines and observed ATR

selectivity with minimal activity against other PIKKs and a large panel of unrelated protein kinases. VE821 inhibited phosphorylation of the ATR target Chk1, but phosphorylation of Chk2, a target of ATM, was not blocked. Again, they observed an increased potency in ATM-deficient cells lines, with the authors proposing that upon ATR inhibition cancer cells are reliant on the ATM and p53 axis to induce a cell cycle checkpoint response (Reaper et al., 2011). Subsequently, VE822, a close analogue of VE821, was studied both *in vitro* and *in vivo* and found to have improved pharmacokinetic (PK) results and ATR-specific potency, and sensitised pancreatic xenograft models to IR and chemotherapy without exacerbating normal tissue toxicity (Charrier et al., 2011, Fokas et al., 2012).

Since the discovery and characterisation of VE821 and VE822, other inhibitors have been described. Firstly, Astra Zeneca described and presented to the market an orally active and bioavailable ATR inhibitor, AZD6738. The first study of AZD6738 focused on non-small cell lung cancer (NSCLC) cell lines, and similarly to the initial studies with VE821, they found it could induce cell death as a single agent, enhanced the cytotoxicity of chemotherapies in ATM intact cell lines and was synergistic in ATM-deficient cell lines (Vendetti et al., 2015). They also importantly found it to be well tolerated in murine models, in contrast to expectations, and they found rapid and near complete tumour regression when AZD6738 was combined with cisplatin in an ATM-deficient lung cancer xenograft model. More recently, BAYER have developed their own ATR inhibitor, named BAY1895344 (Wengner et al., 2020). They found it to be selective for ATR after analysis of its effects on a kinase selectivity panel, however an IC_{50} at a similar order of magnitude to ATR was observed for Mechanistic Target Of Rapamycin Kinase (mTOR), a PI3K. However, analysis of phosphorylation of mTOR targets found BAY1895344 to be 180-fold less active than mTOR-specific inhibitors. In a panel of cancer cell lines they found anti-proliferative effects of BAY1895344 that correlated with ATM-deficiency, and were able to demonstrate anti-tumour effects in several patient-derived xenograft (PDX) models including ovarian, prostate, colorectal and lymphoma. Similarly to previous studies of ATRi, they observed promising combination effects of BAY1895344 with IR and chemotherapies *in vivo* (Wengner et al., 2020).

1.5.2 Inhibition of PARP

Inhibitors of PARP (PARPi) are the most well characterised and developed inhibitors of the DDR. PARPis are most frequently associated with HR deficient (HRD) tumours, primarily BRCA mutated cancers due to a synthetic lethal relationship between PARP and BRCA loss. This relationship was first described in 2005. Bryant et al hypothesised that PARPis mechanism of action involved collapse of replication forks at spontaneous SSB that required repair by HR. In the absence of BRCA, cells were acutely sensitive to PARP inhibition due to the critical roles of BRCA in HR (Bryant et al., 2005). They showed for the first time that a PARPi had utility as a single agent in certain clinical settings. The PARPi olaparib was first approved for use in 2014 for high grade serous ovarian cancer with germline BRCA mutations. Since then, further work and several clinical trials have led to the approval of different PARPis for a range of cancer types, both with and without HRD, as summarised in Table 1.1. In addition, several other PARPis have been described that are at different stages of development, investigations and clinical trials, including veliparib (Donawho et al., 2007, Coleman et al., 2015), fluzoparib (Wang et al., 2019) and pamiparib (Xiong et al., 2020).

Table 1.1. Approved PARP inhibitors and their clinical setting.

	Cancer	Disease setting
Olaparib (2014)	Recurrent high-grade ovarian, fallopian and peritoneum carcinoma	Partial or complete chemotherapy response
	Newly diagnosed high-grade ovarian, fallopian and peritoneum carcinoma	BRCA1/2 mutant with a partial or complete chemotherapy response
	Newly diagnosed high-grade ovarian, fallopian and peritoneum carcinoma	HRD-positive with a partial or complete chemotherapy response
	HER2-negative breast cancer	BRCA1/2 mutant
	Metastatic pancreatic cancer in a maintenance setting after 16 weeks of platinum-based chemotherapy disease stabilisation	Germline BRCA1/2 mutant
	Metastatic prostate cancer	BRCA1/2 mutant
Niraparib (2017)	Newly diagnosed advanced ovarian, fallopian and peritoneum carcinoma	Partial or complete chemotherapy response
	Recurrent advanced ovarian, fallopian and peritoneum carcinoma	Partial or complete chemotherapy response
Rucaparib (2018)	Recurrent advanced ovarian, fallopian and peritoneum carcinoma	Partial or complete chemotherapy response
Talazoparib (2019)	Metastatic HER2-negative breast cancer	BRCA1/2 mutant

Mechanisms of PARPi action are summarised in Figure 1.7. PARP trapping is an important mechanism of PARPi action. It was originally thought that PARPi acted as catalytic inhibitors that competed with NAD^+ to prevent the repair of SSB. Doubts were raised that catalytic inhibition was the sole action of PARP inhibition, as PARPis were more cytotoxic to WT cells than homozygous loss of PARP via small interfering RNA (siRNA). This was first observed by assessing SSB accumulation after induction by alkylating agent dimethyl sulfate (DMS). SSB were efficiently repaired in PARP WT cells by BER and accumulated with inhibition of PARP as expected, but no accumulation was observed in a PARP-deficient cell line (Strom et al., 2011). This led the authors to propose that PARP1 was not required for efficient BER but rather PARPi trap PARP on the SSB intermediate preventing its repair. Similarly, in support of PARP being trapped to sites of damage, Kedar et al showed that PARP1 was associated with DNA by ChIP-qPCR after treatment with DNA alkylating agent MMS and a PARPi but not without an inhibitor (Kedar et al., 2012). Work by Murai et al showed that

trapped PARP was more cytotoxic than unrepaired SSB via PARP inactivation, again suggesting a “poison” activity of PARPi (Murai et al., 2012).

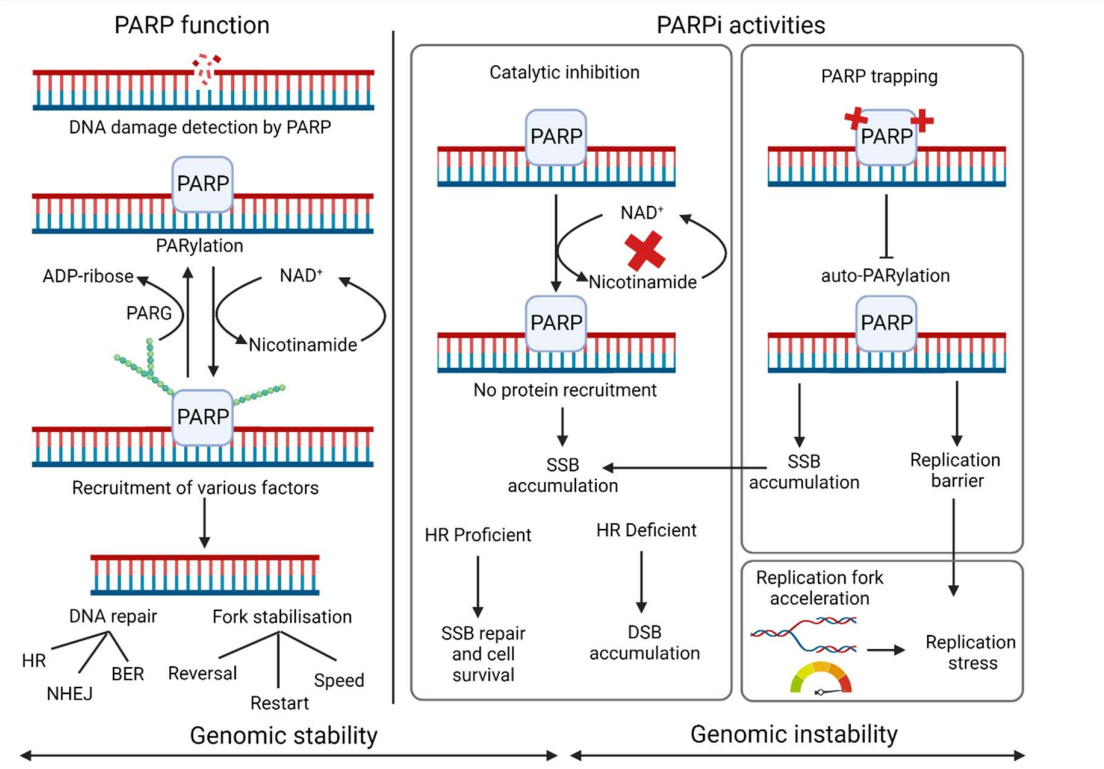

Figure 1.7. PARP and PARPi mechanisms. PARP functions primarily by detection of DNA damage, most commonly SSBs. PARP binds to the site of damage and is activated by the formation of PAR chains using NAD^+ as a substrate, known as PARylation. Cellular NAD^+ is replenished from nicotinamide using ATP. PAR chains recruit multiple proteins and are catabolised by PARG or degraded via auto-PARylation itself to allow PARP release and subsequent repair. PARP is primarily associated with BER but has been implicated in many other DNA repair pathways and replication fork activities. There are many proposed mechanisms of PARPi mechanism of actions. Firstly, via binding to the catalytically active site of PARP to compete with NAD^+ and prevent repair of SSB, resulting in SSB accumulation. Alternatively, PARP trapping results from prevention of auto-PARylation and subsequently PARP cannot be released from DNA, resulting in inefficient repair of damage. An accumulation of SSBs can result in them being converted to detrimental DSBs during S phase. PARPi have been known to accelerate replication forks, which along with trapped PARP can induce RS. Created with BioRender.

Murai et al were also the first to discover that PARPis have different trapping capacities (Murai et al., 2012). Their work, and subsequent studies of more recently described PARPis, have provided a ranking of inhibitors based on PARP trapping capabilities: talazoparib ≫ niraparib > olaparib = rucaparib = pamiparib ≫ veliparib (Murai et al., 2012, Murai et al., 2014, Xiong et al., 2020). PARP trapping capacities were not correlated with catalytic inhibitory properties (Murai et al., 2012) but were found to correlate with cytotoxicity. Talazoparib, the most potent PARP trapper described to date was ~100 fold more efficient at trapping PARP than olaparib and rucaparib, and was also more cytotoxic as a

single agent and when combined with MMS and TMZ, despite similar catalytic inhibition (Murai et al., 2014). Unfortunately, evidence suggests that PARP trapping capacities inversely correlate with tolerability *in vivo* when combined with TMZ, limiting the clinical advantage of this mechanism of action. Due to differing maximum tolerated doses (MTD), PARPis with very different PARP trapping capacities had similar efficacies *in vivo* (Hopkins et al., 2015). Similarly, in the clinic comparable response rates have been reported for veliparib, niraparib, olaparib and talazoparib despite very different PARP trapping potencies (Coleman et al., 2019, de Bono et al., 2017, Fong et al., 2010, Sandhu et al., 2013).

Mechanistically, the ability to trap PARP has been shown to be reliant on cellular NAD^+ levels (Hopkins et al., 2015), and PARP-DNA complexes were as stable with depleted NAD as they were with potent PARP trapper talazoparib (Murai et al., 2014), so it has been hypothesised that PARPis competitively bind the NAD^+ binding domain of PARP1, limiting auto-PARylation and subsequently trapping PARP. Auto-PARylation of PARP has long been established as a mechanism of PARP release from sites of damage, in keeping with this hypothesis (Satoh and Lindahl, 1992).

There are several studies suggesting that progression through S phase is a requirement for PARPi activity. Unsurprisingly, trapped PARP acts as a replication barrier in S phase and if it persists for long enough trapped PARP will encounter a replication fork, leading to stalled forks (Kedar et al., 2012). As described previously these forks can collapse and generate DSB in the absence of efficient RS response mechanisms. Accordingly, PARPis with potent trapping capacities have been linked to increased RS in MYCN-amplified neuroblastomas, leading to increased DNA damage that bypassed cell cycle checkpoints and cell death by mitotic catastrophe (Colicchia et al., 2017). It has also been hypothesised that PARPi generate DSB due to an accumulation of SSB in the absence of PARP that again stall replication forks (Farmer et al., 2005). Subsequently, Simoneau et al showed that an accumulation of DSBs via PARPi required two subsequent S phases, by trapping PARP in the first S phase and subsequent fork collisions in the second (Simoneau et al., 2021). Heacock et al investigated genomic stability after combined MMS treatment and PARP

inhibition and found neither single agent was sufficient to generate DSB but the combination formed DSB in S phase cells expressing PARP1, suggesting a reliance on S phase progression for PARPi effects (Heacock et al., 2010). Similarly, replication-dependent mechanisms of action were observed in glioma cell lines where PARPi was found to be radiosensitising due to RT inducing SSBs which were converted to DSBs with PARPi, but this phenomenon was enhanced when the cells were synchronised in S phase (Dungey et al., 2008).

Other implications for PARPi activities in S phase is the observation of accelerated replication fork speeds (Maya-Mendoza et al., 2018) and more recently a study found that PARP inhibition reduced the integrity of nascent DNA strands, hypothesised to be due to a role of PARP in processing Okazaki fragments (Vaitsiankova et al., 2022). Lastly, some studies suggest there may be utility for PARPis in high RS cancers which are non-HRD, mostly evidenced in SCLC. SCLC has been characterised as having increased DDR gene expression, including PARP, ATR and CHK1, loss of TP53 and MYC amplification, which results in increased RS and reliance on intact DDR and RS responses. SCLC were found to be more sensitive to olaparib *in vitro* than NSCLC which have comparatively lower RS, with associated reduction in PAR levels and DDR factors (Byers et al., 2012). There is strong evidence to suggest that mechanisms of PARP inhibition are intrinsically linked to replication and subsequently RS and the RS response, opening up PARPi for utility in targeting the RS response, as will be discussed below.

1.5.3 Combined ATR and PARP inhibition

It has long been proposed that combinations of DDR inhibitors may prove clinically beneficial, especially as a solution for targeting non-HRD tumours. Many different combinations have been proposed and studied, but the focus in this thesis is on combined ATR and PARP inhibition (CAiPi). Several studies have investigated this combination of inhibitors in a range of cancer types and mutational backgrounds, generally observing a synergistic relationship between the inhibitors (Kim et al., 2017, Ning et al., 2019, Wengner et al., 2020, Kim et al., 2018, Mohni et al., 2015, Schoonen et al., 2019). There are several theories behind why this combination may be clinically active. Firstly, as summarised previously in this chapter PARP inhibition can both induce RS and has roles in the

RS response, which would be exacerbated by the addition of an ATRi. Many studies have observed aberrant cell cycle progression from the combination, where PARP inhibition alone caused a G2-M accumulation but upon addition of an ATRi these cells were released leading to premature mitotic entry (Kim et al., 2017, Lloyd et al., 2020, Jette et al., 2019, Schoonen et al., 2019). This was universally associated with genomic instability and toxic chromosomal aberrations, via accumulation of chromatin bridges, lagging chromosomes and micronuclei. In keeping with this, several studies have found a reliance on the ATR-CHK1 axis for cell survival upon inhibition of PARP. This has been best evidenced by Kim et al, who observed increased pATR, pCHK1 and γH2AX upon inhibition of PARP *in vitro*, which was reversed upon combined inhibition (Kim et al., 2017). They investigated chromosomal breaks by metaphase spread as a mechanism of cell death, no increase was observed with PARPi but ATRi alone increased breakage, however with the combination three times more breaks were observed over ATRi alone, hypothesised to be due to inappropriate entry into mitosis.

These studies by Kim et al were in a BRCA mutant model, which has previously been identified as a biomarker of PARPi sensitivity but not particularly relevant to GBM where BRCA mutations are rare. Similarly, Schoonen et al studied CAiPi in a BRCA2 depleted cell line with very similar results, where ATRi forced early mitotic entry and associated genomic instability via chromatin bridges and micronuclei, and they also showed rescue of these responses by CDK1 inhibition-associated block of mitotic entry (Schoonen et al., 2019). However, many other studies have investigated CAiPi in HR-proficient models. Interestingly, it has been suggested that ATR inhibition induces a 'BRCAness' in cells which could be exploited by PARPi, since one study found a correlation between ATR signalling and elevated levels of HR factors which they hypothesised drives increased DDR in high RS cancers (Kim et al., 2018). Further mechanistic investigations of the relationship between ATRi and HR by Dibitetto et al found that ATR had a crucial role in the DNA end resection step of HR, and inhibition of ATR depleted pools of pro-resection factors, prevented recruitment of the critical HR factors RAD51 and RAD52 and drove cells to more toxic NHEJ repair, subsequently leading to PARPi sensitivity (Dibitetto et al., 2020). However, both of these studies correlating CAiPi mechanisms of response to ATRi roles in HR proposed that

prolonged ATR inhibition would be required to deplete HR-factor levels or shift cells to NHEJ before the introduction of a PARPi, which does not explain why Lloyd et al observed cytotoxic effects of CAiPi within a couple of cell cycles (Lloyd et al., 2020), highlighting the multifaceted and complicated role of ATR. Accordingly, several other markers have been described to predict CAiPi cytotoxicity, including ATM depletion (Jette et al., 2019, Lloyd et al., 2020, Wilson et al., 2022), MYC or MYCN amplification (Ning et al., 2019) and oncogenic RS drivers like cyclin E1 (CCNE1) (Wilson et al., 2022). Current standings on proposed biomarkers will be detailed in 1.5.6.

Combinations of ATR and PARP inhibitors have been investigated in *in vivo* preclinical models, generally finding similar trends towards greater responses in models of BRCA mutations or deficiencies (Kim et al., 2017, Wengner et al., 2020, Wilson et al., 2022), ATM deficiencies (Lloyd et al., 2020) and MYC/MYCN amplification (Ning et al., 2019). However, with the exception of Lloyd et al, all other studies still observed far greater anti-tumour effects and prolonged survival from the combination therapy over either monotherapy in $BRCA^{WT}$ models, PARPi-resistant models (Wilson et al., 2022, Wengner et al., 2020) and non-MYC amplified xenografts (Ning et al., 2019). Generally, all studies observed that the combination was well tolerated but a significant challenge was optimising scheduling. This is indicative of the challenges with all *in vivo* studies but is amplified by utilisation of different mouse models with different tumours, tumour burden, inhibitors and different genetic deficiencies. Only the study by Ning et al has focused on a model of GBM, which will be described below.

1.5.4 Targeting replication stress in glioblastoma

Most of the focus of inhibition of PARP or ATR in GBM has been on sensitising to current therapies. In 2002, Tentori et al showed the chemosensitising effects of PARP inhibition in GBM after observing synergy between TMZ and PARP inhibition in glioma cells, regardless of p53 status or TMZ-sensitivity, which they hypothesised was due to PARP's role in repairing specific TMZ adducts via BER (Tentori et al., 2002). Several years later the same group were able to show synergy between PARPi and TMZ specifically in the resistant GSC population of tumour cells (Tentori et al., 2014). In terms of RT, Barazzuol et al showed enhanced anti-tumour efficacy when RT was combined with veliparib in four

GBM cell lines, which was further enhanced by the addition of TMZ (Barazzuol et al., 2013). Similarly, a study in GSCs saw decreased viability with the addition of a PARPi to RT, which they hypothesised was due to a reliance on PARPs role in the DDR during constitutive DNA damage as a result of chemoradiation (Venere et al., 2014). Searches for a marker of PARPi efficacy with TMZ have found very differing results. Gupta et al showed improved survival with the addition of veliparib to TMZ in MGMT-methylated PDX models which they could reverse by the overexpression of MGMT (Gupta et al., 2016) whereas Erice et al reported that the effect of combining PARPi and TMZ was most pronounced in MGMT deficient cells (Erice et al., 2015), directly in contradiction with each other. Further work is required to elucidate this relationship, identification and stratification of patients by MGMT status in clinical trials will likely aid in understanding this relationship.

Eich et al were the first to identify ATR mutated cells that were hypersensitive to TMZ (Eich et al., 2013). They also showed that knockdown of ATR reduced phosphorylation of H2AX, CHK1 and CHK2 in glioma cell lines, highlighting inhibition of ATR as a potential strategy for chemosensitisation. Jackson et al went on to find that the ATR-CHK1 axis was activated by TMZ specifically in MGMT-deficient cells, which also therefore displayed increased sensitivity to ATR inhibition (Jackson et al., 2019). Similarly, Aasland et al showed that the ATR-CHK1 axis played a critical role in TMZ-induced senescence (Aasland et al., 2019).

The radiosensitising effect of CAiPi specifically in GSCs was shown by Ahmed et al, who hypothesised that concomitant inhibition of repair and cell cycle checkpoints may provide optimal radiosensitisation (Ahmed et al., 2015). They found that several DDR targets were upregulated in GSCs compared to paired differentiated bulk cells and importantly Chk1 was preferentially upregulated following IR, suggesting a reliance on the ATR stress response. Concordantly, they observed rapid G2/M checkpoint activation in GSCs following IR, which ATR inhibition abrogated leading to mitotic catastrophe and increased radiosensitivity, which was further enhanced by the addition of a PARPi through parallel inhibition of DDR and stress response pathways. Carruthers et al similarly showed the radiosensitising effects of CAiPi in GSCs, but for the first

time linked this phenotype to an increase in RS (Carruthers et al., 2018). They were able to replicate this radioresistant phenotype with low dose aphidicolin to induce RS in differentiated bulk cells. They also observed significant, supra-additive effects of CAiPi in GSCs by neurosphere formation, and increased sensitivity in two primary GSC lines compared to their paired bulk counterparts, in keeping with their hypothesis that RS is a targetable vulnerability of GSCs.

Despite promising indicators for the use of PARP and ATR inhibitors in sensitising GBM to current therapies, the focus of this thesis is utilising CAiPi to target increased RS in GSCs and understand mechanisms of sensitivity outwith the effects on standard of care, which remains to be fully determined. The only study of CAiPi alone to target GSCs was carried out by Ning et al, albeit with a focus on PARP inhibition (Ning et al., 2019). The authors described MYC or MYCN amplification as a marker of PARPi sensitivity in GSCs. They identified MYC/MYCN amplification in all their PARPi-sensitive (IC_{50} <10μM) cell lines, which was not present in the PARPi-resistant (IC_{50} >100μM) group of cells. The amplification corresponded to increased expression of MYC or MYCN proteins identified by Western blot. They also found a negative correlation between MYC expression, via knockdown or overexpression, and CDK18 expression, analysed by RNA sequencing (RNAseq) and qPCR. They found that amplified MYC/MYCN acted to repress transcription of CDK18. This conferred PARPi sensitivity, as unrepressed CDK18 activated ATR in response to PARPi to promote HR and cell survival. They went on to find ATR inhibition synergised with PARPi in MYC/MYCN amplified GSCs or sensitised non-MYC/MYCN amplified GSCs to PARP inhibition, they hypothesised due to loss of HR via ATRi. This relationship was specific to ATRi, as they found PARPi did not sensitise GSCs to other DDR inhibitors including ATM, PI3K, PTEN or to TMZ. Importantly, they found that CAiPi did not increase cytotoxicity in normal human astrocytes compared to either monotherapy, despite observing synergistic or sensitising effects in GSCs (Ning et al., 2019). Careful consideration of the effects of CAiPi on normal tissue is required before being taken forward clinically, however several features of ATR and PARP inhibition support their GBM tumour specific targeting. These include frequent loss of TP53 cell cycle checkpoint control in GBM and loss of other DDR targets, specifically targeting increased RS in GSCs and lastly CAiPis specific

targeting of replicating cells may mean that largely non-replicating normal tissue in the surrounding CNS is spared.

1.5.5 Clinical trials of ATR and PARP inhibition in glioblastoma

Combinations of inhibitors and chemoradiotherapies are complicated by overlapping toxicities. Previous studies have identified PARPi exacerbate myelotoxicity commonly associated with TMZ, necessitating a reduction in TMZ dose (Plummer et al., 2013). Therefore, any proposed therapies require careful planning to identify safety and tolerability of the regime. PARPis are the most clinically advanced DDR inhibitors, gaining approval for use in a range of clinical settings and identified as tolerable for their respective uses. Their utility for GBM is being investigated in several clinical trials, as summarised in Table 1.2. Many of these trials are phase I/II and aimed to investigate safety and tolerability of various PARP inhibitors, primarily veliparib and olaparib in combination with TMZ, RT or both. Many have yet to report results, or preliminary reports are so far only in the form of abstracts. Veliparib in GBM has shown limited promise in combination with standard therapies, with one trial not identifying a tolerable dose due to haematological toxicities (Kleinberg et al., 2013), and the other two studies finding no significant benefit over control or conventional therapies (Sarkaria et al., 2022, Sim et al., 2021). This raises the question over the importance of PARP trapping for a clinical benefit in combination with chemotherapy, since veliparib is the least potent PARP trapper. Limited results of olaparib clinical trials have been reported, however the phase I OPARATIC trial identified overlapping toxicities between olaparib and TMZ but could achieve tolerable scheduling through intermittent dosing of olaparib three days a week with daily TMZ (Hanna et al., 2020). They also found that 14/39 evaluable patients were progression free at 6 months and with this promising clinical data two further studies, PARADIGM and PARADIGM-2, have been initiated.

Another important aim of the OPARATIC trial was to assess the brain penetrability of olaparib. Achieving sufficient blood brain barrier (BBB) penetration remains a significant and ongoing challenge for targeting tumours of the brain, necessitating the brain penetrative capacities of all proposed inhibitors to be assessed. Each PARPi appears to have differing capacities for

crossing the BBB, which has primarily been studied in preclinical models. Sun et al compared the brain and tumour penetration of olaparib and niraparib in xenograft mouse models, and found greater tumour penetration and sustainability in the brain by niraparib compared to olaparib (Sun et al., 2018). Similarly, a PK study of olaparib in a GBM PDX model as part of the OPARATIC trial found poor BBB penetration (Hanna et al., 2020). However, as part of the OPARATIC trials, suitable patients with recurrent GBM received olaparib for four days before tumour resection and olaparib concentrations in plasma, tumour core and tumour margins were quantified. This study found olaparib was detected in 71/71 tumour cores from 27 patients, and 21/21 tumour margins from 9 patients at clinically relevant doses (Hanna et al., 2020). This highlighted discrepancies between preclinical models and the clinic and the necessity of assessing BBB penetration in patients. The murine BBB is particularly restrictive, and the human BBB is known to be disrupted in patients with GBM, which may explain differing brain penetrations of the same inhibitor (Watkins et al., 2014).

Table 1.2. Summary of PARP inhibitor clinical trials in GBM.

PARPi	Trial (year) (phase)	Treatments	Disease setting	Outcomes
Pamiparib	NCT03150862 (2017) (I/II) Completed (Piotrowski A, 2019)	Pamiparib + RT / Pamiparib + RT + TMZ / Pamiparib + TMZ	Newly diagnosed or recurrent GBM, stratified by MGMT status	Pamiparib 60mg BID + RT/TMZ generally well tolerated
Veliparib	NCT00770471 (2008) (I/II) Completed (Kleinberg et al., 2013)	Veliparib + RT + TMZ	Newly diagnosed GBM	Veliparib BID + RT/TMZ was not tolerable due to haematological toxicities
	NCT02152982 (2014) (II/III) Active, not recruiting (Sarkaria et al., 2022)	Adjuvant Veliparib + TMZ versus placebo + TMZ after concurrent RT+TMZ	Newly diagnosed GBM with mMGMT	No difference in Veliparib vs placebo for OS: 28.1 vs 24.8 mo. (p=0.15) or PFS: 13.2 vs 12.1 mo. (p=0.31). Evidence of benefit following retreatment with Veliparib + TMZ at first occurrence
	VERTU (2015) (II) Completed (Sim et al., 2021)	Veliparib + RT then adjuvant veliparib + TMZ or TMZ + RT	Newly diagnosed GBM with uMGMT	Veliparib vs control PFS at 6 mo. 46% vs 31%. Median OS: 12.7 mo. vs 12.8 mo. Tolerated but no clinical benefit
Niraparib	NCT01294735 (2011) (I) Completed	Niraparib + TMZ	Advanced cancer including GBM	Niraparib in combination with TMZ was tolerated and demonstrated

	(Kurzrock et al., 2014)			antitumor activity. GBM specific results not yet published
	NCT05076513 (2021) (0/I) Recruiting	Phase 0: Niraparib for 4 days prior to resection. Phase I: niraparib + RT	Newly diagnosed GBM	None reported
Olaparib	NCT03212742 / OLA-TMZ-RTE-01 (2017) (I/II) Recruiting (Lesueur et al., 2019)	Olaparib + TMZ + RT followed by 4 weeks of olaparib or adjuvant TMZ + olaparib	First line treatment in unresectable or partially resectable high-grade glioma	None reported
	NCT01390571 / OPARATIC (2011) (I) Completed (Hanna et al., 2020)	Olaparib + TMZ	Recurrent GBM	Olaparib exacerbated TMZ-related toxicities requiring intermittent dosing. Tolerated 3 days/week with daily TMZ for 42-day cycles. 36% of evaluable patients progression free at 6 mo.
	PARADIGM (2015) (I/II) Recruiting	Phase I – olaparib + RT and olaparib for 4 weeks after RT. Phase II – olaparib + RT or placebo + RT	Newly diagnosed GBM in patients unsuitable for standard treatment e.g. health/age	None reported
	PARADIGM-2 (2016) (I) (Fulton et al., 2018) Recruiting	Parallel 1: Olaparib + RT + TMZ followed by 4 weeks of intermittent olaparib and then adjuvant TMZ (mMGMT) Parallel 2: Olaparib + RT followed by 4 weeks of daily olaparib (uMGMT)	Newly diagnosed GBM, stratified by MGMT status	None reported
Fluzoparib	NCT04552977 (2020) (II) Unknown status	Fluzoparib + TMZ	Recurrent GBM	None reported

Clinical trials of several PARPi in GBM, either combined with RT and/or TMZ are listed, with the schedule, clinical setting and any results that have been reported summarised. BID = twice daily, mMGMT = methylated MGMT, uMGMT = unmethylated MGMT.

There are no current clinical trials of ATR inhibition in GBM. However, several trials of an ATRi in solid tumours have been undertaken, albeit CNS malignancies

are frequently an exclusion criterion for general solid tumour clinical trials likely due to the additional challenges of BBB penetration. VX970 (also known as VE822, berzosertib and M6620) was the first ATRi to be analysed in humans in 2012. VX970 has been studied in combination with carboplatin (Yap et al., 2020), cisplatin (Shapiro et al., 2021), RT (Baschnagel et al., 2021) and chemoradiotherapy (CHARIOT and NCT02567422 trials, not yet reported). Only the trials of VX970 in combination with carboplatin and cisplatin have reported results in which they found VX970 was generally well tolerated with the respective combinations, with the most common toxicities being neutropenia and anaemia. One patient that received VX970 alone who had metastatic colorectal cancer with ATM loss had a complete response, with 29 months PFS as of last assessment, despite being identified as treatment-refractory (Yap et al., 2020). In the same study, of the 23 patients with advanced, treatment-refractory solid tumours who received combined VX970 and carboplatin they observed one partial response and 15 stable disease. A PK study found VX970 exposure increased in a dose-dependent manner and showed no interaction with carboplatin (Yap et al., 2020). Similarly, out of 31 patients who received VX970 combined with cisplatin, four patients with advanced, treatment-refractory solid tumours achieved a partial response (Shapiro et al., 2021). Both studies concluded that there was promising antitumour activity, warranting further investigations. Both AZD6738 and BAY1895344 have also been assessed in clinical trials to identify safety and tolerability, AZD6738 first in 2013 and BAY1895344 in 2017, and since then there are several studies ongoing of both ATRis in combinations with standard therapies. Reports of both have identified dose-limiting but reversible toxicities, most commonly haematological, however these could be managed by intermittent scheduling (M. Dillon, 2019, Yap et al., 2021). The first-in-human study of BAY1895344 achieved a partial response in four patients and stable disease in eight out of 21 patients with advanced solid tumours (Yap et al., 2021). All responders had loss of ATM protein expression or deleterious ATM mutations, suggesting that clinical efficacy of ATRis may be restricted to tumours with ATM loss.

To date, 16 clinical trials have been registered which combine ATR and PARP inhibition, including in head and neck malignancies, NSCLC, SCLC, prostate, pancreatic, gastric, breast and ovarian cancer. One study of veliparib and VX970

also included cisplatin in patients with advanced solid tumours (Mittra et al., 2019). The study found that the combination of all three therapies was safe, with anaemia being the most common adverse event which did limit veliparib delivery. Out of 34 patients, two had a partial response and 22 had stable disease, with prior platinum chemotherapy a predictive marker of response. The largest CAiPi trial to report results was the VIOLETTE trial of combined AZD6738 and olaparib in triple negative breast cancer (Tutt et al., 2022). They identified manageable toxicities, in keeping with the known profiles of each drug, however adverse events increased from 36% with olaparib alone to 47% with the combination. The study stratified patients as $BRCA^{MUT}$, HRR^{MUT} (HR repair genes) and non-HRR^{MUT} and unfortunately found no significant differences in PFS between PARPi alone and CAiPi. Surprisingly, the only difference observed was an increase in objective response rate (ORR) in non-HRR^{MUT} between CAiPi (15%) and PARPi (4%). The authors did not understand the clinical significance of this observation, as preclinical studies suggest HRD cancers to be potently sensitive to CAiPi. Therefore, further investigations are required to elucidate this response. In terms of GBM, more clinical understanding of ATR inhibitor BBB penetration is required, with PK and pharmacodynamic (PD) studies for each inhibitor required before in-human investigations of CAiPi.

1.5.6 Biomarkers of ATR and PARP inhibitor response

There are several previously described biomarkers of PARPi, ATRi and CAiPi response in a range of cancer types, as has been touched upon throughout this chapter. Potential copy number, mutational and transcriptional biomarkers proposed from *in vitro* investigations are summarised in Table 1.3.

Table 1.3. Biomarkers of PARPi and ATRi sensitivity.

Sensitivity	Cancer/cell type	Biomarker
ATRi	Mouse embryonic fibroblasts/U2OS (Toledo et al., 2011)	High RS via CCNE1 amplification
ATRi	Pancreatic cell lines and human organoids (Dreyer et al., 2021)	High RS via curated transcriptional signature
ATRi	Neuroblastoma (King et al., 2021)	High RS via MYCN amplification
PARPi	GSCs (Ning et al., 2019)	MYC or MYCN amplification
PARPi	Breast and ovarian cancer (Dziadkowiec et al., 2016)	HR deficiency (BRCA1, BRCA2, PALB2)
PARPi	NCI-60 human tumour cell line screen including CNS cell lines (Murai et al., 2016)	SLFN11 expression
PARPi	Glioma (Sulkowski et al., 2017) and acute myeloid leukaemia (Molenaar et al., 2018)	IDH1/IDH2 mutations
PARPi	GSCs (Wu et al., 2020)	EGFR amplification
CAiPi	Commercial glioma, fibrosarcoma, colon and chondrosarcoma cell lines (Sule et al., 2021)	IDH1/IDH2 mutations
CAiPi*	Prostate (Rafiei et al., 2020, Neeb et al., 2021, Jette et al., 2020b), lung (Jette et al., 2020a, Jette et al., 2020b) and pancreatic (Jette et al., 2020b) cancer	ATM deficiency

Summary of previously described markers of sensitivity to ATRi, PARPi and CAiPi, in what cancer or cell type it was described in. *ATM deficiency also described extensively as a biomarker for PARPi or ATRi in a range of other cancer types.

ATRi biomarkers are all characterised by increased RS via oncogene-induction or curated transcriptional signatures. The most well described marker of PARPi sensitivity is BRCA1/2 mutations or defective HR without BRCA1/2 mutations, known as ‘BRCAness’. GBM is generally described as BRCA-intact, as BRCA1/2 mutations have rarely been described in GBM patients (Boukerroucha et al., 2015) and cancers of the CNS are not generally characterised by HR defects. An active challenge is to extend the use of PARPis beyond the classically HR-deficient malignancies. It is theorised that other mutations or inhibitors can mechanistically or therapeutically induce BRCAness. This includes IDH1/2 mutations as these cells are less efficient at DSB repair compared to WT cells (Sulkowski et al., 2017), however this is unlikely to be relevant to GBM which is IDH WT. In terms of GBM, MYC/MYCN amplification is the most applicable and comprehensive marker published to date for PARPi sensitivity in BRCA-intact GSCs, as described in detail in 1.5.4, which could be described as BRCAness due to a reliance on ATR for promoting HR under PARPi (Ning et al., 2019). ATM

deficiency is the most frequently identified and characterised marker of ATRi, PARPi and importantly CAiPi-sensitivity, in a range of cancer types and both *in vitro* and in clinical trials. ATM has critical roles in DSB detection and repair, so it is not surprising deficiency of ATM predicts sensitivity to these inhibitors. However, it has been suggested that mechanistically ATM-deficient cells dictate sensitivity differently from the usual HRD mechanisms and instead it is via ATM's activities in counteracting toxic NHEJ (Balmus et al., 2019). The clinical applicability of ATM deficiencies in GBM may be limited, as mutations of ATM are found in only ~2% of GBM patients (c-Bioportal) (Cerami et al., 2012).

However, we hypothesise that PARP and ATR inhibitors are an important therapeutic strategy for GBM warranting further investigations due to their overlapping roles in RS response and studies suggesting an induction of RS by inhibition of PARP. Two other markers have been described for PARPi sensitivity which are more distinct from HR and DSB repair. The first being EGFR amplification, which is present in approximately 50% of GBM patients. The study by Wu et al found that EGFR amplification in a panel of 14 GSCs predicted sensitivity to talazoparib, which was validated in a further panel of 13 GSCs and *in vivo* (Wu et al., 2020). Mechanistically they found that EGFR amplification was associated with reactive oxygen species (ROS) corresponding to upregulation of DNA repair pathways to counteract the oxidative stress and therefore a reliance of PARP repair activities, similar to upregulation of DDR in response to RS in GSCs theorised by Carruthers et al (Carruthers et al., 2018). Interestingly, Wu et al found talazoparib sensitivity did not correlate with other frequently mutated genes in GBM including PTEN, TP53, CDKN2A or MYC amplification (Wu et al., 2020), the last of which is in contrast to work by Ning et al (Ning et al., 2019). Lastly, sensitivity to PARPis has been associated with Schlafen 11 (SLFN11) expression, which has been identified in a large panel of human cell lines including cell lines from CNS malignancies (Murai et al., 2016). The authors of this work also showed that SLFN11 expression predicted synergistic effects of talazoparib and TMZ in MGMT-proficient cells. They found SLFN11 acted to induce irreversible S phase arrest independently of ATR, while SLFN11-deficient cells were reliant on ATR-mediated S phase checkpoint control in the face of talazoparib, and accordingly they observed greater synergy of CAiPi in SLFN-deficient cells versus SLFN-proficient cells (Murai et al., 2016). They validated

this mechanism in SCLC, however the relevance of this mechanism in GSCs remains to be determined. Despite several proposed biomarkers, genomic alterations are unlikely to explain differing CAiPi sensitivities between isogenic paired GSC and bulk cell lines observed by Carruthers et al (Carruthers et al., 2018), and therefore we hypothesise that a RS-associated biomarker may best predict CAiPi sensitivity.

1.6 Research aims and hypotheses

Since the discovery of GSCs in GBM and their association with treatment resistance and tumour recurrence, there has been a drive to find ways of targeting this subpopulation of cancer cells. Identification of increased RS in GSCs reveals a targetable vulnerability that requires further investigation. This thesis aims to investigate this increased RS as a method of targeting GSCs and study the mechanisms of sensitivity to inhibited RS response to inform biomarker development. To investigate this rationale and to address the hypothesis that inhibition of RS response presents a promising therapeutic potential for GSCs, the main objectives were as follows:

1. To investigate the response to CAiPi in a panel of paired GSC and bulk primary cell lines.

2. To characterise the genomic and transcriptomic profiles of the panel of primary paired GBM cell lines

3. To investigate the mechanisms of sensitivity to CAiPi

4. To explore the feasibility of CAiPi in a preclinical GBM model

Chapter 2 Materials and Methods

2.1 Cell culture

GBM cell lines were handled in a Class II sterile laminar flow hood, using sterile plastic ware and solutions. Aseptic technique was maintained to avoid contamination.

2.1.1 Source and derivation of primary GBM cell cultures

E2, G7, S2, R9, R10, R15 and R24 primary cell lines were gifted to the lab by Dr Colin Watts, University of Cambridge, UK. These cell lines were derived from freshly resected GBM specimens, by the Watts' laboratory via the method previously derived by their lab (Fael Al-Mayhani et al., 2009) Tissue samples were obtained in accordance with local ethical guidelines. Anonymised tissue was mechanically minced in phosphate buffered saline solution (PBS) before enzymatic digestion. Single cells were then isolated by filtration through a 40-µm filter and washed with 10ml red blood cell lysis buffer. Live cells were quantified, seeded at standard density of 15,000 cells/cm^2 in GSC media (defined below) and allowed to form primary aggregates. These were collected and plated, without dissociation, onto ECM-coated flasks (1:10 dilution, Sigma) and allowed to form a primary monolayer. As the primary monolayer approached confluence cells were dissociated by incubation with Accutase™ (Life Technologies) at room temperature and washed with PBS. Cell viability was assessed and cells were reseeded onto ECM-coated flasks at a density of 150 cells/cm^2 to generate the secondary monolayer. To generate subsequent monolayers cells were seeded at standard density 15,000 cells/cm^2 at each passage. Cell numbers were expanded in this fashion and aliquots frozen at -80°C in dimethyl sulfoxide (DMSO) as a cryopreservant before being transferred to liquid nitrogen.

2.1.2 Culture of paired GSC and bulk populations

GSC cultures were maintained in serum-free, growth factor-enriched stem cell enriching conditions. GSC media was made up of Advanced DMEM/F-12 medium (Gibco™) supplemented with 1% B27 (Invitrogen™), 0.5% N2 (Invitrogen™), 1% L-glutamine (Invitrogen™), 4µg/ml heparin, 20ng/ml EGF (Sigma) and 10ng/ml

bFGF (Sigma). GSC cultures were maintained as monolayers on Matrigel™ Matrix (Corning®) coated tissue culture flasks or plasticware, at a 1:40 dilution with media. Neurosphere cultures did not require Matrigel™ coated plasticware.

Tumour bulk cultures were derived from GSC cultures via differentiating media for minimum five passages. Bulk medium was made up in MEM (Gibco™), supplemented with 10% FCS (Sigma), 1% L-glutamine (Invitrogen™) and 1% sodium pyruvate (Invitrogen™). Bulk cells were grown as adherent monolayers on uncoated flasks and plasticware.

2.1.3 Growth conditions

GSC and bulk cell cultures were maintained as adherent monolayers in 75cm^2 flat sided flasks (Corning®), containing 10 to 15ml of GSC or differentiating medium respectively. Cell cultures were grown in a 37°C humidified incubator, at 5% CO_2 and 21% O_2.

2.1.4 Serial passaging of cells

Cells were passaged when cells reached 70-80% confluency from microscopic appearance, approximately every 3-4 days. Medium was aspirated off and the cells were washed with PBS to remove any residual medium. Cell monolayers were then incubated with 0.5-1.0ml Accutase™ (Gibco™) for five minutes before the flask was agitated to allow cells to detach from the growth surface. Media was added to the cell suspension to reach 10ml before centrifugation at 2000rpm for 5 minutes. Media was discarded, the cell pellet resuspended in fresh media and cells distributed into new flasks at appropriate cell densities, noting the passage number. Low passage numbers were routinely used for experiments, between 4 and 10.

2.1.5 Counting cells

Cells were detached from monolayers and centrifuged as per 2.1.4. The cell pellet was resuspended in 3ml of media and passed through a 19-gauge needle 10 times to create a single cell suspension. Media was added to make the cell suspension up to 10ml. 10µl of cell suspension was added to each chamber of a haemocytometer. Cells were counted on all nine quadrants of a haemocytometer

and the total number of cells was divided by nine to give a mean cell count, 'C', per square. The cell concentration was calculated as C x 10^4 cells/ml.

1.6.1 Cell storage and cryopreservation

Cells were detached from monolayers and centrifuged as per 2.1.4. Cell pellets were resuspended in cryo-preservative medium, consisting of DMSO and medium at a 1:10 ratio. Approximately 1x10^6 cells in 1ml of cryo-preservative medium were aliquoted into cryo-vials (Corning®). Cells were initially frozen at -80°C before being transferred to liquid nitrogen for long term storage.

2.1.6 Thawing cells from liquid nitrogen

Cryo-vials from liquid nitrogen were rapidly thawed in a 37°C water bath. 1ml of cell suspension was added to 9ml of media and centrifuged at 2000rpm for 5 minutes. Media was discarded and the cell pellet was resuspended in fresh media and transferred to a 75cm^2 flask. Cells were incubated overnight to allow adherence and medium replaced after 24 hours.

2.2 Flow cytometry cell sorting

E2 GSC-enriched cultured cells were sorted by the presence or absence of cell surface marker CD133. Briefly, flow cytometry technology can sort heterogenous populations of cells into two or more groups, based on fluorophore-conjugated antibodies attached to cell surface markers. Cells are sorted one at a time, detecting cell size and granularity by light scattering as well as fluorescence. Hydrodynamic focusing creates a single cell suspension so each cell passes through a laser light one at a time. When a cell passes the laser, forward scatter (FSC) and side scatter (SSC) of the beam are detected. FSC is light that is scattered at small angles and is indicative of cell size, and SSC is light scattered at larger angles away from the beam and provides information on cellular granularity. FSC and SSC can be used to exclude cell debris, dead cells and doublets. Lastly, laser beams can excite the fluorophore-conjugated antibodies resulting in a change in charge, which is used to divert each cell into different populations.

2.2.1 Procedure

Cell cultures grown as monolayers in 75cm^2 flasks that were 50-70% confluent were utilised. Cells were dissociated as described in 2.1, however cells were incubated with Accutase™ for up to 10 minutes to ensure a single cell suspension was created. Cells were harvested into a 15ml Falcon™, a total cell count was taken before centrifugation. The cell pellet was resuspended in 2ml PBS with 4′,6-diamidino-2-phenylindole (DAPI) (1 in 1000), 200µl was collected as a gating control and diluted with 1ml PBS with DAPI (1 in 1000). PE-conjugated anti-CD133 antibody was added to the cell suspension (see Table 2.2) and protected from the light. Cells were incubated with the antibody or no antibody control for 30 minutes at room temperature on a rotating disc. The antibody-containing sample was centrifuged, PBS aspirated and the cell pellet resuspended in 2mls of fresh PBS. Both samples were passed through a 70µM filter to remove any cell aggregates and kept on ice until sorting. 15ml Falcon™ tubes were prepared for collection of cells, containing GSC media plus 50U Penicillin-Streptomycin (Gibco™) per 1ml media to prevent infections.

Sorting of cells was carried out by flow cytometry technicians at the Beatson Institute using a BD FACSAria™ Fusion. SSC and FSC characteristics and DAPI allowed for identification of cells of interest and a region gate was used to exclude cellular debris, doublet nuclei and dead cells, as shown in Figure 2.1. The no antibody control allowed for gating to isolate PE-positive cells, as shown in Figure 2.2. This allowed for sorting of cells into a CD133$^+$ population and a CD133$^-$ population by fluorochrome excitation using a 565nm laser.

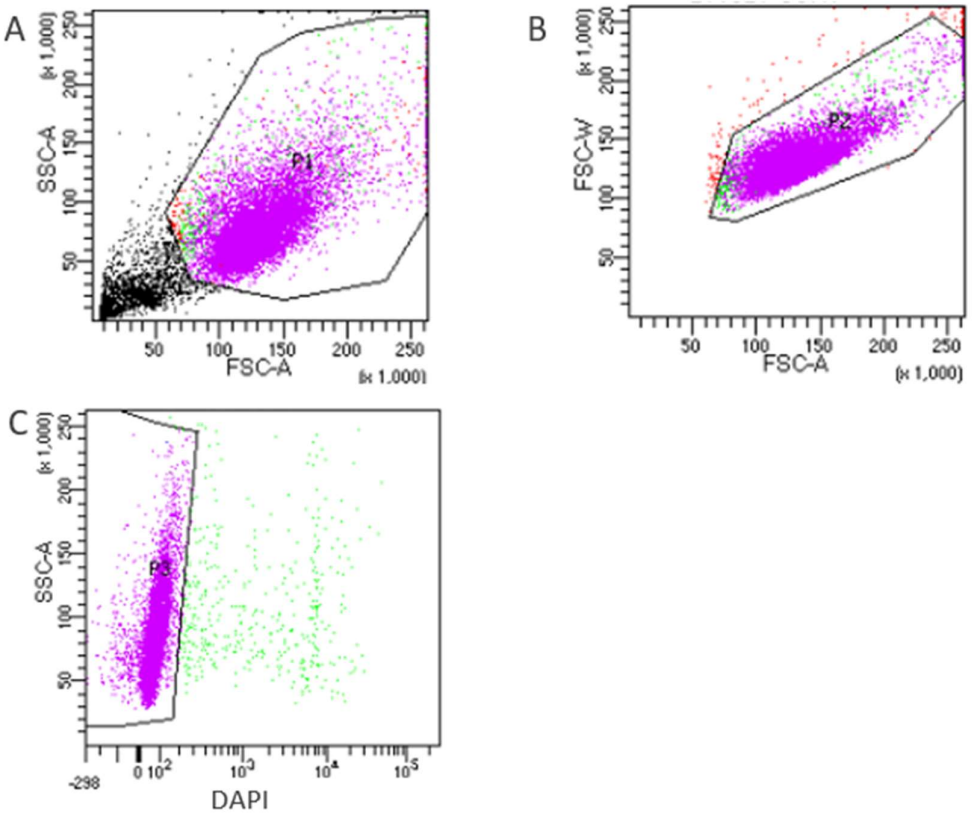

Figure 2.1. Gating to exclude debris and doublets from flow cytometry analysis. A. Region gates for exclusion of debris by FSC-A (area) and SSC-A. B. Region gates for exclusion of doublet nuclei by FSC-A and FSC-W (width). C. Region gates to exclude dead cells, which were DAPI-positive since viable cells exclude DAPI from penetrating cell membranes.

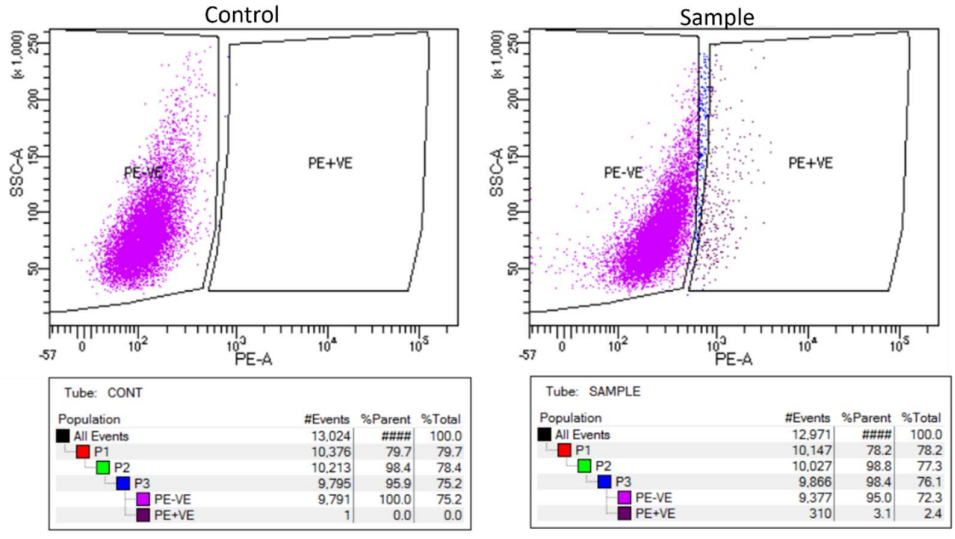

Figure 2.2. Gating and results of CD133 cell sort in E2. Representative flow cytometry gating plots showing isolation of CD133$^+$ E2 cells by PE-conjugated antibody versus no antibody control.

2.2.2 Culture of sorted cells

CD133$^+$ and CD133$^-$ populations were maintained in GSC media. Sorted cells were utilised in neurosphere assays, as detailed in 2.6, within two days of sorting to

maintain both high and low CD133 positivity at the initiation of the experiment. Sorted cells were cultured in the presence of 50U Penicillin-Streptomycin (Gibco™) per 1ml of media throughout experiments to prevent infections.

2.3 Inhibitors

Inhibitors were dissolved in DMSO for *in vitro* experiments or 60% polyethene glycol 400 (PEG 400), 10% ethanol and 30% distilled water for *in* vivo experiments. VE821 was utilised at 5μM and olaparib at 1μM throughout the thesis, as these have previously been identified as sufficient to inhibit *in vitro* phosphorylation of Chk1 and PARylation respectively. Concentrations of other inhibitors or variations in VE821 or olaparib concentrations utilised are stated throughout the thesis. Table 2.1 details the inhibitors used.

Table 2.1. Inhibitor details.

Inhibitor	Manufacturer	Stock concentration
VE821	Sigma, SML14155	100mM stock in DMSO
Olaparib	Stratech, s1060-SEL	10mM stock in DMSO
Veliparib	Stratech, ABT-888	10mM stock in DMSO
AZD6738	AstraZeneca, AZD6738	75.7mM in DMSO
Roscovitine	Sigma, R7772	25mM stock in DMSO
Pamiparib	SelleckChem, S8592	Appropriate concentration* in PEG solution (*in vivo*) 10mM stock in DMSO (*in vitro*)
BAY1895344	BAYER (under an MTA)	Appropriate concentration* in PEG solution (*in vivo*) 10mM stock in DMSO (*in vitro*)

*Varied concentrations of pamiparib and BAY1895344 made up depending on dosage due to requirement of 100μl administered to mouse. PEG solution = 60% PEG 400, 10% ethanol and 30% distilled water.

2.4 Cell viability by CellTiter-Glo®

2.4.1 Procedure

Single cell suspensions of GSCs and bulk cells were prepared and counted as described in 2.1. Cell numbers for plating were determined by plating serial cell numbers on a clear 96-well plate (Corning®) and assessing optimal cell density of 70-80% confluency after seven days. Optimised cell numbers were plated in 100μl of media per well on 96-well white plates (Greiner CELLSTAR®) and incubated for 24 hours. Media was prepared containing inhibitors at double the required concentration, DMSO at an equivalent volume or media alone and 100μl

was added on top of 100µl in the well and returned to the incubator for 24 hours. The inhibitor/DMSO media was carefully aspirated and replaced with 200µl of fresh media, or alternatively left for a further five days. After six days post drug treatment, plates were analysed for cell viability using CellTiter-Glo® assay (Promega).

CellTiter-Glo® works via a luciferase reaction, which is reliant on ATP. Luciferase acts on beetle luciferin to release energy in the form of luminescence, only in the presence of Mg^{2+} and ATP. The luminescent signal is proportional to the amount of ATP present, which in turn is directly proportional to cellular metabolic activity and therefore is an indicator of cell viability. Plates were treated as per the manufacturer's instructions. 100µl of CellTiter-Glo® solution was added to each well before mixing of contents for two minutes on an orbital shaker to lyse cells. Plates were incubated at room temperature for 10 minutes to stabilise luminescent signals before analysis. Luminescence was assessed by a Promega GloMax®-Multi Detection System. Readouts for wells containing inhibitors were normalised to wells containing DMSO vehicle control media.

2.5 Clonogenic survival assay

2.5.1 Procedure

Single cell suspensions of GSCs and bulk cells were prepared and counted as described above. 500 cells per well were plated for drug treated wells and 250 cells per well for vehicle control in six-well plates (Corning®). Cells were seeded in 2ml of medium per well and incubated overnight. Medium was then aspirated and replaced with medium containing inhibitors in DMSO or DMSO alone at an equivalent volume. Plates were returned to the incubator for 24, 48 and 72 hours. After this time, medium was aspirated and replaced with 2ml of fresh medium. Plates were returned to the incubator for two weeks for E2 or three weeks for G7, to allow colonies of >50 cells to form.

Once colonies had formed, they were fixed and stained. Medium was aspirated and 1ml of 50% Methanol in PBS added to each well for 15 minutes. This was aspirated and 1ml of 100% Methanol added per well for 15 minutes. After

methanol fixation, colonies were stained with a Crystal Violet (Sigma) solution, made up 1 in 30 with PBS. 1ml was added to each well for a minimum of 2 hours before it was removed, any excess was washed off with water and the plates dried overnight.

2.5.2 Analysis of clonogenic survival assay results

Colonies with >50 cells were counted manually. Colony counts were obtained from triplicate wells for each condition. Mean colony counts were obtained for each experimental condition and plating efficiency calculated by dividing mean colony counts by the number of cells plated. Surviving fractions were calculated relative to DMSO control.

2.6 Neurosphere formation assay

2.6.1 Procedure

GSCs were exposed to inhibitors in flasks prior to plating for roscovitine studies and in 96-well plates for all other studies. For drugging in the wells, single cell suspensions were prepared and counted as previously described and seeded at 10 cells per well in 100µl of media. Medium was prepared with inhibitors or a corresponding DMSO volume before the addition of cells and plating. Plates were incubated at 37°C for 48 hours before the addition of 150µl of fresh media to dilute the inhibitors and the cells were left to form neurospheres. For drugging in flasks prior to plating, cells in 75cm^2 flasks that had reached approximately 50% confluency were incubated in media containing inhibitors or a corresponding DMSO volume for 24 hours. After this, single cell suspensions were prepared and cells counted as previously described and 10 cells per well were plated in 100µl of fresh media containing no inhibitors. After two days 150µl of fresh media was added to each well. Plates were incubated for three weeks for unsorted populations and four weeks for sorted populations to allow neurospheres to form.

2.6.2 Analysis

Once neurospheres had formed, 20µl of MTT (5mg/ml) (Thiazolyl Blue Tetrazolium Bromide) (Sigma) was added to each well to stain neurospheres.

Images of the neurospheres were taken on a GelCount™ (Oxford Optronix) colony counter and neurospheres counted manually using the GelCount™ software. Outer wells for each plate were excluded from analysis and an average neurosphere/well was assessed for the remaining 60 wells. Neurosphere surviving fractions were assessed relative to DMSO control.

2.7 DNA fibre assay

A DNA fibre assay is the gold standard assay for measuring replication fork structures and dynamics. Cells are exposed sequentially to two differently coloured fluorescent, thymidine analogues and analysis of replication velocity, ongoing forks, stalled forks and new origins can be carried out.

2.7.1 Procedure

GSC and bulk cells were seeded in 75cm^2 flasks for 24 hours to reach approximately 50% confluency. Cells were incubated in medium containing inhibitors or a corresponding DMSO volume for 24 hours. A DNA fibre assay, as detailed in Figure 2.3, was then carried out. Cells were incubated in medium containing the thymidine analogue chloro-deoxyuridine (CldU) (25μM from 10mM stock made up in 1N NaOH) (Sigma, C6891) plus inhibitors or DMSO at 37℃ for 20 minutes. CldU containing media was removed and cells washed with medium containing no thymidine analogues. Cells were then incubated at 37℃ in media containing the thymidine analogue iodo-deoxyuridine (IdU) (250μM from 10mM stock made up in 1N NaOH) (Sigma, 17125-59) plus inhibitors or DMSO for 20 minutes. Cells were washed once with PBS before dissociation with Accutase™. Dissociated cells were collected and centrifuged at 950 x g for five minutes. Accutase™ was aspirated and cells diluted to a concentration of 1x10^6 cells per ml in PBS. 2μl of cell suspension was pipetted on the top edge of glass microscopy slides and lysed by the addition of 7μl of spreading buffer (see Table 2.4) with mixing using a pipette tip. Cells were incubated on the glass slide for two minutes before the slides were tilted to an angle of approximately 30° to allow the drop to run slowly down the slide and spread DNA fibres. Slides were air dried before fixation in a 3:1 ratio of methanol and acetic acid for 10 minutes. Slides were stored at 4℃ until immunostaining. A minimum of three slides per condition were processed.

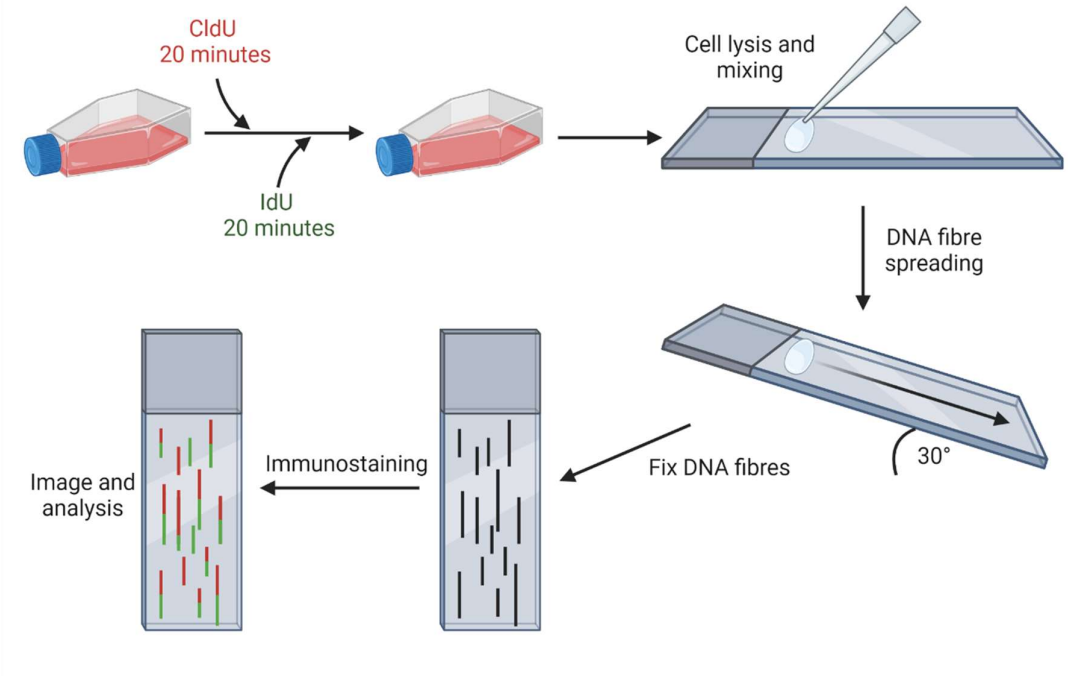

Figure 2.3. Schematic of DNA fibre assay. Cells were stained sequentially with CldU and IdU thymidine analogues for 20 minutes each before transfer of cell suspension to a glass slide. Cells were then lysed before DNA fibres were spread down a glass slide by tilting. DNA fibres were fixed and stained to allow for imaging and analysis. Created using BioRender.

2.7.2 Immunostaining

Slides containing spread DNA fibres were washed twice with deionised water before a rinse with 2.5M hydrochloric acid (HCl). DNA was denatured by incubation of slides in 2.5M HCl for 80 minutes at room temperature. Slides were washed twice with PBS and once with blocking buffer (1% BSA (bovine serum albumin) in 0.1% Tween®-PBS). Slides were then incubated for one hour in fresh blocking buffer. Primary antibody solution was made up in BlockAid™ (Invitrogen™) containing both rat monoclonal anti-BrdU (bromodeoxyuridine) and mouse monoclonal anti-BrdU (see Table 2.2) and 100µl added to each slide. Antibody solution was spread across the slide with Parafilm™ and slides incubated at 37°C for one hour in darkness. Slides were washed three times in PBS before incubation in 4% paraformaldehyde (PFA) for 10 minutes. Slides were washed three times in PBS and three times in blocking buffer for 1, 5 and 25 minutes. Slides were then incubated with secondary Alexa Fluor™ conjugated antibodies made up in BlockAid™ (Invitrogen™) (see Table 2.3) at 37°C for one hour in darkness. Slides were washed twice in PBS, three times in blocking buffer for 1, 5 and 25 minutes and then washed two more times in PBS. Using ProLong™ Gold Antifade Mountant (Invitrogen™), coverslips were mounted onto

the glass slides and sealed with CoverGrip™ coverslip sealant (Biotium). Slides were stored at -20°C until imaging.

2.7.3 Confocal microscopy

Images of immunofluorescent staining of DNA fibres were obtained using a x63 oil-immersion lens on a Zeiss 710 confocal microscope. On average ten images were taken to assure >100 fibres for analysis per replicate.

2.7.4 Analysis of fibres

Only clear, non-overlapping fibres were analysed. For analysis of fork velocity, both CldU and IdU fibre lengths were measured in µm which was divided by pulse length to give µm/min. This was converted to kb/min utilising a commonly used conversion factor of 2.59kb per µm (Jackson and Pombo, 1998). Ongoing forks were analysed by fibres with both CldU and IdU present, a stalled fork was any fibre with only the first thymidine analogue CldU fork and a new origin any fibre with only the second thymidine analogue IdU present, as visualised in Figure 2.4. All fibre analysis was carried out by R Carruthers, to keep analysis consistent between replicates and cell lines.

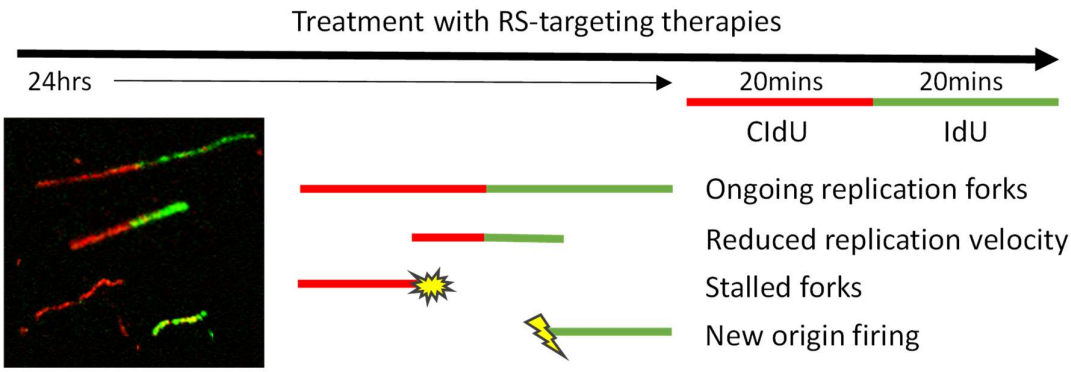

Figure 2.4. Schematic of DNA fibre assay analysis. DNA fibre assay set-up for GSC and bulk analysis of replication dynamics. Cells were exposed to RS-targeting therapies for 24 hours before incorporation of red fluorescent CldU for 20 minutes and green fluorescent IdU for 20 minutes. Subsequent immunostaining of the thymidine analogues allowed for analysis of individual DNA tracts for ongoing replication forks, reduced or increased replication velocity, analysed by length of CldU or IdU tracts, indicative of rate of incorporation. DNA tracts only labelled for CldU are indicative of forks that have stalled during the first labelling step, and tracts labelled for IdU only are replication origins that have fired during the second labelling step.

2.8 Flow cytometric analysis of cell cycle and re-replication

Flow cytometry was used to analyse cell cycle distributions and re-replication. Similarly to flow cytometry described in 2.2 for cell sorting, flow cytometry for cell analysis utilises FSC and SSC to exclude debris, doublets and dead cells, and fluorochromes are used for quantification.

2.8.1 Procedure

For analysis of entry into S phase with roscovitine, cell cultures grown as monolayers to 70% confluency in 75cm^2 flasks were utilised. Cells were incubated with increasing concentrations of roscovitine or an equivalent volume of DMSO, plus BrdU (10μM) (BD Pharmingen) for 24 hours. A no BrdU control was included. For analysis of cell cycle and re-replication, 1x10^5 cells per flask were plated and after 24 hours the media was replaced with media containing inhibitors or an equivalent DMSO volume for 72 hours. BrdU (10μM) (BD Pharmingen) was added to each flask for one hour, except for a no BrdU control flask.

After BrdU incorporation, cells were dissociated using Accutase™ as above, centrifuged and cell pellets were resuspended and fixed in 70% ethanol and stored at 4°C. Fixed cells were centrifuged and ethanol aspirated. Cell pellets were washed twice with PBS and centrifuged before denaturation of DNA with 2M HCl at room temperature for 30 minutes with frequent mixing. Cells were centrifuged and the acid was removed before cell pellets were washed twice with PBS. Cells were resuspended and permeabilised using 100μl 0.05% Triton™ X-100 in PBS and 20μl of the FITC-conjugated anti-BrdU antibody was added (see Table 2.2). Cells were incubated for 30 minutes at room temperature. To wash away unbound antibody, 1ml 0.05% Triton™ X-100 in PBS was added, cells centrifuged and primary antibody mixture removed by aspiration. Cell pellets were resuspended in 300-500μl of PBS containing 200μg/ml RNase A to degrade RNA and 10μg/ml propidium iodide (PI) to stain DNA and incubated for 10 minutes protected from light.

2.8.2 Quantification and analysis

Flow cytometry was carried out using a BD FACSVerse™. FSC and SSC was used to exclude debris and PI width and area to isolate single cells using FlowJo™ software, as detailed in Figure 2.5. Analysis of BrdU and PI incorporation was carried out using FlowJo™ software.

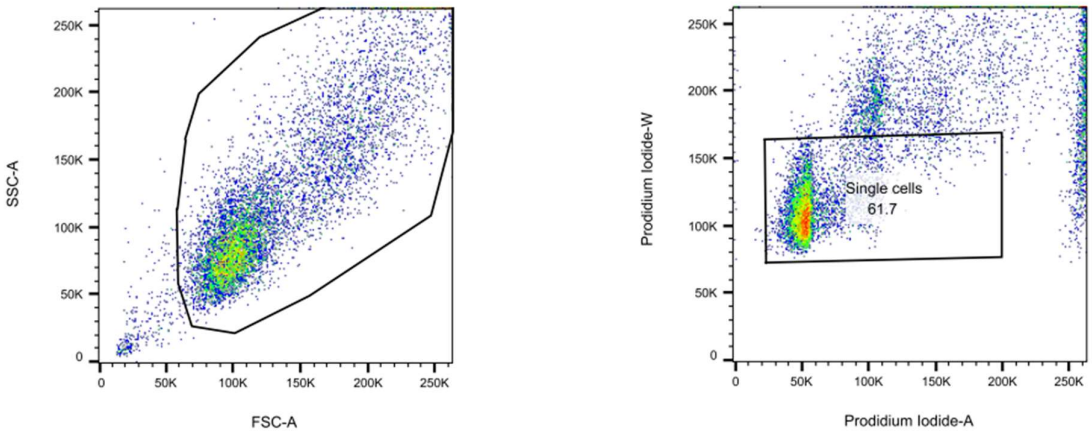

Figure 2.5. Region gating by FlowJo software. Region gating to exclude debris by FSC and SSC and doublets by PI from flow cytometry analyses.

2.9 53BP1 nuclear body analysis

2.9.1 Procedure

GSC and bulk single cell suspensions were prepared and counted as described previously. Cells were seeded in 1ml of medium on 19mm diameter glass coverslips placed in 12 well plates (Corning®). Plates were incubated overnight at 37°C to allow cells to attach. Medium was aspirated and replaced with 1ml of medium containing inhibitors or DMSO at an equivalent volume, or roscovitine (Table 2.1) with and without inhibitors. Plates were returned to 37°C incubation for 48 hours for studies of inhibitors alone or 24 hours for plates with roscovitine. After this time, medium was removed and coverslips washed with PBS. Cells were fixed with cold 4% PFA in PBS for 20 minutes before replacement with 1ml PBS. Plates were stored at 4°C.

2.9.2 Immunostaining

PBS was removed from coverslips and fixed cells were permeabilised with 0.05% Triton™ X-100 in PBS for 5 minutes at room temperature and washed with PBS.

Blocking buffer (0.05% Triton™ X-100 in PBS with 5% FCS and 0.05% BSA) was added to wells for 30 minutes at room temperature to prevent non-specific antibody binding. Primary antibody solutions containing antibodies for 53BP1 and centromere protein F (CENP-F) (see Table 2.2) were made up in REAL™ Antibody Diluent (DAKO) and 60µl added to parafilm®. Coverslips were inverted onto primary antibody solution and incubated overnight at 4℃ in the dark. After this, coverslips were washed three times on a rocking platform with PBS for one minute each. Cells were then incubated with secondary Alexa Fluor™ conjugated antibodies (see Table 2.3) in REAL™ Antibody Diluent (DAKO) on Parafilm® at room temperature for one hour in darkness. Coverslips were subsequently washed three times in 0.1% Triton™ X-100 in PBS on a rocking platform for 5 minutes each, to remove excess antibody. Coverslips were mounted onto glass slides with 20µl of Vectashield® antifade mounting medium with DAPI (Vector Laboratories) and sealed with CoverGrip™ coverslip sealant (Biotium). Mounted coverslips were stored at 4℃ or -20℃ for long term storage.

2.9.3 Confocal microscopy

Z stacks of immunofluorescent staining of cells were obtained on a Zeiss 710 confocal microscope. A minimum of 4 sections were produced per Z stack and images were processed by maximum intensity projection (Zen software, Zeiss) to allow analysis and nuclear body quantification. Microscope settings were kept constant between experimental conditions.

2.9.4 Quantification of 53BP1 nuclear bodies

Analysis was carried out using ImageJ software. CENP-F accumulates during G2 and M phase and is rapidly degraded upon completion of mitosis (Rattner et al., 1993) so CENP-F negative cells were used to identify G1 phase cells. Integrated density of nuclear CENP-F staining was quantified and a cut off below the 75th percentile was used to define G1-phase cells in which to quantify 53BP1NB. 53BP1NB were counted both manually and by automated counting. An arbitrary cut off 12 pixels per foci was used to identify nuclear bodies. For analysis of 53BP1NB with roscovitine, a pipeline was created to automate the identification of DAPI and CENP-F stained nuclei and quantification of 53BP1NB. A validation process comparing manual and automated counts was carried out, and results

shown in Figure 2.6. No statistically significant differences were observed between median values of manual and automated counts.

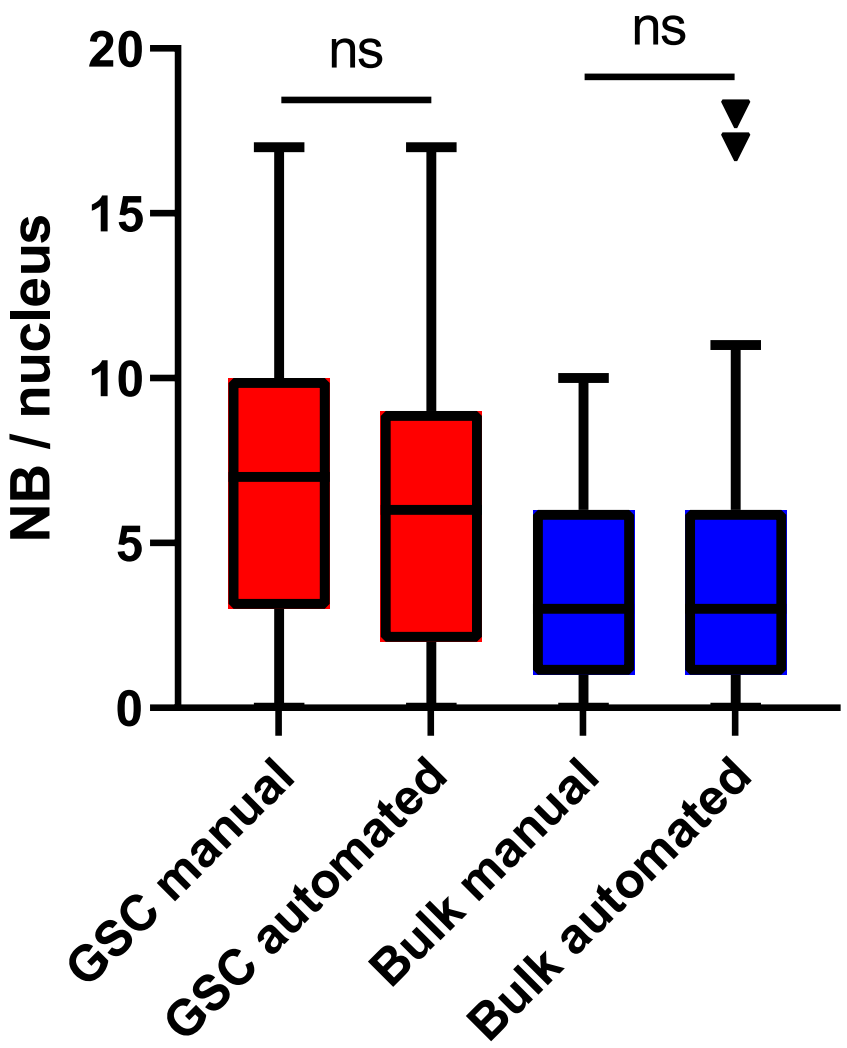

Figure 2.6. Comparison of manual and automated 53BP1NB counts in GSC and bulk cells. 53BP1 nuclear body analysis in E2 GSC and bulk cells after 48-hour exposure to CAiPi. Nuclear bodies were initially scored manually and then validated by automated analysis in ImageJ. Tukey boxplots compare median NB/nucleus with comparisons of median by Mann-Whitney U test (ns = not significant).

2.10 Chromatin bridge and micronuclei analysis

2.10.1 Procedure

Chromatin bridge and micronuclei analysis was carried out concurrently with 53BP1NB analysis, as described in 2.9.1.

2.10.2 Immunostaining

Coverslips were incubated with antibody solutions as described in 2.9.2. For analysis of DAPI-stained chromatin bridges and micronuclei, coverslips were mounted onto glass slides with 20µl of Vectashield® antifade mounting medium with DAPI (Vector Laboratories) and sealed with CoverGrip™ coverslip sealant (Biotium).

2.10.3 Confocal microscopy

Z stacks of DAPI staining of cells were obtained on a Zeiss 710 confocal microscope. A minimum of 4 sections were produced per Z stack and images were processed by maximum intensity projection (Zen software, Zeiss) to allow analysis. Microscope settings were kept constant between experimental conditions.

2.10.4 Quantification

Chromatin bridges and micronuclei were identified and quantified manually from DAPI nuclear staining. Figure 2.7 highlights the characteristic teardrop nuclear shape corresponding to a chromatin bridge, and subsequent conformation by increasing DAPI intensity to visualise a bridge staining positively for DAPI between two nuclei. Micronuclei were identified visually by DAPI and quantified as a percentage of nuclei with corresponding micronuclei. Figure 2.8 shows an example of the induction of micronuclei.

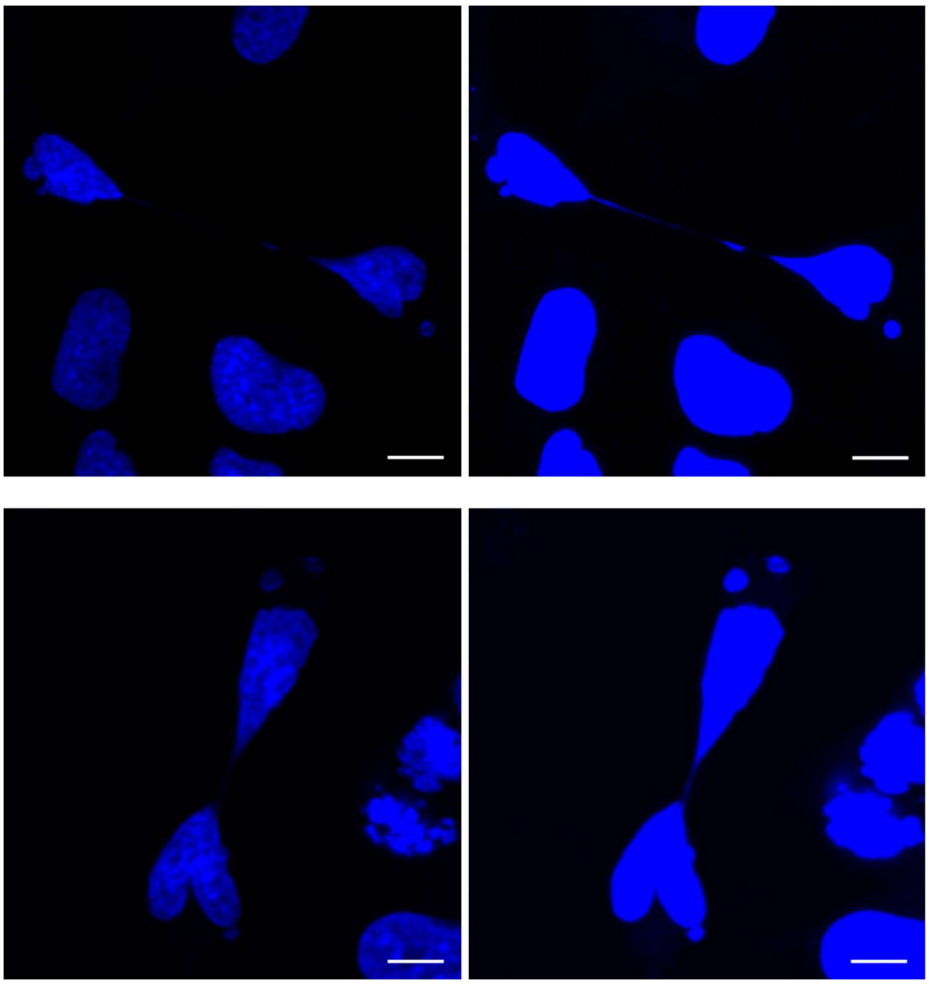

Figure 2.7. Chromatin bridges after CAiPi-exposure. Representative images of two chromatin bridges induced in E2 GSC after 48-hour CAiPi exposure. Chromatin bridges identified by DAPI staining. DAPI contrast adjusted to confirm bridge of DAPI-stained DNA between two nuclei on right (scale bar = 5μm).

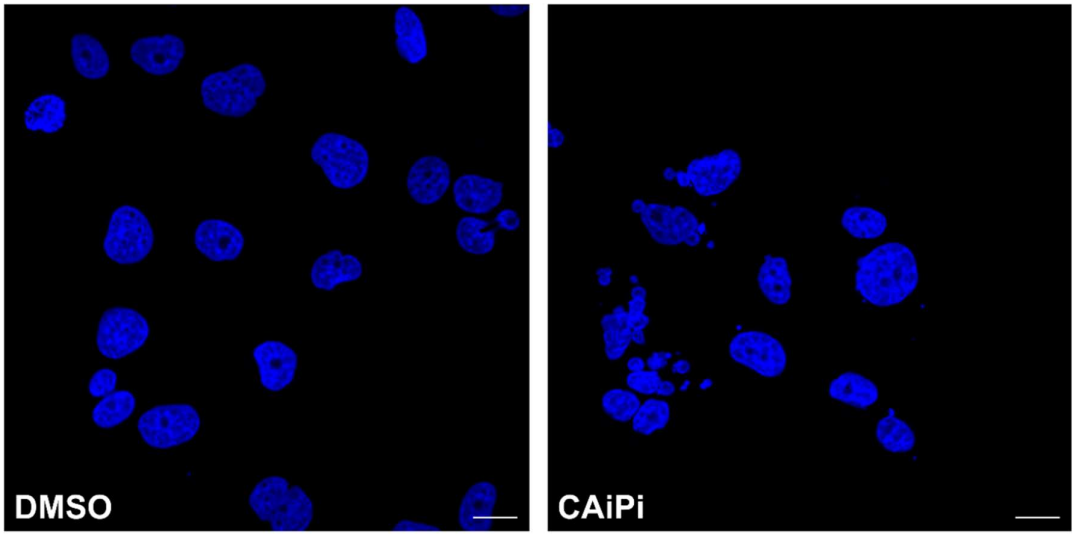

Figure 2.8. Micronuclei induction by CAiPi-exposure. Representative images of micronuclei staining using DAPI, induced in G7 bulk with 48-hour CAiPi or DMSO vehicle control exposure (scale bar = 10μm).

2.11 Western blot

2.11.1 Sample preparation

GSCs grown as monolayers on 10cm diameter petri dishes (Corning®) were harvested after treatment with inhibitors, HU or hydrogen peroxide (H_2O_2). Medium was aspirated and cells were washed with PBS before the addition of 100µl of cell lysis buffer (see Table 2.4) plus protease and phosphatase inhibitors (7X cOmplete™, Roche). After three minutes, a cell scraper was used to homogenise the lysate which was transferred to an Eppendorf and left on ice for 15 minutes to complete cell lysis. Lysate was passed through a QIAshredder spin column and supernatant collected and stored at -20℃.

2.11.2 Protein estimation

A BCA protein assay kit (Pierce™, 32106) was used to estimate protein concentrations of cell lysates. This assay involves the reduction of Cu^{2+} to Cu^{1+} by the proteins in an alkaline medium and the colorimetric detection of Cu^{1+} by bicinchoninic acid (BCA). This reaction forms a stable purple coloured complex that can be detected at 562nm by a spectrophotometer.

BSA was used as a standard at concentrations ranging from 0.08mg/ml to 2000mg/ml and plated in duplicate wells of a 96-well plate. Experimental samples were diluted 1:3 with double distilled water (DDW) and plated in duplicate in a 96-well plate. BCA reagents A and B were mixed at a 50:1 ratio and 200µl added to each well of the 96 well plate. Plates were incubated at 37℃ for 20 minutes before being read using a spectrophotometer (Tecan Infinite M200 PRO). Linear regression based on the standard curve of the BSA standards was used to estimate the protein concentration of each sample.

2.11.3 Gel electrophoresis of protein

Protein samples were mixed with Bolt™ 4X LDS sample buffer (Life technologies) with 10% ß-mercaptoethanol (Sigma) to a final concentration of 2µg/µl and final volume of 250µl. Bromophenol blue within the sample buffer allowed for monitoring of samples within the gel and ß-mercaptoethanol denatured samples. Samples were heated at 100℃ for 5 minutes.

Approximately 50µg of protein was loaded per well into a Bolt™ 4-12% Bis-Tris Plus (Invitrogen™) precast gel. A protein standard (Precision Plus Protein Dual Color Standards, Bio-Rad) was loaded to allow visualisation of approximate molecular weights of the detected proteins. Electrophoresis of gels was carried out in a XCell SureLock™ Mini-Cell (Invitrogen™) electrophoresis tank for one hour at 150V. Tanks were filled with electrophoresis buffer (see Table 2.4).

2.11.4 Protein transfer

Gel was transferred into a Mini Trans-Blot® Cell tank system (Bio-Rad) filled with cold transfer buffer (see Table 2.4). Two fibre pads, 3MM blotting paper and nitrocellulose membrane (ThermoScientific) were soaked in transfer buffer before being loaded into a cassette with the gel, ensuring the correct orientation for transfer of proteins to the nitrocellulose membrane. The electrophoretic transfer was run at 100V for 90 minutes or overnight at 30V.

2.11.5 Immunodetection

After transfer, membranes were placed in 1X TBS-Tween® (Tris-buffered saline) (TBST) (see Table 2.4) with 5% non-fat milk powder (Marvel) (TBST-M) for one hour with rocking to block non-specific binding of antibodies. Membranes were washed three times in TBST before the addition of 5mls of 5% BSA in TBST with an appropriate dilution of primary antibody (see Table 2.2). Membranes were incubated with primary antibody solution overnight at 4°C on a rocking platform followed by washing of membrane three times with TBST. Membranes were incubated with an appropriate dilution of horse-radish peroxidase (HRP) conjugated secondary antibody (see Table 2.3) in TBST-M for one hour at room temperature. Membranes were then washed three times in TBST.

Protein visualisation was carried out using an enhanced chemiluminescent (ECL) kit (Pierce™, 32106), which produces a detectable, visible light as luminol oxidises in the presence of HRP and a peroxide buffer. ECL reagents were mixed at a 1:1 ratio and immediately applied to the protein-containing membrane and incubated for one minute. Proteins were visualised using a myECL Imager (ThermoScientific) for periods of 30 seconds to 5 minutes to achieve optimal band intensities.

Table 2.2. Details of antibodies used.

Antigen	Manufacturers details	Application and dilution
CD133/2 (293C3)-PE Human	Miltenyi Biotec 130-098-046	Flow cytometry 0.5µl / $1x10^7$ cells
BrdU (rat)	AbCam ab6326	Fibre analysis 1:200
BrdU (mouse)	BD Bioscience, 347580	Fibre analysis 1:250
FITC anti-BrdU	BD Bioscience 556028	Flow cytometry 1:6
53BP1 (BP13)	Millipore, 05-726	IF 1/100
CENP-F	AbCam, ab5	IF 1/200
Phospho-Chk1 (Ser345)	Cell Signalling, 2348	Western blot 1/1000
Poly (ADP-Ribose) Polymer	AbCam, ab14459	Western blot 1/1000
Actin	Sigma, A5228	Western blot 1/1000

Table 2.3. Secondary antibody details.

Antigen	Manufacturer details	Application and dilution
Alexa Fluor™ 595 goat anti-rat IgG (H+L)	Invitrogen™, A11007	Fibre analysis 1:150
Alexa Fluor™ 488 goat anti-mouse IgG (H+L)	Invitrogen™, A11017	Fibre analysis 1:150 IF 1/500
Alexa Fluor™ 633 goat anti-rabbit IgG (H+L)	Invitrogen™, A21071	IF 1/500
Anti-mouse IgG, HRP -linked	Cell Signalling, 7076	Western blot, 1/5000
Anti-rabbit IgG, HRP-linked	Cell Signalling, 7074	Western blot, 1/5000

Table 2.4. Buffer details.

Buffer	Details
Spreading buffer	200mM Tris HCl and 50µM EDTA in DDW with 0.5% sodium dodecyl sulphate (SDS)
Cell lysis buffer	1% SDS as an ionic detergent, 50mM Tris pH6.8 in cold DDW
Electrophoresis buffer	20X MOPS SDS Running Buffer (NuPAGE™) diluted to 1X in DDW
Transfer buffer	20X Transfer Buffer (NuPAGE™) diluted to 1X in 10% methanol in DDW
TBS-T	50nM TRIS (pH7.5) in 150ml NaCl

2.12 RNA extraction and sequencing

2.12.1 Extraction procedure

E2, G7 and R10 GSC and bulk cultures were grown as monolayers on 10cm diameter petri dishes. Cells were incubated overnight to allow adherence. For E2 and G7, medium was replaced by medium containing inhibitors or an equivalent volume of DMSO and incubated for 72 hours. For R10, no inhibitors were added. RNA was extracted using the RNeasy® Mini Kit (QIAGEN, 74104) as per the manufacturer's instructions. Briefly, cells were dissociated with

Accutase™, centrifuged and resuspended in buffer 'RLT'. Cell lysate was homogenised by centrifugation in a QIAshredder spin column. One volume of 70% ethanol was added to the lysate and centrifuged in an RNeasy® spin column and the flow-through discarded. Buffer 'RW1' was added and the tube centrifuged and flow-through discarded followed by the addition of buffer 'RPE' twice, with the tube centrifuged and flow-through discarded. RNA was eluted in 30-50µl of RNase-free water by centrifugation. RNA samples were stored at -20°C.

2.12.2 RNA sequencing

RNAseq was carried out by Novogene™. Sample requirements were ≥1µg, ≥20µl, and A260/280 ratio ≥2.0 and a A260/230 ratio ≥2.0. RNA concentration, quality and purity was assessed using a NanoDrop™ 2000 Spectrophotometer (ThermoScientific).

The RNAseq workflow is outlined on the Novogene™ website. Briefly, they performed additional sample quality control followed by RNA library preparation using polyA capture and reverse transcription of cDNA. Sequencing was carried out by Illumina NovaSeq™ platform and a paired-end 150bp sequencing strategy to generate ~30M read pairs.

RNA extraction and sequencing of seven paired GBM cell lines utilised within this thesis was carried out by S. Ahmed, as described previously (Carruthers et al., 2018). Briefly, a TruSeq stranded mRNA library was generated and sequenced on an Illumina HiSeq 2000™ to generate 30-45 M 100bp paired-end reads.

2.13 RNAseq bioinformatics analysis

2.13.1 Processing

Data provided by Novogene™ was processed in Galaxy to generate count files (Jalili et al., 2020). Quality of data was assessed using 'FastQC' (Andrews, 2010). 'Trimmomatic' trimming tool was ran using default settings with the addition of an 'ILLUMINACLIP' step to remove adaptor and illumina-specific sequences, a 'SLIDINGWINDOW' step which required an average quality of 20 across four bases and 'MINLEN' to remove reads less than 25bp (Bolger et al., 2014). Reads were aligned to the GrCh37 reference genome using 'HiSat2' using default settings

(Kim et al., 2015). Aligned reads were quantified by ‘HtSeq-count’ using default settings (Anders et al., 2015) and exported as count files.

2.13.2 Differential expression

Further data processing of the RNAseq count files and analysis of differential expression was carried out in the R 4.2.1 platform using the ‘DESeq2’ package (v1.36.0) (Love et al., 2014). ‘DESeq2' was used to normalise counts using a median of ratios method and assess differential expression between sample groups. Where required, scaling of normalised counts was carried out using the ‘scale’ function in R. Scaling worked by subtracting mean expression from actual expression for a gene then dividing by the standard deviation (SD) to produce a Z-score.

2.13.3 Functional analysis

Gene lists for analysis of subtypes and RS transcriptional signatures were extracted from published papers (Dreyer et al., 2021, Guerrero Llobet et al., 2022, Wang et al., 2018). Analysis of these signatures was carried out using the ‘GSVA’ (Gene Set Variation Analysis) package (v1.44.2) (Hanzelmann et al., 2013), using single sample Gene Set Enrichment Analysis (ssGSEA) with normalisation turned off, which reduced the effect that sample size had on the score (Barbie et al., 2009). Principal component analysis (PCA) was carried out using the ‘prcomp’ function within R.

Gene Set Enrichment Analysis (GSEA) was carried out using the ‘gseGO’ function within the ‘clusterProfiler’ package (v4.4.4) (Yu et al., 2012, Wu et al., 2021). All gene ontology categories were assessed, with 500 permutations, gene set sizes of 3 to 800 and a p-adjust method of ‘BH’. Results from ‘gseGO’ were visualised by ‘dotplot’, ‘emapplot’, ‘cnetplot’, ‘heatplot’ and ‘gseaplot’ functions within the ‘clusterProfiler’ and ‘DOSE’ packages (v3.22.0) (Yu et al., 2015). Enrichment of gene sets was further assessed using the ‘enrichKEGG’ and ‘enrichGO’ functions within the ‘clusterProfiler’ package.

2.13.4 Visualisation and statistical analysis

RNAseq plots were created in R. Bar plots, boxplots, volcano, MA and PCA plots were created using the 'ggplot2' package (v3.3.6) (Wickham, 2016). Heatmaps were created using the 'heatmap.2' function in the 'gplots' package (v3.1.3) (Warnes et al., 2022). Statistical analysis of RNAseq data was carried out using the 'ggpubr' package (v0.4.0) (Kassambara, 2020).

2.13.5 Analysis of published GBM RNAseq datasets

For reproducibility and consistent comparisons between datasets, all RNAseq and associated clinical data for different populations of glioma patients was downloaded from GlioVis (Bowman et al., 2017). Data was filtered, selecting only GBM histology and any missing survival data was removed.

Forest plots were created using the 'forest_plot' function in the 'survivalAnalysis' package (v0.3.0) (Wiesweg, 2022) and correlation plots were created using the 'corrplot' package (v0.92) (Wei and Simko, 2021). The curated RS signature score was calculated for each GBM patient using the 'GSVA' and 'ssGSEA' package. Cox proportional-hazards (CoxPH) regression models were fitted using the 'coxph' function in the 'survival' package (v3.3.1) (Therneau, 2022). Kaplan Meier plots were created comparing the top and bottom quarters of patients ranked by signature score, using the 'ggsurvplot' function in the 'Survminer' package (v0.4.9) (Kassambara et al., 2021).

2.14 Whole genome sequencing

2.14.1 DNA extraction

DNA was extracted from seven GSC lines using the Blood and Cell Culture DNA kit (QIAGEN, 13323), as per the manufacturer's instructions. GSCs grown as monolayers were harvested using Accutase™ and total number of cells was counted as described previously. Cells were centrifuged for 10 minutes at 1500 x g, supernatant was discarded and the cells washed two times in PBS with centrifugation. Cells were resuspended in cold PBS to a concentration of 10^7 cells/ml. To lyse the cells, 0.5ml of cell suspension was mixed with one volume of cold buffer 'C1' and three volumes of cold DDW and incubated for 10 minutes

on ice. Lysed cells were centrifuged at 1300 x g for 15 minutes at 4℃ and the supernatant discarded. Cell pellet was resuspended in 0.25ml cold buffer 'C1' and 0.75ml cold DDW to remove residual cell debris, before centrifugation. Nuclei were resuspended in 1ml of buffer 'G2' with 10-30 seconds of vortexing before the addition of 25µl QIAGEN protease solution and incubation for 30-60 minutes at 50℃, ensuring the lysate becomes clear. A QIAGEN Genomic-tip was equilibrated with 1ml of buffer 'QBT' and allowed to drip through. Lysate was vortexed for 10 seconds before it was transferred to the equilibrated QIAGEN Genomic-tip. The Genomic-tip was washed 3x1ml of buffer 'QC' and allowed to drip through. Genomic DNA was eluted with 2x1ml of buffer 'QF' and the eluate collected before DNA was precipitated with the addition of 1.4ml isopropanol. Sample was mixed and centrifuged immediately at >5000 x g for 15 minutes at 4℃ and the supernatant removed. The DNA pellet was washed with 1ml cold 70% ethanol before centrifugation at >5000 x g for 10 minutes at 4℃, supernatant was removed. The DNA pellet was allowed to air dry for 5-10 minutes before resuspension in 250µl of TE buffer pH 8.0 and DNA was dissolved overnight on a shaker. DNA was stored at -20℃. DNA extraction was carried out by K Strathdee for six of the seven cell lines.

2.14.2 Sequencing

Whole genome sequencing (WGS) of extracted DNA was carried out by Novogene™. Sample requirements were ≥0.6µg, ≥20µl, a A260/280 ratio =1.8 and a A260/230 ratio ≥2.0. DNA concentration, quality and purity was assessed using a NanoDrop™ Spectrophotometer (ThermoScientific).

The WGS workflow is outlined on the Novogene™ website. Briefly, they performed additional sample quality control followed by library construction via DNA fragmentation, end repair, adaptor ligation and PCR amplification. Sequencing was carried out by Illumina NovaSeq™ 6000 platform, which utilised a paired-end 150bp sequencing strategy to generate >60X read depth.

2.14.3 Analysis

Initial WGS data analysis was carried out by Novogene™. They performed data quality control and sequence alignment to the hg38 reference genome using

Burrows-Wheeler Aligner (BWA). They detected single nucleotide polymorphisms (SNP), InDels (insertion/deletion), structural variants (SV) and copy number variation (CNV). They used the 'ANNOVAR' tool to annotate the variants, which reported on features such as protein coding changes, allele frequency and deleteriousness prediction (Wang et al., 2010).

A literature review was carried out to identify specific mutations and variants of interest for GBM. A subset of the SNPs, InDels, SV and CNV provided by Novogene™ was created based on these specified variants. SNPs were filtered for exonic, non-synonymous SNPs with a population frequency <0.5 and a FATHMM score >0.7 (Shihab et al., 2013). A FATHMM algorithm predicts the functional, molecular and phenotypic consequences of protein missense variants and a score ≥0.7 is indicative of a pathogenic variant. SNPs in EGFR were further assessed for their prediction to be driver mutations, using EGFR driver as described by Anoosha et al (Anoosha et al., 2015). TERT promoter SNPs were investigated by analysis of C228T (hg38, Chr5: 1,295,113) and C250T (hg38, Chr5: 1,295,135) substitutions. InDels were filtered for frameshift InDels within exons. CNV analysis filtered for amplifications or deletions within exons.

2.15 In vivo investigations

All mouse experiments were carried out in accordance with the Animals Act 1986 (Scientific Procedures on living animals) and the regulatory guidelines of the EU Directive 2010 under project licence PP679129 and ethical review (University of Glasgow). Six-week-old CD-1 nude female mice were purchased from Charles River.

2.15.1 Intracranial injection of GSCs

For tumour-bearing mice, iRFP (near-infrared fluorescent protein)-tagged G7 GSCs were prepared and made available by A Koessinger, as described previously (Koessinger et al., 2020). Cells were grown as monolayers and single cell suspensions created as described in 2.1. Cells were diluted to a concentration of $0.2x10^5$ cells per µl in PBS and 5µl of cells injected.

Intracranial injection of GSCs was performed with K Strathdee as surgical lead. Anaesthesia (isoflurane) was administered at 2L/min in an induction chamber. Once anaesthesia reached a suitable depth, assessed via respiration rate and foot pinch, the mouse was transferred to the surgical frame. Isoflurane was supplied through a nosecone at a maintenance level. Vetergesic, an acute analgesic, was administered at 30µl/g via subcutaneous injection. The skull was sterilised and a 1cm incision created through the skin along the length of the skull. The Bregma was located, the junction point of the sagittal and coronal sutures of the skull, and a hole drilled in the skull (Harvard apparatus, 0.027inch diameter) 3mm towards the tail and 2mm to the right, avoiding blood vessels. Cells were mixed and 10µl loaded into a 10µl Hamilton® syringe (Sigma), which was attached to an injector holder and box to ensure steady rate of injection at 2µl/min. The needle was inserted to a 3mm depth before injection of cells. Needle was left in the brain for five minutes following injection to ensure no reflux of the cells. 3M™ Vetbond™ tissue adhesive was applied to wound. Mouse was returned to a warming cabinet and recovery observed in the immediate aftermath, a few hours after surgery and the following day. Post operative chronic analgesia (Rimadyl) was supplied in drinking water for 1-2 days.

Mice were monitored for any signs of distress (hunched posture, reduced mobility, weight loss >20%) or neurological symptoms (hemiparesis, paraplegia) twice weekly, increasing to three times a week at 10 weeks post-surgery and subsequently daily after symptom development. Symptomatic mice were humanely sacrificed. Haemoglobin and white cell count (WCC) were assessed from a tail vein blood sample and quantified by a ProCyte Dx® Haematology analyser (IDEXX).

2.15.2 Dosing and irradiation

Dosing of BAY1895344 and pamiparib (see Table 2.1) was carried out by oral gavage. IR of the mice was carried out by K Stevenson. Anaesthetic was administered via isoflurane at 2L/min in an induction chamber. Once anaesthesia reached a suitable depth, assessed via respiration rate and foot pinch, the mouse was transferred to a Small Animal Radiation Research Platform (SARRP) (Xstrahl). Isoflurane was supplied through a nosecone at a maintenance

level. Mice were dosed with 2 Gy whole brain irradiation Monday, Wednesday and Friday. Mouse was returned to a warmed cage and recovery observed.

2.15.3 Imaging of iRFP intracranial tumours

To assess growth of intracranial tumours harbouring iRFP-positive cells, mice were monitored periodically by bioluminescence Pearl® imaging (Li-Cor®). Anaesthetic was administered via isoflurane at 2L/min in an induction chamber. Once anaesthesia reached a suitable depth, assessed via respiration rate and foot pinch, the mouse was transferred to the imaging platform and immediately imaged. The mouse was returned to a cage and recovery observed.

RFP signal was quantified using ImageStudio™ software (Li-Cor®), which measured signal for a defined area of the skull relative to background signal, as shown in Figure 2.9. A baseline scan was performed at week seven and any subsequent scans were represented as a percentage change from baseline. An arbitrary 20% increase cut off was defined as an indicator of tumour growth.

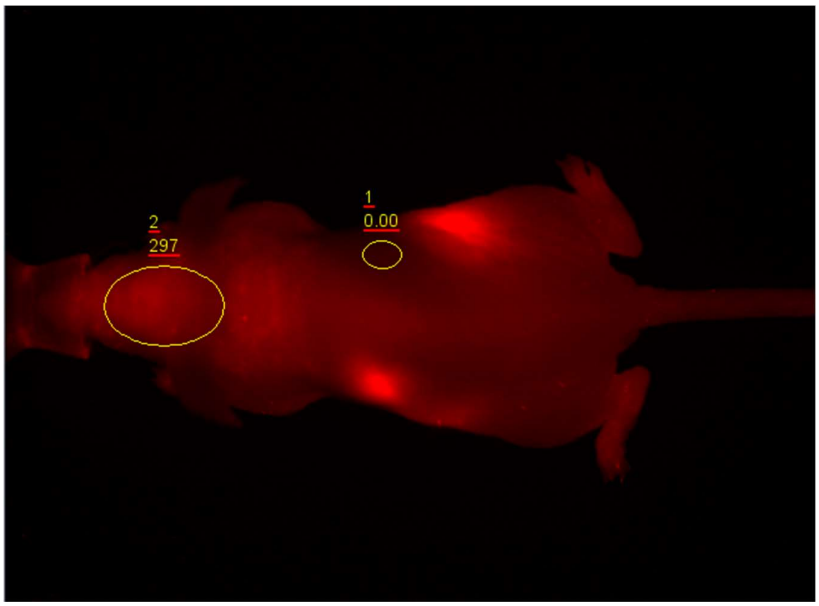

Figure 2.9. Pearl® image of iRFP signal. Representative image produced by Pearl® imaging of iRFP-tagged G7 GSCs injected intracranially and analysis by ImageStudio™ software (Li-Cor®). Background signal was used to produce a baseline, and relative signal calculated for defined region of the head.

2.15.4 Pharmacokinetic study

To assess brain and tumour penetration of BAY1895344 and pamiparib, a PK study was carried out. At the scheduled end point, mice were humanely

sacrificed. Blood samples, brain (left hemisphere) and tumour (right hemisphere focused around injection site if no tumour was visible) specimens were immediately collected and frozen.

Bioanalysis of samples was carried out by Pharmidex. Control tumour was included as matrix for blanks and standards. Quantitative bioanalysis of BAY1895344 and pamiparib in blood, normal brain and tumour samples was carried out by liquid chromatography- mass spectrometry (MS).

2.16 Statistical methods

Mean values were compared using a student's t-test or multiple comparisons were carried out by ANOVA with post-hoc Sidak test. Mean values were presented with standard error of the mean (SEM) and 95% confidence intervals (CI) reported where appropriate. Median values were compared using a Mann Whitney U test or multiple comparisons were carried out by Kruskal-Wallis one-way analysis of variance with post-hoc Dunn's test. GraphPad Prism software was used to calculate statistical significance.

Chapter 3 Model characterisation

3.1 Introduction

To characterise the response to CAiPi in GBM, *in vitro* models of GSCs and differentiated tumour bulk cells were utilised. As discussed in Chapter 1, there are several challenges to isolation of GSCs using GSC markers since no universal marker has been identified, with even the most commonly used cell surface marker CD133 not correlating with the GSC phenotype in all GBM tumours (Beier et al., 2007). Therefore, a model of GSC-enriched and GSC-depleted cultures was utilised to allow isogenic, paired cell lines to be maintained. As detailed previously in this thesis, GSCs can be enriched by culturing in serum-free media with the addition of growth factors. The use of differentiating media, containing FCS and no supplemented growth factors, generates a differentiated population, representing the tumour 'bulk' cells. *In vivo* tumorigenicity, neurosphere formation and expression of GSC markers have been studied previously (Carruthers, 2015) and validated this model's ability to isolate GSC-enriched and -depleted populations.

This thesis focused on a panel of seven primary paired GBM cell lines and this chapter aims to characterise the mutational and transcriptional landscape within this panel. These cell lines have previously been well characterised in terms of GSC marker expression via Western blot and flow cytometry, *in vivo* tumorigenicity, proliferation, cell cycle and enhanced RS in GSCs (Ahmed et al., 2015, Carruthers, 2015, Carruthers et al., 2018). Therefore, further characterisation of these cell lines focused on WGS and RNAseq available to identify common GBM mutations and transcriptional signatures of GBM subtypes, GSC markers and RS. Lastly, the status of previously described biomarkers of ATR and PARP inhibition were characterised in the cell line panel.

3.2 MGMT promoter methylation and IDH mutant status

Gliomas are frequently clinically categorised by the prognostic biomarkers MGMT promoter methylation status and IDH mutation status. In GBM, MGMT promoter methylation is an important biomarker for response to TMZ and there is some evidence that MGMT promoter methylation or expression is predictive of PARPi

sensitivity as discussed in Chapter 1. The MGMT promoter methylation status of the seven paired GSC and bulk cell lines was assessed. There are many methods for analysing MGMT methylation status, including methylation-specific PCR and pyrosequencing, however none of these methods were available at the time of analysis. Analysis of MGMT gene expression can be utilised as a surrogate method to assess promoter methylation, as epigenetic silencing of MGMT by promoter methylation has long been established (Costello et al., 1994). RNA was extracted from seven paired GSC and bulk cell lines, before sequencing, processing and analysis. MGMT count data was normalised using 'DeSeq2' in R and the expression results shown in Figure 3.1. MGMT was only expressed in R9, S2 and R24 GSC and bulk pairs, suggesting that these cell lines have unmethylated MGMT promoters and E2, R10, G7 and R15 have methylated promoters. No change in methylation status appeared to occur between GSC and bulk cell lines.

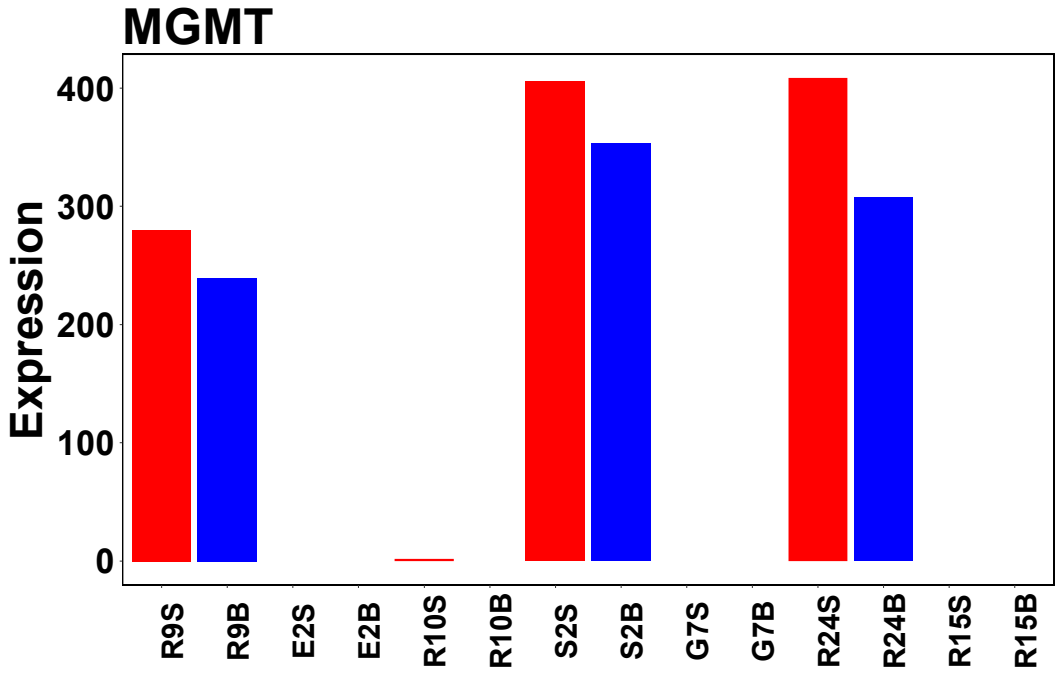

Figure 3.1. MGMT gene expression in primary paired GBM cell lines. Gene expression of MGMT was analysed in seven paired GSC (S) and bulk (B) lines. RNA was extracted from cells before RNA sequencing and data processing. Bar plots represent count data, normalised using 'DeSeq2' to produce a median of ratios, for one replicate.

Since all seven cell lines used in this thesis were characterised as GBM before the WHO reclassification by IDH status, it was of interest to investigate the mutational status of IDH1 and IDH2 by WGS. DNA was extracted from seven GSC cell lines before sequencing, data processing and analysis by Novogene™. All identified SNPs were filtered for SNPs within exonic regions of IDH1 or IDH2. This

analysis only identified missense SNPs in E2 and R15, however it resulted in a V178I substitution affecting exon six in both cell lines, so were not the critical R132 amino acid substitution in exon four. In addition, investigations of the V178I substitution found it retains wild type IDH1 enzymatic activity and is not within any known functional domains so is unlikely to be pathogenic (Ward et al., 2012). These studies suggested that all seven cell lines were IDH WT in respect to the WHO classification and were therefore most likely GBM as opposed to other high-grade gliomas.

3.3 Glioblastoma subtype

To subtype the panel of GBM cell lines used throughout this thesis, the 50 gene per subtype signature by Wang et al was utilised, which categorises cell lines as mesenchymal, classical or proneural (Wang et al., 2018). RNA was extracted from seven paired GSC and bulk cell lines, before sequencing, processing and analysis. Mesenchymal, classical and proneural gene set enrichment was assessed by the 'GSVA' package in R. Figure 3.2 shows the heatmap for the enrichment analysis and the results are summarised in Table 3.1. GSC lines were enriched for the classical and proneural subtypes, no GSC lines were mesenchymal. Conversely, bulk cell lines were enriched for the mesenchymal subtype, with only R9 and E2 being proneural and classical respectively. All cell lines had differing subtypes between their GSCs and bulk cell lines except R9.

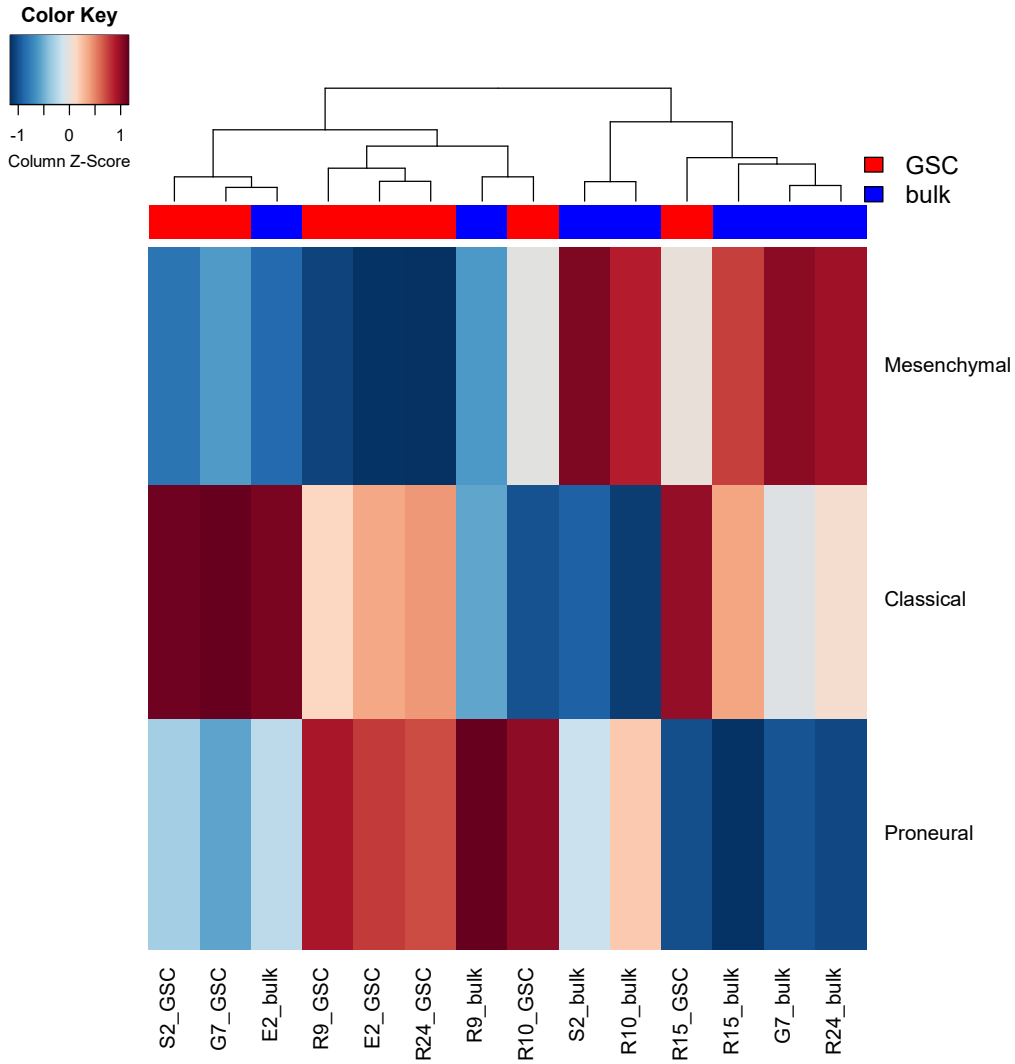

Figure 3.2. GBM subtype heatmap for primary paired GBM cell lines. Subtype gene signatures were extracted (Wang et al., 2018). Enrichment of each subtype was quantified using ssGSEA in the 'GSVA' package in R. Enrichment score was displayed in a heatmap, using the 'heatmap.2' package in R to visualise hierarchical clustering of cell lines. Clustering method was Euclidean. Scaling by column visualised the most enriched subtype per cell line.

Table 3.1. GBM subtypes for GSC and bulk cell lines.

	GSC	Bulk
R9	Proneural	Proneural
E2	Proneural	Classical
R10	Proneural	Mesenchymal
S2	Classical	Mesenchymal
G7	Classical	Mesenchymal
R24	Proneural	Mesenchymal
R15	Classical	Mesenchymal

The most enriched GBM subtype for each cell line was extrapolated from Figure 3.2.

3.4 Glioblastoma mutational landscape

The mutational landscape of the panel of seven GSCs was investigated by WGS. Analysis aimed to investigate the most commonly mutated genes in GBM. EGFR,

PTEN, TP53, TERT and CDKN2A have often been reported as the most frequently mutated or altered genes in GBM (Sakthikumar et al., 2020, Parsons et al., 2008, Brennan et al., 2013). Since these five gene alterations are frequently found in GBM, and can be informative for prognosis, treatment stratification and progression they were all studied in the panel of seven primary GSC lines. Gene mutations and CNV was assessed by WGS. SNPs and InDels were assessed in TP53, EGFR, PTEN and TERT promoter regions and CNV in EGFR and CDKN2A. To find variants most likely to affect protein function and be relevant clinically, only exonic, non-synonymous SNPs were assessed, with a population frequency <0.5 and indicated to be cancer-associated predicted by FATHMM score (Shihab et al., 2013) and EGFR SNPs were selected for driver mutations by EGFR driver (Anoosha et al., 2015). Only previously described GBM-associated TERT promoter mutations (C228T and C250T) were investigated (Nonoguchi et al., 2013). InDels of interest were identified by filtering for exonic InDels resulting in a frameshift insertion or deletion. CNV analysis focused on exonic amplifications or deletions. Further analysis of the WGS data such as structural variation and mutational signatures were not explored due to a lack of a matched normal genome. Results from these analyses are summarised in Table 3.2.

Table 3.2. SNPs, CNV and InDels in commonly mutated genes in a panel of primary GSC lines.

		R9	E2	R10	S2	G7	R24	R15
TP53	SNP	R273H	R273H	R248W	R273H	R282W R248Q	C277F	
	InDel							DEL
EGFR	SNP	R521K	A289V		R521K		R521K	R521K
	CNV							
PTEN	SNP						C105Y	P95L
	InDel	INS			INS			
TERT	SNP	C228T	C250T	C250T	C228T	C250T	C250T	C228T
CDKN2A	CNV		HomDel	HomDel			HomDel	HomDel

SNPs, CNV and InDels were analysed from WGS data for a panel of seven primary GSC cell lines in TP53, EGFR, PTEN, TERT and CDKN2A. SNPs of interest were identified by location in an exon, non-synonymous, low frequency and indicated to be pathogenic by FATHMM score and EGFR driver, or for C228T and C250T SNPs in the TERT promoter region. SNPs are represented as the amino acid substitution that occurred, InDels were identified as likely detrimental to protein function due to being exonic and frameshift insertions (INS) or deletions (DEL). CNV were filtered for exonic amplifications or deletions, HomDel indicates a homozygous deletion.

SNPs were identified in TP53 in six of the seven cell lines (85.7%) and two were identified in G7. R15 did not have a SNP of known clinical significance in TP53 however it was the only cell line with a frameshift deletion (14.3%). EGFR had SNPs in five of the seven cell lines (71.4%). Despite the high prevalence of EGFR

amplification in patients, no cell lines displayed evidence of EGFR amplification. Two cell lines had PTEN SNPs (28.6%) and a different two cell lines had a frameshift insertion (28.6%). GBM-associated TERT promoter mutations were found in all seven cell lines, with C228T found in three cell lines (42.9%) and C250T found in four (57.1%). Homozygous deletions in CDKN2A were identified in four of the seven cell lines (57.1%), which was confirmed by RNAseq expression in Figure 3.3.

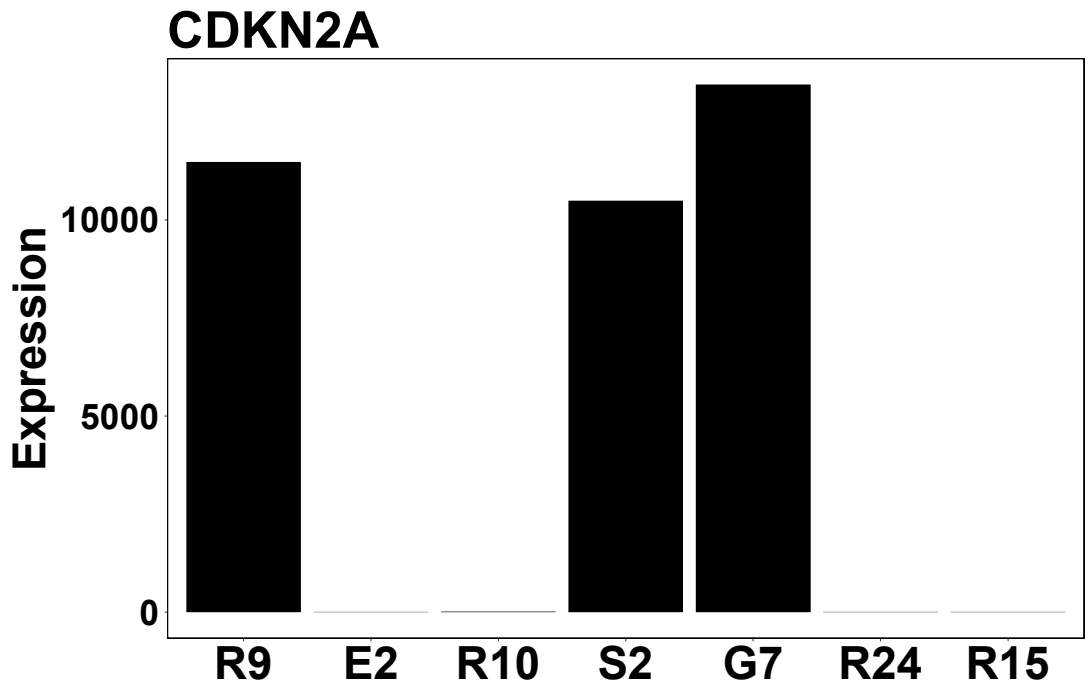

Figure 3.3. CDKN2A expression. Gene expression of CDKN2A was analysed in seven GSC lines. RNA was extracted from cells before RNA sequencing and data processing. Bar plots represent count data, normalised using 'DeSeq2' to produce a median of ratios, for one replicate.

3.5 Comparison of GSC marker expression in GSC and bulk cells

As discussed previously in this thesis, challenges remain surrounding the identification of a universally applicable GSC marker. However, panels of GSC markers can provide an indication of GSC state. Frequently used GSC markers include CD133, SOX2 and nestin, which have previously been analysed in E2 and G7 by Western blot and flow cytometry, which found upregulation of all three markers in GSCs versus their paired bulk lines (Carruthers, 2015). Expression of these markers was assessed following RNA extraction and sequencing in a dataset produced from three replicates in E2, R10 and G7, as shown in Figure 3.4. CD133 had increased expression in E2 and R10 GSCs, however not in G7.

SOX2 had higher expression in E2 and G7 GSCs, but no difference was found in R10. Nestin was expressed more in E2 GSCs, G7 GSCs showed a small but significant increase in expression but R10 had no significant differences between GSC and bulk.

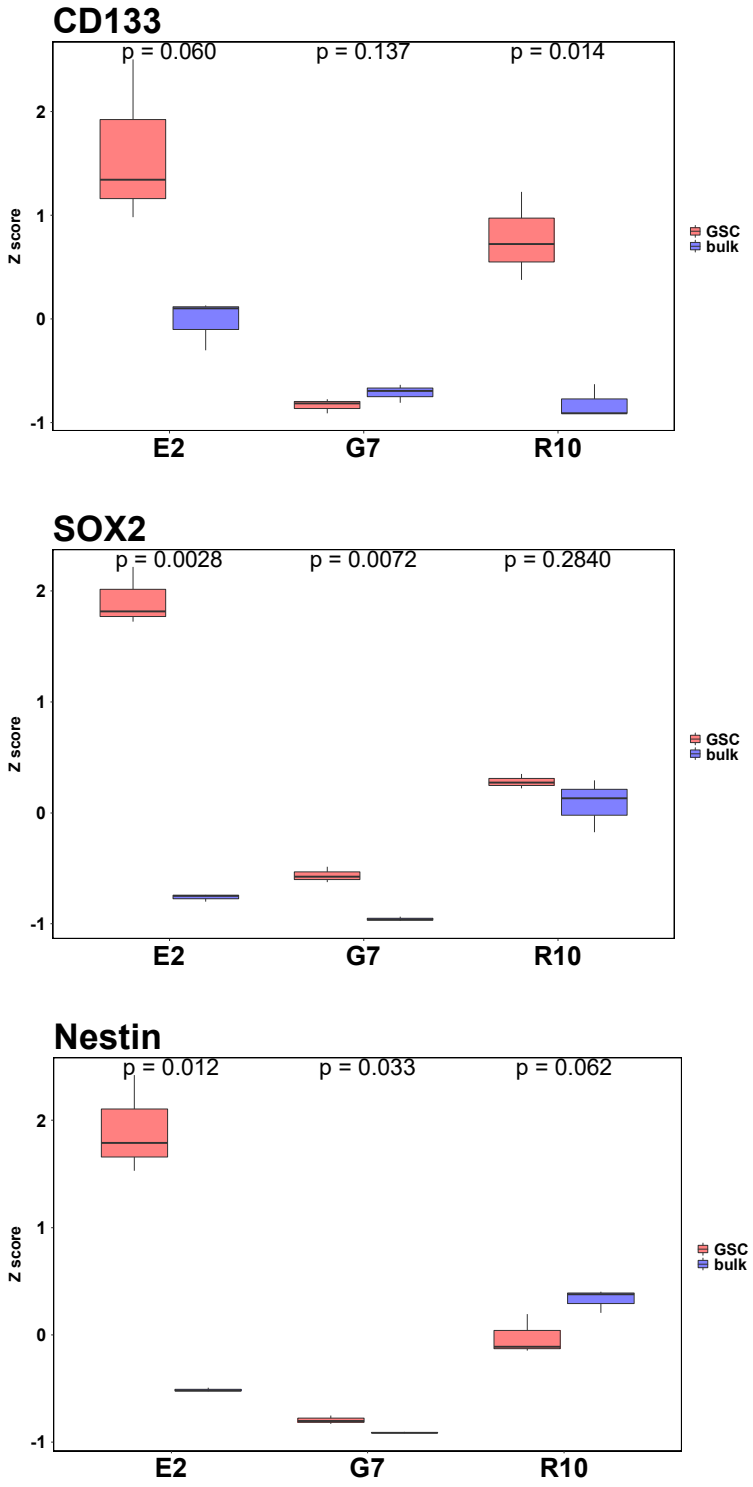

Figure 3.4. GSC marker expression in E2, G7, R10 Baseline gene expression was analysed in E2, R10 and G7 paired GSC and bulk cells. RNA was extracted from cells before RNA sequencing and data processing. Count data was normalised using DeSeq2 and scaled to produce a z-score which was used to compare gene expression of CD133, SOX2 and nestin. Box plots represent data from three independent experiments, p-values calculated by T test using 'ggpubr' package in R.

3.6 Characterisation of endogenous replication stress in GSC and bulk cultures

An overarching hypothesis of this thesis is that GSCs can be selectively targeted by inhibiting the RS response. It has previously been shown by Carruthers et al that GSCs have elevated RS compared to their paired bulk cells in E2, G7 and R15, assessed by reduced fork velocity via a DNA fibre assay, a gold standard assay for replicative stress studies (Carruthers et al., 2018). Since an aim of this thesis is to investigate targeting of the RS response, transcriptional indicators of RS were analysed.

RS was first assessed using a RS signature, curated and described by Dreyer et al (Dreyer et al., 2021). They identified a transcriptomic signature that predicted RS in pancreatic patient-derived cell lines, and importantly predicted response to ATR inhibition. The RS signature included 20 GO terms and their associated genes and analysis involved gene set enrichment scoring for each GO term. The R package ‘GSVA’ was used to score each GO term within the signature, and results shown in Figure 3.5. In general, GSCs scored higher than bulk cells, and furthermore within each pair the GSC line ranked higher than its paired bulk cell.

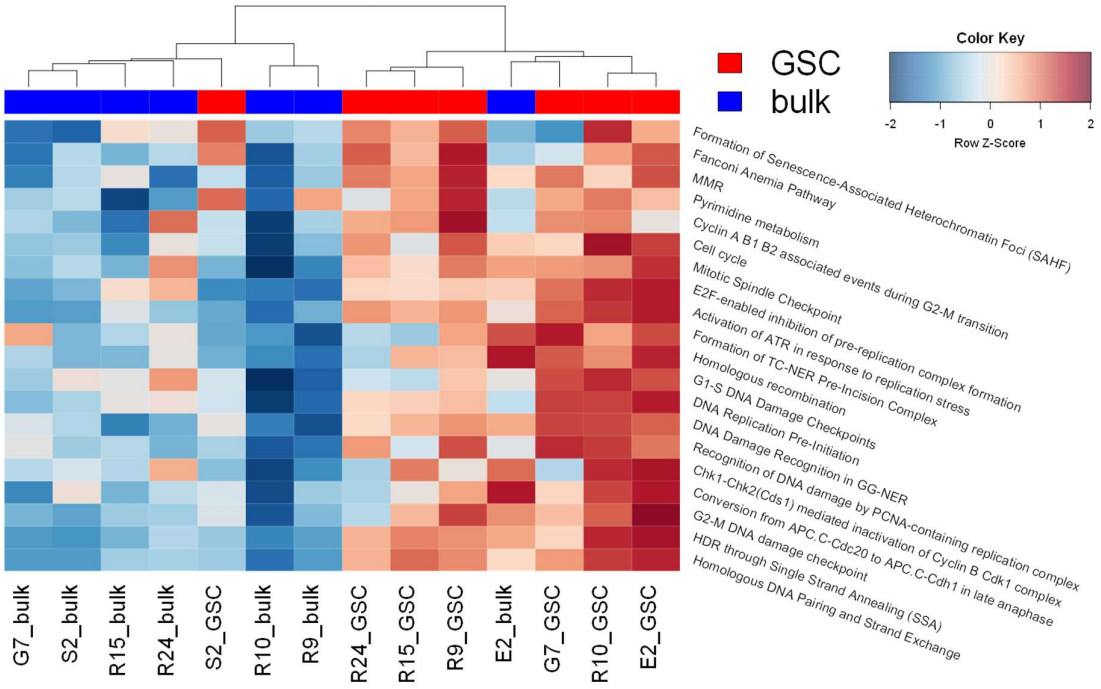

Figure 3.5. Replication stress signature. RS signature was made available by the PrecisionPanc group (Dreyer et al., 2021). Enrichment of each GO term within the signature was quantified using ssGSEA in the 'GSVA' package in R. Enrichment score was displayed in a heatmap, using the 'heatmap.2' package in R to visualise hierarchical clustering of cell lines, scaling was carried out by row.

Increased RS in GSCs was further validated by analysis of a second transcriptional signature of eight RS-inducing oncogenes, described by Guerrero et al (Guerrero Llobet et al., 2022). This gene set was assessed by the 'GSVA' R package to create a signature score for both GSC and bulk cells. The difference between GSC and bulk cells within each cell line was quantified and the results shown in Figure 3.6. All GSCs scored higher for this oncogene RS signature, except S2 where bulk had a slightly higher score. Overall, transcriptional analysis suggests that GSCs tend to have more endogenous RS, in keeping with DNA fibre analysis.

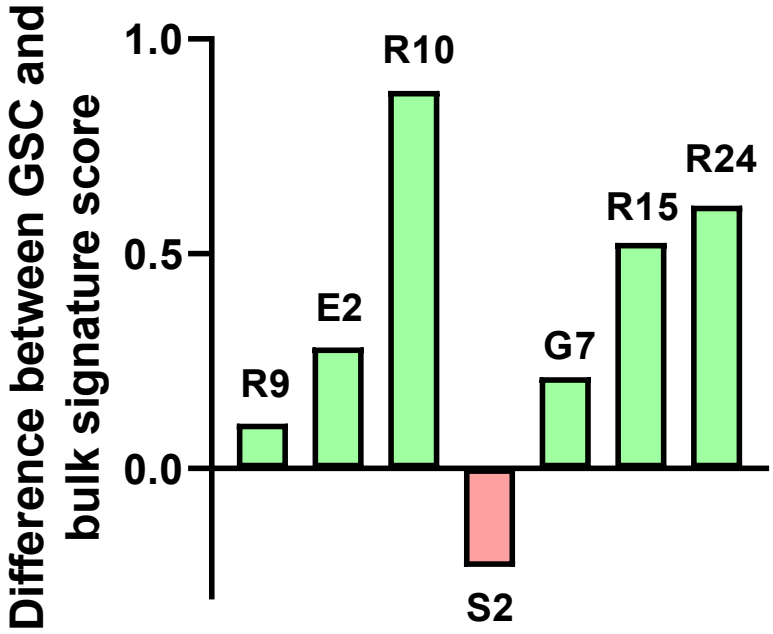

Figure 3.6. RS-inducing oncogene signature. Oncogenic RS signature was extracted (Guerrero Llobet et al., 2022). Enrichment of the gene set was quantified using the 'GSVA' package in R. Change in enrichment score in GSCs versus bulk is represented by a bar plot, with green bars indicating a higher score in GSC, and red indicating a higher score in bulk.

3.7 Investigations of previously discussed ATRi and PARPi biomarkers in GSCs

Biomarkers of PARPi, ATRi and CAiPi have been described in a range of cancer types, as discussed in Chapter 1 and summarised in Table 1.3. These biomarkers were explored to investigate their relevance to GSC response to CAiPi. These investigations utilised baseline RNAseq data, and CNV and SNPs from WGS analysis, as described previously in this chapter. These lists were parsed for genes of interest and only SNPs that induced a missense mutation and that reached a FATHMM score cut off 0.7 for pathogenicity included (Shihab et al., 2015). Pathogenic missense SNPs in ATM, BRCA1, BRCA2 and PALB2 were analysed. Gene expression of candidate biomarkers are assessed in Figure 3.7.

MYC/MYCN amplification has been described as a marker of PARPi sensitivity in GSCs, which also predicted synergy when combined with an ATR inhibitor (Ning et al., 2019). Amplification of MYCN was only found in R24 with a copy number of three, which corresponded to an increase in MYCN gene expression, as shown in Figure 3.7. ATM deficiency has frequently been identified as a marker of PARPi, ATRi and CAiPi sensitivity in a range of different cancer types, so ATM

CNV, SNP mutations and gene expression were investigated in a panel of GSCs. No CNV for ATM was observed in any cell line, but ATM expression was variable across the seven cell lines. Pathogenic, missense ATM SNP mutations were identified in all cell lines except E2 and R10 (Table 3.3).

Table 3.3. Pathogenic, missense, SNP mutations in ATM

	SNP ID	Amino acid change
R9	rs1800056	F858L
	rs138398778	R337C
	rs1800057	P1054R
E2		
R10		
S2	rs1800056	F858L
	rs138398778	R337C
	rs1800057	P1054R
G7	rs148993589	K1454N
	rs1801516	D1853N
R24	rs1801516	D1853N
R15	rs1801516	D1853N

Candidate SNPs identified after analysis of WGS in seven GSC lines. Likely pathogenic SNPs parsed by missense mutation and FATHMM score >0.7.

Other previously described biomarkers of ATR inhibition and or PARP inhibition, that were discussed in Chapter 1 and investigated in this panel of GSC lines, included IDH1/2 mutations (Sulkowski et al., 2017), SLFN11 expression (Murai et al., 2016), CCNE1 amplification (Toledo et al., 2011) and HR-associated genes such as BRCA1/2 and PALB2 (Dziadkowiec et al., 2016). No pathogenic, missense SNP mutations were identified for BRCA1, BRCA2 and PALB2 and as previously discussed the cell lines were all IDH1/2 WT. SLFN11 expression varied markedly between cell lines, including no expression in R9 or S2. No CNV was identified for CCNE1, however gene expression did vary across the seven cell lines.

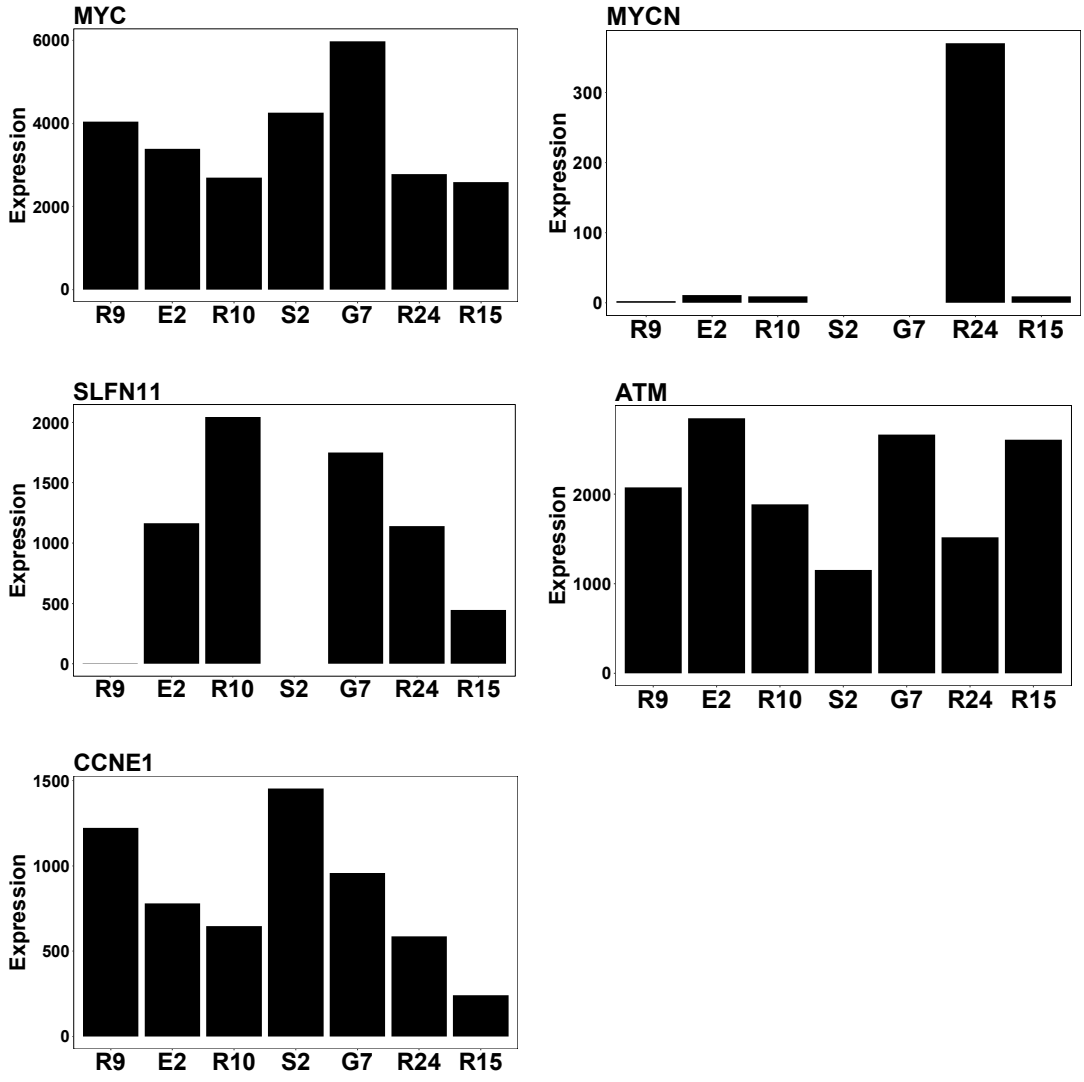

Figure 3.7. Expression of candidate biomarkers in a panel of paired GBM cell lines. Baseline gene expression was analysed in seven GSC lines. RNA was extracted from cells before RNA sequencing and data processing. Count data was normalised using 'DeSeq2' to produce a median of ratios. Bar plots represent data from one replicate.

3.8 Expression of inhibitor targets

Targeting of RS in this thesis is via combined inhibition of ATR and PARP. It was therefore of interest to investigate the expression levels of both ATR and PARP1, to gain insight into expression of target molecules. Gene expression was analysed in the panel of seven paired GBM cell lines, and the results shown in Figure 3.8. Both ATR and PARP1 were highly expressed in all paired cell lines, and therefore the targets of the inhibitors were present and any variable responses to CAiPi would not be explained by lack of target expression.

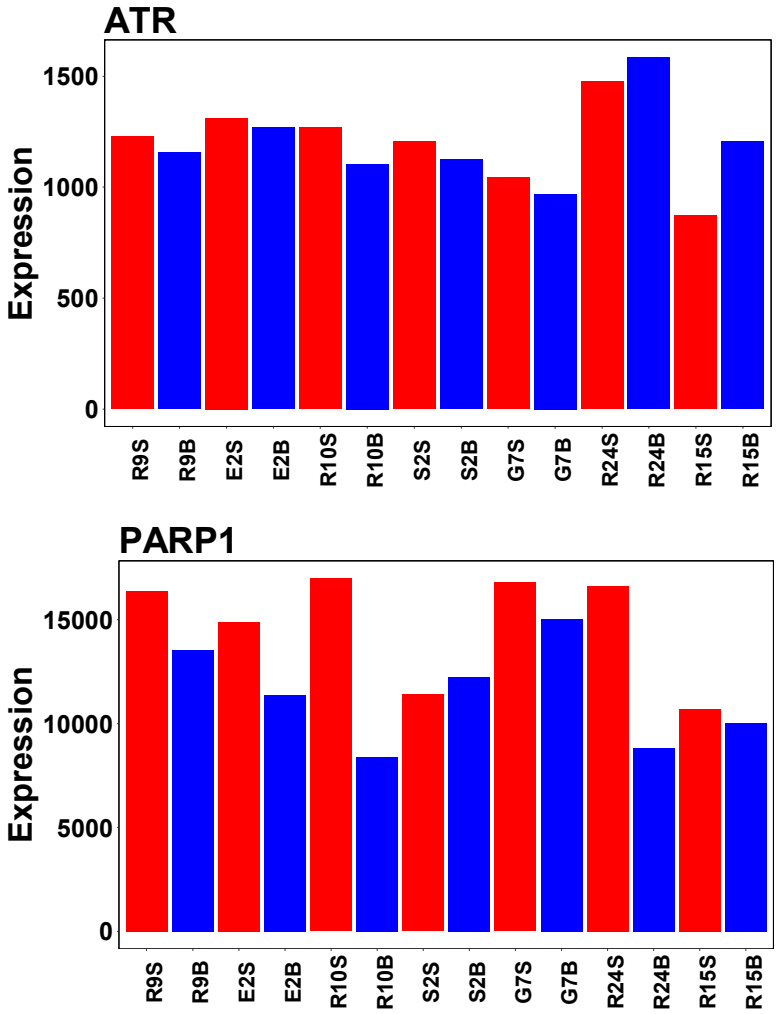

Figure 3.8. Gene expression of targets PARP and ATR inhibitors. Gene expression of ATR and PARP1 was analysed in seven paired GSC (S) and bulk (B) lines. RNA was extracted from cells before RNA sequencing and data processing. Bar plots represent count data, normalised using 'DeSeq2' to produce a median of ratios, for one replicate.

3.9 Conclusions

This chapter has characterised the genomic and transcriptomic landscapes of paired GSC and bulk cultures, which will be utilised throughout this thesis. Three of the seven primary cell lines likely have unmethylated MGMT promoters based on gene expression analysis, and the other four appeared to have MGMT promoter methylation. Therefore, there is relatively good representation of MGMT methylation, since MGMT methylation is found in ~45% of GBM patients (Hegi et al., 2005). No IDH1 or IDH2 mutations were found in the respective critical amino acids. This data supports the proposal that all seven cell lines were derived from IDH WT GBM tumour samples. Analysis of GBM subtypes found

that GSCs tended to be classical or proneural and bulk cells were largely mesenchymal.

Analysis of mutations and alterations in commonly mutated genes in GBM found no evidence of EGFR amplification. Additionally, the most common EGFR mutation in GBM, EGFRvIII which results in a deletion of 801b, was not detected in any cell lines despite being expressed in ~50% of GBM patients. However, studies have found a close correlation between EGFR amplification and EGFRvIII expression (Shinojima et al., 2003), so it may not be surprising these cell lines did not express EGFRvIII. Five of the seven cell lines did have missense mutations within EGFR, which is slightly more than has been previously reported which has varied from 12.5% to 50% (Parsons et al., 2008, Lee et al., 2006b, Sakthikumar et al., 2020, Cimino et al., 2015). Of those five mutations, four resulted in an R521K substitution, which was found in 26.4% of GBM patients in a study by Cimino et al (Cimino et al., 2015). The remaining SNP, leading to an A289 substitution in E2 has been reported in 3.7% of GBM patients (Lee et al., 2006b). Therefore, these are likely important, GBM-associated SNPs that have been identified.

SNP mutations in TP53 were also identified at a higher rate than has been reported in the literature. Four of the five different affected amino acids in these cell lines were within a TP53 “hotspot” for mutations (Zhang et al., 2018). The remaining substitution, C277F, has been implicated in TP53 DNA binding as it introduces a large hydrophobic side chain (Olivier et al., 2010). There are no reports on the clinical significance of the specific TP53 deletion in R15, however a frameshift deletion likely has a detrimental effect on protein function. CDKN2A homozygous deletions were found in 57.1% of the GSC lines, which is a good representation of the clinical landscape of CDKN2A which is deleted in ~50% of GBM patients. Additionally, PTEN SNPs had a similar prevalence in these cell lines and in the general GBM population, being present in ~25% of both. No studies have linked the specific PTEN SNPs to GBM, but they have been associated with cancer (Mehenni et al., 2005, Rodriguez-Escudero et al., 2011). There are no reports of the specific PTEN frameshift insertions found in two cell lines but they likely have detrimental effects on the protein product. No homozygous deletions were observed in TP53 or PTEN, despite being observed in

5% of GBM patients (Parsons et al., 2008), although this may be a limitation of the sample size. The TERT promoter mutation SNPs C228T and C250T were identified in all seven cell lines, largely in keeping with reported frequencies of 80-90% in primary GBM (Simon et al., 2015, Mosrati et al., 2015) and *in vitro* models of GBM (Johanns et al., 2016) albeit C228T were reported more frequently than C250T (Mosrati et al., 2015), which was the opposite to those observed in these cell lines. In general, with the exception of EGFR amplification, these cell lines appear to be a good representation of common GBM mutations.

Analysis of GSC markers confirmed the challenges that have been reported in finding a universally satisfactory GSC marker, as varied expression was observed. However, a panel of GSC markers may prove the most informative and may help identify cell line-specific markers that can be used to isolate GSCs by cell sorting. Conversely to the observations here, flow cytometry cell analysis in G7 did identify more $CD133^{+}$ cells within a GSC-enriched population compared to bulk (Carruthers, 2015). This highlights a potential limitation of RNAseq analysis, which represents mRNA levels but not necessarily protein levels. Additionally, RNAseq may be limited in its potential to accurately correlate with cell surface markers like CD133. Therefore, flow cytometry or Western blot may be more robust methods for identification of GSC marker expression.

Investigations of previously described biomarkers found only one incidence of MYC/MYCN amplification in R24 therefore any analysis of this as a biomarker within this dataset may be limited. However, there are contrasting reports of MYC amplification as a marker of PARPi sensitivity (Ning et al., 2019, Wu et al., 2020). Five of the seven cell lines had pathogenic ATM SNPs. Analysis of key HR genes found no pathogenic SNP mutations, in keeping with GBM being regarded as a BRCA-intact cancer, with BRCA mutations arising very infrequently (Boukerroucha et al., 2015). Strikingly, R9 and S2 did not express SLFN11, which could predict resistance to PARPi. Overall, there are variations in biomarker expression or presence, which could be analysed for predictors of GSC response to CAiPi.

Lastly, transcriptional signatures of RS were increased in GSCs compared to bulk cells, in keeping with previous reports of RS in GSCs by DNA fibre assay

(Carruthers et al., 2018). Not only did Carruthers et al find increased RS in GSCs, but they also showed GSC-specific cytotoxicity to targeting RS via PARPi and ATRi. Additionally, the RS transcriptional signature by Dreyer et al predicted sensitivity to ATRi (Dreyer et al., 2021). It was therefore hypothesised that increased RS is a biomarker for CAiPi in GSCs, and the rest of this thesis aimed to investigate mechanisms of GSC response to CAiPi.

Chapter 4 Characterisation of GSC and bulk cell responses to combined ATR and PARP inhibition

4.1 Introduction

The aim of this chapter was to characterise responses to CAiPi in a panel of paired GSC and bulk primary GBM cell lines. This was assessed by clonogenic survival assays and higher throughput cell viability assays in GSC-enriched populations by culturing under serum-free conditions with the addition of growth factors and bulk-enriched populations under differentiating conditions. Differential GSC and bulk responses to CAiPi were further confirmed in CD133 sorted populations by neurosphere assay. As demonstrated previously by Carruthers et al (Carruthers et al., 2018) and further characterised by transcriptomic analysis in Chapter 3, GSCs have higher levels of RS than their paired bulk counterparts. Since ATR and PARP are both active in the RS response, it was hypothesised that the GSC population would be selectively targeted by CAiPi.

4.2 Effects of ATR and PARP inhibition by clonogenic survival assay

Analysis of CAiPi in GSC and bulk pairs carried out previously by Carruthers et al (Carruthers et al., 2018) utilised a cell viability assay, which measures metabolically active 'healthy' cells and is indicative of cytotoxicity but is not a measure of cell survival. Therefore, the gold standard clonogenic survival assay was carried out in E2 and G7 to validate their findings that GSCs were selectively targeted by CAiPi compared to their paired bulk counterparts. Cells were incubated with vehicle, olaparib (1μM), VE821 (5μM) and the combination for 24, 48 and 72 hours. After this time, drug media was replaced with fresh, drug-free media and cells were incubated to allow colonies to form. Clonogenic survival fractions were normalised to vehicle control after correcting for plating efficiencies.

Figure 4.1 displays clonogenic survival assay results in E2 with representative images of colonies formed. This analysis confirmed that E2 GSCs were more

sensitive than their bulk counterpart at all time points. The survival fraction was significantly reduced with CAiPi compared with ATRi alone at all time points except 24 hours in E2 bulk. Analysis of cell survival over the three time points showed that PARPi and ATRi alone were not significantly affected by time exposed to the monotherapies. However, cell survival decreased with increased length of exposure to CAiPi in both GSC and bulk cells (Figure 4.2).

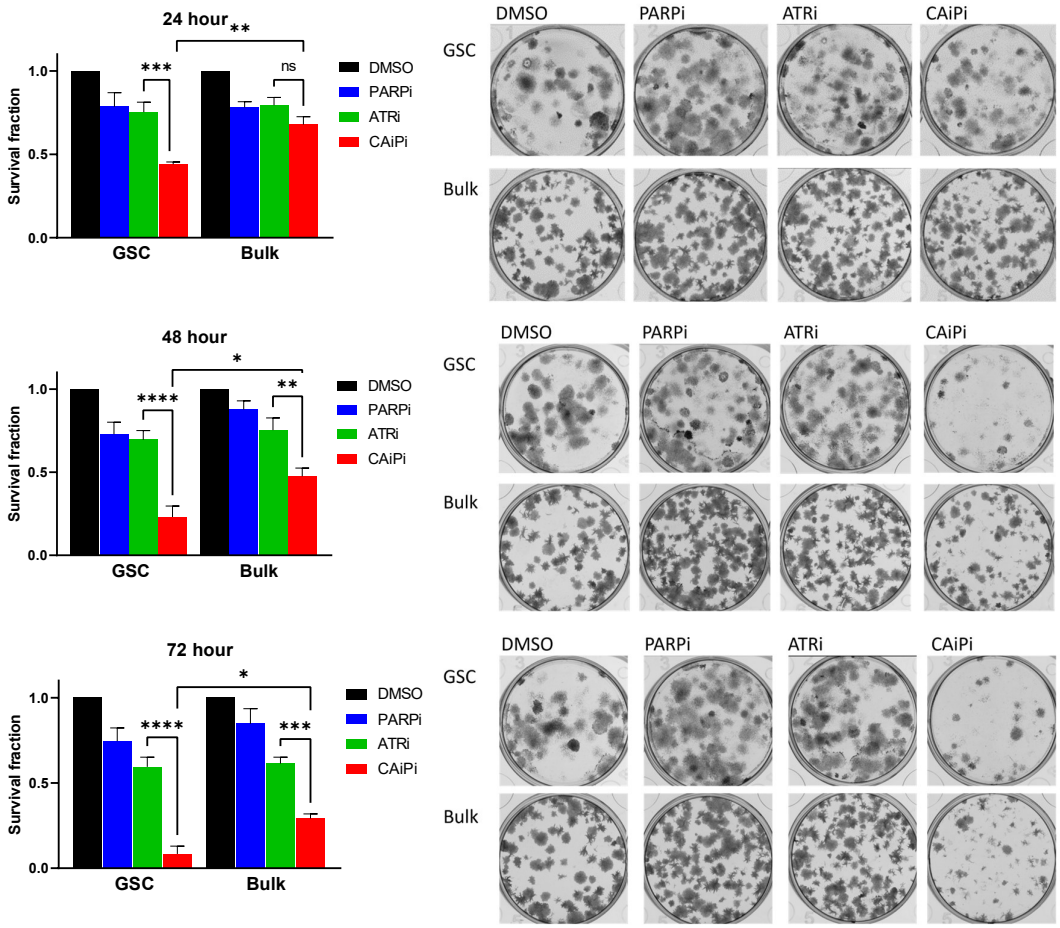

Figure 4.1. Clonogenic survival analysis of E2 GSC versus bulk cultures following ATR and PARP inhibition. E2 GSC and bulk cell survival analysed by colony formation assay after increasing length of exposure to VE821 (5μM), olaparib (1μM) and the combination, relative to vehicle control after correcting for plate efficiency. Bar charts represent mean and SEM of ≥3 independent experiments, adjusted p-values calculated by one-way ANOVA with post-hoc Sidak test (*p<0.05, **p<0.01, ***p<0.001, ****p<0,0001, ns = not significant). Representative images of colony formation for each condition are shown.

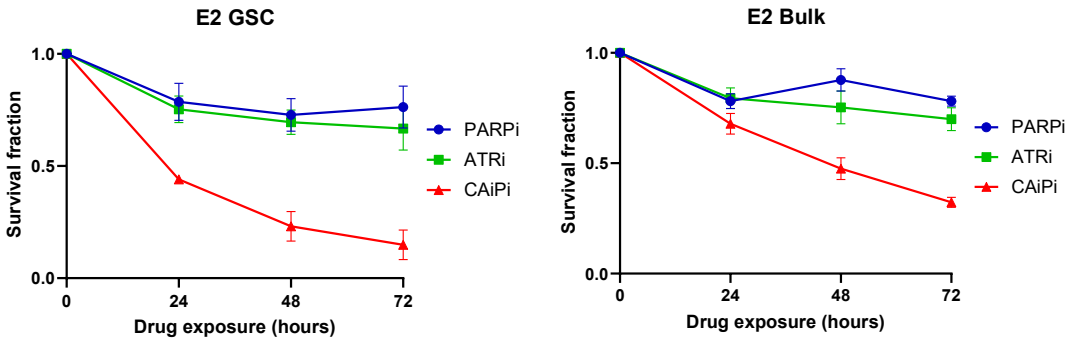

Figure 4.2. E2 clonogenic survival time course. Clonogenic assay data from Figure 4.1 was plotted to show changes in cell survival with increasing drug exposure time, relative to control.

Figure 4.3 shows the results of a clonogenic survival assay in G7. Conversely to E2, the survival fraction of G7 bulk was reduced in comparison to their paired GSCs, although it did not reach significance at 72 hours. There was also a general trend for a greater reduction in survival fraction with CAiPi versus ATRi, although it did not reach significance at all time points, suggesting that the addition of a PARPi had less effect in G7 versus E2. Analysis of cell survival over the three time points in G7 found that increased length of exposure to PARPi had little effect in GSCs and bulk cell lines (Figure 4.4). However, unlike E2, increased length of ATRi exposure induced a reduction in cell survival in G7 along with CAiPi.

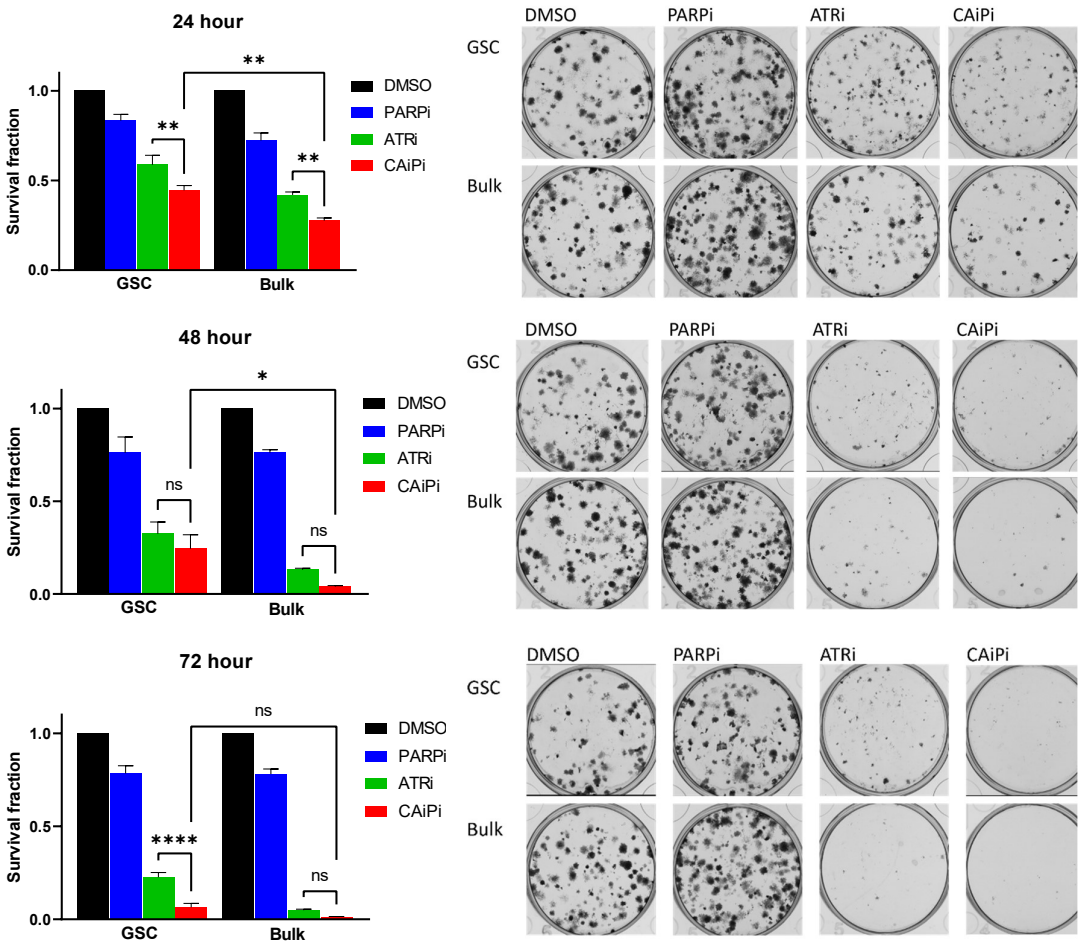

Figure 4.3. Clonogenic survival analysis of G7 GSC versus bulk cultures following ATR and PARP inhibition. G7 GSC and bulk cell survival analysed by colony formation assay after increasing length of exposure to VE821 (5μM), olaparib (1μM) and the combination, relative to vehicle control after correcting for plate efficiency. Bar charts represent mean and SEM of ≥3 independent experiments, adjusted p-values calculated by one-way ANOVA with post-hoc Sidak test (*p<0.05, **p<0.01, ****p<0,0001, ns = not significant). Representative images of colony formation for each condition are shown.

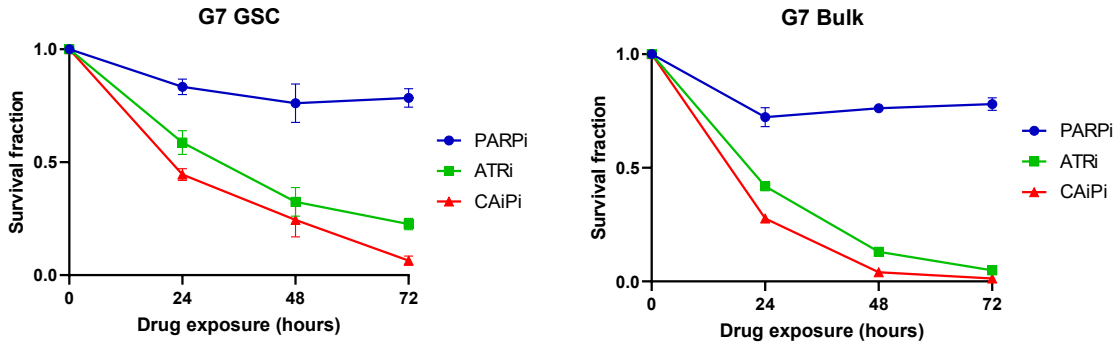

Figure 4.4. G7 clonogenic survival time course. Clonogenic assay data from Figure 4.3 was plotted to show changes in cell survival with increasing drug exposure time, relative to control.

To investigate the drug interactions between ATRi and PARPi in different cell lines, the coefficient of drug interaction (CDI) was calculated, as described

previously (Xu et al., 2007). CDI is used to assess interactions between drug combinations and is calculated by: CDI = AB / (A x B), where AB is the combined treatment response, and A or B is the single agent treatment response, relative to control. A CDI<1 indicates supra-additive drug interactions and a CDI<0.7 is indicative of a greater degree of supra-additive effects. CDIs for E2 and G7 GSC and bulk pairs were therefore calculated as CAiPi/(ATRi x PARPi) using 24, 48 and 72 hour clonogenic cell survival data and the results are shown in Figure 4.5. In all cell lines there was evidence of supra-additive drug interactions with CDI<1.0, except E2 bulk at 24 hours. There was a trend towards greater supra-additive effects in E2 GSC versus G7 GSC, although this observation was only significant at 48 hours. E2 GSC had greater drug interactions compared to E2 bulk by 72 hours. At 48 hours G7 bulk showed evidence of greater drug interactions compared to G7 GSC, although this difference was lost by 72 hours.

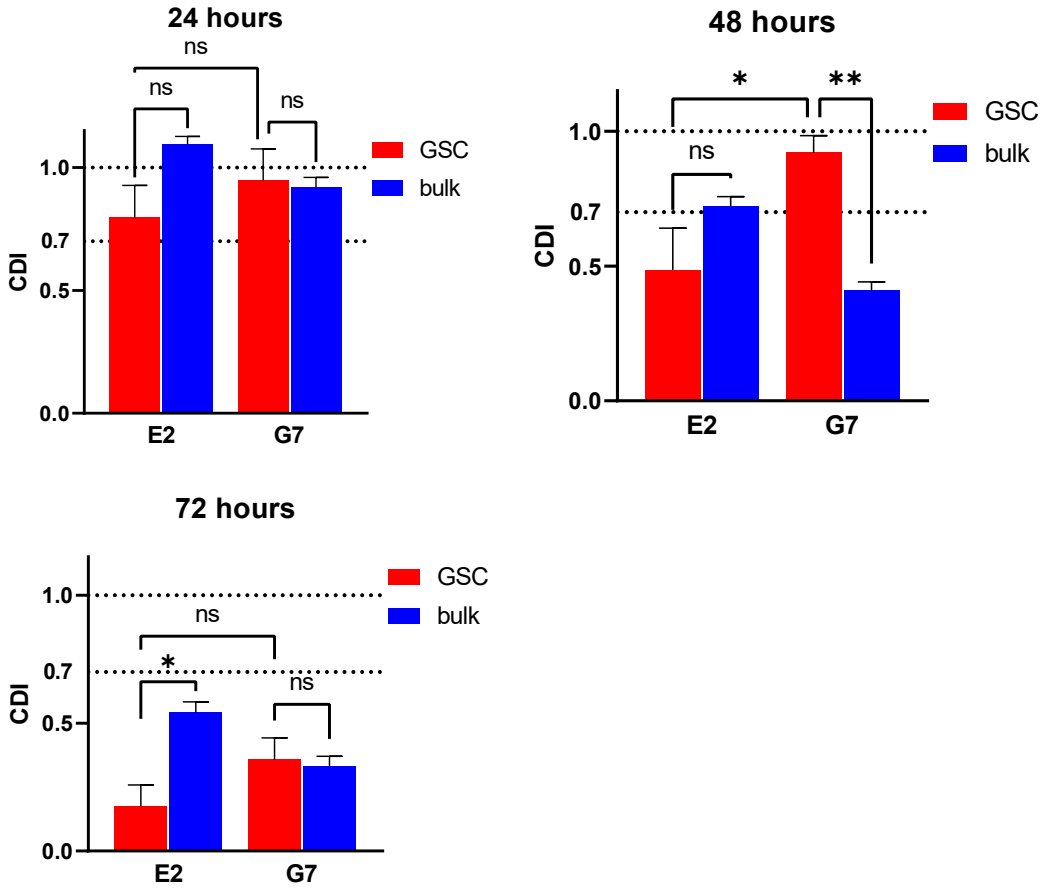

Figure 4.5. CDI values for ATR and PARP interactions in E2 and G7. CDI values were calculated as CAiPi / (ATRi*PARPi) using clonogenic data from ≥3 independent experiments. Line at 1.0 is a pre-defined cut off for supra-additive drug interactions, and at 0.7 is indicative of significant supra-additive effects. Bar charts represent mean and SEM of ≥3 independent experiments, adjusted p-values calculated by one-way ANOVA with post-hoc Sidak test (*p<0.05, **p<0.01, ns = not significant).

4.3 Analysis of cell viability in response to ATR and PARP inhibition on GSC cultures

Since G7 GSCs did not have a significant reduction in cell survival in comparison to G7 bulk by targeting the RS response, contradicting the proposed hypothesis that GSC-associated RS would predict sensitivity, cell responses to CAiPi were further characterised by a higher throughput cell viability assay in a panel of seven paired GBM cell lines. Responses to ATRi, PARPi and CAiPi were first assessed in GSCs. GSCs were plated in 96-well plates in media containing olaparib (1μM), VE821 (5μM), the combination and a DMSO vehicle control. Length of drug exposure was 24-hours followed by five days of drug-free media (Figure 4.6) or six days continuous exposure (Figure 4.7). Cell viability at the end of the six days was assessed by CellTiter-Glo®. All seven GSC lines had a statistically significant decrease in cell viability after 24-hour exposure to CAiPi over vehicle control. The greatest reduction in cell viability with CAiPi was seen in R9, E2 and R10, representing 36.1% [95% CI: 12.6, 59.7], 46.9% [95% CI: 27.5, 66.3] and 55.2% [95% CI: 21.7, 88.7] of control cell viability respectively. After 24-hour exposure, five of the seven GSCs showed a statistically significant benefit of CAiPi over ATRi alone. No statistically significant decreases in cell viability after 24-hour PARP inhibition was observed.

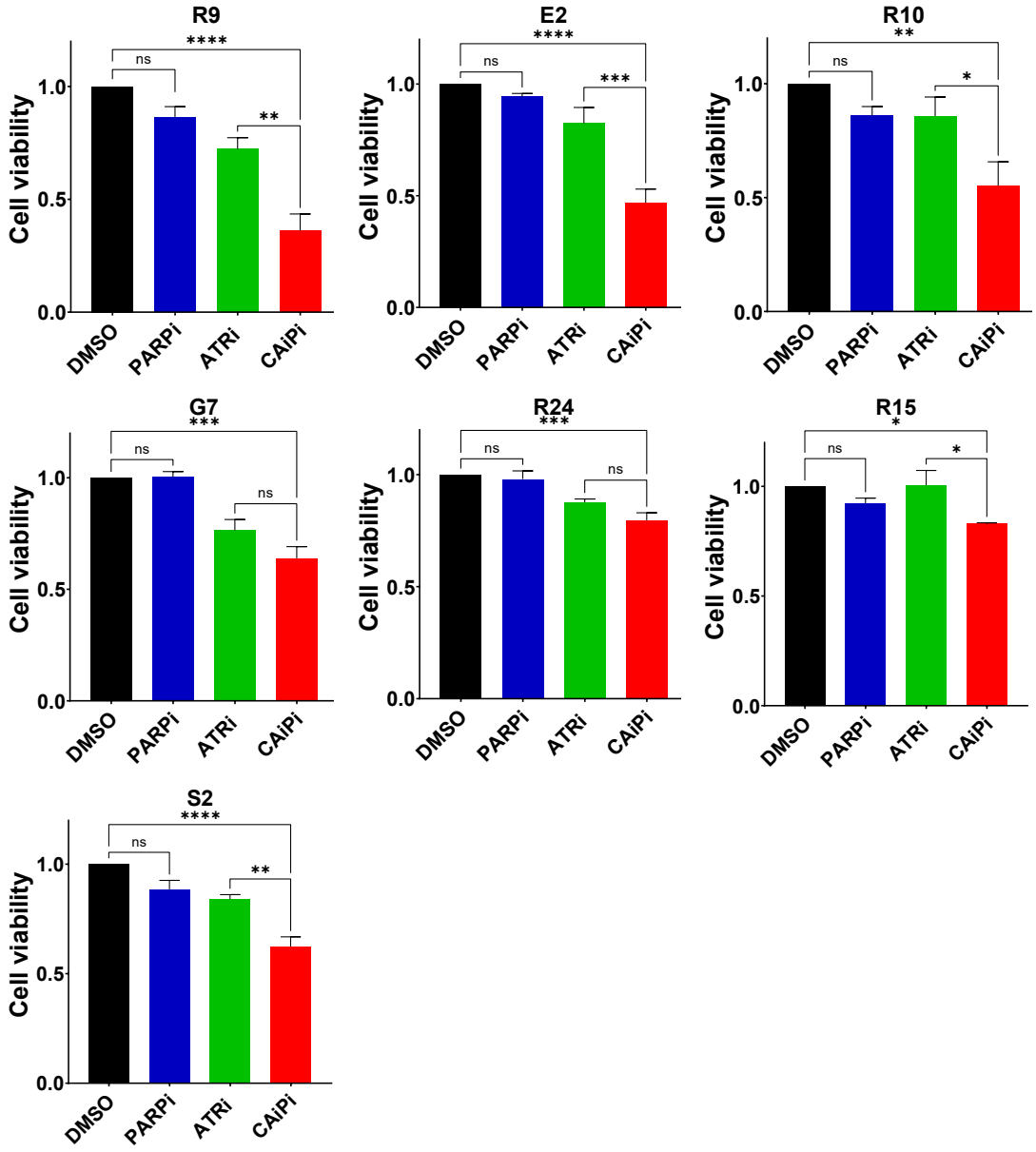

Figure 4.6. GBM GSC viability following 24-hour exposure to ATR and PARP inhibition. Average cell viability in GSCs was analysed using CellTiter-Glo® after 24-hour exposure to olaparib (1μM), VE821 (5μM) and the combination, relative to vehicle control. Cell viability in E2 and R10 was carried out previously by K. Strathdee (Carruthers et al., 2018). Bar charts represent mean and SEM of ≥3 independent experiments, adjusted p-values calculated by one-way ANOVA with post-hoc Sidak test (*p<0.05, **p<0.01, ***p<0.001, ****p<0.0001, ns=not significant).

After six-day exposure to the drugs all seven GSC lines had a statistically significant decrease in cell viability after CAiPi compared to control. R9, E2 and R10 continued to be the most sensitive to CAiPi, in keeping with 24-hour data, with cell viabilities of 9.8% [95% CI: -0.02, 21.3], 23.8% [95% CI: 14.2, 33.4] and 28.6% [95% CI: 4.2, 52.9] relative to vehicle control. PARPi single agent activity after six-day exposure remained minimal, however statistically significant decreases in cell viability were observed in E2, R10 and R15 GSCs. R9, E2, R10

and R15 all had statistically significant decreases in cell viability in response to CAiPi when compared to ATRi alone.

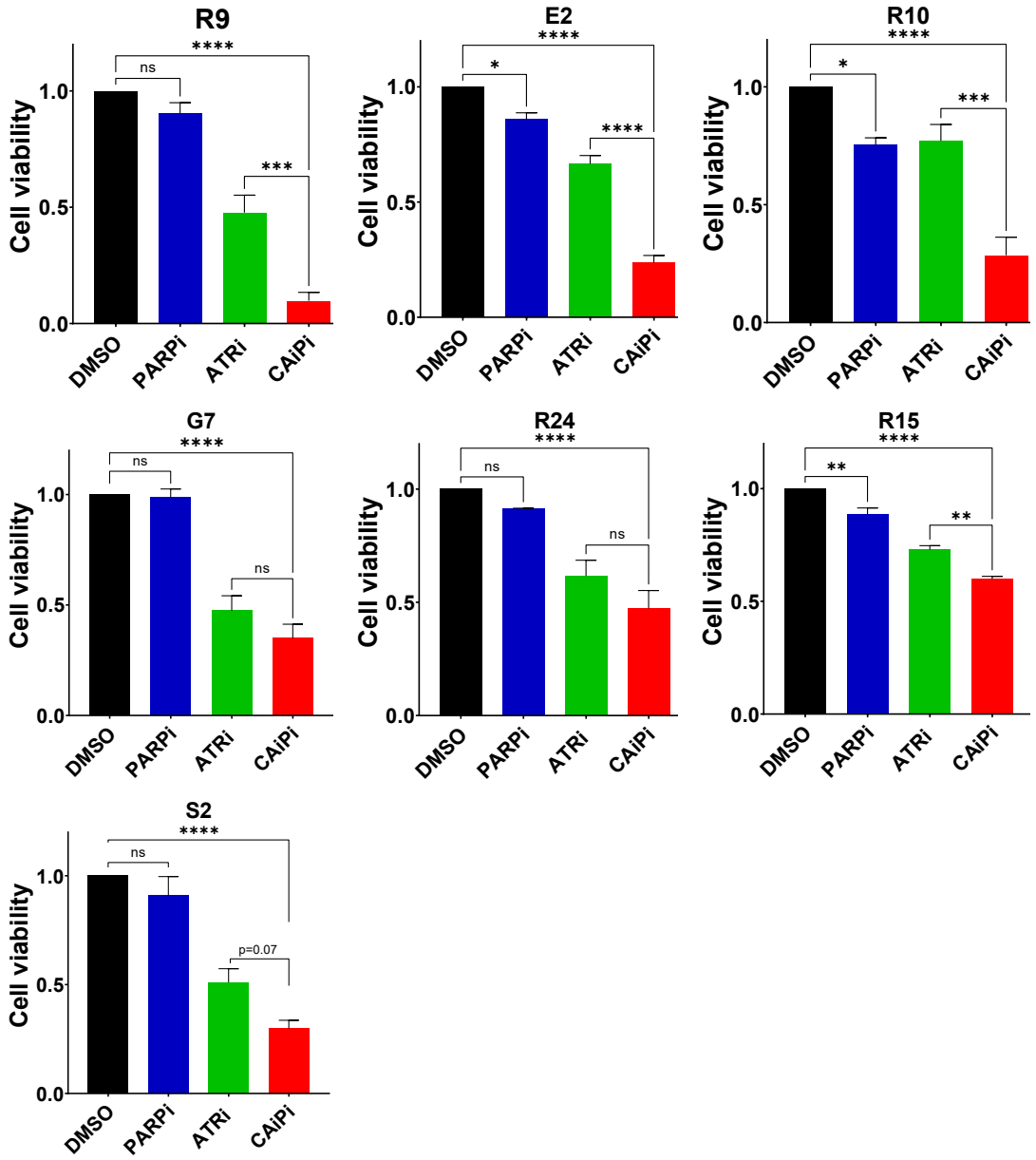

Figure 4.7. GBM GSC viability following 6-day exposure to ATR and PARP inhibition. Average cell viability in GSCs was analysed using CellTiter-Glo® after 6-day exposure to olaparib (1μM), VE821 (5μM) and the combination, relative to vehicle control. Cell viability in E2 and R10 was carried out previously by K. Strathdee. Bar charts represent mean and SEM of ≥3 independent experiments, adjusted p-values calculated by one-way ANOVA with post-hoc Sidak test (*p<0.05, **p<0.01, ***p<0.001, ****p<0.0001, ns=not significant).

4.4 Analysis of cell viability in response to ATR and PARP inhibition on bulk cultures

CAiPi was analysed in bulk cell lines, as described previously for GSCs. Analysis of 24-hour incubation with the inhibitors showed that CAiPi induced a

statistically significant decrease in cell viability compared to vehicle control in all bulk cell lines except R9 and E2 (Figure 4.8). The biggest decrease in cell viability with CAiPi was observed in G7, representing 54.8% of control [95% CI: 49.3, 60.1]. However, there was no significant difference between ATRi alone and CAiPi so this could be an ATRi-associated sensitivity. In bulk at 24 hours, only R15 reached statistical significance when comparing CAiPi versus ATRi alone and no significant differences between PARPi and vehicle control were observed.

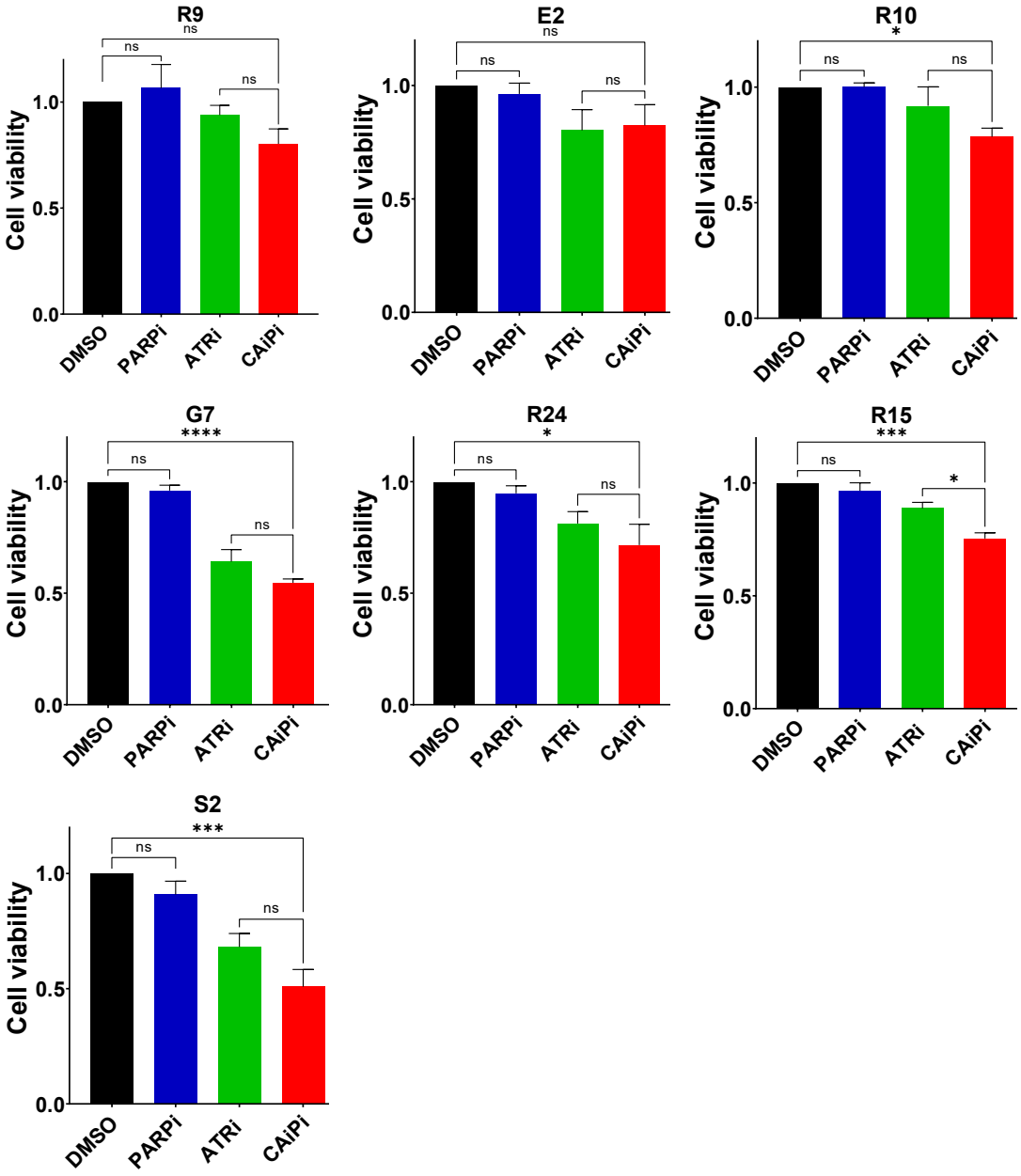

Figure 4.8.GBM bulk cell viability following 24-hour exposure to ATR and PARP inhibition. Average bulk cell viability was analysed using CellTiter-Glo® after 24-hour exposure to olaparib (1μM), VE821 (5μM) and the combination, relative to vehicle control. Cell viability in E2 and R10 was carried out previously by K. Strathdee (Carruthers et al., 2018). Bar charts represent mean and SEM of ≥3 independent experiments, adjusted p-values calculated by one-way ANOVA with post-hoc Sidak test (*p<0.05, **p<0.01, ***p<0.001, ****p<0.0001, ns=not significant).

Greater reductions in cell viability were observed after six-days of CAiPi exposure compared to 24 hours, with all seven bulk cell lines displaying statistically significant reductions compared to vehicle control (Figure 4.9). The greatest reduction in cell viability with CAiPi was still in G7, with a reduction in cell viability to 15.8% [95% CI: 14.5, 17.2] after six-days. However, similarly to 24 hours, no significant difference was observed between ATRi and CAiPi in G7 bulk. Statistically significant differences between ATRi and CAiPi were observed

in R9, R10 and R15. PARP inhibition had limited single agent activity after six-days, with no statistically significant decreases in cell viability observed in comparison to control.

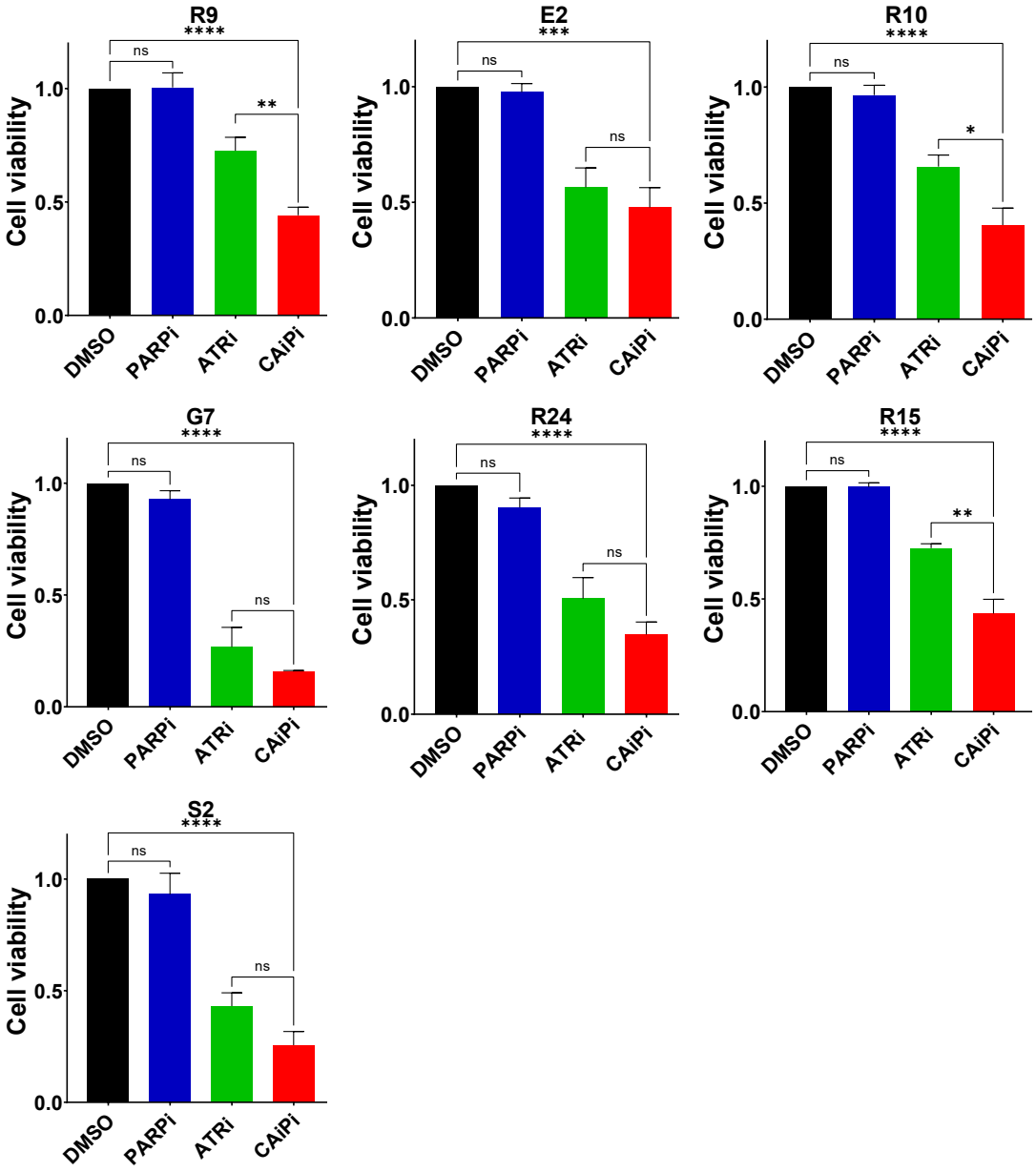

Figure 4.9. GBM bulk cell viability following 6-day exposure to ATR and PARP inhibition. Average bulk cell viability was analysed using CellTiter-Glo® after 6-day exposure to olaparib (1μM), VE821 (5μM) and the combination, relative to vehicle control. Cell viability in E2 and R10 was carried out previously by K. Strathdee. Bar charts represent mean and SEM of ≥3 independent experiments, adjusted p-values calculated by one-way ANOVA with post-hoc Sidak test (*p<0.05, **p<0.01, ***p<0.001, ****p<0.0001, ns=not significant).

4.5 ATRi and PARPi drug interactions

Analysis of cell viability in this chapter has identified varying significance between responses to ATRi alone and CAiPi. Even after six-days of exposure some cell lines did not exhibit any significant differences, especially bulk cells, suggesting that most of the effects observed with CAiPi were associated with sensitivity to ATRi alone in these cells. However, there was also varying effects of PARPi alone, with some cell lines displaying no sensitivity to PARPi and some displaying a statistically significant reduction in cell viability, albeit this reduction was generally minimal. It was therefore challenging to determine ATRi and PARPi drug interactions. To overcome this, CDIs were analysed as described previously in this chapter using six-day cell viability data to investigate evidence of supra-additive effects, and the results are shown in Figure 4.10.

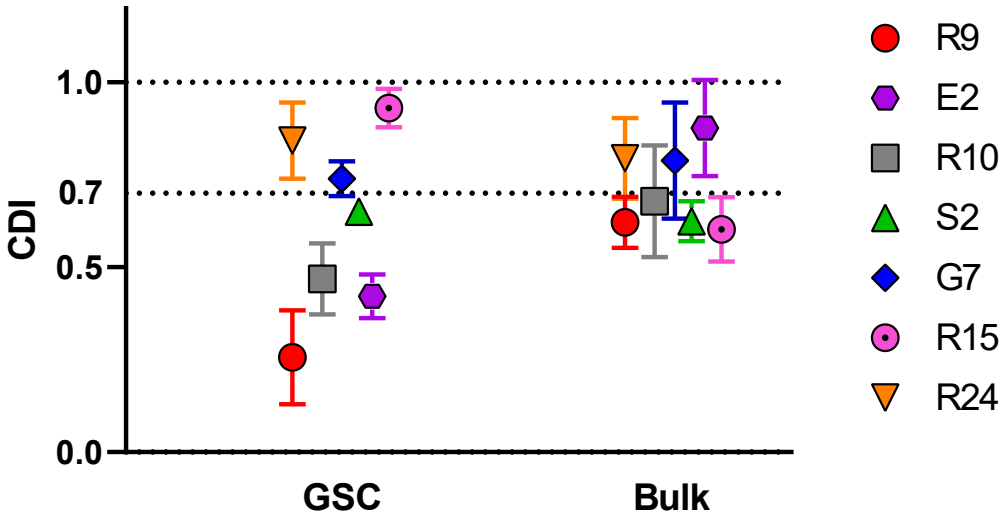

Figure 4.10. CDI values for ATR and PARP interactions in GBM primary cell lines. CDI values were calculated as CAiPi / (ATRi*PARPi) using six-day cell viability data from ≥3 independent experiments. Line at 1.0 is a pre-defined cut off for supra-additive drug interactions, and at 0.7 is indicative of significant supra-additive effects. and plotted as a dot plot and SEM.

All GSC and bulk cell lines had CDIs below 1.0, indicative of combined effects that were greater than just additive. Despite G7 and R24 GSCs having no significant differences between ATRi and CAiPi they both had CDI<1.0, likely due to no effect of PARPi alone. Four GSC lines had a CDI<0.7, indicative of significant supra-additive effects, which were R9, E2, R10 and S2. GSCs had a broad range of CDIs whereas all seven bulk cell lines were largely similar.

4.6 Comparison of paired GSC and bulk sensitivity to CAiPi by cell viability assay

Response to CAiPi was assessed in the panel of seven paired primary GBM cell lines to characterise differential drug responses in GSC and bulk populations. Cell viability was analysed using CellTiter-Glo® after six-day exposure to combined VE821 (5μM) and olaparib (1μM) (Figure 4.11). R9 and E2 had more sensitive GSCs than their differentiated bulk counterparts. R10 also appeared to have more sensitive GSCs but did not reach statistical significance. G7, R24 and R15 GSCs were relatively more resistant to targeting of the RS response than their paired bulk cells, however only G7 reached statistical significance. The S2 cell line showed no difference in response between GSCs and bulk populations.

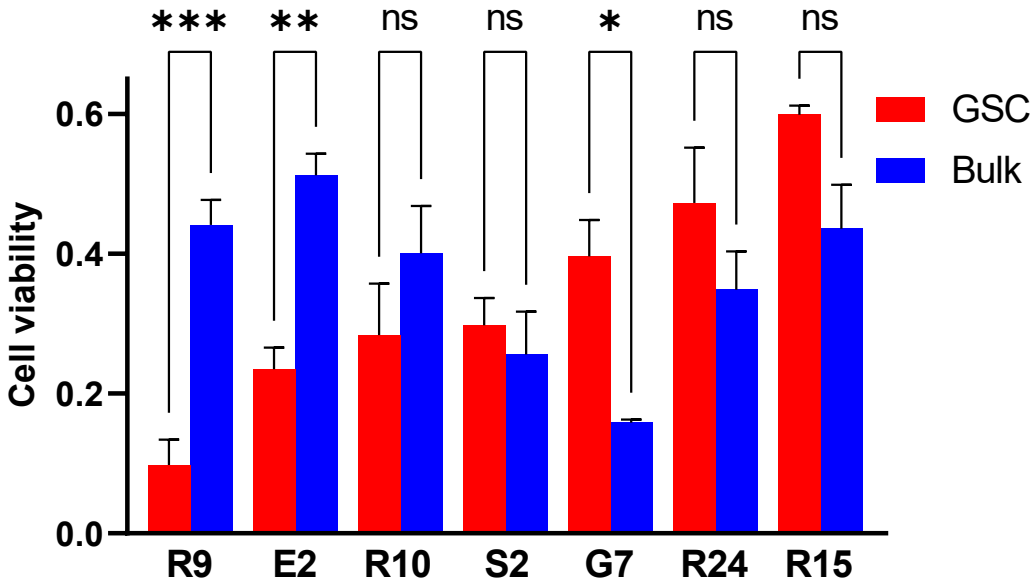

Figure 4.11. Comparison of CAiPi responses in paired GSC and bulk cell lines. Average cell viability in a panel of primary GSC and bulk cell lines was analysed using CellTiter-Glo® after six-day exposure to combined VE821 (5μM) and olaparib (1μM), relative to vehicle control. Cell viability in E2 and R10 was carried out previously by K. Strathdee. Bar charts represent mean and SEM of ≥3 independent experiments, adjusted p-values calculated by one-way ANOVA with post-hoc Sidak test (*p<0.05, **p<0.01, ****p<0.0001, ns=not significant).

4.7 Effects of ATR and PARP inhibition on CD133 sorted cells by neurosphere formation assay

The validity of the clonogenic survival assay and cell viability data was further established by neurosphere formation assay. E2 GSC cultures were sorted using the GSC-marker CD133, producing a population of $CD133^{+}$ cells and a population of $CD133^{-}$ cells which were both maintained in GSC medium. This assay and

utilisation of a different GSC model allowed for the analysis of drug cytotoxicity without any medium-related confounding factors. CD133 sorted cells were plated in 96-well plates at a density of 10 cells per well in media containing vehicle control, VE821 (5μM), olaparib (1μM) and the combination. After one week the drugs were diluted to 50% drug concentration and cells left to form neurospheres for four weeks. Neurospheres were stained with MTT, imaged and manually counted (Figure 4.12).

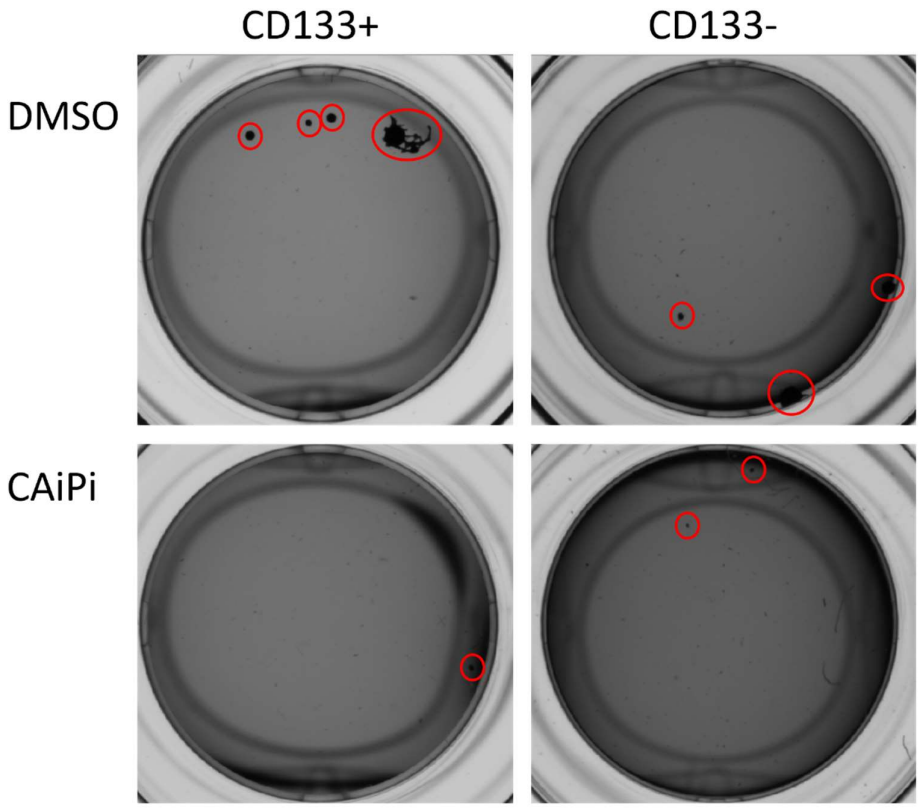

Figure 4.12. CD133 sorted neurospheres after CAiPi treatment. Representative images of neurospheres formed under vehicle control and CAiPi conditions in $CD133^{+}$ and $CD133^{-}$ cell populations.

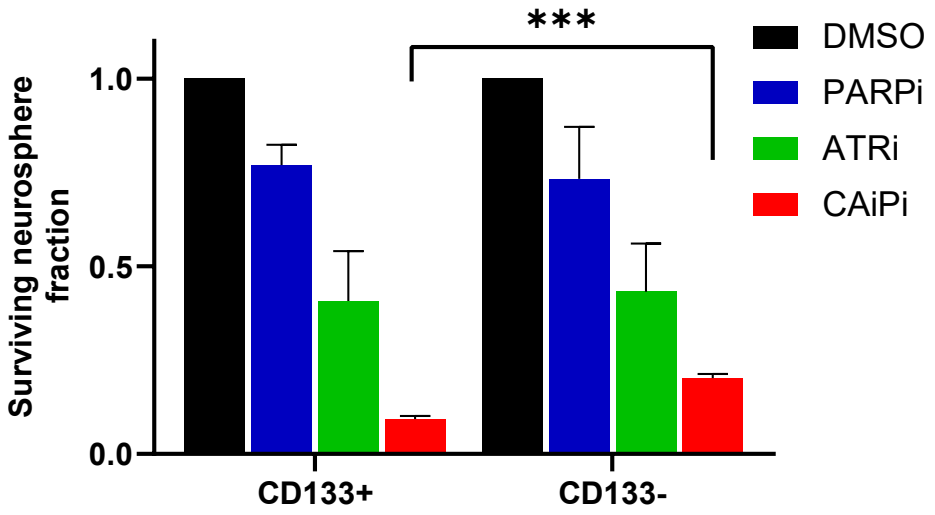

Figure 4.13. E2 CD133 sorted cell survival by neurosphere assay. Cell survival in response to VE821 (5μM), olaparib (1μM) and the combination in E2 CD133 sorted cell populations was analysed by neurosphere formation assay. Bar charts represent mean and SEM of three independent replicates, p-value calculated by unpaired t-test (***p<0.001).

Figure 4.13 shows surviving neurosphere fractions in E2 $CD133^+$ and $CD133^-$ populations relative to vehicle control. $CD133^+$ cells were more sensitive to CAiPi, in keeping with previous cell viability and clonogenic cell survival investigations in E2. The neurosphere assay also identified lower CDI values in $CD133^+$ cells (0.37 [95% CI: -0.11, 0.85]) than in $CD133^-$ cells (0.73 [95% CI: 0.31, 1.15]). These studies confirmed a differential response between E2 GSC and bulk cells using an alternative culture model.

4.8 Analysis of combined ATR and PARP inhibition with AZD6738

AZD6738 is an ATR inhibitor with promising preclinical data indicating anti-tumour activity as a monotherapy and in combination with olaparib and is currently the subject of several early phase clinical trials (Wilson et al., 2022). Therefore, the efficacy of AZD6738 as a monotherapy and combined with olaparib in our GBM paired cell line model was investigated. A relatively sensitive GSC line with an associated low CDI, R9 (Figure 4.14), and a relatively resistant GSC line which exhibited a much higher CDI, R15 (Figure 4.15), based on cell viability data combining VE821 with olaparib (Figure 4.11) were selected. Cells were plated in 96-well plates in media containing AZD6738 (0.5μM and 1μM), olaparib (1μM) and the combinations for six days. Cell viability at the end of the six days was assessed by CellTiter-Glo®.

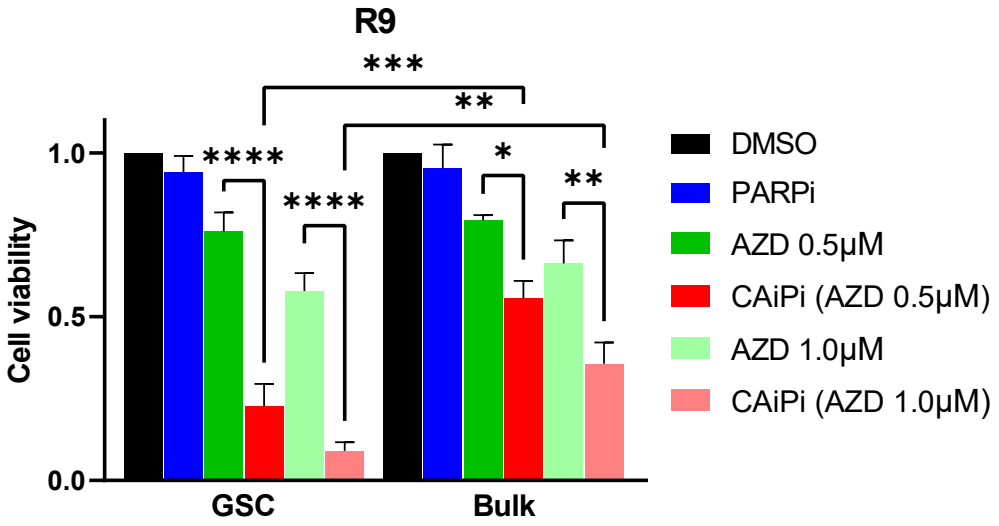

Figure 4.14. R9 GSC and bulk responses to AZD6738 combined with olaparib. Average cell viability was analysed using CellTiter-Glo® after 6-day exposure to olaparib (1μM), AZD6738 (0.5μM and 1μM) and the combination, relative to vehicle control. Bar charts represent mean and SEM of ≥3 independent experiments, adjusted p-values calculated by one-way ANOVA with post-hoc Sidak test (*p<0.05, **p<0.01, ***p<0.001, ****p<0.0001).

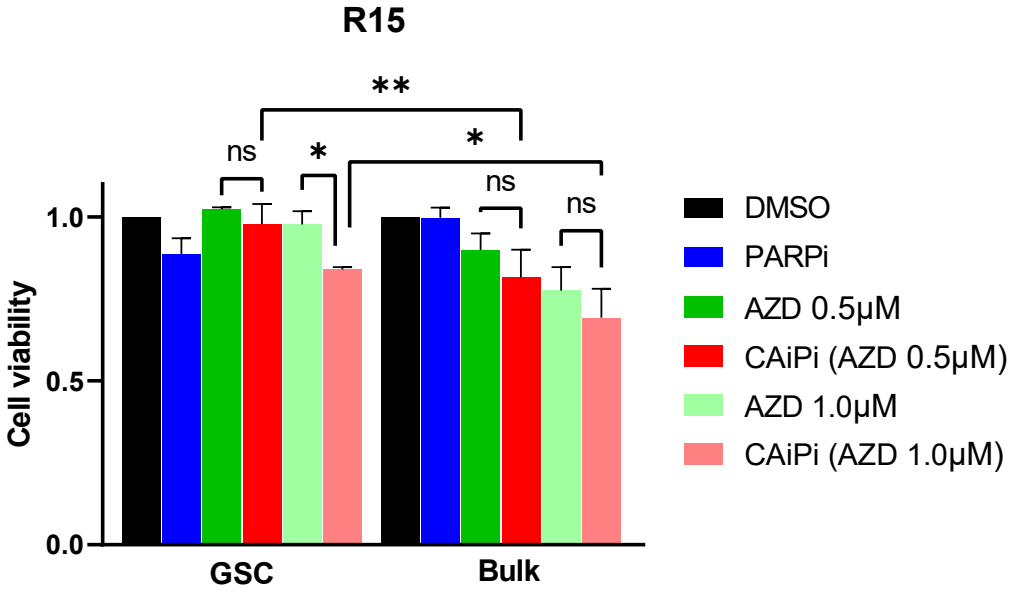

Figure 4.15. R15 GSC and bulk responses to AZD6738 combined with olaparib. Average cell viability was analysed using CellTiter-Glo® after 6-day exposure to olaparib (1μM), AZD6738 (0.5μM and 1μM) and the combination, relative to vehicle control. Bar charts represent mean and SEM of ≥3 independent experiments, adjusted p-values calculated by one-way ANOVA with post-hoc Sidak test (*p<0.05, **p<0.01, ns=not significant).

R9 GSCs were significantly more sensitive to combined AZD6738 (0.5μM and 1μM) and olaparib than their paired bulk counterparts. R9 displayed potent CAiPi-sensitivity at both concentrations of AZD6738 in GSC and bulk lines. There was a significant decrease in cell viability when olaparib was added to AZD6738

compared to AZD6738 alone. This was in keeping with potent cytotoxicity and low CDI observed in R9 with VE821. R15 was much more resistant to CAiPi with AZD6738. R15 bulk were more sensitive than their paired GSC counterparts, however there was no significant decrease in cell viability observed when olaparib was added to AZD6738 apart from R15 GSC at 1μM, suggesting that the combination is not particularly potent. This was also similar to VE821 cell viability data for R15.

4.9 Summary of genomic and transcriptomic GBM markers, biomarkers and CAiPi sensitivity

Response to ATRi, PARPi and CAiPi has now been well characterised in the panel of seven primary paired GSC and bulk cell lines. Increased RS did not appear to solely predict response to CAiPi, as some paired, comparatively low RS bulk cells displayed relatively more sensitivity to targeting the RS response than their GSC counterparts. Therefore, commonly mutated genes in GBM and previously described biomarkers of response to ATRi and PARPi identified in Chapter 3 were investigated for their ability to predict sensitivity to targeting the RS response (Table 4.1). Analysis of patterns of mutations, subtypes and expression data found no obvious correlations between these markers and sensitivity to targeting the RS response in GSCs, as relative GSC sensitivity increased to the left of Table 4.1 indicated by the arrow. Common GBM mutations or characteristics, including MGMT methylation, EGFR SNPs, PTEN mutations, TERT promoter SNPs and CDKN2A homozygous deletions were found throughout the panel, in both GSC- and bulk-sensitive cell lines. MYCN amplification was only found in a relatively CAiPi-resistant cell line. The relatively sensitive E2 and R10 GSCs were ATM-proficient, with no identified ATM SNPs and comparatively high expression of ATM. Expression of SLFN11 did not predict CAiPi-sensitivity, as the most CAiPi-sensitive cell line, R9, did not express SLFN11. Lastly, CCNE1 expression did not robustly predict CAiPi-sensitivity as it was variable across the panel. Overall, no previously described biomarker for CAiPi or GBM mutations reliably predicted GSC sensitivity to targeting the RS response.

Table 4.1. Summary of CAiPi sensitivity, GBM mutations and previously described biomarkers in a panel of seven primary paired GBM cell lines.

	R9	E2	R10	S2	G7	R24	R15
	←						→
GSC vs. bulk	GSC	GSC	GSC*	=	Bulk	Bulk*	Bulk*
MGMT	uMGMT	mMGMT	mMGMT	uMGMT	mMGMT	uMGMT	mMGMT
IDH	WT	WT	WT	WT	WT	WT	WT
GSC/bulk subtypes	Pro/Pro	Pro/Cla	Pro/Mes	Cla/Mes	Cla/Mes	Pro/Mes	Cla/Mes
TP53	R273H	R273H	R248W	R273H	R282W R248Q	C277F	DEL
EGFR	R521K	A289V		R521K		R521K	R521K
PTEN	INS			INS		C105Y	P95L
TERT	C228T	C250T	C250T	C228T	C250T	C250T	C228T
CDKN2A		HomDel	HomDel			HomDel	HomDel
MYC/ MYCN						MYCN amp.	
ATM	F858L R227C P1054R			F858L R227C P1054R	K1454N D1853N	D1853N	D1853N
BRCA1/2, PALB2	WT	WT	WT	WT	WT	WT	WT
SLFN11 expression	0	++	+++	0	+++	+	+
ATM expression	++	+++	++	+	+++	+	+++
CCNE1 expression	+++	++	++	+++	++	++	+

Summary of findings from Chapter 3 and Chapter 4. Arrow indicates increasing GSC sensitivity to targeting the RS response by CellTiter-Glo®. Differential GSC and bulk sensitivity indicated for each pair, asterisk indicates a non-statistically significant relationship. Expression data from Figure 3.7 summarised by relative increases in expression within the seven cell lines, with 0 indicating no expression. uMGMT = unmethylated MGMT promoter, mMGMT = methylated MGMT promoter, Pro = proneural, Mes = mesenchymal, Cla = classical, DEL/INS = InDels, HomDel = homozygous deletions.

4.10 Conclusions

A detailed comparison of responses to targeting the RS response in GBM primary paired GSC and bulk cells has been documented. The response to CAiPi was first assessed in a clonogenic survival assay in two cell lines known to form colonies. E2 was identified as having sensitive GSCs in comparison to paired bulk cells, but G7 had comparatively more sensitive bulk cells than GSCs. A cell viability screen of seven primary GBM cell lines identified heterogenous responses to CAiPi. This screen identified three cell lines, R9, E2 and R10, that had sensitive GSCs relative to their bulk counterparts. Whereas G7, R24 and R15 bulk cells were more sensitive to targeting the RS response in comparison to GSCs. S2 displayed similar sensitivities in GSC and bulk cells.

Previous studies have found synergistic interactions between ATR and PARP inhibitors. Analyses of drug interactions in this thesis were limited as synergistic relationships were not assessed, however CDI was used as an indicator of supra-additive relationships. Supra-additive relationships between ATR and PARP inhibitors were observed in all GSCs, highlighting the clinical potential of these therapies. However, there appeared to be a subset of GSCs, namely R9, E2 and R10, that displayed both potent CAiPi cytotoxicity and greater supra-additive effects from combining an ATR inhibitor with a PARP inhibitor. These cell lines were also more sensitive to targeting the RS response than their paired bulk counterparts. In depth quantitative analysis of drug synergy would be beneficial to fully characterise drug responses. Several cell lines, especially bulk cell lines, appeared to exhibit primarily ATRi sensitivity after the addition of a PARPi showed insignificant additional benefit.

A neurosphere assay using a cell sorted population model also confirmed E2 GSC as a potently CAiPi-sensitive cell line, utilising CD133 as a GSC marker. Despite controversies surrounding the validity of certain GSC markers which was detailed in Chapter 1, CD133 is still the most utilised GSC marker. Ahmed et al previously showed that E2 GSCs have higher CD133 expression by Western blot (Ahmed et al., 2015), which was corroborated by RNAseq analysis in Chapter 3. It is of note that $CD133^-$ cells still formed neurospheres, which is indicative of GSC proliferative capacities. However, previous analyses have shown $CD133^-$ cells have a reduced capacity to form neurospheres and the neurospheres that do form are smaller and abortive (Carruthers, 2015), so overall lack the proliferative capacities of $CD133^+$ GSCs.

Analysis of AZD6738 as an alternative ATRi exhibited promising *in vitro* responses as a monotherapy and when combined with olaparib in selected cell lines, similarly to ATR inhibition with VE821. Work by Wilson et al identified highly heterogenous AZD6738 single agent activities in 276 cancer cell lines, however their analysis did not include any glioma malignancies (Wilson et al., 2022). Our analyses of GBM primary cells support their hypothesis that not all cells are ATRi sensitive. Analysis of AZD6738 as a useful ATRi for brain tumours found it was not BBB penetrant and was not retained for a useful duration of time (data not published). Despite ongoing developments of AZD6738 as a successful

monotherapy and in combination with olaparib, primarily in breast and ovarian cancer (Wilson et al., 2022, Kim et al., 2017), this ATRi was not investigated further in this thesis due to the limited *in vivo* potential.

Since ATR and PARP are active in the RS response and GSCs have increased RS, it was our hypothesis that the most indicative biomarker of response to CAiPi would be high levels of RS and therefore that targeting the RS response would be potently cytotoxic to GSCs. Previous studies by Carruthers et al supported this hypothesis, as they observed greater GSC-specific CAiPi-sensitivity in two GBM cell lines (Carruthers et al., 2018). However, we observed highly heterogenous sensitivity profiles in a larger panel of GBM paired cell lines, so a predictor of CAiPi-sensitivity remained unclear. Investigations of previously described biomarkers and common GBM mutations found that none robustly predicted CAiPi-sensitivity in this panel of GSCs. A mutational signature of sensitivity is unlikely to explain differing GSC and bulk response to targeting the RS response since they arise from the same tumour and represent an isogenic model. A transcriptomic signature or differing mechanistic vulnerabilities will more likely explain differing sensitivities between GSC and bulk pairs.

Investigations are required to elucidate the mechanism of sensitivity to targeting the RS response in this GBM cell line panel. The differences in relative sensitivities between GSCs and bulk cells can be exploited in mechanistic studies to identify underlying differences between these populations that could direct the future search for biomarkers of response. Throughout this thesis to investigate GSC-specific cytotoxicity, E2 and G7 are frequently used to compare differential responses to targeting the RS response. Using different assays and timepoints, E2 GSCs were consistently more sensitive to treatment with CAiPi than their bulk counterparts, but in G7 there was generally no evidence of increased GSC sensitivity versus bulk. Additionally, analysis of drug interactions suggested that there was a greater benefit of combining an ATR and a PARP inhibitor in E2 GSCs versus G7 GSCs. The rest of this thesis will investigate drug mechanisms and transcriptional changes which will allow for further understanding of the drug sensitivity phenotype in GSC and bulk populations.

Chapter 5 Investigations of CAiPi-induced transcriptional changes

5.1 Introduction

Responses to CAiPi were highly heterogenous. The hypothesis that increased RS would predict CAiPi-sensitivity was disproved, since several bulk cell lines displayed increased sensitivity to targeting the RS response compared to their paired GSCs. Therefore, mechanistic investigations were required to elucidate differential responses. To inform mechanistic *in vitro* investigations, analysis of transcriptomic alterations in response to CAiPi were carried out in two cell lines with differing GSC sensitivity profiles. Differential RNA expression was analysed, and functional analysis of dysregulated transcriptomes assessed by Gene Ontology (GO) and Kyoto Encyclopedia of Genes and Genomes (KEGG) analysis. This chapter aimed to characterise transcriptional responses to CAiPi, to aid identification of culprit mechanisms.

5.2 Differential RNA expression after RS-targeting therapies

To characterise differential CAiPi-induced transcriptomes, RNA sequencing data was analysed in two paired GBM cell lines, E2 and G7, after exposure to RS-targeting therapies. E2 GSCs were more sensitive than E2 bulk, whereas in contrast G7 GSCs were more resistant to targeting of the RS response than its paired bulk counterpart, as discussed in Chapter 4 and summarised in Figure 5.1. Cells were incubated with VE821 (5μM), olaparib (1μM), the combination or vehicle control for 72 hours, in triplicate. RNA was then extracted and sequenced before RNAseq processing and analysis by Galaxy and R packages.

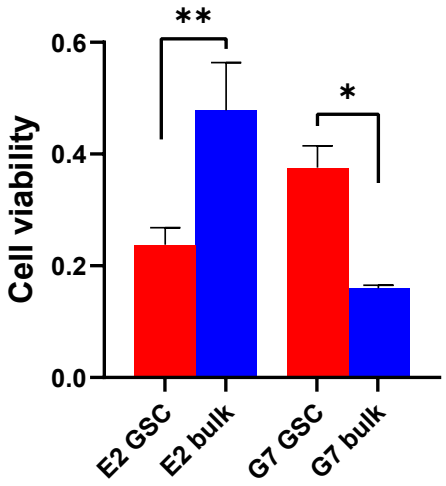

Figure 5.1. Response to CAiPi in E2 and G7 cell line pairs. Summary of cell viability results from Chapter 4. Average cell viability in E2 and G7 GSC and bulk cell lines was analysed using CellTiter-Glo® after six-day exposure to combined VE821 (5μM) and olaparib (1μM), relative to vehicle control. Cell viability in E2 was carried out previously by K. Strathdee. Bar charts represent mean and SEM of ≥3 independent experiments, adjusted p-values calculated by one-way ANOVA with post-hoc Sidak test, as in Chapter 4 (*p<0.05, **p<0.01)

Clustering of samples and replicates was analysed by PCA (Figure 5.2). PCA assesses inter- and intragroup variability and visualises how different conditions cluster. There appeared to be more intra-condition variability in the GSC samples for both E2 and G7 as the samples tended to spread out. Generally, DMSO and PARPi samples clustered together, and ATRi and CAiPi together, especially in the bulk cell lines. In both G7 cell lines, Principal Component 1 (PC1) separated DMSO/PARPi and ATRi/CAiPi suggesting that the differences between these groups explain most of the variability within the samples. Whereas these groupings in E2 appear to be explained by PC2, suggesting that another factor is explaining most of the variation in these cell lines.

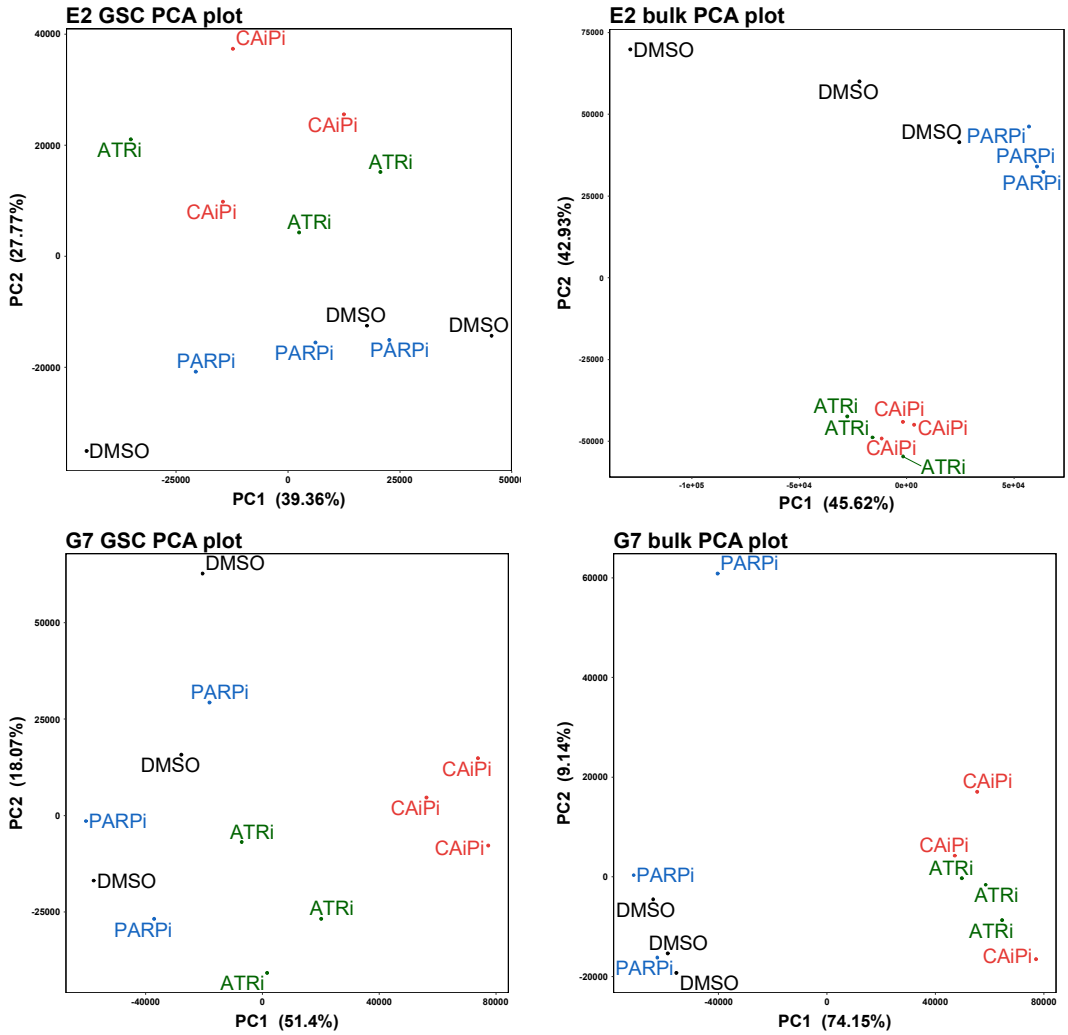

Figure 5.2. PCA analysis of ATRi, PARPi and CAiPi in E2 and G7 GSCs and bulk cells. Plot of principal component analysis of triplicate RNAseq data after 72-hour exposure to olaparib (1μM), VE821 (5μM), the combination and DMSO control in E2 and G7 paired GSC and bulk cell lines. PCA analysis was carried out using the 'prcomp' function in R, and principal components one and two were plotted and variance calculated.

Analysis of differentially expressed genes (DEGs) was carried out using the 'DeSeq2' package in R. The number of DEGs, with an adjusted p-value cut off 0.05, was assessed after PARPi, ATRi and CAiPi exposure, versus DMSO control (Figure 5.3). In both E2 and G7 bulk cell lines CAiPi induced more DEGs than their paired GSC lines. Interestingly, E2 GSC which exhibited potent CAiPi-sensitivity, had the least number of DEGs after CAiPi, with only 1086 genes differentially expressed. Both bulk cell lines had relatively similar numbers of DEGs after ATRi and CAiPi, whereas the two GSC lines had a large increase of DEGs after CAiPi exposure over ATRi alone. Lastly, PARPi induced little to no transcriptional changes in all cell lines except E2 bulk, where it appeared to result in a relatively large amount of dysregulation.

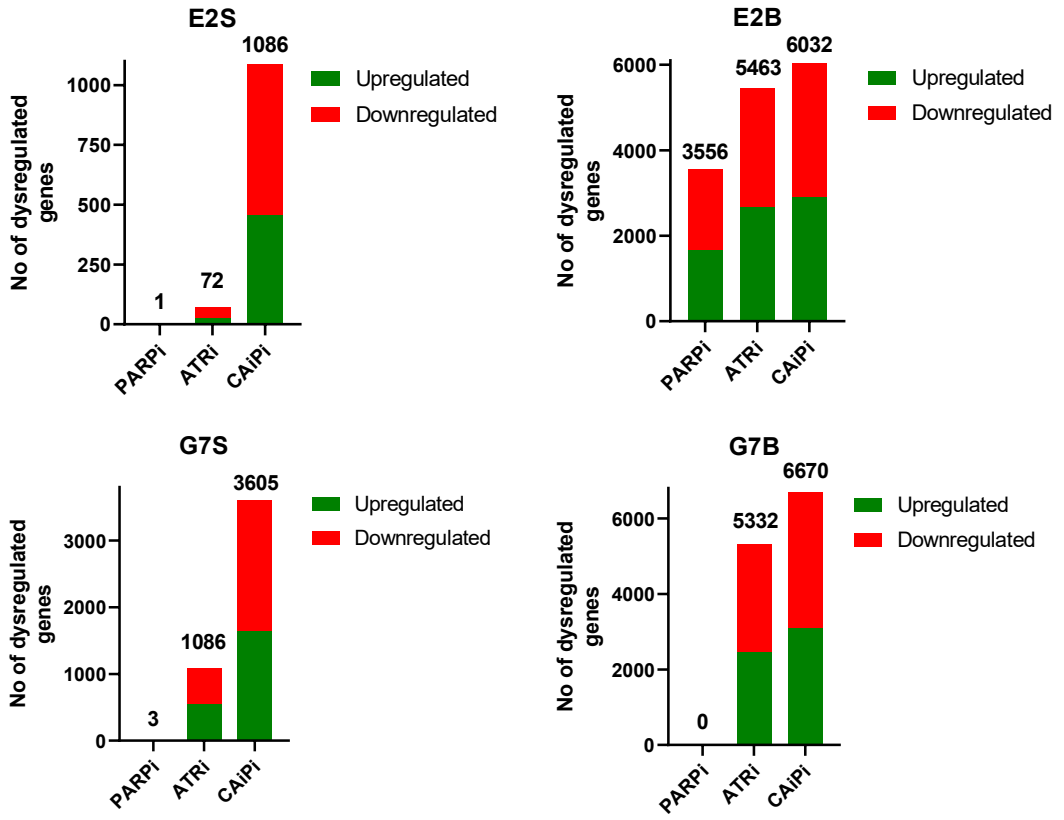

Figure 5.3. Dysregulated genes in E2 and G7 GSC and bulk cells after ATR, PARP and combined inhibition. Dysregulated genes (adjusted p-value<0.05) were analysed by 'DeSeq2' in both E2 and G7 GSC (S) and bulk (B) pairs, after 72-hour exposure to olaparib (1μM), VE821 (5μM) and the combination versus DMSO control. Bar charts are split by number of upregulated and downregulated genes and total number of dysregulated genes is highlighted above each bar.

Further analysis of CAiPi-induced gene dysregulation was carried out by clustering analysis via a heatmap. DEGs (adjusted p-value<0.05) between DMSO vehicle control and CAiPi were identified, and clustering of all conditions based on these DEGs plotted. Figure 5.4 shows the clustering for E2 GSC and bulk cell lines and Figure 5.5 the clustering for G7 GSC and bulk cell lines. In both GSC lines, there was a distinct CAiPi-specific set of DEGs that clearly clustered together. In the two bulk cell lines, the CAiPi samples clustered separately from DMSO and PARPi samples but clustered with ATRi. This is in keeping with the pattern of DEGs identified in Figure 5.3, suggesting similar patterns of DEGs by ATRi and CAiPi in bulk cell lines. DMSO and PARPi samples clustered interchangeably in E2 GSC and G7 GSC and bulk cell lines, not unexpectedly since they clustered together in PCA analysis and there was ≤3 DEGs identified between these conditions.

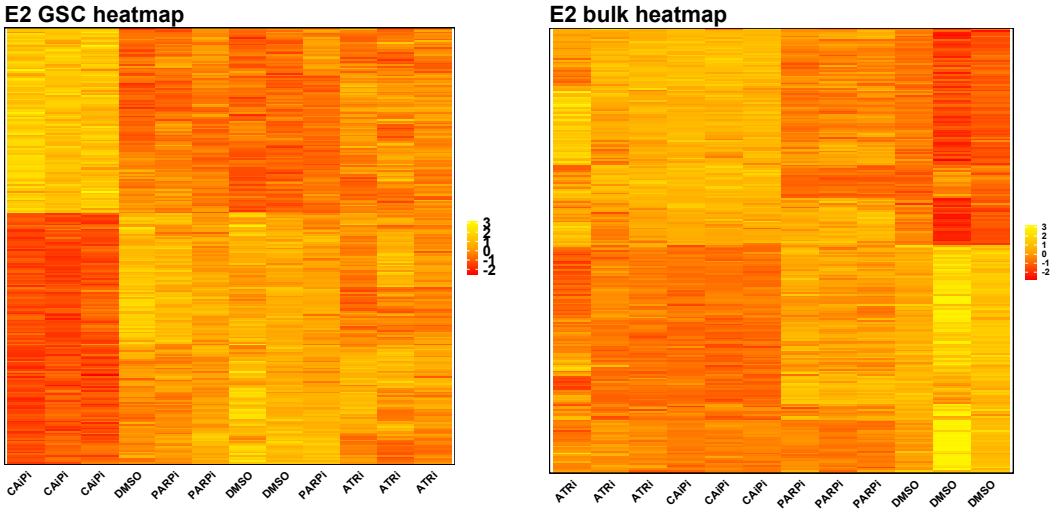

Figure 5.4. Heatmap of CAiPi-differentially expressed genes in E2 GSCs and bulk cells. Differentially expressed genes (adjusted p-value<0.05) between DMSO control and CAiPi in E2 GSC and bulk cells were identified by 'DeSeq2' analysis in R. Cells were exposed to DMSO control, olaparib (1μM), VE821 (5μM) and the combination for 72 hours before RNA extraction, sequencing and analysis. All samples were clustered on the differentially expressed genes and scaled expression values plotted in a heatmap. Z-score scale is shown in the legend.

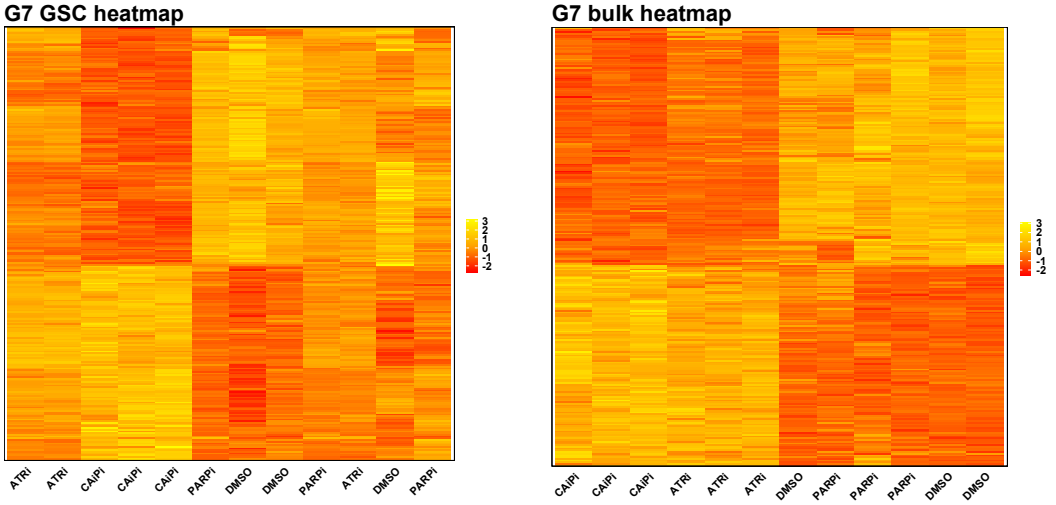

Figure 5.5. Heatmap of CAiPi-differentially expressed genes in G7 GSCs and bulk cells. Differentially expressed genes (adjusted p-value<0.05) between DMSO control and CAiPi in G7 GSC and bulk cells were identified by 'DeSeq2' analysis in R. Cells were exposed to DMSO control, olaparib (1μM), VE821 (5μM) and the combination for 72 hours before RNA extraction, sequencing and analysis. All samples were clustered on the differentially expressed genes and scaled expression values plotted in a heatmap. Z-score scale is shown in the legend.

Volcano plots were used to visualise all genes, plotting significance versus log fold change (LFC), and significantly upregulated and downregulated genes in CAiPi versus control were highlighted in E2 and G7 GSC and bulk pairs (Figure 5.6). Both bulk cell lines had DEGs with a greater fold change than their paired GSCs and more genes with a greater statistical significance, likely related to increased total number of DEGs in bulk cells. The volcano plots also highlighted

the top five statistically significant upregulated and downregulated genes in each sample. Analysis of these genes found a large array of different cellular processes. Of interest, two of the top five upregulated genes in E2 GSC in response to CAiPi were histones potentially suggestive of chromatin remodelling and at least one of the top upregulated genes in each cell line was associated with apoptosis or stress response, namely TRIB3, PRUNE2, GDF15 and PPP1R15A. This warranted further analysis of the functional implications of this dysregulation.

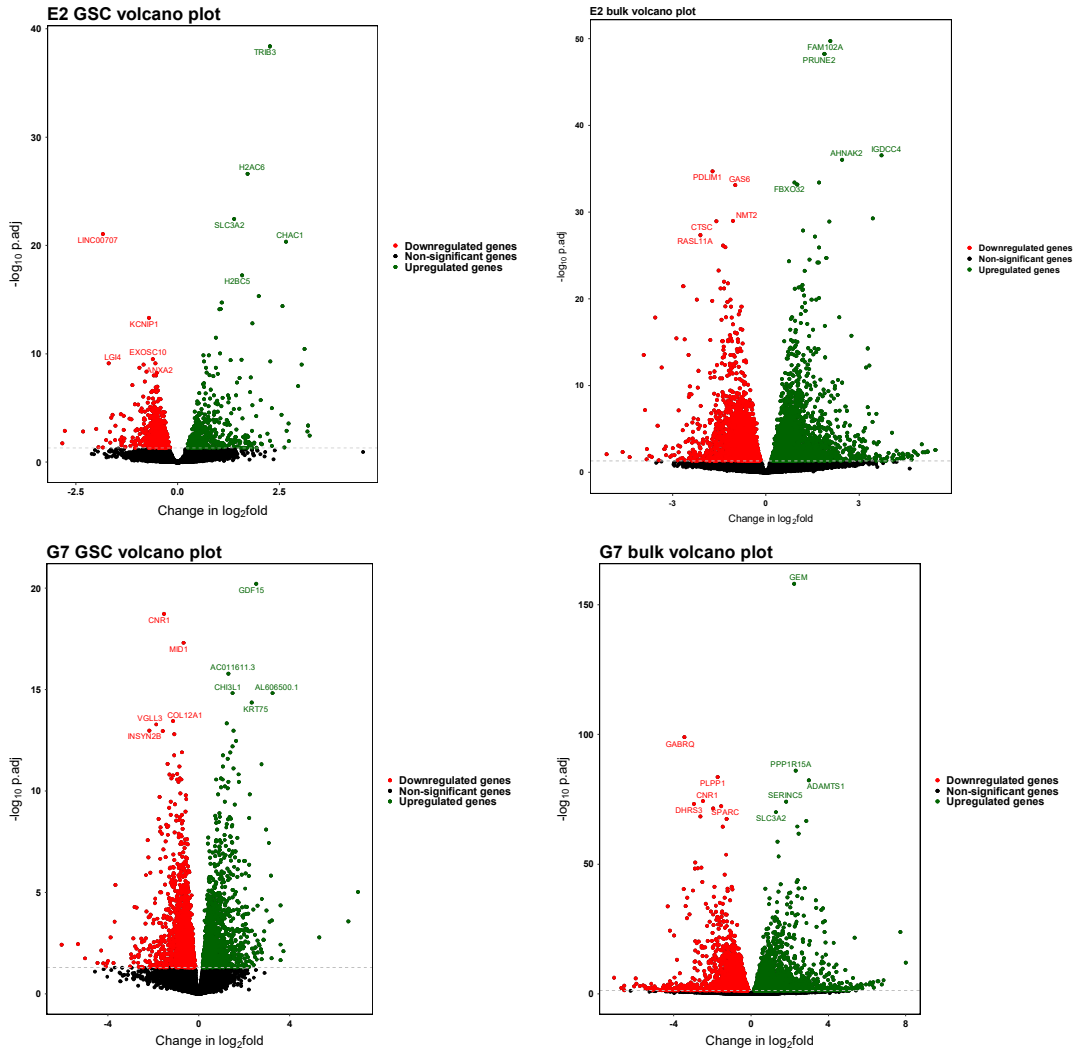

Figure 5.6. Volcano plots of CAiPi-induced dysregulated genes. Scatter plots of -$\log_{10}$ of adjusted p-values versus LFC show differential gene expression between DMSO and CAiPi samples in E2 and G7 GSC and bulk cells. Cells were exposed to DMSO control and combined VE821 (5μM) and olaparib (1μM) for 72 hours, before RNA extraction, sequencing and 'DeSeq2' analysis. Significantly dysregulated genes with an adjusted p-value <0.05 are highlighted in green if LFC>0 and red if LFC<0, non-significant genes with an adjusted p-value >0.05 are in black. The top five statistically significant up- and down- regulated genes are highlighted on each plot next to their corresponding data point.

An MA plot was created for E2 and G7 GSC and bulk cells (Figure 5.7). An MA plot visualises gene expression changes, plotting LFC between two conditions against mean normalised expression across all conditions. Differential gene expression was plotted for CAiPi versus DMSO control, after 72-hour exposure and significantly upregulated and downregulated genes were identified by an adjusted p-value cut off 0.05. The MA plot visualised the reduction in statistically significant dysregulated genes in GSCs versus bulk lines, especially for E2. Across all cell lines but especially in bulk cells, lower mean expression was associated with a highly variable LFC, as expected. Genes with a lower mean expression are also less likely to have statistically significant LFC, indicated by an increase in non-significant genes as mean expression trends towards zero.

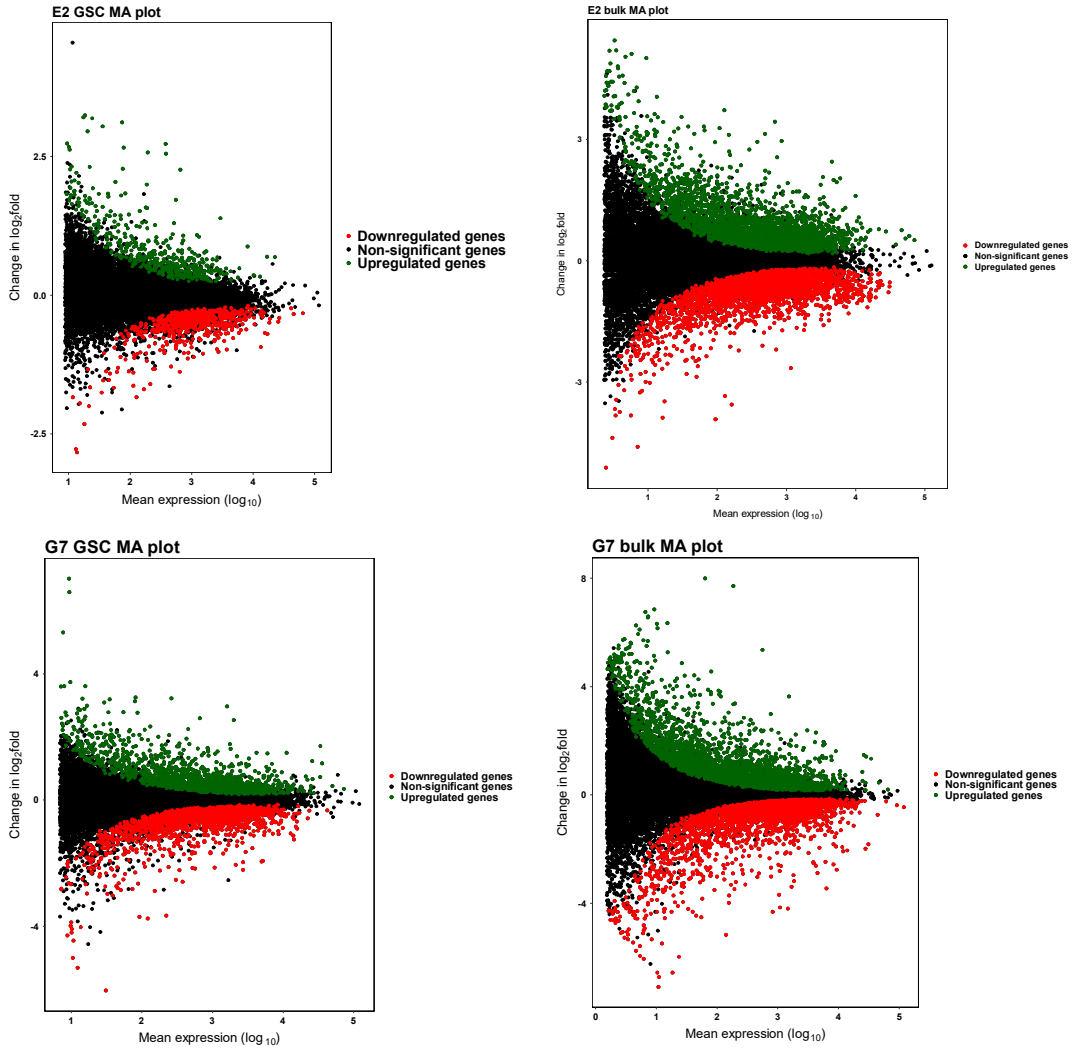

Figure 5.7. MA plot of CAiPi-induced dysregulated genes. Scatter plots of LFC versus mean expression (log_{10}) across all samples show differential gene expression between DMSO and CAiPi samples in E2 and G7 GSC and bulk cells. Cells were exposed to DMSO control and combined VE821 (5μM) and olaparib (1μM) for 72 hours, before RNA extraction, sequencing and 'DeSeq2' analysis. Significantly dysregulated genes with an adjusted p-value <0.05 are highlighted in green if LFC>0 and red if LFC<0, non-significant genes with an adjusted p-value >0.05 are in black.

5.3 Gene set enrichment analysis of CAiPi-induced gene dysregulation

Differential transcriptomic alterations induced by CAiPi treatment have now been well characterised, however the functional significance of these changes remains unclear. Therefore, GSEA was carried out, using 'gseGO', for E2 (Figure 5.8) and G7 (Figure 5.9) paired cell lines. This analysis identified the top upregulated (activated) and downregulated (suppressed) GO terms, based on the LFC between DMSO control and CAiPi of all genes.

Only E2 GSCs exhibited GO terms that were significantly activated or suppressed. E2 GSC GSEA showed that gene sets related to replication, chromosome segregation and mitosis were all suppressed, and several top activated GO terms related to chromatin organisation, such as ‘nucleosome’ and ‘DNA packaging complex’. Although not significant, both E2 bulk and G7 GSCs neared statistical significance for GSEA ($p=0.08$ and $p=0.07$ respectively). Downregulated GO terms for E2 bulk largely related to ribosomes and several upregulated GO terms covered axon and neuron development. No apparent similarities between the downregulated GO terms in G7 GSC were observed whilst upregulated GO terms in G7 GSCs were enriched for terms associated with chromatin organisation and nucleosome, similarly to E2 GSC. No GO terms neared significance for G7 bulk ($p=0.27$).

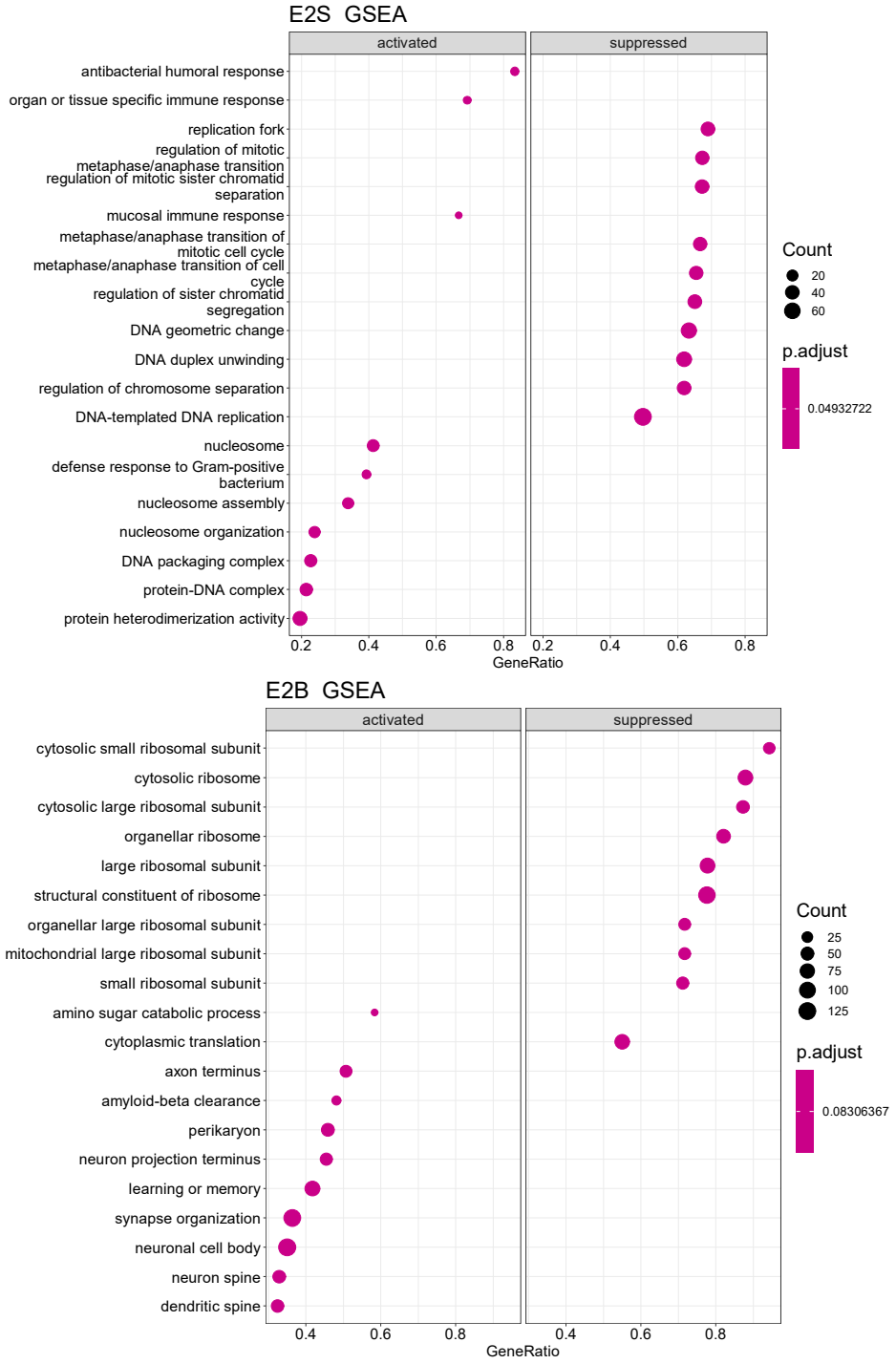

Figure 5.8. E2 GSEA of CAiPi-dysregulated genes. E2 GSC (S) and bulk (B) cells were exposed to DMSO control and combined VE821 (5μM) and olaparib (1μM) for 72 hours before RNA extraction and sequencing. Gene expression LFC between the two conditions was quantified by 'DeSeq2' analysis, and corresponding upregulated (activated) and downregulated (suppressed) GO terms were assessed by 'gseGO'. Plots show the top 10 GO terms for each category, with associated gene count, adjusted p-value and ratio of genes dysregulated: total genes in GO term.

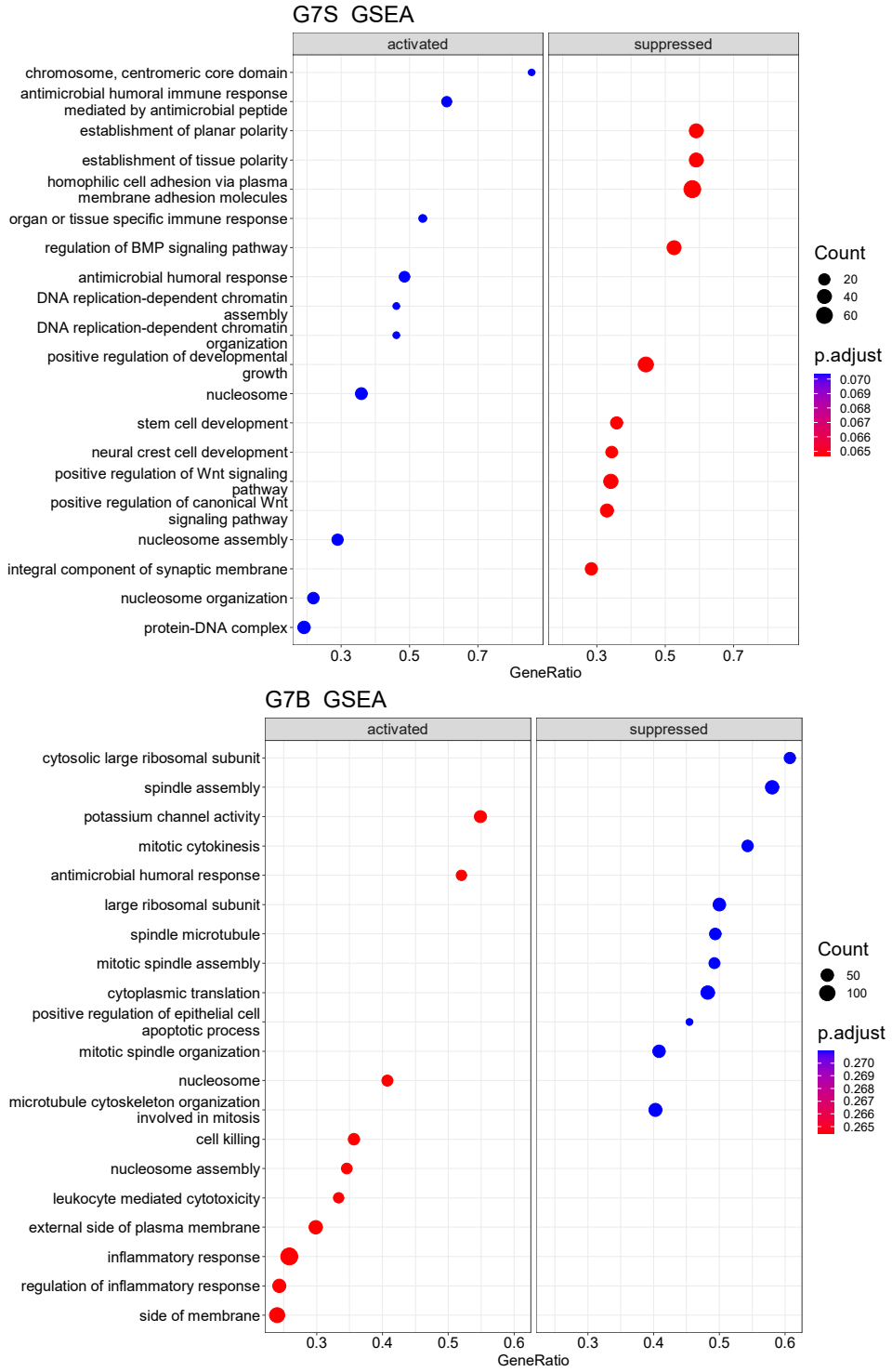

Figure 5.9. G7 GSEA of CAiPi-dysregulated genes. G7 GSC (S) and bulk (B) cells were exposed to DMSO control and combined VE821 (5μM) and olaparib (1μM) for 72 hours before RNA extraction and sequencing. Gene expression LFC between the two conditions was quantified by 'DeSeq2' analysis, and corresponding upregulated (activated) and downregulated (suppressed) GO terms were assessed by 'gseGO'. Plots show the top 10 GO terms for each category, with associated gene count, adjusted p-value and ratio of genes dysregulated: total genes in GO term.

Since E2 GSCs appeared to have enriched GO terms with similar functions, an enrichment map plot (emapplot) was utilised to visualise E2 GSC gene sets as a

network with mutually overlapping gene sets clustering together (Figure 5.10). Visualisation of the top 20 overlapping dysregulated GO terms by GSEA identified four functional gene set modules in E2 GSC. The largest module related to mitosis and chromosomal segregation, followed by a DNA replication module, a nucleosome module and a module containing only the DNA secondary structure binding module. Additionally, a cnetplot (category network plot) visualised the links between mutually dysregulated genes and gene sets (Figure 5.11). The cnetplot visualised the gene interconnections between the top five dysregulated GO terms in E2 GSC, after CAiPi exposure. Regulation of mitotic sister chromatid separation and regulation of sister chromatid segregation had almost identical gene sets, and both had four genes linking them with DNA-templated DNA replication. In turn, DNA-templated DNA replication had mutually dysregulated genes with DNA geometric change, while the nucleosome GO term stood alone.

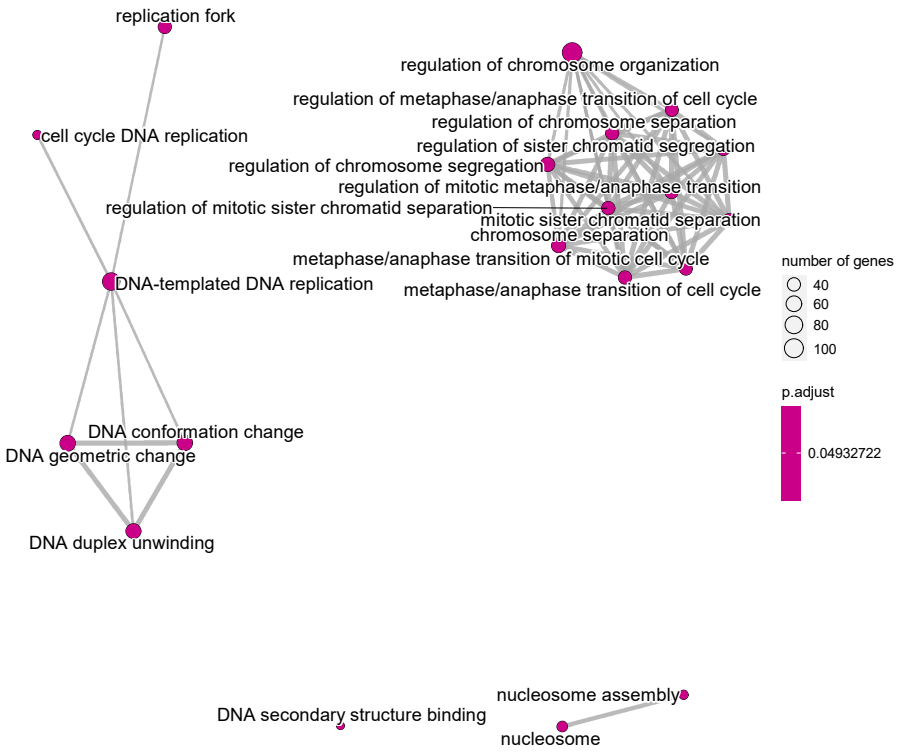

Figure 5.10. Emapplot of top 20 CAiPi dysregulated GO terms in E2 GSCs. E2 GSCs were exposed to DMSO control and combined VE821 (5μM) and olaparib (1μM) for 72 hours before RNA extraction and sequencing. Gene expression LFC between the two conditions was quantified by 'DeSeq2' analysis, and corresponding dysregulated GO terms were assessed by 'gseGO'. Gene set similarity was assessed by the 'pairwise_termsim' function in R. Plots show enrichment map for the top 20 GO terms, lines indicate a similarity between GO terms that meet a threshold of 0.2 (scale of 0-1). Line thickness and length indicates extent of similarity, circle size displays associated gene number dysregulated within each GO term and colour indicates adjusted p-value.

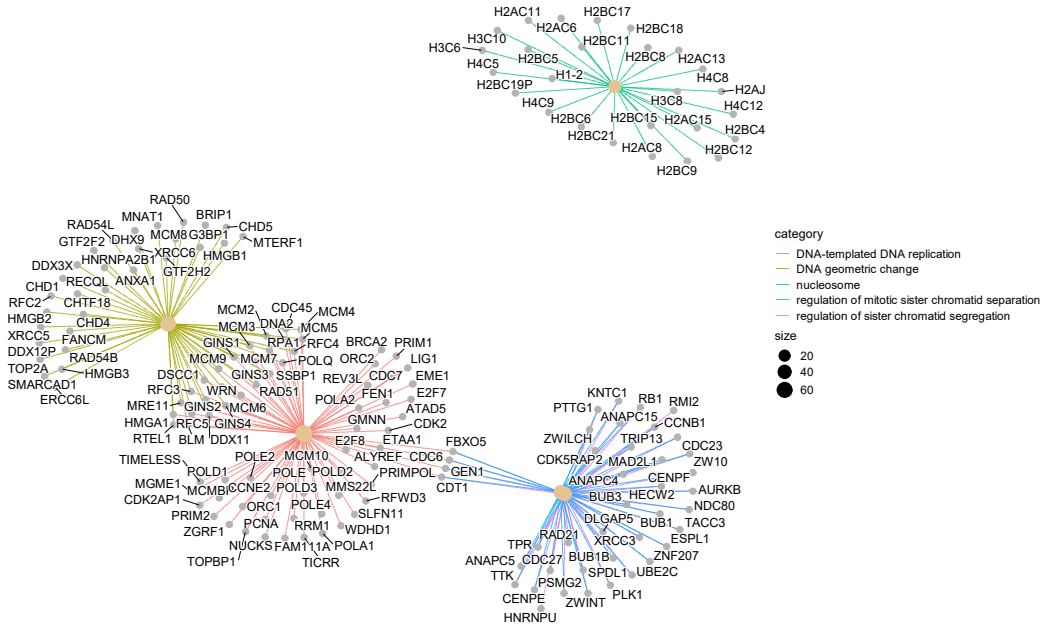

Figure 5.11. Cnetplot of top 5 CAiPi dysregulated GO terms and associated genes in E2 GSCs. E2 GSCs were exposed to DMSO control and combined VE821 (5μM) and olaparib (1μM) for 72 hours before RNA extraction and sequencing. Gene expression LFC between the two conditions was quantified by 'DeSeq2' analysis to identify corresponding dysregulated GO terms by 'gseGO'. Plots show category network for the top 5 GO terms, with any gene links between enriched GO terms highlighted. Line colour highlights each GO term, and circle size indicates the number of genes dysregulated within a gene set.

Analysis of CAiPi-dysregulated GO term interconnections by GSEA in G7 GSC was also carried out. While E2 GSCs had only four functional modules, an emapplot of G7 GSC GO terms identified twelve distinct modules (Figure 5.12). Lastly, a cnetplot in G7 GSC identified mutually dysregulated genes between the top five GO terms (Figure 5.13).

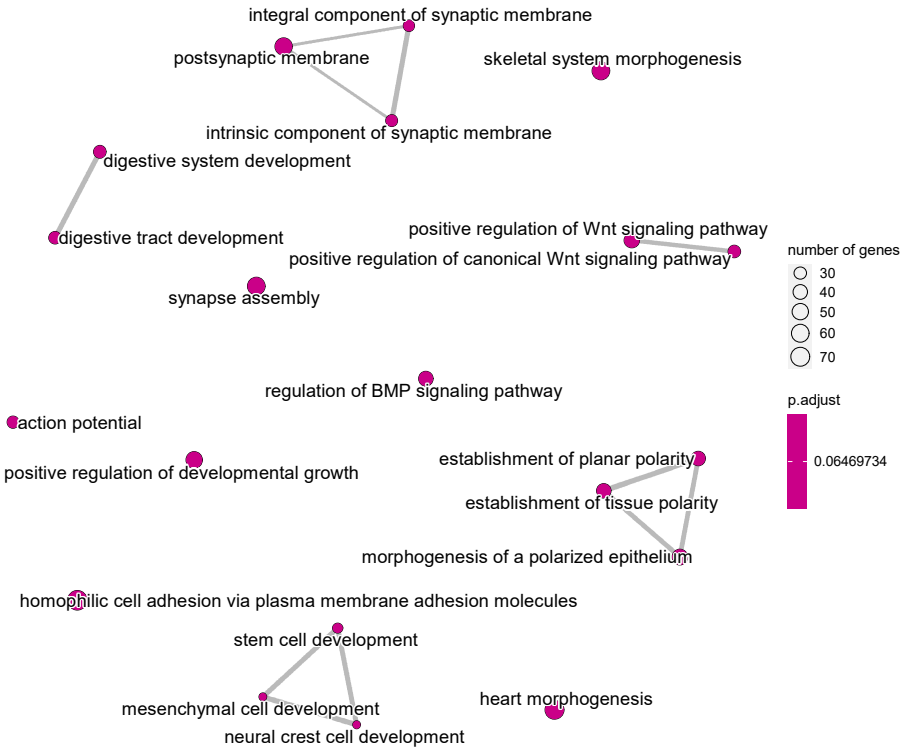

Figure 5.12. Emapplot of top 20 CAiPi dysregulated GO terms in G7 GSCs. G7 GSCs were exposed to DMSO control and combined VE821 (5μM) and olaparib (1μM) for 72 hours before RNA extraction and sequencing. Gene expression LFC between the two conditions was quantified by 'DeSeq2' analysis, and corresponding dysregulated GO terms were assessed by 'gseGO'. Gene set similarity was assessed by the 'pairwise_termsim' function in R. Plots show enrichment map for the top 20 GO terms, lines indicate a similarity between GO terms that meet a threshold of 0.2 (scale of 0-1). Line thickness and length indicates extent of similarity, circle size displays associated gene number dysregulated within each GO term and colour indicates adjusted p-value.

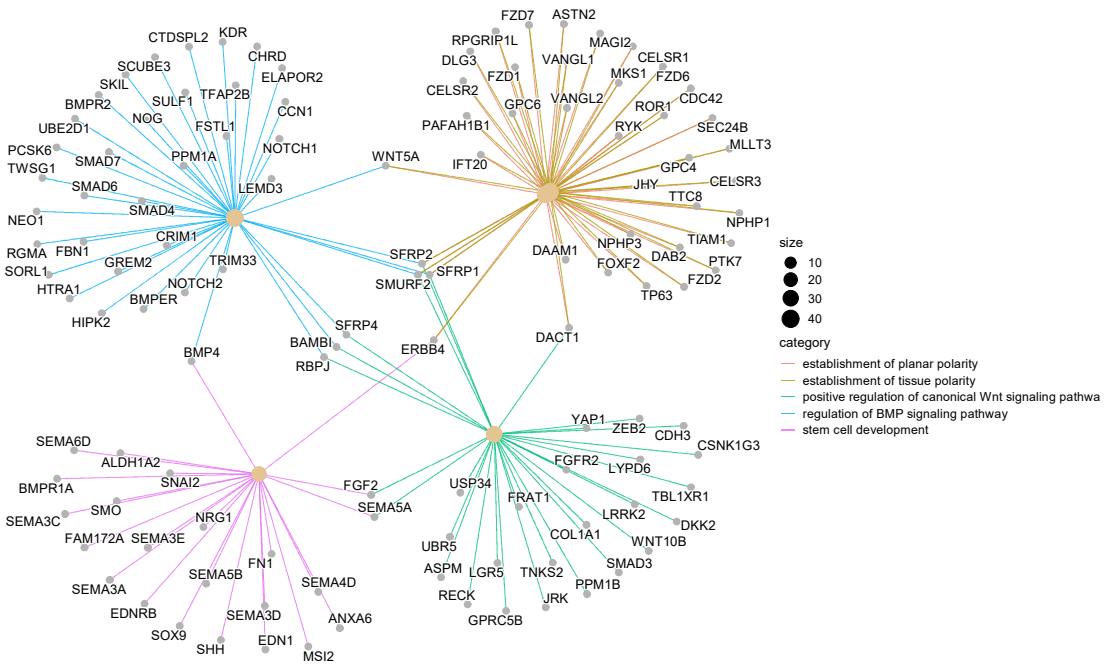

Figure 5.13. Cnetplot of top 5 CAiPi dysregulated GO terms and associated genes in G7 GSCs. G7 GSCs were exposed to DMSO control and combined VE821 (5μM) and olaparib (1μM) for 72 hours before RNA extraction and sequencing. Gene expression LFC between the two conditions was quantified by 'DeSeq2' analysis to identify corresponding dysregulated GO terms by 'gseGO'. Plots show category network for the top 5 GO terms, with any gene links between enriched GO terms highlighted. Line colour highlights each GO term, and circle size indicates the number of genes dysregulated within a gene set.

5.4 Analysis of CAiPi dysregulated KEGG pathways

In addition to GO term analysis, KEGG pathway analysis was carried out in E2 and G7 GSC and bulk cell lines to identify CAiPi-dysregulated pathways. RNA sequencing data from both vehicle control and combined VE821 (5μM) and olaparib (1μM) for 72 hours was used to identify statistically significant DEGs (adjusted p-value<0.05), and the 'enrichKEGG' R package used to identify associated dysregulated KEGG pathways.

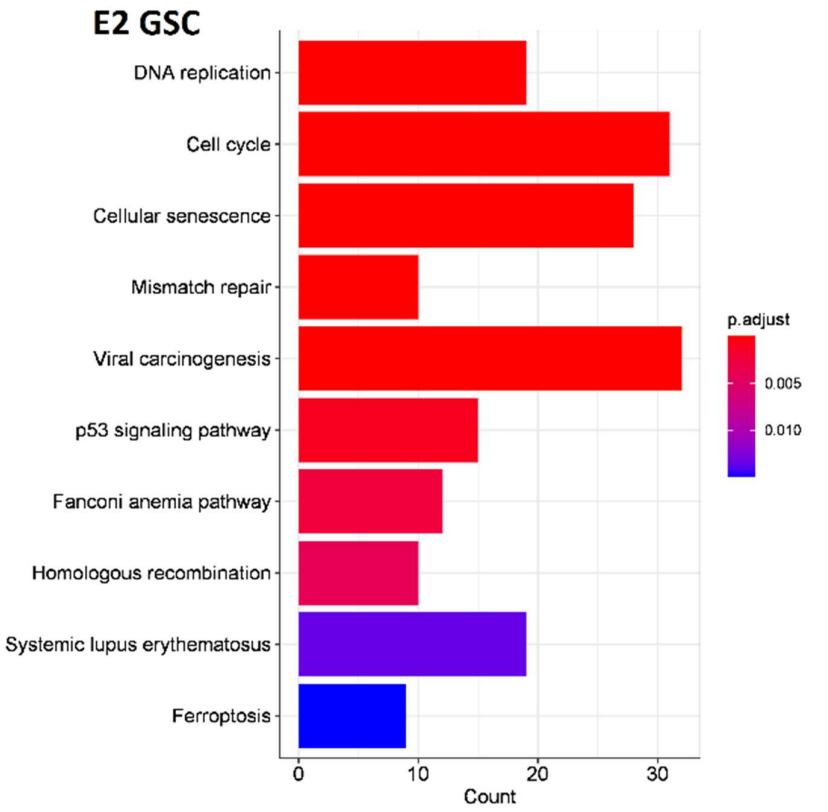
E2 GSC
DNA replication
Cell cycle
Cellular senescence
Mismatch repair
Viral carcinogenesis
p53 signaling pathway
Fanconi anemia pathway
Homologous recombination
Systemic lupus erythematosus
Ferroptosis
0
10
20
30
Count
p.adjust
0.005
0.010

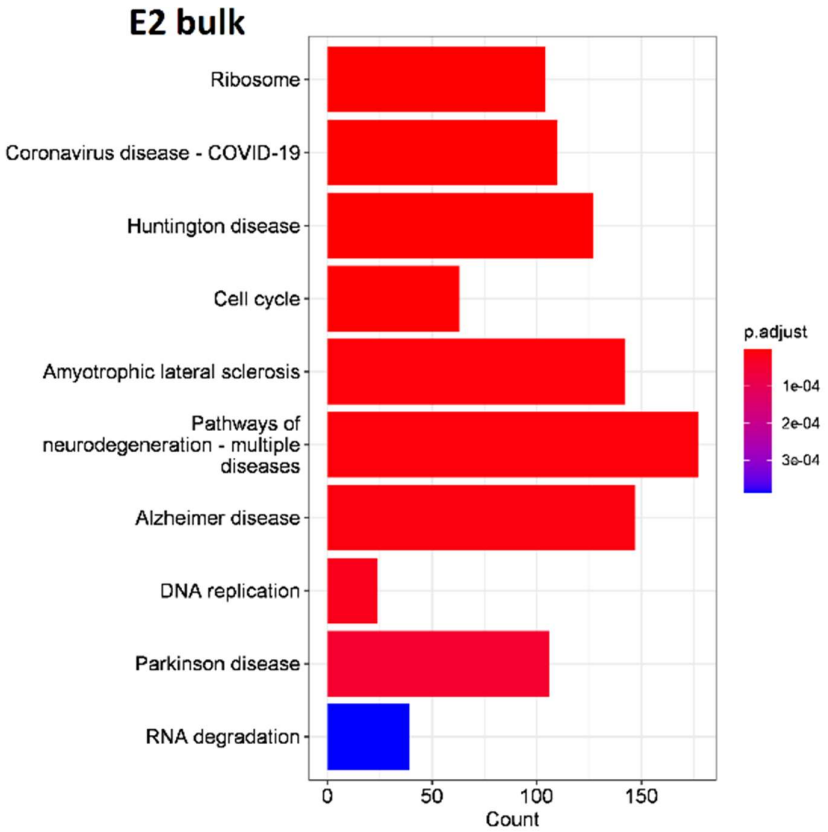
E2 bulk
Ribosome
Coronavirus disease - COVID-19
Huntington disease
Cell cycle
Amyotrophic lateral sclerosis
Pathways of neurodegeneration - multiple diseases
Alzheimer disease
DNA replication
Parkinson disease
RNA degradation
0
50
100
150
Count
p.adjust
1e-04
2e-04
3e-04

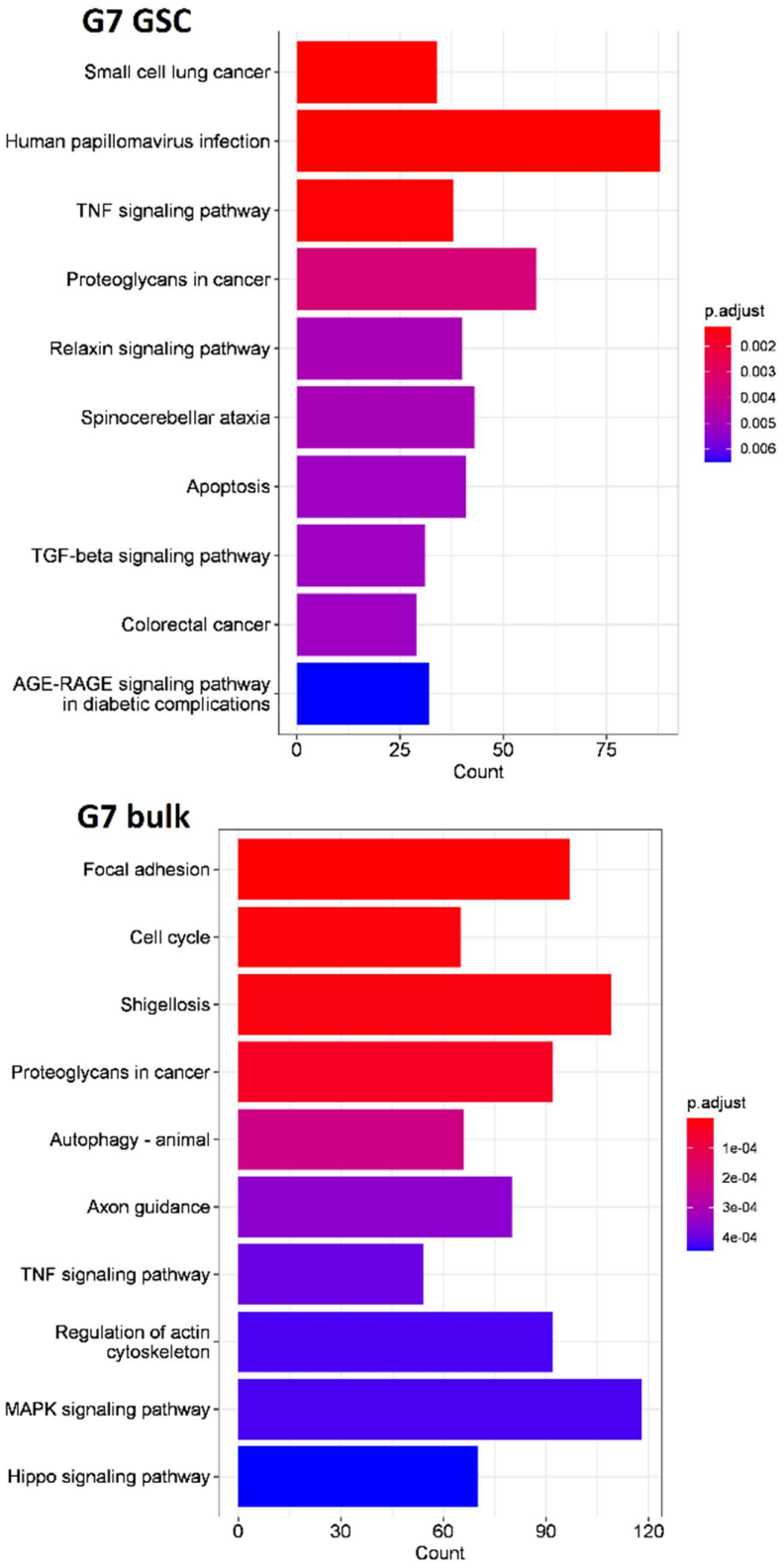

Figure 5.14. Top 10 CAiPi-induced dysregulated KEGG terms. E2 and G7 GSC and bulk cells were exposed to DMSO control and combined VE821 (5μM) and olaparib (1μM) for 72 hours before RNA extraction and sequencing. Significantly dysregulated genes (adjusted p-value<0.05) between the two conditions were identified by 'DeSeq2' analysis and associated enriched KEGG pathways identified by 'enrichKEGG' R package. Bar charts plot the top 10 dysregulated KEGG pathways, with associated adjusted p-value and number of dysregulated genes within KEGG pathway.

E2 GSCs only had 14 dysregulated pathways versus 39 for E2 bulk, and G7 GSCs had 46 dysregulated pathways and 68 for G7 bulk, in keeping with the number of total DEGs. The top ten dysregulated KEGG pathways for each cell line is shown in Figure 5.14. The most statistically significant dysregulated KEGG pathway in CAiPi-sensitive E2 GSC was DNA replication (adjusted p-value = $3.6x10^{-12}$). Other E2 GSC pathways of interest were associated with cell cycle, DNA damage and p53 signalling. E2 bulk, G7 GSC and G7 bulk exhibited some dysregulated pathways of interest. DNA replication and cell cycle were also both dysregulated KEGG pathways in E2 bulk. In G7 GSCs, KEGG pathways of note included transforming growth factor-beta (TGF-ß) signalling and apoptosis. In G7 bulk, the cell cycle pathway was also dysregulated, as well as pathways related to axons, actin, focal adhesions and proteoglycans.

5.5 Functional analysis of replication GO and KEGG terms

CAiPi treatment targets the RS response and it was hypothesised that replication-specific transcriptional changes would be induced in response to CAiPi treatment. This chapter previously identified DNA replication as the top dysregulated GO term and KEGG pathway in CAiPi-sensitive E2 GSC, however it was not known from these investigations if DNA replication was dysregulated in the other cell lines. A DNA replication GO signature was therefore curated to investigate dysregulation of replication in the other cell lines. The signature contained four GO terms that were statistically significant in E2 GSC and with minimal gene overlap between terms, as assessed by a heatplot (Figure 5.15).

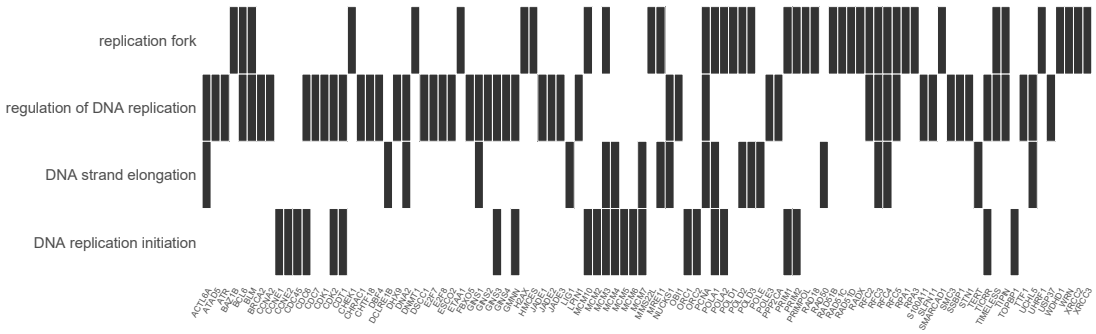

Figure 5.15. Heatplot of curated replication GO terms for E2 GSC. Dysregulated gene expression was quantified by 'DeSeq2' analysis, after 72-hour exposure to vehicle control and combined VE821 (5μM) and olaparib (1μM) and RNA extraction and sequencing. Analysis of significantly CAiPi-dysregulated GO terms was carried out using the 'enrichGO' R package, and a heatplot displays the mutually dysregulated genes within each term, represented by a vertical line. GO terms were selected due to statistical significance in E2 GSC and relevance to replication.

To quantify extent of dysregulation for each GO term, $-\log_{10}$ of the adjusted p-values was plotted for each of the four cell lines (Figure 5.16). For all four GO terms, E2 GSC displayed the greatest replication-associated transcriptional dysregulation. G7 bulk displayed more dysregulation than its paired GSC counterpart, in keeping with G7 bulk being more sensitive to targeting the RS response. G7 GSC did not reach significance for any of the replication-associated GO terms.

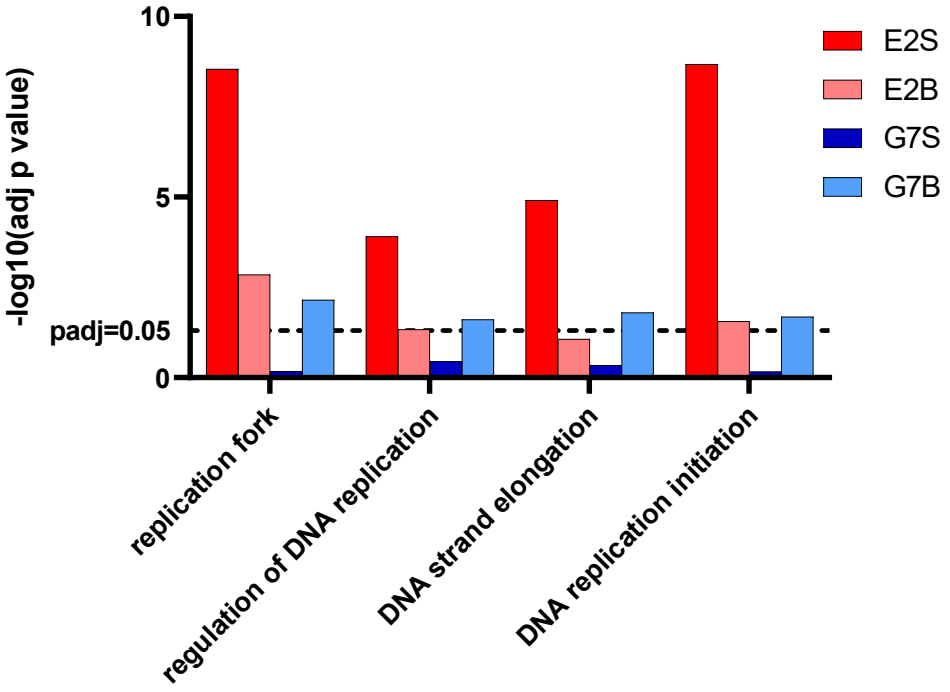

Figure 5.16. Differential DNA replication and origin firing GO term dysregulation. Dysregulated gene expression was quantified by 'DeSeq2' analysis, after 72-hour exposure to vehicle control and combined VE821 (5μM) and olaparib (1μM) and RNA extraction and sequencing in E2 and G7 GSC (S) and bulk (B) pairs. Analysis of significantly CAiPi-dysregulated GO terms was carried out by 'enrichGO' R package, and a bar chart displays the extent of significance of dysregulation within each gene set. GO terms were selected due to statistical significance in E2 GSC and relevance to replication.

GSEA dot plots in E2 GSC suggested that DNA replication-associated GO terms were generally suppressed after CAiPi. This was further assessed by GSEA plots for all cell lines. Visualisation of GSEA in Figure 5.17 confirmed that the DNA replication GO terms were downregulated in all cell lines, with a negative enrichment score (ES) for all four gene sets, but only E2 GSC reached significance.

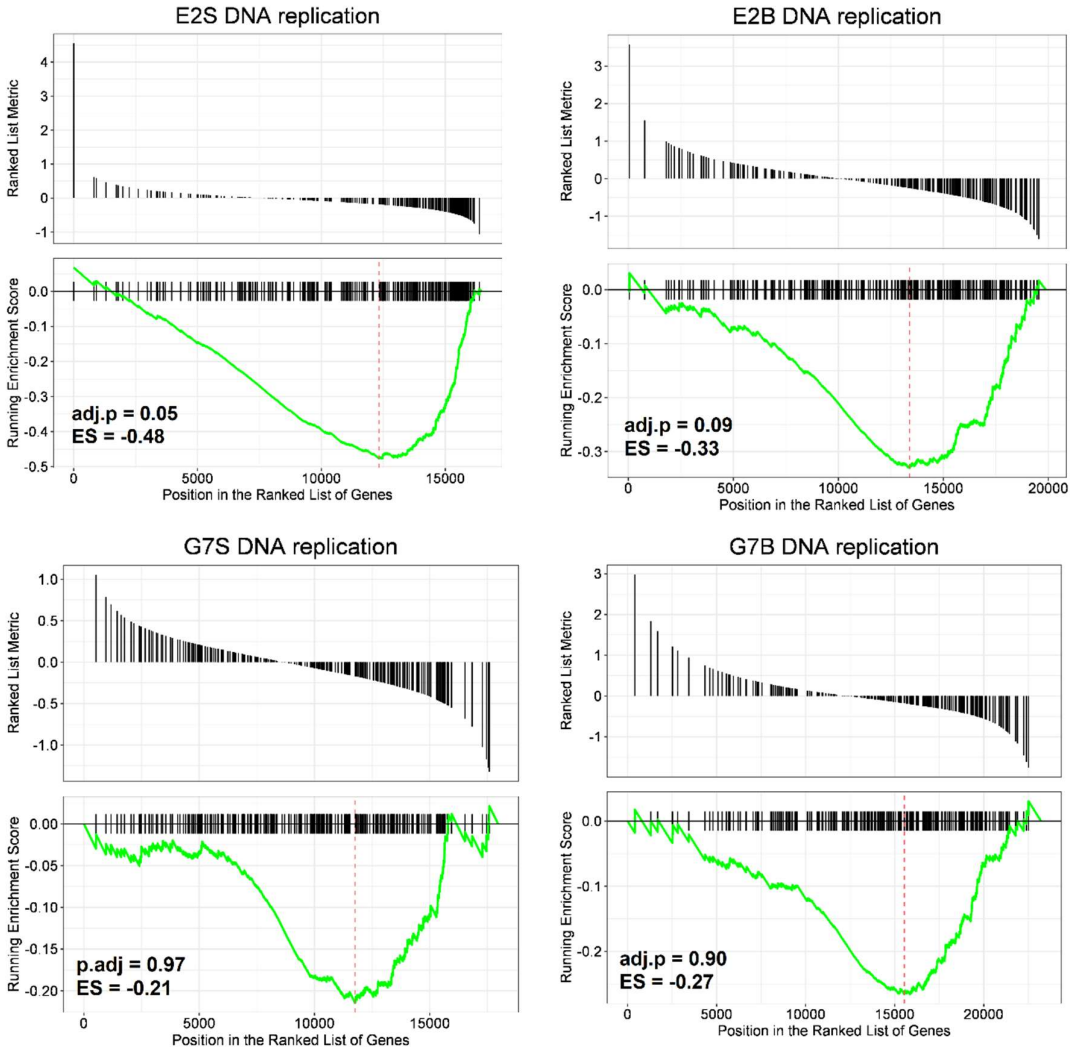

Figure 5.17. DNA replication GSEA plot. E2 and G7 GSC (S) and bulk (B) cells were exposed to vehicle control and combined VE821 (5μM) and olaparib (1μM) before RNA extraction and sequencing to identify LFC between the two conditions by 'DeSeq2' R package. GSE analysis and plotting was carried out by 'gseGO' and 'DOSE' R packages. Plots show GSEA for the DNA replication GO term and associated adjusted p-value and enrichment score. Top figure shows where DNA replication genes plot relative to all genes ranked by LFC. Bottom figure shows a running enrichment score (green) based on the ranking and LFC of all DNA replication genes, and the peak of the running score provides the enrichment score for that gene set (red), either positively or negatively enriched.

5.6 Conclusions

The differential transcriptomes in E2 and G7 paired cell lines in response to CAiPi have been characterised utilising DeSeq2. DeSeq2 allows for quantitative analysis and visualisation of RNAseq data. The package developed a statistical framework to produce gene rankings based on stable estimation of effect size, trying to overcome the issues of highly statistically significant but biologically insignificant genes being identified and count size effects on LFC (Love et al., 2014). PCA plots identified clustering of the inhibitor conditions in all four cell

lines, however with more variability in both E2 and G7 GSCs. This may be due to more innate heterogeneity within stem-enriched populations than in bulk. For all cell lines, CAiPi and ATRi clustered separately from DMSO and PARPi, especially in both bulk cell lines. These treatment groupings were only separated by PC2 on the y-axis for E2 GSC and bulk, suggesting that other transcriptional changes within these cell lines was explaining more variation in PC1. In E2 bulk, it was likely a DMSO outlier sample was driving the variability. In E2 GSC, a smaller subset of DEGs in response to CAiPi could mean that heterogeneity between the repeats were driving more variability than the treatment itself. Clustering of CAiPi DEGs by heatmap identified patterns largely similar to PCA analysis. Both E2 and G7 GSC lines had more distinctive CAiPi groups of dysregulated genes whereas bulk clustered ATRi and CAiPi together.

There was a greater increase in the number of DEGs with CAiPi over ATRi alone in GSCs versus bulk cells. This may explain the clustering of ATRi and CAiPi conditions in bulk cells via PCA and heatmaps. This pattern of dysregulation suggests there is maybe a GSC-specific transcriptomic response to CAiPi despite differing sensitivities. Lastly, volcano and MA plots visualised DEGs under each condition, and unsurprisingly since both bulk cell lines identified the most DEGs, both E2 and G7 bulk had genes with greater LFC and higher significance. Differential gene expression analysis in response to CAiPi has generally identified trends within the GSC and bulk cell types.

Functional analysis of DEG sets was performed by GO and KEGG analysis. Most interestingly, CAiPi-sensitive E2 GSCs were enriched for GO terms and pathways associated with DNA replication, cell cycle, chromosome segregation and DNA damage, all previously associated with RS or CAiPi activities. In general, GO and KEGG analysis in E2 bulk, G7 GSC and G7 bulk identified more pathways not previously associated with CAiPi. Of interest, across both G7 cell types was dysregulation of terms and pathways associated with axons, cell motility and adhesion. Axon development and axon guidance appeared for both cell types across GO and KEGG analysis. Across both GSC lines there was dysregulation of chromatin-associated GO terms, including activation of GO terms related to nucleosomes, chromatin and chromosome assembly. These GO terms did not reach significance in either bulk cell lines.

Since this thesis sought to investigate mechanisms of CAiPi sensitivity, further analysis focused on DNA replication gene sets since DNA replication-associated GO terms were significantly dysregulated in CAiPi-sensitive E2 GSCs. Analysis of the significance of DNA replication GO term dysregulation found that within each cell line pair extent of dysregulation correlated with sensitivity to targeting the RS response, since E2 GSCs and G7 bulk were the most dysregulated within their cell line pairs. GSEA found that GO terms related to replication were suppressed in response to CAiPi in E2 GSCs. A GSEA plot visualised the suppression of the DNA replication GO term in E2 GSCs, and although DNA replication was associated with a negative ES for the other three cell lines, none were statistically significant.

In conclusion, CAiPi induced differing transcriptional landscapes across all analysed cell lines. However, the most sensitive cell line, E2 GSC, had the smallest subset of DEGs and subsequently less enrichment of GO terms and KEGG pathways. Despite this, the gene sets that were enriched were highly relevant to CAiPi mechanisms of action. CAiPi in E2 GSCs was therefore inducing a highly specific transcriptomic response, whereas other cell lines induced a more non-specific response. Within each cell line pair, dysregulation of DNA replication gene sets predicted sensitivity to CAiPi.

Chapter 6 Analysis of DNA replication dynamics in GSC and bulk cell cultures in response to CAiPi

6.1 Introduction

Chapter 4 concluded that endogenous RS was not the sole predictor of CAiPi response. However, CAiPi was still potently cytotoxic to a subset of GSCs and therefore has clinical potential. Further understanding of differential CAiPi cytotoxicity is required to elucidate mechanisms of sensitivity. CAiPi-induced transcriptomic alterations indicated that replication was dysregulated specifically in a CAiPi-sensitive GSC line, and ATR and PARP have crucial roles in the maintenance of successful replication. Therefore, a DNA fibre assay was utilised to allow analysis of replication dynamics including fork velocity and replication fork structures, as described in Chapter 2. A DNA fibre assay is the accepted gold standard assay to analyse genome-wide replication dynamics (Quinet et al., 2017). In this assay, DNA is labelled sequentially with fluorescently labelled thymidine analogues; CldU and IdU. Immunostaining of these analogues allows for visualisation of individual DNA tracts and cumulative analysis of tracts gives insight into genome-wide replication mechanisms. Incorporation of inhibitors into a DNA fibre assay allows for analysis of perturbed replication.

The complete picture of replication dynamics in GSCs and bulk cells after ATR and PARP inhibition remains unclear. Previous work by Carruthers et al found that replication velocities were lower in GSCs than in their paired bulk counterparts at baseline, in keeping with higher rates of RS in GSCs (Carruthers et al., 2018). Their analysis of mean replication velocities with ATRi and CAiPi found a decrease in both GSC and bulk cells, whilst no effect was seen with PARPi alone. Studies of replication velocity alterations in other cancer types have observed decreased replication velocity with ATRi, indicative of increased RS (Kim et al., 2020, Gout et al., 2021). Several studies described no dysregulation of fork velocities by a PARPi alone, however Kim et al observed synergistic decreases in fork velocity with the addition of a PARPi to ATRi in ovarian cancer models (Kim et al., 2020, Gout et al., 2021, Bryant et al., 2009). Contradictory to these studies, Maya-Mendoza et al observed a concentration

and time dependent effect of PARPi on increased replication velocity, which in turn induced DNA damage (Maya-Mendoza et al., 2018). Further analysis is required to fully elucidate effects on replication velocities in GSCs and bulk cells after ATR and PARP inhibition.

No analysis of stalled forks or new origins with CAiPi has been published in GBM. Analysis of the effects of CAiPi on replication structures has been undertaken in other cancer types. The effects of ATRi on increasing unscheduled origin firing is well established, due to ATR's role in reducing global origin firing under RS conditions via Chk1 (Moiseeva et al., 2017, Couch et al., 2013). Analysis of stalled forks, measured by an increase in asymmetric forks, found an increase in stalled forks with ATRi but not PARPi (Kim et al., 2020, Gout et al., 2021, Maya-Mendoza et al., 2018). However, analysis of stalled forks by CldU-only stained tracts identified an increase in stalled forks by PARPi-alone (Bryant et al., 2009). Due to varied observations of replication dynamics across different cancer types and methods, this chapter also aims to elucidate the effects of CAiPi on replication machinery in GSC and bulk cell models.

6.2 Replication velocity analysis by DNA fibre assay

Initial investigations into CAiPi effects on replication using a DNA fibre assay looked at DNA fork velocity. Cells were incubated with vehicle, olaparib (1μM), VE821 (5μM) and the combination for 24 hours, then thymidine analogue CldU (25μM) was added to drug-containing media for 20 minutes before being washed off and replaced with IdU (250μM) for 20 minutes. DNA fibres were fixed and immunostained. Replication velocity was quantified by CldU and IdU fork length in kb / time exposed to the thymidine analogue.

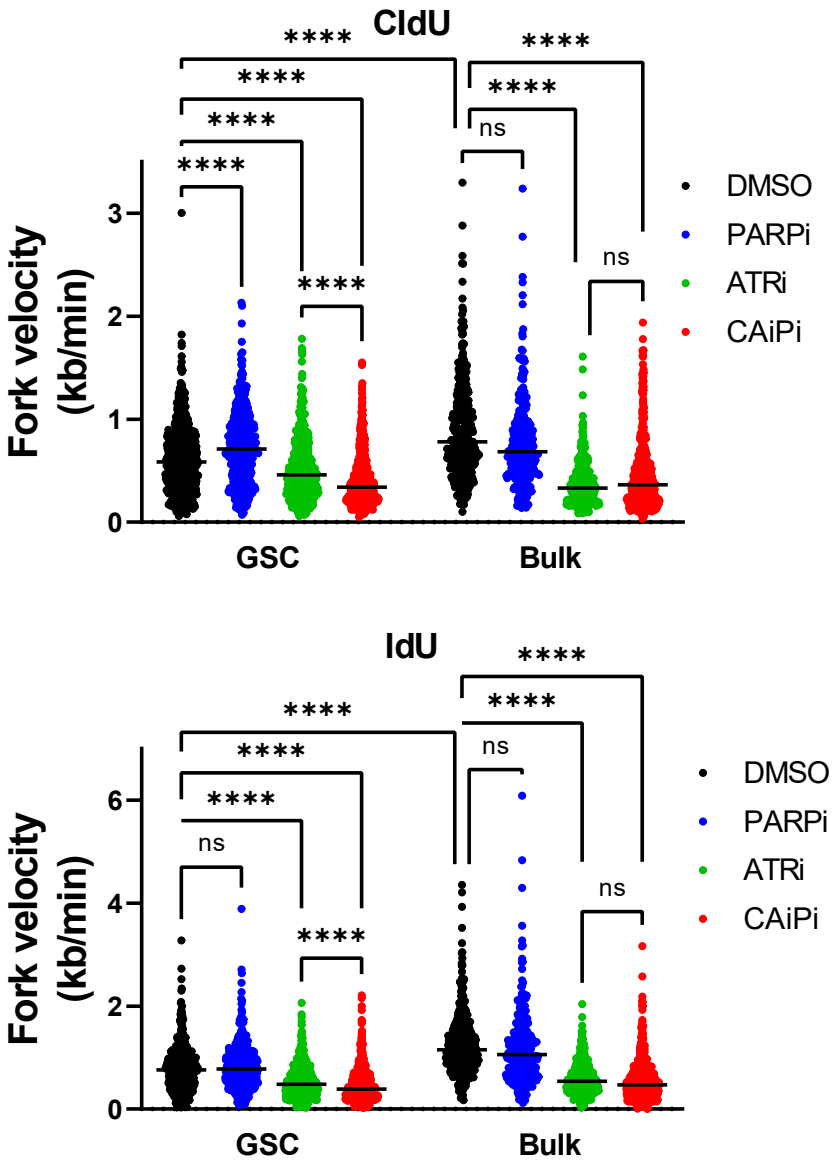

Figure 6.1. E2 replication fork velocity. Replication fork velocity in E2 GSCs and bulk cells was measured by rate of CldU and IdU incorporation using a DNA fibre assay, after 24-hour exposure to vehicle, olaparib (1μM), VE821 (5μM) and the combination. Fibre assay and manual quantification was carried out by K. Strathdee and R. Carruthers. Dot plot displays all data points from three independent experiments, with median indicated, adjusted p-values calculated by Kruskal-Wallis one-way analysis of variance with post-hoc Dunn's test (****p<0.0001, ns=not significant).

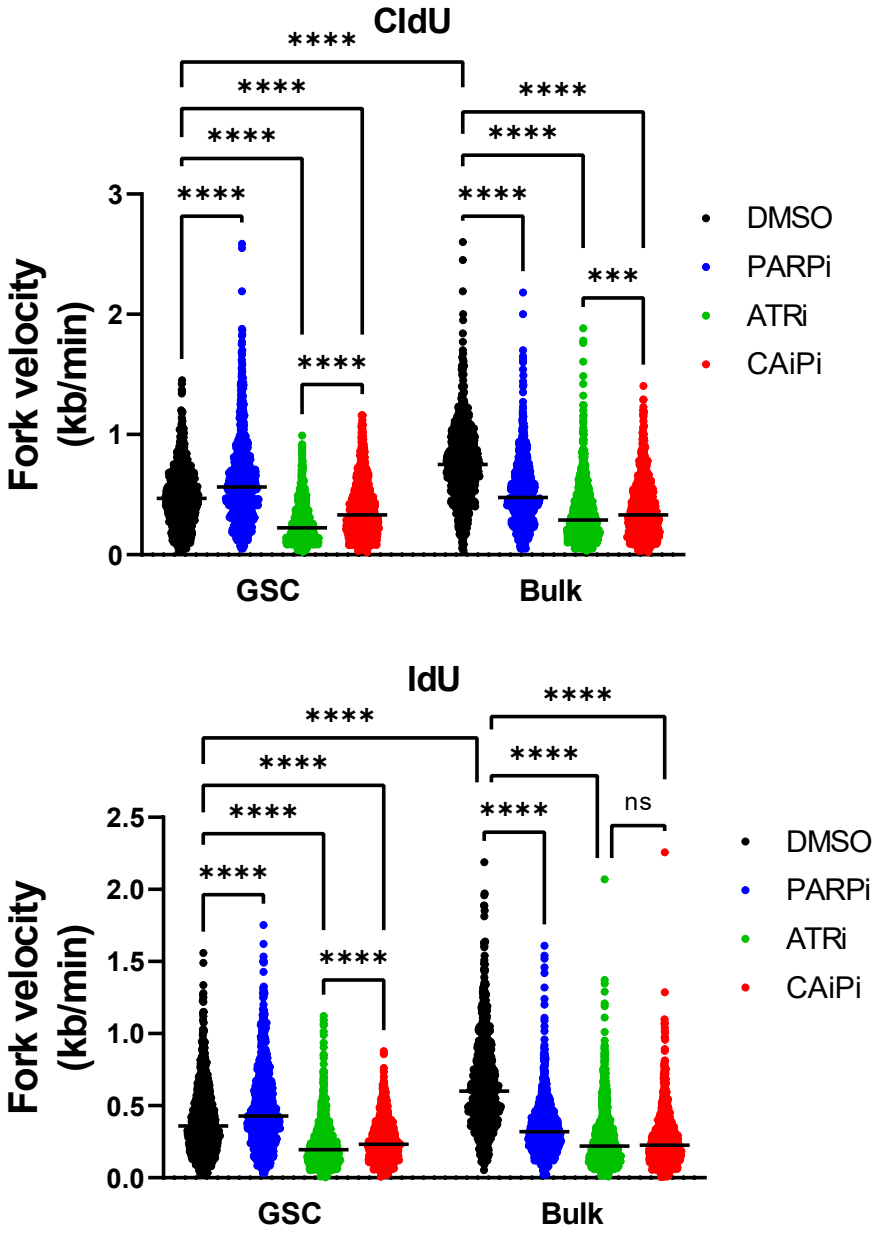

Figure 6.2. G7 replication fork velocity. Replication fork velocity was measured by rate of CldU and IdU incorporation in G7 GSC and bulk cells using a DNA fibre assay, after 24-hour exposure to vehicle, olaparib (1μM), VE821 (5μM) and the combination. Manual quantification was carried out by R. Carruthers. Dot plot displays all data points from 2 independent experiments, with median indicated, adjusted p-values calculated by Kruskal-Wallis one-way analysis of variance with post-hoc Dunn's test (***p<0.001, ****p<0.0001, ns=not significant).

Replication fork velocities were analysed in two cell lines with differing GSC and bulk-sensitivity profiles to targeting the RS response: E2, a GSC-sensitive line (Figure 6.1), and G7, a bulk-sensitive line (Figure 6.2). In both E2 and G7, fork velocities were slower in the GSC lines at baseline compared to bulk, indicative of higher RS in GSCs. CAiPi induced a statistically significant reduction in fork velocities compared to vehicle control in all cell lines. The total reduction in

fork velocity by CAiPi was greater in both bulk cell lines compared to GSCs, likely a result of higher fork velocity at baseline in bulk cell lines. ATRi alone reduced fork velocities in all cell lines.

In G7 GSCs, PARPi alone increased replication fork speed. PARPi also increased replication fork speed in E2 GSCs, although only with CldU. Conversely, PARPi reduced replication fork speed in G7 bulk cells and had no effect in E2 bulk. CAiPi reduced fork velocity compared to ATRi alone only in E2 GSCs. Conversely, fork velocity increased with CAiPi compared to ATRi alone in G7 GSCs and in G7 bulk with CldU.

6.3 Replication structure analysis by DNA fibre assay

To comprehensively characterise replication in GSC and bulk cells exposed to CAiPi, a DNA fibre assay was utilised to analyse replication fork structures. Ongoing forks, stalled forks and new origins were analysed in E2 and G7 (Figure 6.3), by a DNA fibre assay as described previously in this thesis. Ongoing forks can be identified by fibres that stain for both CldU and IdU, stalled forks by fibres that stain only for the first analogue CldU and new origins by those that stain only for the second analogue IdU. CAiPi induced no statistically significant changes in ongoing or stalled forks in E2 GSCs and bulk cells or G7 GSCs. G7 bulk cells had a statistically significant decrease in ongoing forks with CAiPi treatment compared to control. This reduction in the proportion of ongoing forks was largely replaced by a marked increase in stalled forks in G7 bulk cells. Stalled forks at baseline were not significantly different between GSC and bulk pairs for both E2 and G7, however GSCs trended towards more stalled forks, in keeping with them having increased RS. Most interestingly, the greatest number of new origin firings was observed in E2 GSCs after PARPi, representing 22.0% [95% CI: -0.5, 44.6] of all replication structures under that condition. No change in origin firing with PARPi was observed in either bulk cell line, or in the G7 GSC line.

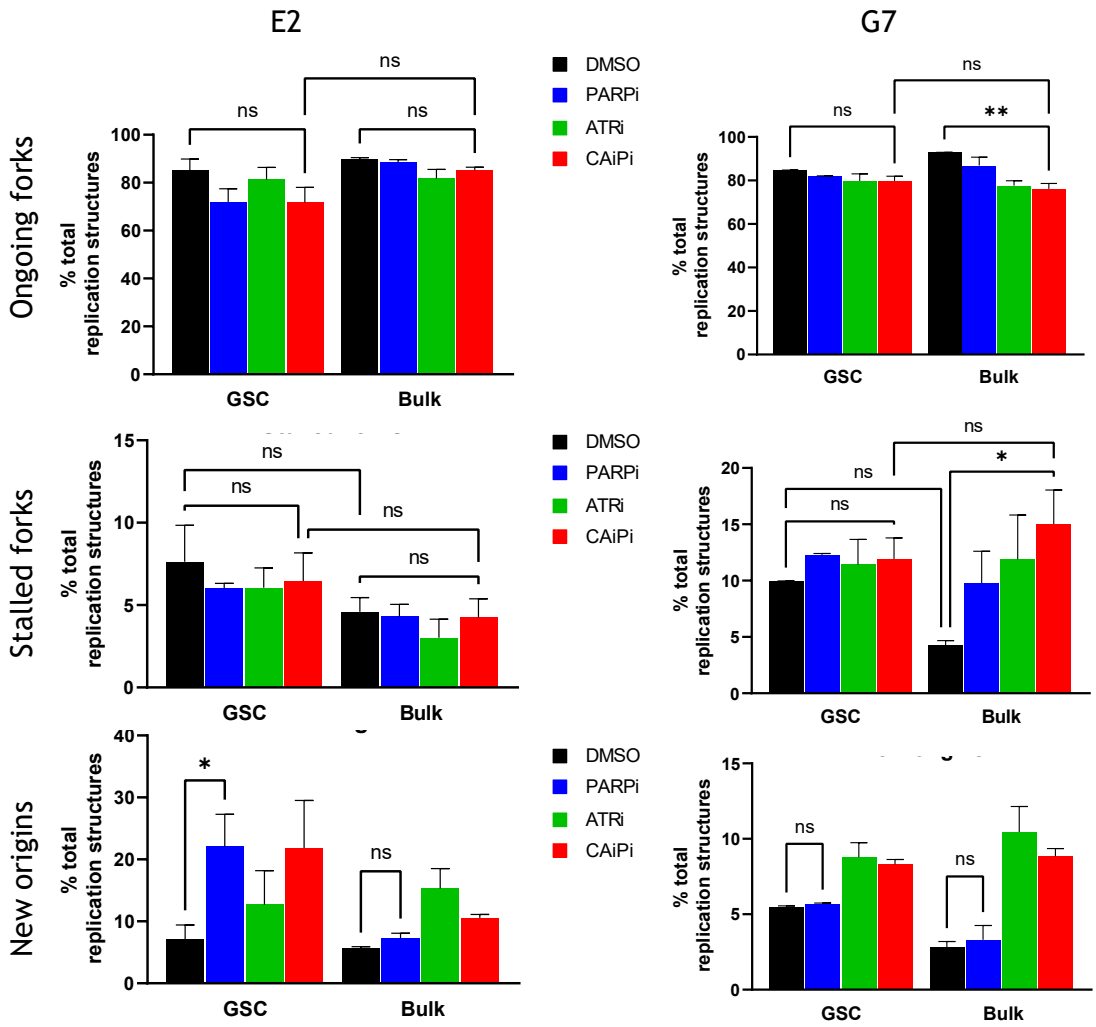

Figure 6.3. E2 and G7 replication structures. Ongoing forks, stalled forks and new origins were quantified in E2 and G7 GSC and bulk cells using a DNA fibre assay after 24-hour exposure to vehicle control, olaparib (1μM), VE821 (5μM) and the combination. Fibre assay for E2 was carried out by K. Strathdee and analysis was carried out by R. Carruthers. Bar charts represent mean and SEM of three independent experiments for E2 and two independent experiments for G7, adjusted p-values calculated by one-way ANOVA with post-hoc Sidak test (*p<0.05, ns=not significant).

6.4 PARP trapping drives origin firing in GSCs

PARP trapping is a well-established mechanism of PARPi activity, so it was of interest to investigate if PARP trapping was causally implicated in the cytotoxicity and increased origin firing mechanism. Therefore, the PARPi veliparib was analysed along with olaparib in E2, since olaparib is a much more potent PARP trapper than veliparib (Murai et al., 2012). To investigate comparable inhibitory concentrations of olaparib and veliparib, PARylation levels were assessed. PARylation is a post-translational modification, catalysed by PARP in response to DNA damage and forms PAR chains at sites of lesions. PAR chains can be induced by treatment with H_2O_2 and detected by Western blot.

Figure 6.4 shows the effect of increasing concentrations of olaparib and veliparib on PAR levels, as an indicator of their ability to inhibit PARP activity. Complete ablation of PARylation was observed at 1μM for both olaparib and veliparib. Consequently, their ability to fire new origins was analysed by DNA fibre assay at 1μM for both inhibitors, as described previously in this chapter. Only olaparib in E2 GSCs induced a statistically significant increase in origin firing, with no significant change in origin firing induced by veliparib (Figure 6.5). No statistically significant changes in origin firing were observed in E2 bulk with olaparib or veliparib.

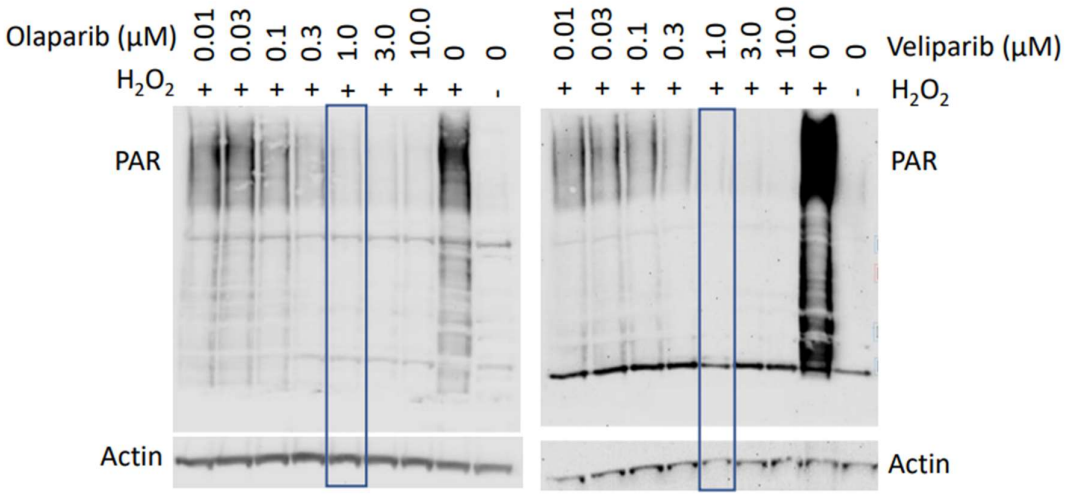

Figure 6.4. Inhibition of PARylation by olaparib and veliparib. Investigation of expression of PAR in G7 GSCs by Western blot after one hour incubation with increasing concentrations of olaparib and veliparib followed by 20-minute incubation with 20mM H_2O_2. Actin was analysed as a loading control. Western blot carried out by K Strathdee.

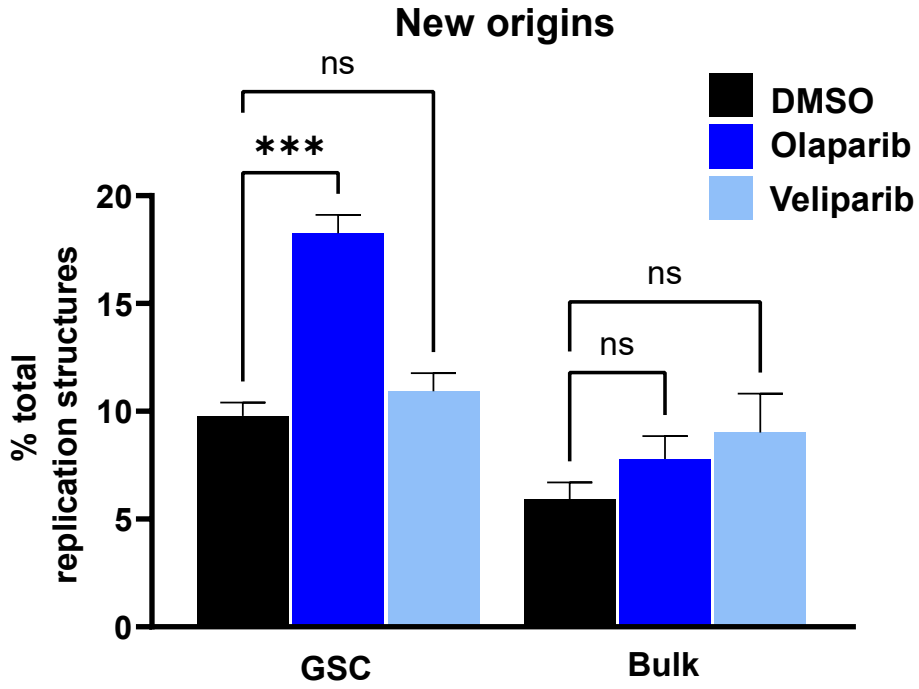

Figure 6.5. New origin firing in response to different PARPi. New origins were quantified in E2 GSC and bulk cells using a DNA fibre assay after 24-hour exposure to DMSO vehicle control, olaparib (1μM) and veliparib (1μM). Fibre assay and quantification was carried out by K. Strathdee and R. Carruthers. Bar charts represent mean and SEM of 3 independent experiments, adjusted p-values calculated by one-way ANOVA with post-hoc Sidak test (***p<0.0001, ns=not significant).

To correlate an increase in origin firing with CAiPi mechanism of sensitivity, olaparib and veliparib cytotoxic effects were compared in E2 GSCs by neurosphere assay. Cells were seeded in 96-well plates at a density of 10 cells per well in media containing vehicle control, VE821 (5μM), olaparib and veliparib at increasing concentrations and combined with VE821 (5μM). After two days the drugs were diluted to 40% drug concentration and left to form neurospheres for three weeks. Neurospheres were stained with MTT, imaged and manually counted (Figure 6.6).

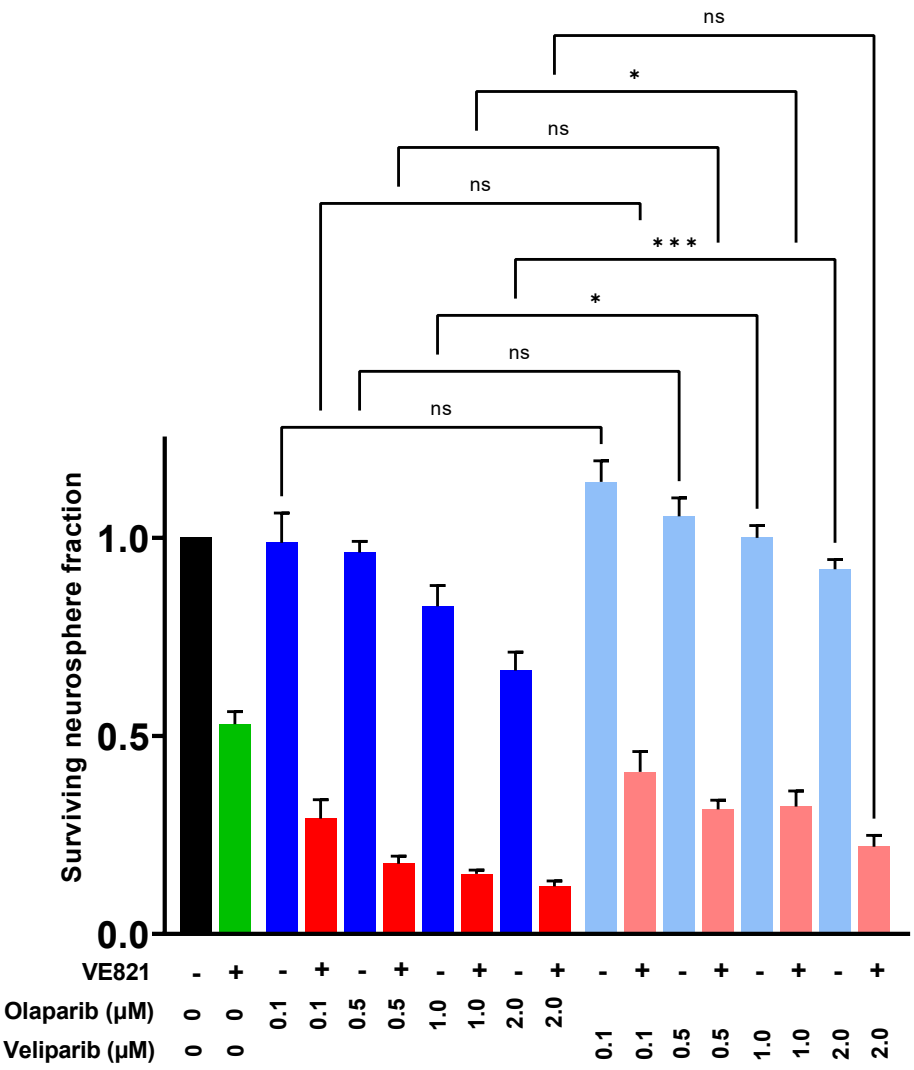

Figure 6.6. Surviving neurosphere fraction from differing PARP trapping capacities. Cell survival in response to VE821 (5μM), olaparib, veliparib and the combination in E2 GSCs was analysed by neurosphere formation assay. Bar charts represent mean and SEM of four independent replicates, adjusted p-values calculated by one-way ANOVA with post-hoc Sidak test (*p<0.05, ***p<0.001, ns=not significant).

Both olaparib and veliparib decreased the surviving neurosphere fraction in relation to vehicle control in a dose-dependent manner. At the higher doses (1μM and 2μM) olaparib reduced the surviving neurosphere fraction in comparison to veliparib as a single agent. When combined with ATRi, olaparib induced a statistically significant reduction in surviving neurosphere fraction compared to veliparib at the comparable dose of 1μM. Other concentrations were not significant but there was a general trend towards more cytotoxicity with olaparib. These analyses support the hypothesis that PARP trapping is involved in the increased origin firing via PARPi and is causally linked to CAiPi cytotoxicity.

6.5 Inhibition of origin firing via roscovitine

To further investigate the relevance of new origin firing to CAiPi response in sensitive GSCs, origin firing was modified to analyse the effects on CAiPi cytotoxicity. Origin firing is coordinated by CDKs, with cyclin-CDK2 complexes and CDC7 working together to regulate and activate the pre-RC. To disrupt the regulation of replication and reduce origin firing, the CDK inhibitor roscovitine was utilised. Roscovitine selectively targets CDK1, 2, 5, 7 and 9, with CDK2 being the main target of roscovitine (Bach et al., 2005). Due to roscovitine's role as a CDK inhibitor, Petermann et al investigated its effects on origin firing and saw roscovitine was able to reduce origin firing by DNA fibre assay (Petermann et al., 2010). The authors also reported roscovitine treatment led to prolonged S phase progression, due to reduced origin firing not being compensated by increased replication velocity. High doses of roscovitine therefore may disrupt S phase entry and since CAiPi is hypothesised to act during S phase, roscovitine may reduce cytotoxicity by cell cycle disruption as opposed to reducing excess origin firing. Therefore, we aimed to investigate S phase entry with roscovitine. Entry into S phase was investigated after 24-hour exposure to vehicle control and increasing concentrations of roscovitine combined with BrdU (10μM) in E2 GSCs. Cells were then fixed with ethanol, before denaturation of DNA, cell permeabilisation and incubation with FITC-conjugated α-BrdU antibody and PI.

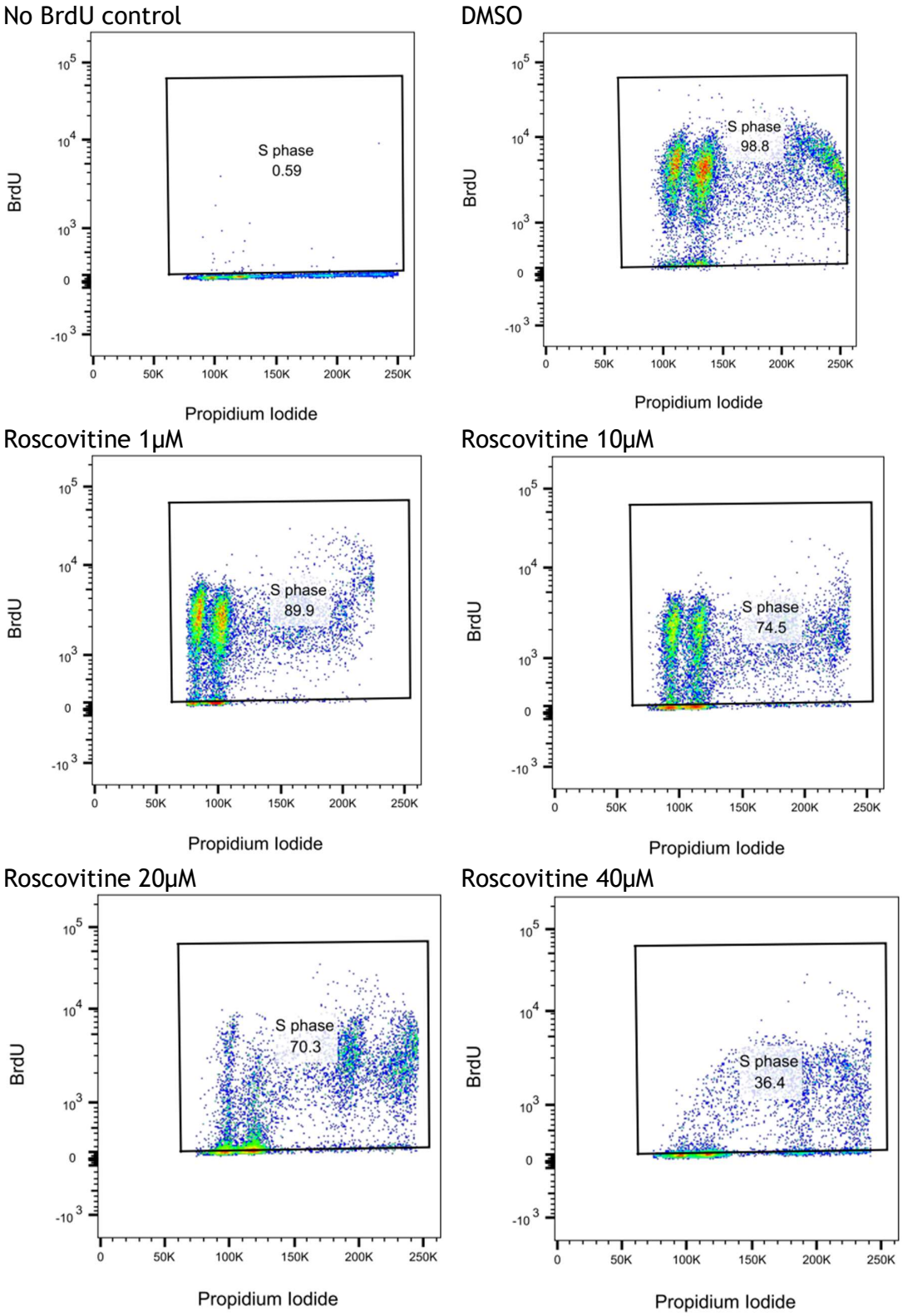

Figure 6.7. BrdU profiles to assess S phase entry with roscovitine. Representative images of gating strategy after exposure of E2 GSCs to vehicle control or increasing concentrations of roscovitine combined with BrdU (10μM) to identify E2 GSCs that have progressed into S phase. No BrdU control included for gating strategy. DNA content was assessed by PI. PI and BrdU was assessed by flow cytometric quantification via BD FACSVerse™ and analysed by FlowJo™.

Entry into S phase was assessed by BrdU positive cells and representative BrdU cell cycle profiles and gating strategies are shown in Figure 6.7, and quantification in Figure 6.8. GSC entry into S phase at the lowest concentration of 1μM was largely unperturbed in comparison to control (91.0%), and at 10μM was only slightly reduced (75.4%). As roscovitine concentrations increased, cells that entered S phase continued to decrease, and was drastically reduced at the highest roscovitine concentration of 40μM with only 36.8% of cells entering S phase in 24 hours in comparison to control. Therefore, further investigations of roscovitine utilised the lower doses of 1μM and 10μM to prevent roscovitine's effects on cell cycle progression at higher concentrations influencing CAiPi-sensitivity.

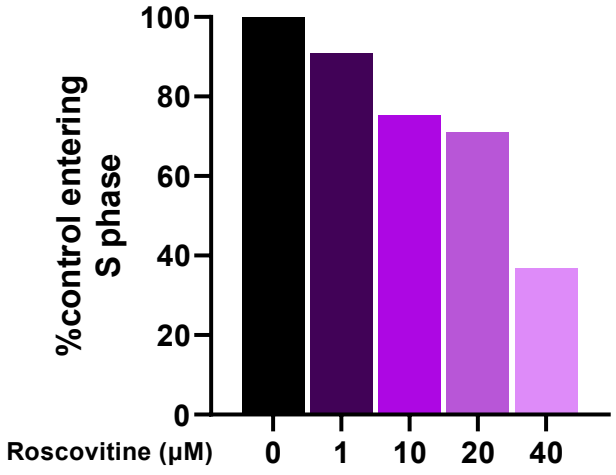

Figure 6.8. S phase entry after roscovitine. Quantification of BrdU-positive E2 GSCs by flow cytometry, as shown in Figure 6.7. Bar charts represent the results from one experiment.

To establish the effects of reduced origin firing on CAiPi cytotoxicity, a neurosphere survival assay was utilised. Cells were incubated with CAiPi (VE821 (5μM) and olaparib (1μM)) with or without roscovitine at 1μM and 10μM for 24 hours, before being seeded in 96-well plates at a density of 10 cells per well in fresh media. Cells were left to form neurospheres for three weeks, before being stained with MTT, imaged and manually counted.

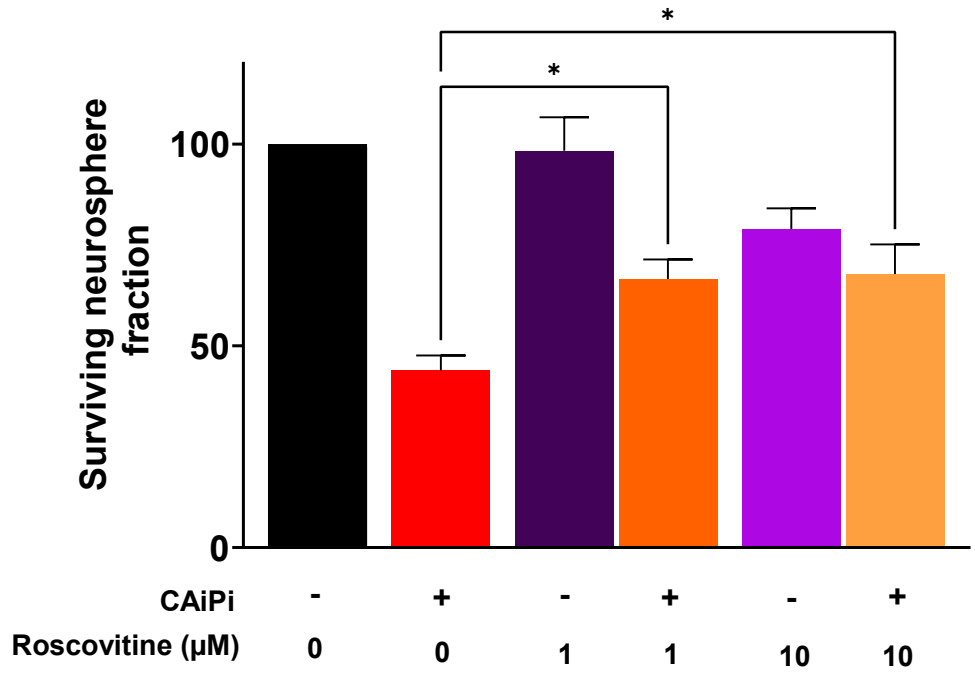

Figure 6.9. E2 rescue of CAiPi by roscovitine. Cell survival in response to combined VE821 (5μM) and olaparib (1μM), in combination with roscovitine (1μM and 10μM) in E2 GSCs was analysed by neurosphere formation assay. Bar charts represent mean and SEM of 4 independent experiments, adjusted p-values calculated by one-way ANOVA with post-hoc Sidak test (*p<0.05).

Roscovitine's effects on CAiPi-induced cytotoxicity was assessed in E2 GSCs (Figure 6.9), which previously displayed a PARPi-induced increase in origin firing and in G7 GSCs (Figure 6.10) which conversely saw no PARPi-induced increase in origin firing. In E2 GSCs, the addition of low dose roscovitine to CAiPi induced a statistically significant increase in surviving neurosphere fractions in comparison to CAiPi alone, indicating partial rescue of CAiPi cytotoxic effects. In G7 GSCs, where origin firing was not increased to the same extent, the addition of roscovitine had no effect on the reduction of surviving neurosphere fractions by CAiPi.

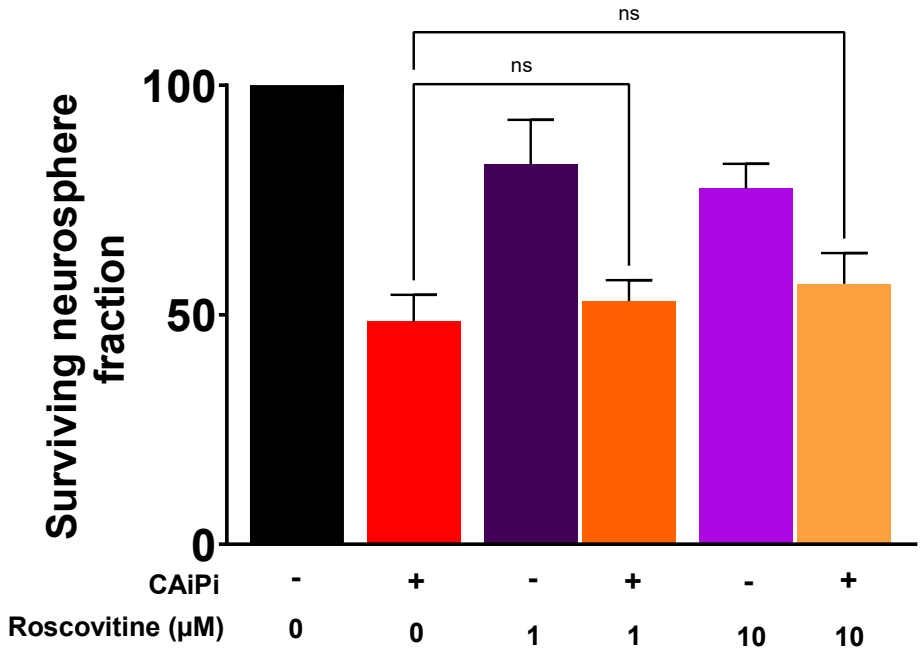

Figure 6.10. No change in CAiPi cytotoxicity by roscovitine in G7. Cell survival in response to combined VE821 (5μM) and olaparib (1μM), in combination with roscovitine (1μM and 10μM) in G7 GSCs was analysed by neurosphere formation assay. Bar charts represent mean and SEM of 4 independent experiments, adjusted p-values calculated by one-way ANOVA with post-hoc Sidak test (ns=not significant).

6.6 Conclusions

This chapter has provided a detailed characterisation of replication dynamics in GSCs and bulk cells in response to CAiPi. Carruthers et al had previously reported that CAiPi reduced replication velocity at clinically relevant concentrations (Carruthers et al., 2018). Slowed replication forks are a clear indicator of the cell's response to increased RS, as decreased fork speeds reduce RS-induced damage induction (Somyajit et al., 2017, Zeman and Cimprich, 2014). The combined treatment therefore appears to successfully target the RS response and enhance RS within the cells. However, the reduction in fork speed was greater in bulk cells relative to GSCs and comparable patterns of reduction in fork velocity were observed in G7 and E2 in response to CAiPi, suggesting that extent of reduction in fork speeds does not explain GSC-specific responses to targeting the RS response.

Analysis of the effect of PARPi alone on fork velocity found increased fork speeds exclusively in GSCs. No change compared to vehicle control was observed for E2 bulk while PARPi decreased fork velocity in G7 bulk. PARP has critical roles in regulating fork speeds in the face of RS, with previous studies observing that

inhibition of PARP resulted in either loss of the fork speed reduction to manage RS (Ray Chaudhuri et al., 2012, Sugimura et al., 2008, Zellweger et al., 2015) or accelerated fork speeds (Maya-Mendoza et al., 2018), as was observed in these GSCs. No studies have reported a reduction in fork speed in response to PARPi, as seen in G7 bulk, so this relationship remains to be elucidated, potentially indicating variable reliance on PARP for replication velocity maintenance. Lastly, in E2 GSC there was a significant reduction in fork velocity with CAiPi compared to ATRi alone, while G7 GSC had an increase in fork velocity with CAiPi compared to ATRi. It could be hypothesised that reduced fork speeds in the E2 cell lines could be a mechanism of sensitivity, whereby these cell lines do not successfully complete replication before entry into mitosis, whereas G7 maintain faster replication speeds to complete replication.

Utilisation of a DNA fibre assay allowed for further analysis of replication dynamics, namely quantification of stalled forks and new origins. Percentage of stalled forks, along with reduced fork velocity, is a well-established measure of RS. Interestingly, the only significant increase in stalled forks after CAiPi exposure was observed in G7 bulk. This was despite CAiPi's activity in targeting the RS response, which was hypothesised to exacerbate RS rates and was confirmed by slowed replication rates, and despite several studies observing ATRi-induced increases in stalled forks as discussed previously. However, these previous studies quantified asymmetric forks as a measure of stalled forks as opposed to CldU only tracts. Future analysis could utilise this alternative method to quantify stalled forks and assess any differences in results. Due to a lack of aberrations in stalled fork proportions quantified by CldU-only tracts in CAiPi-sensitive E2 GSCs, this measure of induced RS does not appear to be predicting sensitivity.

Unexpectedly, the greatest increase in aberrant origin firing was observed in E2 GSCs in response to PARPi. This increase in origin firing was not matched by a potentially cell-protective decrease in replication velocity, instead PARPi also increased fork speed in E2 GSCs. Since this coupled increase in origin firing and fork speed has potentially detrimental effects on accurate and successful cell replication, and no previous reports have discussed this PARPi-induced origin firing phenotype, this chapter further investigated this phenomenon.

Analysis of origin firing with a DNA fibre assay found that this increase in origin firing in CAiPi-sensitive GSCs was seen with olaparib, however not with an alternative PARPi veliparib despite using doses that produced equivalent abrogation of PARylation. This novel observation was hypothesised to be due to differences in PARP trapping between the inhibitors, since olaparib is a potent PARP trapper whereas veliparib does not efficiently trap PARP to sites of damage (Murai et al., 2012). Increased origin firing is often in response to stalled forks or slower replication, to ensure timely and successful completion of replication before entry into mitosis, however PARPi alone did not induce fork stalling or slower replication. The mechanism of increased origin firing in response to PARP trapping remains unclear, as it appears to not be in response or compensatory to other replication dynamics. However, we hypothesise that this increase in origin firing, not matched by a decrease in replication velocity or stalled forks, is detrimental to cell survival. To further elucidate this relationship between PARP trapping and origin firing, a much more potent PARP trapper talazoparib could be utilised in DNA fibre assay analysis (Hopkins et al., 2019), or knockdown of the PARP protein would differentiate a PARP-trapping phenotype from a PARPi catalytic inhibitory phenotype. Investigations of origin firing in other CAiPi-sensitive GSCs, namely R9 and R10, would be advantageous.

Origin firing was inhibited with the CDK inhibitor roscovitine to investigate its links to CAiPi mechanism of response. CAiPi activity is reliant on S phase entry since ATR and PARP are active during replication. Due to roscovitine's CDK inhibitor activity, which can have a knock-on effect on cell cycle progression, effects of roscovitine on S phase entry were investigated. The lowest doses of roscovitine only slightly reduced S phase entry. At these lower doses, the inhibition of origin firing partially rescued CAiPi cytotoxicity in E2 GSCs which exhibited the PARPi-induced origin firing increase. A study by Besteiro et al showed a similar modest rescue of Chk1i cytotoxic effects by roscovitine, and they proposed the extent of the rescue was solely down to roscovitine's origin firing activities due to silencing of factors affecting replication barriers and progression having no effect on the extent of rescue (Gonzalez Besteiro et al., 2019). Roscovitine had no effect on CAiPi response in G7, which exhibited no PARPi-induced origin firing, and a much more modest increase in origin firing from CAiPi treatment overall. Further assays need to be carried out to explore

the extent of origin firing depletion in these GBM cell lines at lower roscovitine concentrations but overall, these investigations show that an increase in origin firing, induced by PARP trapping, is crucial for CAiPi sensitivity.

Chapter 7 Investigations of dysregulated S phase by replication stress-targeting therapies

7.1 Introduction

CAiPi-sensitive GSCs have increased origin firing in response to PARPi, however the consequence of this phenotype remains unclear. There are no studies of CAiPi effects on successful DNA synthesis, however it was hypothesised that loss of origin firing regulation would influence timely and successful replication. Tightly organised replication is essential to maintain genomic stability (Aguilera and Gomez-Gonzalez, 2008). Loss or disruption of any of the regulatory processes can have detrimental consequences for the cell. Therefore, this chapter aimed to elucidate any S phase challenges the cell faces in response to CAiPi.

7.2 53BP1 nuclear bodies increase in GSC sensitive cell lines

The previous chapter described dysregulated origin firing in CAiPi-sensitive GSC lines. The consequence of dysregulated origin firing on successful completion of replication was investigated here. Several studies have described 53BP1NBs in G1 phase as markers of UR-DNA (Lukas et al., 2011, Harrigan et al., 2011), as discussed in detail in Chapter 1. A quantitative analysis of UR-DNA, measured by 53BP1NB in G1 phase, was carried out in four primary, paired GBM cell lines. E2 and R9 were selected as GSC-sensitive cell lines, G7 and R15 displayed more sensitive bulk cells to targeting the RS response in comparison to their paired GSCs, as identified by CellTiter-Glo® in Chapter 4. Cells were incubated with vehicle control, VE821 (5μM), olaparib (1μM) and the combination for 48 hours before fixation. Immunostaining of DAPI identified nuclei for analysis. CENP-F associates with the centromere-kinetochore complex and is therefore a marker of G2/M phase cells, therefore absent CENP-F staining was used to identify G1 phase cells. Immunostaining of 53BP1 allowed for quantification of 53BP1NB. Nuclear bodies were defined as foci between 12 and 150 pixels and were counted manually. Manual counts were validated by automated analysis as

discussed in Chapter 2. Representative immunofluorescence of CENP-F, 53BP1 and DAPI are shown in Figure 7.1.

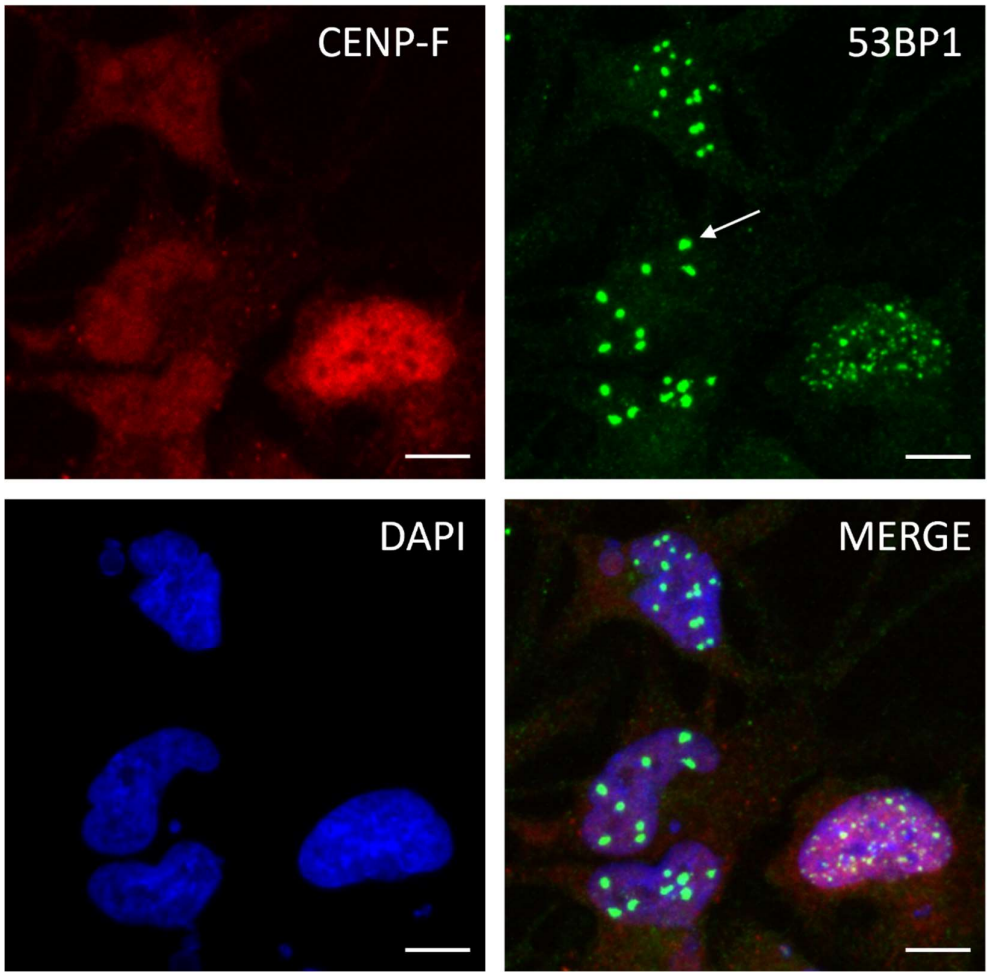

Figure 7.1.Immunofluorescence of CENP-F, 53BP1 and DAPI. Representative images of immunofluorescence of CENP-F (red), 53BP1 (green) and DAPI (blue) in E2 GSC exposed to combined olaparib (1μM) and VE821 (5μM) for 48 hours. White arrow highlights a 53BP1 nuclear body within a CENP-F negative cell. Nuclei were stained with DAPI (scale bar = 5μm).

Figure 7.2 shows the results for E2 and R9 quantification of 53BP1NBs. CAiPi induced a statistically significant increase in 53BP1NB over vehicle control in E2 GSCs, with the median number of 53BP1NB per nucleus increasing from 0 [95% CI: 0, 1] to 6 [95% CI: 5, 6]. This was also true for R9 GSCs with median 53BP1NB increasing from 3 [95% CI: 3, 4] in the vehicle control up to 6 [95% CI: 6, 7] after CAiPi treatment. E2 bulk also displayed an increase in median CAiPi-induced 53BP1NB, increasing from 1 [95% CI: 0, 1] before CAiPi to 4 [95% CI: 3, 4] after, whereas median 53BP1NB in R9 bulk was 3 with [95% CI: 3, 3] and without [95% CI: 2, 3] CAiPi. Interestingly, for both E2 and R9, CAiPi induced a greater number

of 53BP1NB in GSCs compared to bulk, suggesting that CAiPi induced more UR-DNA in sensitive GSC lines.

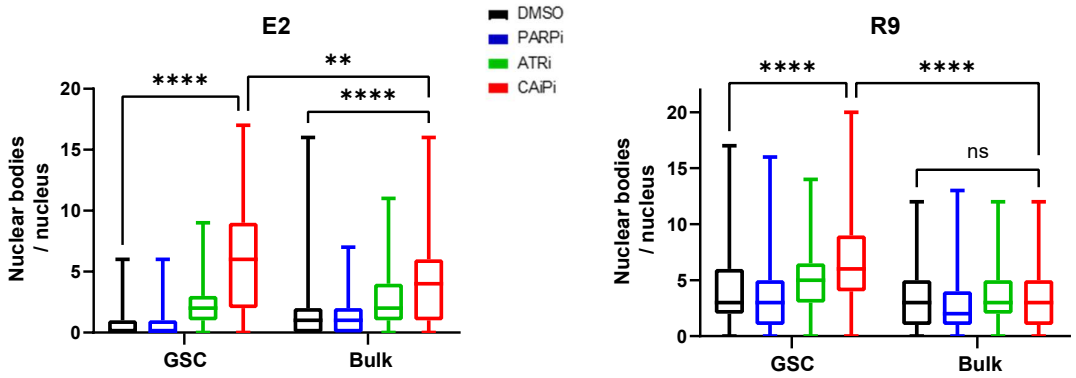

Figure 7.2. 53BP1 nuclear bodies in GSC-sensitive paired cell lines. 53BP1NB per CENP-F negative nucleus were quantified in E2 and R9 paired GSCs and bulk cells after 48-hour incubation with olaparib (1μM), VE821 (5μM), the combination and vehicle control. Box plots were from ≥3 independent experiments, representing a minimum of 200 nuclei analysed, adjusted p-values calculated by Kruskal-Wallis one-way analysis of variance with post-hoc Dunn's test (**p<0.01, ****p<0.0001, ns = not significant).

Conversely, Figure 7.3 investigated two cell lines whose bulk cell lines were more sensitive to targeting the RS response than their paired GCSs, and the GSCs were comparatively less sensitive than E2 and R9. CAiPi induced 53BP1NB in a statistically significant manner in G7 and R15 GSC and bulk cells, compared to vehicle control. In G7, more 53BP1NBs were induced in bulk than in GSCs after CAiPi treatment (8 [95% CI: 8, 9] versus 4 [95% CI: 4,5]). This was an opposite relationship to E2 and R9 53BP1NB induction but was in keeping with G7 sensitivity profiles. R15 displayed no statistically significant differences between the median number of 53BP1NB induced in GSC and bulk with a median of 3 for both. However, the 75th percentile of 53BP1NB was greater in the bulk cell line than in GSCs (6 versus 5), suggesting there may be a small population of R15 bulk cells with an increase in 53BP1NB. Taken together, these studies indicate that induced 53BP1NB is a marker of sensitivity to targeting the RS response.

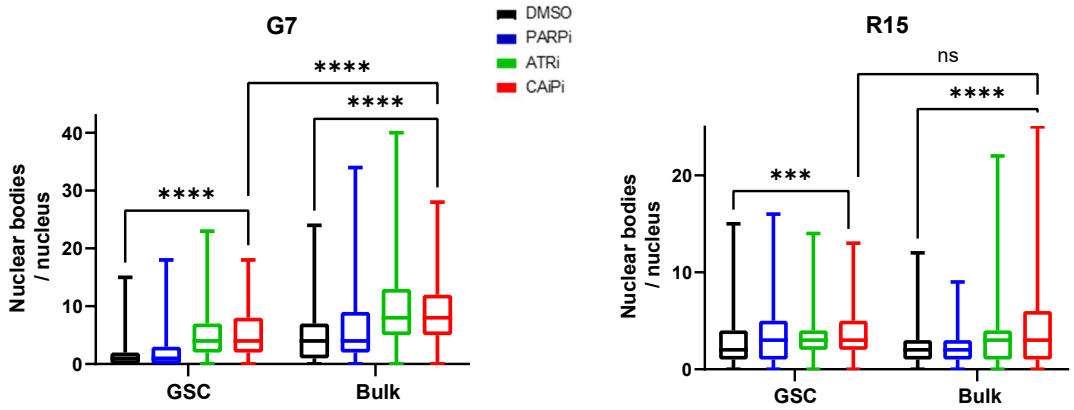

Figure 7.3. 53BP1 nuclear bodies in bulk-sensitive paired cell lines. 53BP1NB per CENP-F negative nucleus were quantified in G7 and R15 paired GSCs and bulk cells after 48-hour incubation with olaparib (1μM), VE821 (5μM), the combination and vehicle control. Box plots were from three independent experiments, representing a minimum of 200 nuclei analysed, adjusted p-values calculated by Kruskal-Wallis one-way analysis of variance with post-hoc Dunn's test (***p<0.001, ****p<0.0001, ns=not significant).

7.3 Inhibition of origin firing rescued CAiPi phenotype

Since we hypothesised that UR-DNA was a marker of response to targeting the RS response and was a consequence of dysregulated origin firing, a causal link between the two was investigated. Similarly to the previous chapter, the CDK inhibitor roscovitine was utilised to reduce dysregulated origin firing. The consequence of reduced dysregulated origin firing on 53BP1NB induction was investigated in CAiPi-sensitive E2 GSCs. Cells were incubated with vehicle, combined VE821 (5μM) and olaparib (1μM), with or without roscovitine at 1μM and 10μM for 24 hours. Immunofluorescence and analysis of 53BP1NB was as previously described in this chapter. Results of roscovitine's effects on 53BP1NB induction are shown in Figure 7.4.

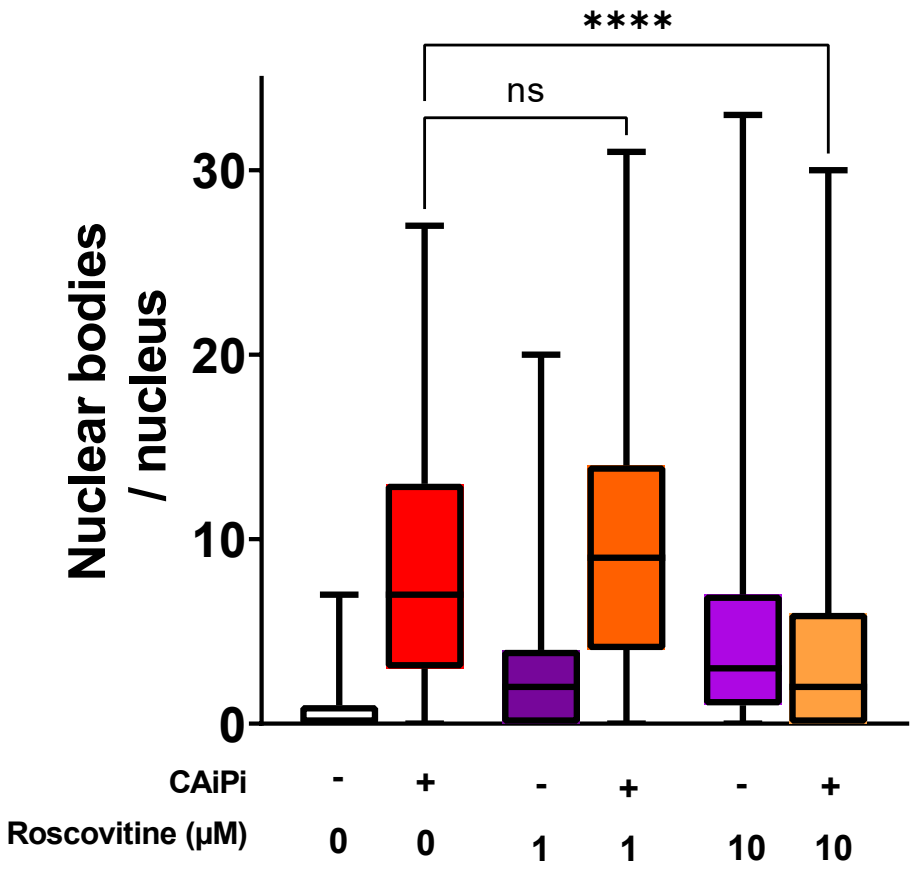

Figure 7.4. Inhibition of origin firing reduced CAiPi-induction of 53BP1NB. 53BP1NBs per CENP-F negative nucleus were quantified in E2 GSCs after 24-hour incubation with combined olaparib (1μM) and VE821 (5μM), plus or minus roscovitine at 1μM or 10μM and vehicle control. Box plots were from two independent experiments, representing a minimum of 100 nuclei analysed, adjusted p-values calculated by Kruskal-Wallis one-way analysis of variance with post-hoc Dunn's test (****p<0.0001, ns = not significant).

As previously described, CAiPi induced 53BP1NB in E2 GSCs versus control. Roscovitine alone at 1μM and 10μM also induced 53BP1NB to form, perhaps broadly due to roscovitine's role as a CDK inhibitor and its effects on cell cycle. Despite this, at 10μM roscovitine significantly reduced CAiPi's ability to induce 53BP1NB, to levels lower than roscovitine alone. Median 53BP1NB per nucleus reduced from 7 [95% CI: 5, 9] to 2 [95% CI: 1, 3] with roscovitine-induced reduction in origin firing. No reduction in CAiPi-induced 53BP1NBs was observed with 1μM roscovitine. To summarise, roscovitine at sufficient concentrations induced partial rescue of 53BP1NB, linking the phenotype of UR-DNA observed in CAiPi-sensitive cell lines to increased origin firing.

7.4 Re-replication in CAiPi-sensitive GSCs

Licensing of replication forks is tightly regulated in normal cells to ensure DNA is accurately and precisely duplicated only once per cell cycle, however an increase in origin firing could be an indicator of relicensing of origins during the same cell cycle. As discussed in Chapter 1, re-replication via relicensing of origins can be a cause of RS and genomic instability. Additionally, Liu et al found that disruption of licensing control and induction of re-replication by CDT1 overexpression induced phosphorylation of Chk1 in an ATR-dependent manner, and loss of ATR induced more re-replication, suggesting a crucial role for ATR in re-replication suppression through S phase checkpoint activities (Liu et al., 2007). Re-replication was therefore analysed post CAiPi treatment in a GSC-sensitive cell line pair due to the many RS implications of re-replication. E2 GSC and bulk cells were incubated with vehicle control, VE821 (5μM), olaparib (1μM) and the combination for 72 hours, before exposure to BrdU (10μM) for one hour. To identify re-replicating cells, they were incubated with FITC-conjugated α-BrdU antibody and PI after ethanol fixation, denaturation of DNA and permeabilisation. Re-replication was defined as BrdU-positive replicating cells, containing >4N DNA content measured by PI. Representative gating strategies for re-replicating cells are shown in Figure 7.5.

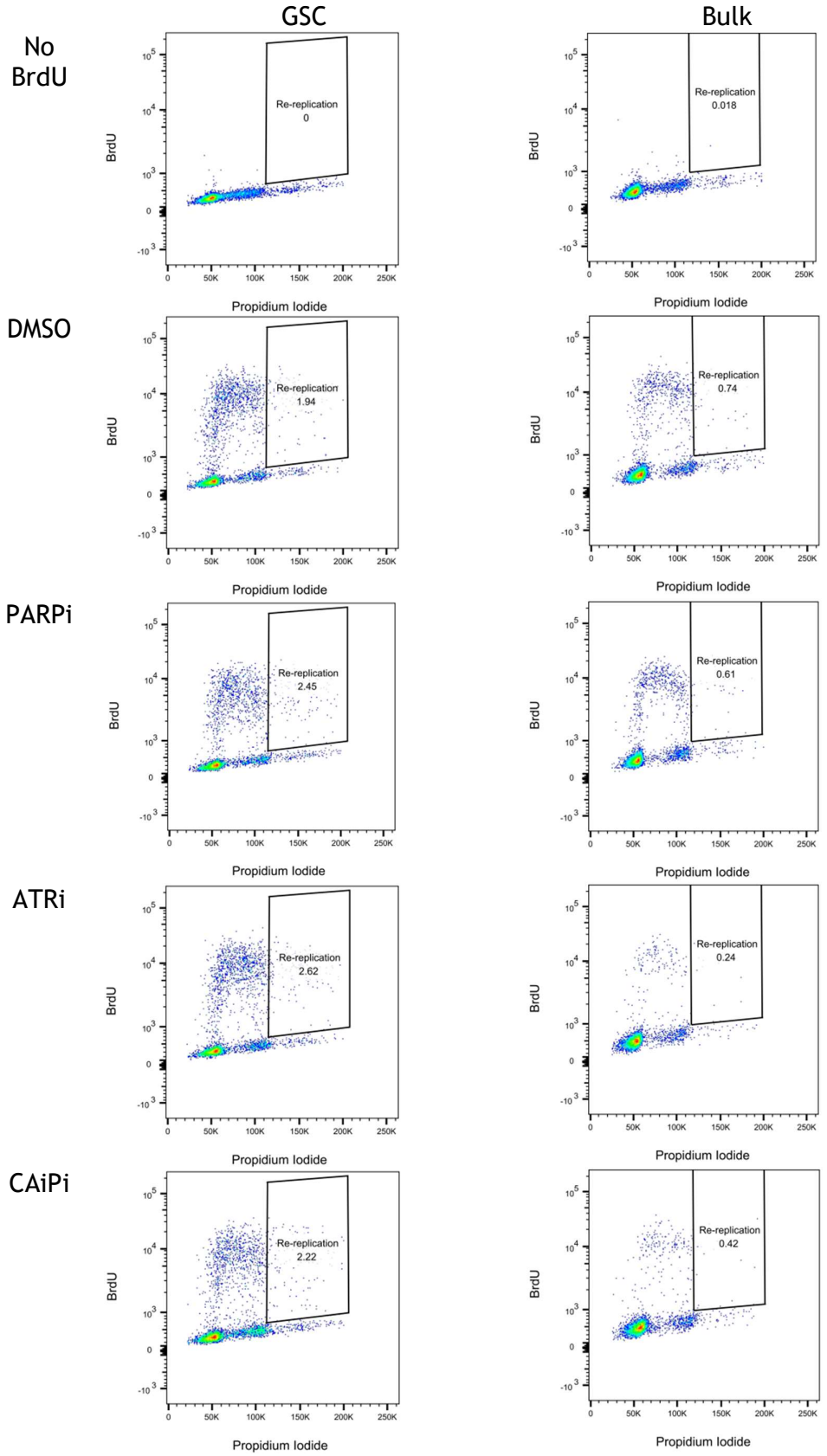

Figure 7.5. Re-replication gating strategies. Representative images of gating of re-replicating cells by BrdU incorporation and >4N DNA content by PI. E2 GSCs and bulk cells were incubated with vehicle control, VE821 (5μM), olaparib (1μM) and the combination for 72 hours. Cells were then incubated with BrdU for one hour following drug exposure, and analysis of DNA content by PI and BrdU was by flow cytometric quantification via BD FACSVerse™ and analysis by FlowJo™.

Quantification of re-replicating cells are shown in Figure 7.6. In CAiPi-sensitive E2 GSCS, there was a statistically significant increase in cells undergoing re-replication, increasing from 1.38% [95% CI: 0.07, 2.69] with vehicle control to 2.33% [95% CI: 2.22, 2.45] after CAiPi treatment. Whereas the more resistant E2 bulk cells displayed a decrease in re-replicating cells after CAiPi exposure, reducing from 0.91% [95% CI: 0.22, 1.59] to 0.45% [95% CI: 0.04, 0.86], although it did not reach significance. There was a much greater proportion of cells undergoing re-replication under CAiPi conditions in GSCs versus bulk (2.33% versus 0.45% respectively). Re-replication in GSCs appears to be an important mechanism of CAiPi treatment sensitivity.

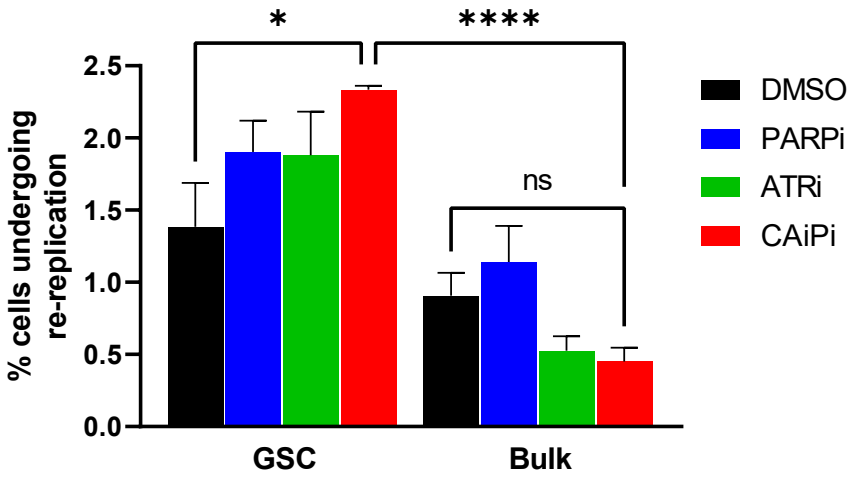

Figure 7.6. Re-replication increased in E2 GSCs. Proportion of re-replicating cells in E2 GSCs and bulk cells after 72-hour incubation with olaparib (1μM), VE821 (5μM), the combination and vehicle control, quantified by flow cytometry as BrdU positive replicating cells with >4N DNA content. Bar plots were from three independent experiments, adjusted p-values calculated by ANOVA with post-hoc Sidak test (*p<0.05, ****p<0.0001, ns=not significant).

7.5 Chromatin bridges are induced in a CAiPi-sensitive manner

Since CAiPi-sensitive GSCs displayed dysregulated origin firing in S phase, it was hypothesised that this would have consequences on DNA and chromosomal stability. UR-DNA can lead to replication intermediates, as summarised in Figure 1.6. Since chromatin bridges are implicated in resolution of UR-DNA intermediates, and chromosome segregation-associated GO terms were highly dysregulated in E2 GSCs (Chapter 5), chromatin bridges were quantified in a panel of GSC and bulk cells to investigate their relevance to mechanisms of sensitivity to CAiPi.

Immunofluorescence of DAPI and therefore visualisation of DNA allowed for identification and quantification of chromatin bridges. Chromatin bridges were analysed in four paired GSC and bulk cell lines; E2 and R9 whose GSC lines were sensitive to targeting the RS response, and G7 and R15 whose bulk cell lines were more sensitive. Cells were incubated with vehicle control, VE821 (5μM), olaparib (1μM) and the combination for 48 hours before fixation and immunostaining with DAPI. Chromatin bridges were identified and counted manually.

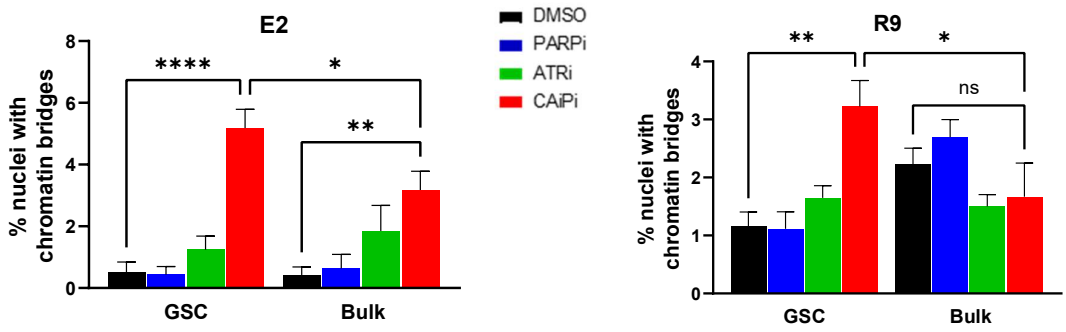

Figure 7.7. Chromatin bridges in GSC-sensitive paired cell lines. Chromatin bridges were quantified in E2 and R9 paired GSCs and bulk cells after 48-hour incubation with olaparib (1μM), VE821 (5μM), the combination and vehicle control. Bar plots were from ≥3 independent experiments, representing a minimum of 200 nuclei analysed, adjusted p-values calculated by ANOVA with post-hoc Sidak test (*p<0.05, **p<0.01, ****p<0.0001, ns=not significant).

CAiPi induced more chromatin bridges to form in GSCs compared to bulk in both E2 (5.18% [95% CI:3.25, 7.11] versus 3.18% [95% CI: 1.24, 5.11]) and R9 (3.22% [95% CI: 1.30, 5.15] versus 1.67% [95% CI: -0.83, 4.16]) (Figure 7.7). This relationship of chromatin bridge induction was in keeping with the sensitivity profiles of these cell lines. There was a statistically significant increase in chromatin bridges with CAiPi over vehicle control in E2 GSCs, R9 GSCs and E2 bulk. R9 bulk showed no change in chromatin bridge frequency with CAiPi.

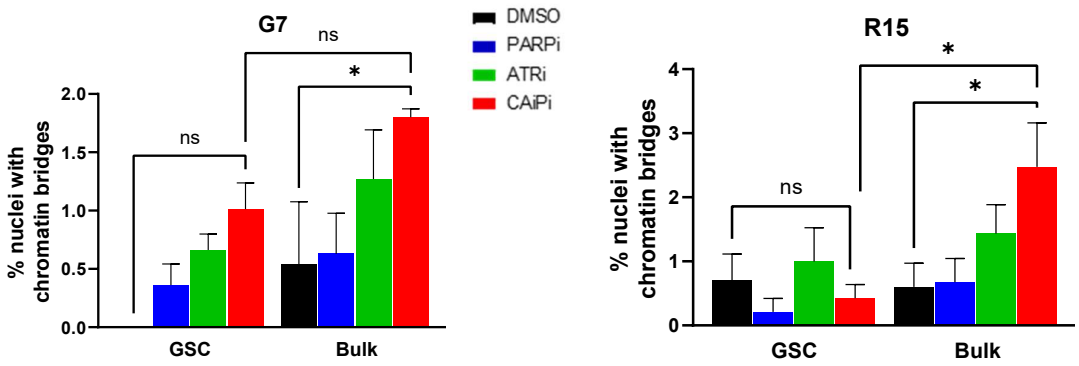

Figure 7.8. Chromatin bridges in bulk-sensitive paired cell lines. Chromatin bridges were quantified in G7 and R15 paired GSCs and bulk cells after 48-hour incubation with olaparib (1μM), VE821 (5μM), the combination and vehicle control. Bar plots were from ≥3 independent experiments, representing a minimum of 200 nuclei analysed, adjusted p-values calculated by ANOVA with post-hoc Sidak test (*p<0.05, ns=not significant).

Both G7 and R15 bulk cell lines displayed a greater frequency of chromatin bridges with CAiPi in comparison to their paired GSCs (Figure 7.8). CAiPi induced 2.47% [95% CI: -0.47, 5.42] of nuclei to form chromatin bridges in R15 bulk versus only 0.42% [95% CI: -0.49, 1.34] in R15 GSC. In G7 bulk, 1.80% [95% CI: 1.49, 2.11] of nuclei formed chromatin bridges, whereas only 1.01% [95% CI: 0.44, 1.98] in G7 GSC, however this difference did not reach statistical significance. Both G7 and R15 bulk cells displayed a statistically significant increase in chromatin bridges after CAiPi exposure compared to vehicle control, whereas their GSCs saw no change or did not reach significance. The pattern of chromatin bridge induction in GSCs and bulk pairings largely follows the same pattern as both under-replication by 53BP1NB analysis and sensitivity to targeting the RS response.

7.6 Micronuclei form under CAiPi conditions

Additionally, chromosomal instability is frequently assessed by the induction of micronuclei as they are a sign of damaged chromosome fragments or whole chromosomes. As discussed in Chapter 1, micronuclei are intrinsically linked to RS and resolution of chromatin bridges. Therefore, their formation after CAiPi exposure was analysed in a panel of paired GBM cell lines. Immunofluorescence of DAPI allowed for identification and quantification of micronuclei. In keeping with chromatin bridge analysis, micronuclei were analysed in four paired GSC and bulk cell lines; E2, R9, G7 and R15. Cells were incubated with vehicle control, VE821 (5μM), olaparib (1μM) and the combination for 48 hours before

fixation and immunofluorescence of DAPI. Micronuclei were identified manually and quantified as a frequency of nuclei exhibiting one or more micronuclei.

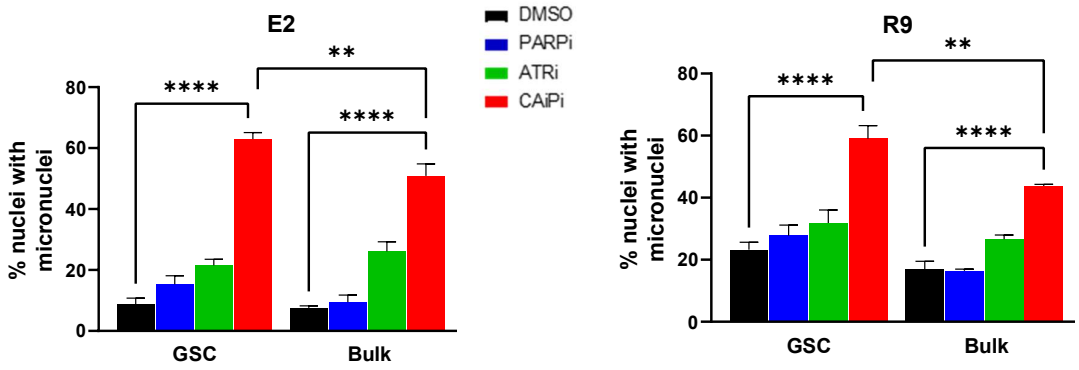

Figure 7.9. Micronuclei in GSC-sensitive paired cell lines. Frequency of nuclei with ≥1 micronuclei were quantified in E2 and R9 paired GSCs and bulk cells after 48-hour incubation with olaparib (1μM), VE821 (5μM), the combination and vehicle control. Micronuclei and nuclei were visualised with DAPI staining. Bar plots were from ≥3 independent experiments, representing a minimum of 200 nuclei analysed, adjusted p-values calculated by ANOVA with post-hoc Sidak test (**p<0.01, ****p<0.0001).

Figure 7.9 displays the results of micronuclei quantification in GSC-sensitive cell lines E2 and R9. CAiPi treatment induced more micronuclei to form in GSCs compared to bulk in both cell lines, in a statistically significant manner. In E2, the difference was 62.9% [95% CI: 56.1, 69.6] in GSCs versus 50.8% [95% CI: 38.3, 63.4] in bulk. The difference between GSCs and bulk cells in R9 was 59.0% [95% CI: 41.0, 77.0] and 43.7% [95% CI: 41.5, 46.0] respectively. E2 and R9 GSCs and bulk cells all had a statistically significant increase in micronuclei after CAiPi treatment versus vehicle control. The increase in micronuclei formation appeared to heavily rely on the combination treatment, as both monotherapies induced only small increases versus control compared to CAiPi, especially in the GSC lines.

Micronuclei formation was also quantified in two cell lines that displayed more sensitivity to targeting the RS response in bulk cell lines compared to GSC and is shown in Figure 7.10. In G7, CAiPi induced more micronuclei in the bulk cell lines (66.0% [95% CI: 45.0, 87.0]) compared to GSCs (38.3% [95% CI: 28.5, 48.2]). R15 bulk also had a greater percentage of micronuclei formed after CAiPi treatment compared to R15 GSC (41.8% [95% CI: 32.4, 51.3] versus 13.7% [95% CI: 9.0, 18.3]). Again, this pattern matched sensitivity profiles, with more sensitive cell lines having increased micronuclei formation post CAiPi-treatment. Similarly

to E2 and R9, both GSC and bulk cells in G7 and R15 showed a statistically significant increase with CAiPi over vehicle control. Although the combination did not increase micronuclei as dramatically over ATRi alone as with E2 and R9. Overall, it appears that micronuclei formation is a marker of CAiPi exposure in all cell lines, and extent of induction correlates with sensitivity to targeting the RS response.

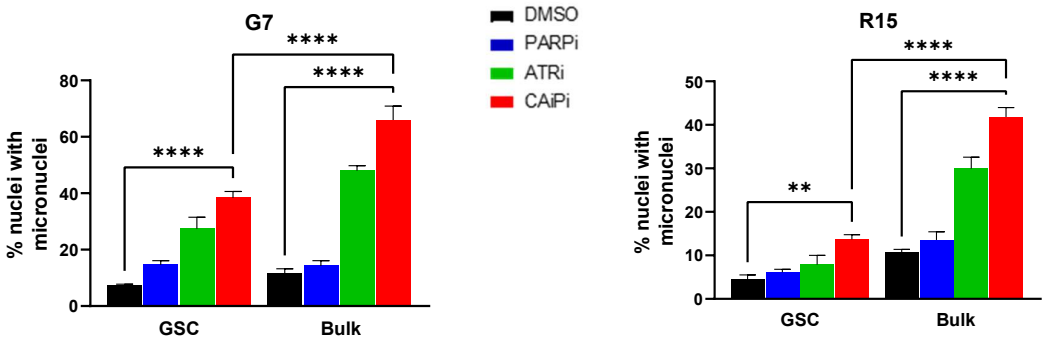

Figure 7.10. Micronuclei in bulk-sensitive paired cell lines. Frequency of nuclei with ≥1 micronuclei were quantified in G7 and R15 paired GSCs and bulk cells after 48-hour incubation with olaparib (1μM), VE821 (5μM), the combination and vehicle control. Nuclei and micronuclei were visualised with DAPI staining. Bar plots were from ≥3 independent experiments, representing a minimum of 200 nuclei analysed, adjusted p-values calculated by ANOVA with post-hoc Sidak test (**p<0.01, ****p<0.0001).

7.7 Cell cycle characterisation following ATR and PARP inhibition

Previous studies have shown that GSCs have a greater proportion of cells in S phase compared to bulk, despite similar proliferation rates, indicating GSCs have slower progression through S phase (Carruthers et al., 2018, Ahmed et al., 2015). Studies of CAiPi on the cell cycle have found an accumulation of cells in G2 phase in response to PARPi, with the addition of an ATRi resulting in the unscheduled release of these cells into mitosis (Kim et al., 2017, Lloyd et al., 2020, Schoonen et al., 2019). Due to the cell cycle checkpoint activities of ATR, changes in cell cycle phases were investigated after 72-hour exposure to vehicle control, VE821 (5μM), olaparib (1μM) and the combination in E2 GSCs and bulk cell cultures. After drug treatment cells were incubated with BrdU (10μM) for one hour before ethanol fixation and denaturation of DNA. Cells were then permeabilised before incubation with FITC-conjugated α-BrdU antibody and PI. Representative cell cycle profiles by DNA content are shown in Figure 7.11.

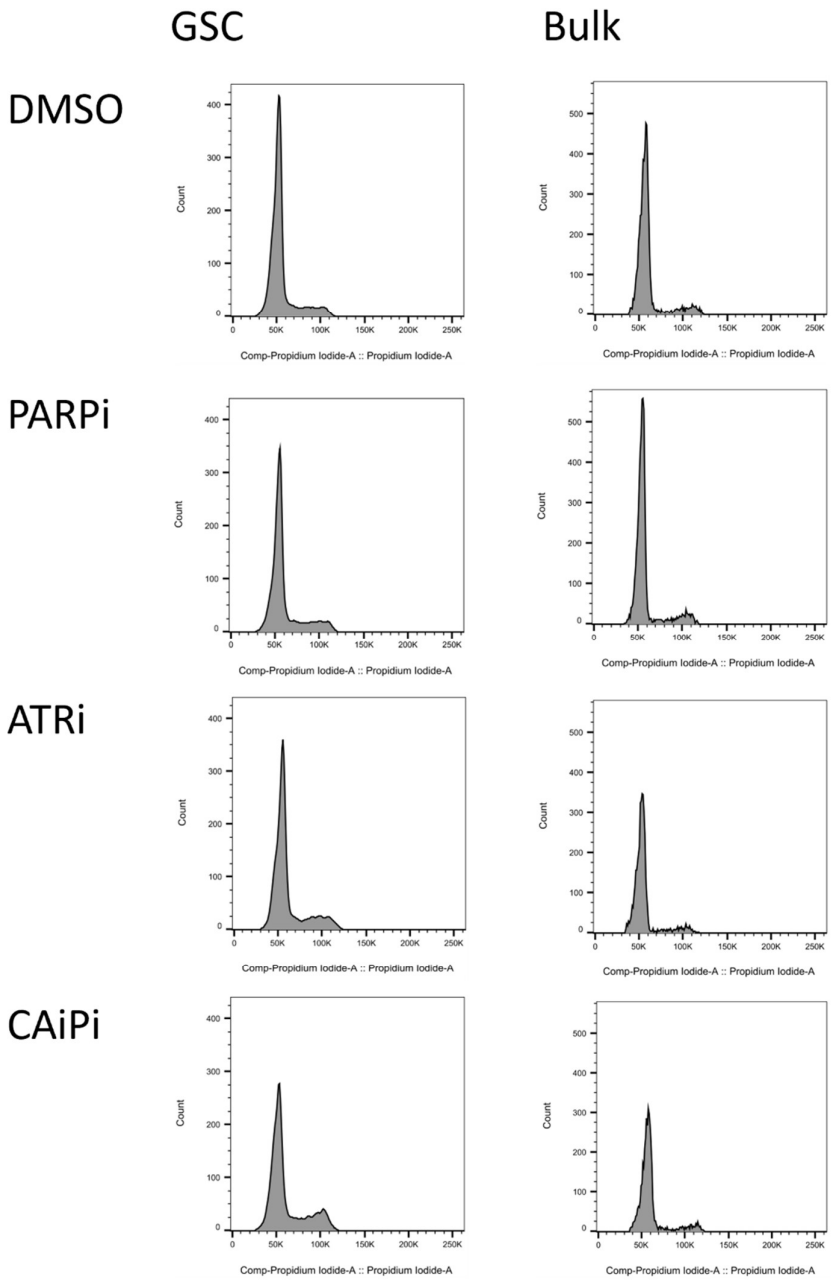

Figure 7.11. E2 GSC and bulk cell cycle profiles in response to ATRi, PARPi and CAiPi. Representative cell cycle profiles of E2 GSC and bulk cultures following 72-hour exposure to VE821 (5μM), olaparib (1μM) and the combination. DNA content analysed by incubation with PI and subsequent flow cytometry on a BD FACSVerse™ and analysis by FlowJo™.

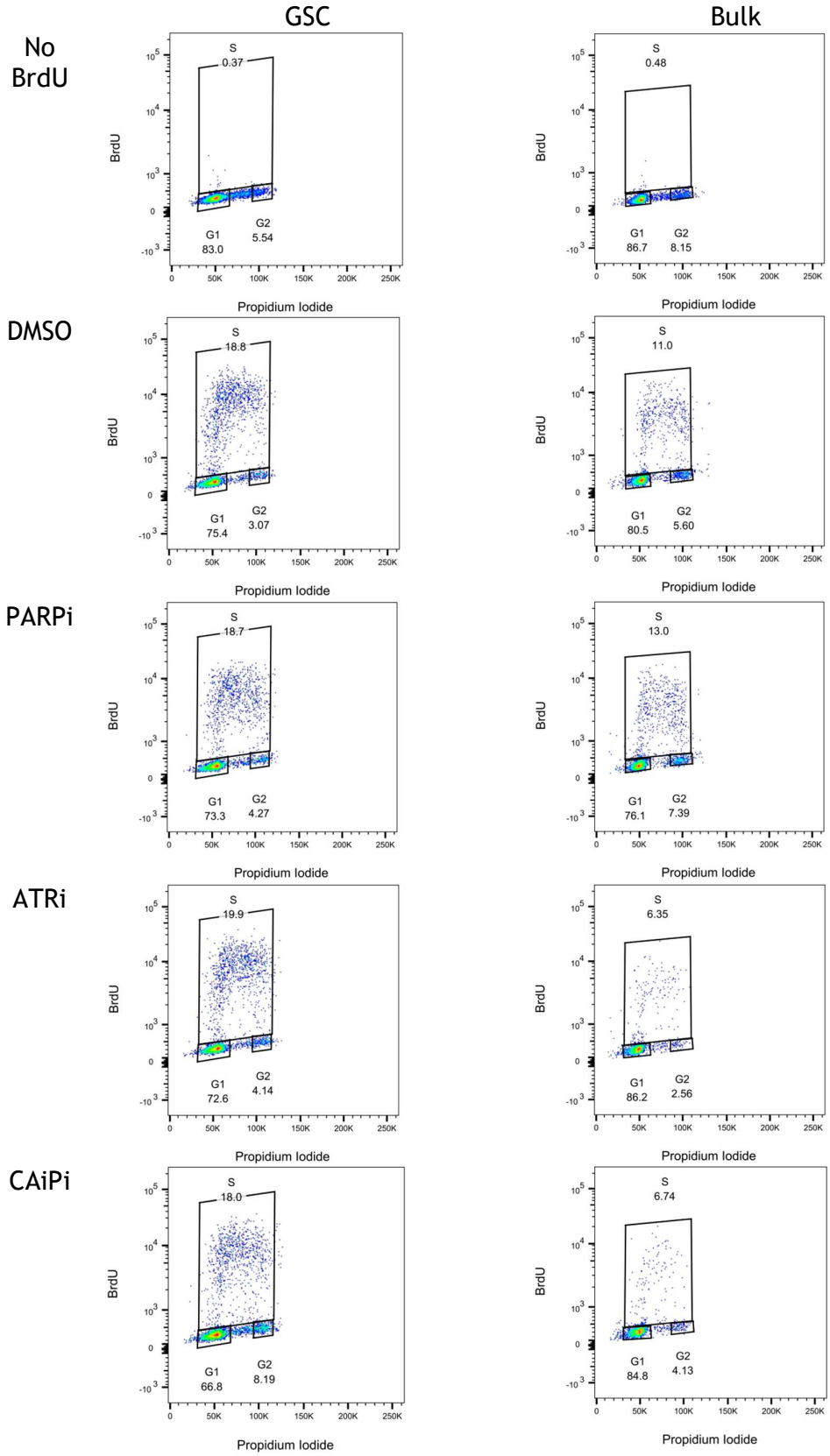

Figure 7.12. Analysis of cell cycle phases by BrdU incorporation in E2 GSCs and bulk cells following ATRi, PARPi and CAiPi. Representative images of gating of active S phase by BrdU incorporation, and G1 and G2 phase by DNA content via PI in E2 GSCs and bulk cells, following 72-hour exposure to VE821 (5μM), olaparib (1μM) and the combination. Cells were incubated with BrdU (10μM) for one hour following drug exposure, and analysis of DNA content by PI and BrdU was by flow cytometric quantification via BD FACSVerse™ and analysis by FlowJo™.

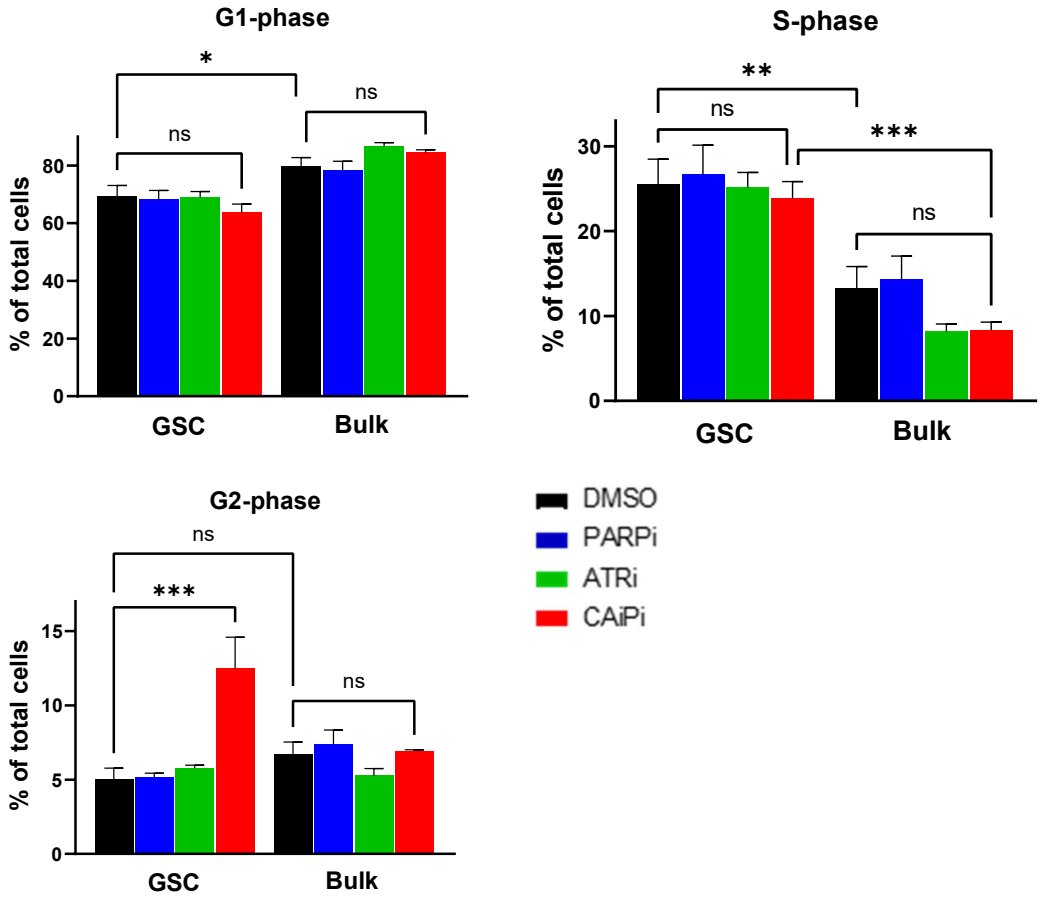

Figure 7.13. Cell cycle phase distribution in E2 GSCs and bulk cells after PARPi, ATRi and CAiPi. Quantification of G1, S and G2 phases in E2 GSCs and bulk cells by flow cytometry, as shown in Figure 7.12. Bar charts represent mean and SEM of 3 independent experiments, adjusted p-values calculated by one-way ANOVA with post-hoc Sidak test (*p<0.05, **p<0.01, ***p<0.001, ns = not significant).

Cell cycle phase proportions were quantified by analysis of BrdU incorporation, to visualise cells in active S phase. Representative BrdU cell cycle profiles and gating strategies are shown in Figure 7.12, and quantification of cell cycle phases shown in Figure 7.13. Proportions of G1 phase cells remained largely unchanged after CAiPi exposure in both GSC and bulk. At baseline, there was a slight increase in bulk cells in G1 phase (79.8% [95% CI: 67.0, 92.6]) compared to GSCs (69.4% [95% CI: 53.7, 85.1]). This deficit in GSCs was made up by an increase of GSCs in active S phase, in keeping with previous reports. In GSCs, 25.6% [95% CI: 13.0, 38.1] were in S phase versus 13.2% [95% CI: 2.0, 24.4] of bulk cells. Although not statistically significant, there appeared to be a small decrease in bulk cells in active S phase after ATRi and CAiPi, which was not observed in GSCs. A statistically significant increase in cells in active S phase under CAiPi conditions was observed in GSCs (23.9% [95% CI: 15.5, 32.3])

compared to bulk (8.3% [95% CI: 4.2, 12.4]). CAiPi induced an increase in G2 phase GSCs compared to control, increasing from 5.0% [95% CI: 1.8, 8.3] to 12.5% [95% CI: 3.3, 21.6]. No difference in G2 was observed in bulk after CAiPi treatment. PARPi did not result in an accumulation of cells in G2 phase.

7.8 Conclusions

This chapter has characterised the dysregulation of replication during S phase in response to CAiPi, to explain differing sensitivities in GSC and bulk pairs. 53BP1NB induction correlated with sensitivity to targeting the RS response, with E2 and R9 GSCs and G7 bulk cells displaying a greater number of 53BP1NB than their paired counterpart in response to CAiPi. CAiPi treatment therefore resulted in UR-DNA, with extent of incomplete DNA synthesis linked to sensitivity to the treatment. This suggests that sensitive GSCs are having to deal with the consequences of RS suffered in the previous cell cycle, and potentially highlights a GSC subtype with a unique DNA replication vulnerability. There does not appear to be a correlation between the number of 53BP1NB at baseline and treatment response. Therefore, baseline levels of UR-DNA did not seem to be predictive of response.

An investigation into the effects of reduced origin firing on 53BP1NB was carried out, since an increase in origin firing via PARPi appeared to be a crucial and novel finding in CAiPi response. When 1μM of roscovitine was added to CAiPi it had no effect on 53BP1NB numbers, however at 10μM there was a significant reduction. The numbers of 53BP1NB did not reduce to control levels with roscovitine, so UR-DNA induction is probably a multifaceted response to cellular stresses. Since 1μM of roscovitine partially rescued the cytotoxic effects of CAiPi but had no effect on 53BP1NB, the extent of origin firing reduction needs to be elucidated at this lower concentration. It may seem counter-intuitive that a reduction in origin firing reduced UR-DNA, but this connection between origin firing and reduced DNA synthesis in response to CAiPi provides a novel mechanism of response to be explored.

CAiPi-sensitive GSCs also showed signs of re-replication. E2 GSCs had an increase in replicating cells that had increased DNA content. It is generally accepted that the BrdU positive cells with >4N are a consequence of re-replication and not

aneuploidy since a broad range of DNA content is observed, as opposed to discrete peaks (Hook et al., 2007). No literature discusses what extent of re-replication is detrimental to the cell, many investigations induce re-replication by overexpression of CDT1 so induce rates of re-replication greater than observed in GSCs here. In E2 GSCs, only 2.33% of cells were showing signs of re-replication with CAiPi, however this was still a statistically significant increase over vehicle control and a large increase over the 0.45% observed in E2 bulk. Additionally, the rate of re-replication in E2 bulk decreased with CAiPi. This opposite response to CAiPi in GSC and bulk cells suggest that cell responses to re-replication, including cell cycle checkpoints, are potentially more intact in E2 bulk. Despite these seemingly low rates of re-replication, cell cycle arrest has been observed in cells with very limited re-replication suggesting that even a small amount of re-replication can induce a cellular response (Green and Li, 2005).

It is well established that both re-replication and under-replication can have devastating effects on cell survival, via genomic instability and DNA damage. Chromatin bridges, an RS DNA damage marker, and micronuclei which is a marker of chromosomal instability, both increased in accordance with sensitivity to targeting the RS response. Therefore, inducing chromosomal and DNA damage via dysregulated replication is a likely mechanism of cell death via CAiPi. No studies have shown both re-replication and under-replication concurrently under CAiPi treatment, but we hypothesise that this total loss of replication coordination is highly detrimental to the cell.

The most striking effect of CAiPi on cell cycle dysregulation was an increase in G2 phase cells in E2 GSCs, which was not seen in E2 bulk. This was despite presumed loss of G2/M checkpoint activation by ATRi and previous reports of reversal of PARPi-induced G2 accumulation by the addition of an ATRi (Kim et al., 2017, Lloyd et al., 2020, Schoonen et al., 2019). It may be that the longer 72-hour exposure to CAiPi resulted in alternative G2/M checkpoint activation, potentially via ATM, for which E2 appears to be wildtype based on WGS analysis in Chapter 3. Accordingly, many of these reports observed this cell cycle checkpoint activation between 8 and 24 hours, and in ATM or BRCA mutant models, so the cell cycle controls in these GSCs may be different. PARPi alone

did not have an effect on G2 accumulation, despite this observation in the aforementioned studies, however this may again be in part due to the mutational backgrounds of their models, as Jette et al also observed a PARPi-induced G2 accumulation in an ATM mutant model but not in a wild type model, including at 72 hours and with 4μm olaparib (Jette et al., 2019). There was an increase in E2 GSCs still undergoing S phase replication compared to E2 bulk under CAiPi conditions. Since CAiPi activities are largely focused during S phase, it could be hypothesised that this difference in S phase exposure is exacerbating S phase dysregulation and subsequent genomic instability in sensitive GSCs.

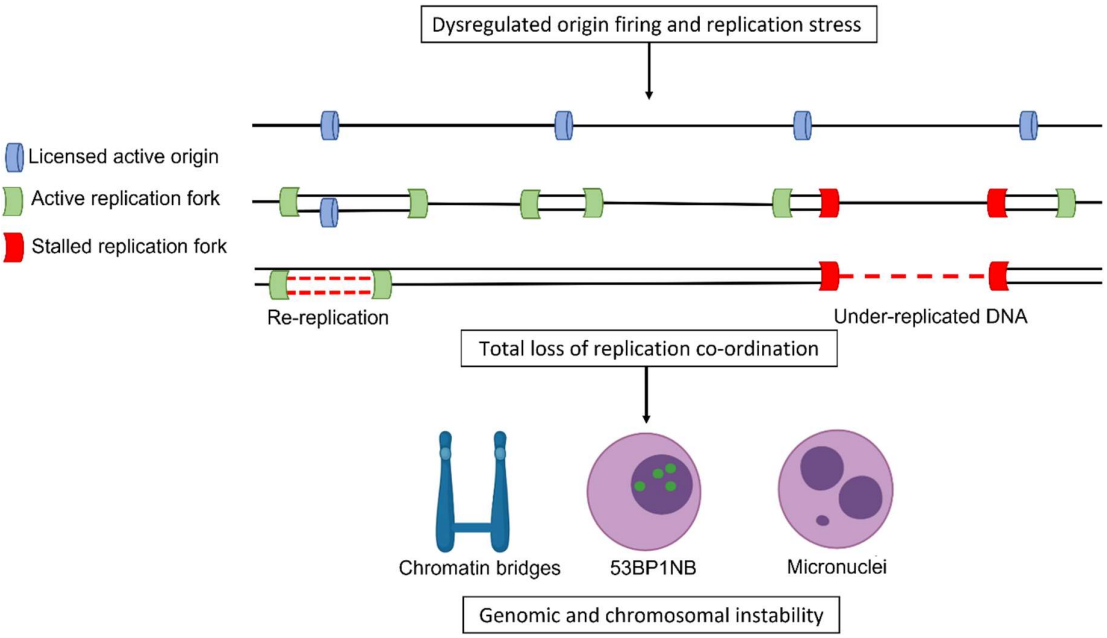

Figure 7.14. Mechanisms of CAiPi action working hypothesis. CAiPi induces dysregulated origin firing and increased replication stress, leading to both re-replication and under-replication of DNA in GSCs with increased sensitivity to targeting the RS response. This leads to genomic and chromosomal instability, measured via chromatin bridges, 53BP1NB and micronuclei, a proposed mechanism of cell death. Created in part using BioRender.

This chapter has characterised the total loss of S phase coordination by CAiPi, primarily in GSCs with increased sensitivity to targeting the RS response. In keeping with the hypothesis proposed at the start of this chapter, this loss of S phase regulation can be linked to the previously reported increase in origin firing. Additionally, cells with loss of S phase coordination also have evidence of increased chromosomal damage. This working hypothesis is summarised in Figure 7.14. This supports the hypothesis that this accumulation of detrimental damage and genomic instability is resulting in GSC-specific cell death and differing sensitivities.

Chapter 8 Investigations of transcriptional predictors of CAiPi sensitivity

8.1 Introduction

There is a lack of robust transcriptional signatures or genomic biomarkers correlated with CAiPi response in GSCs. Several markers of PARPi sensitivity and ATRi sensitivity have been described in a range of cancer types, as discussed in Chapter 1, however their applicability to CAiPi sensitivity in GSCs appeared to be limited, as discussed in Chapter 4. We aimed to investigate a novel signature of response directed by mechanistic in vitro studies. Previously this thesis has found that dysregulated replication is a key feature of GSCs sensitive to targeting the RS response, namely via UR-DNA, re-replication and dysregulated origin firing. It was hypothesised that dysregulated replication in sensitive GSCs would correspond with transcriptional aberrations. Therefore, a literature search was carried out to identify key factors in all these cellular processes. Gene expression of candidate genes, based on in vitro investigations, were investigated at baseline in GSCs and bulk cells and a collective gene signature curated and investigated for its ability to predict CAiPi-sensitivity in GSCs. The gene signature was also assessed for its ability to predict survival in publicly available RNAseq datasets.

8.2 CMG complex origin firing genes upregulated in GSCs sensitive to targeting the RS response

As discussed in Chapter 1 and summarised in Figure 8.1, replication initiation requires origin licensing and subsequent origin firing. Briefly, the ORC binds to origins of replication and recruits CDT1 and CDC6, which in turn directs the loading of the six subunit MCM complex. This forms an inactive helicase known as the pre-RC and the origin is licensed. Surplus origins of replication are licensed throughout the genome, and only once activated does it initiate replication. Origin firing and activation of the pre-RC occurs after formation of the CMG complex, consisting of Cdc45, the MCM proteins and the GINS complex comprising of four subunits. All factors of the CMG complex are essential for replication initiation and mutually dependent for CMG formation (Moyer et al., 2006, Miyazawa-Onami et al., 2017). Although essential for replication initiation,

overexpression of MCM had no effects on replication timing, suggesting that MCM levels are not rate limiting (Dukaj and Rhind, 2021). However, both Cdc45 and the GINS complex have been found to be important limiting factors on replication initiation (Kohler et al., 2016, Aparicio et al., 2009). Although an important part of replication licensing, Yeeles et al found that ORC proteins, CDC6 and CDT1 were not essential for initiation after MCM has loaded (Yeeles et al., 2015). Due to the crucial role of CMG complex formation in replication initiation, an 11 gene CMG complex signature was curated to investigate the transcriptional activities of origin firing factors in GSC and bulk cells.

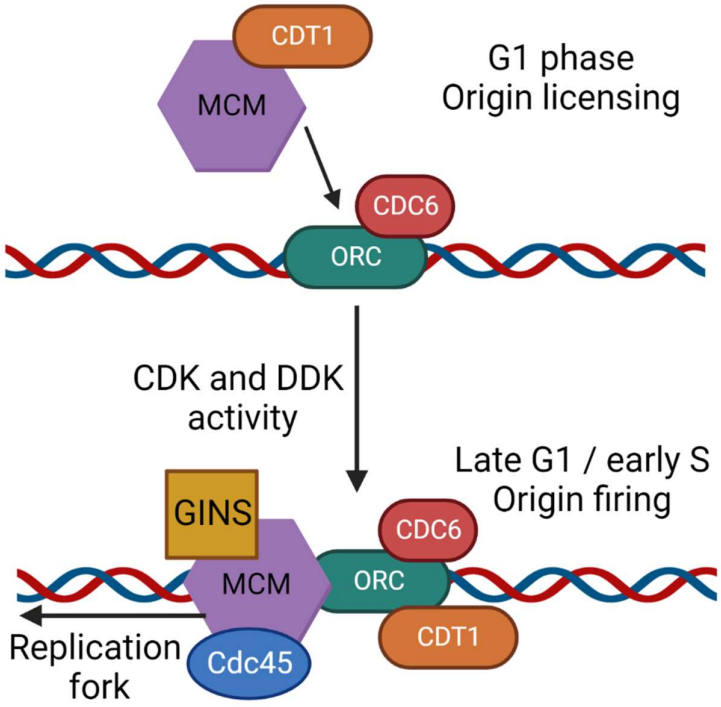

Figure 8.1. Origin licensing and origin firing by CMG formation. Origin licensing occurs in G1 phase. ORC binds to origins of replication, and the origin becomes licensed through recruitment of the six subunit MCM complex and CDT1, facilitated by CDC6. Surplus origins are licensed throughout the genome, and only a subset become activated in late G1 and early S phase through cell cycle-dependent fluctuations in CDK and DDK levels. An origin becomes activated, resulting in origin firing, through recruitment of Cdc45 and GINS complex to the MCM complex, forming the active CMG complex helicase and replication fork. Created using BioRender.

Scaled gene expression of Cdc45, MCM 2-7 and GINS 1-4 was analysed in E2, R10 and G7 GSC and bulk pairs, as shown in Figure 8.2. Seven of the CMG genes were significantly upregulated in E2 GSCs versus E2 bulk, only GINS 2-4 and MCM5 did not reach significance. The origin firing genes GINS1, GINS4, MCM2 and MCM4 were all significantly upregulated in R10 GSCs versus R10 bulk. There were no

statistically significant differences in any of the CMG genes between G7 GSCs and bulk cells. An increase in CMG gene signature expression appeared to predict GSC and bulk sensitivity to targeting of the RS response, since E2 GSCs were more sensitive than E2 bulk, R10 had no statistically significant difference between GSC and bulk sensitivities but trended towards more sensitive GSCs and G7 GSCs were less sensitive than their paired bulk cell lines, as discussed in Chapter 4 and summarised in Figure 8.3.

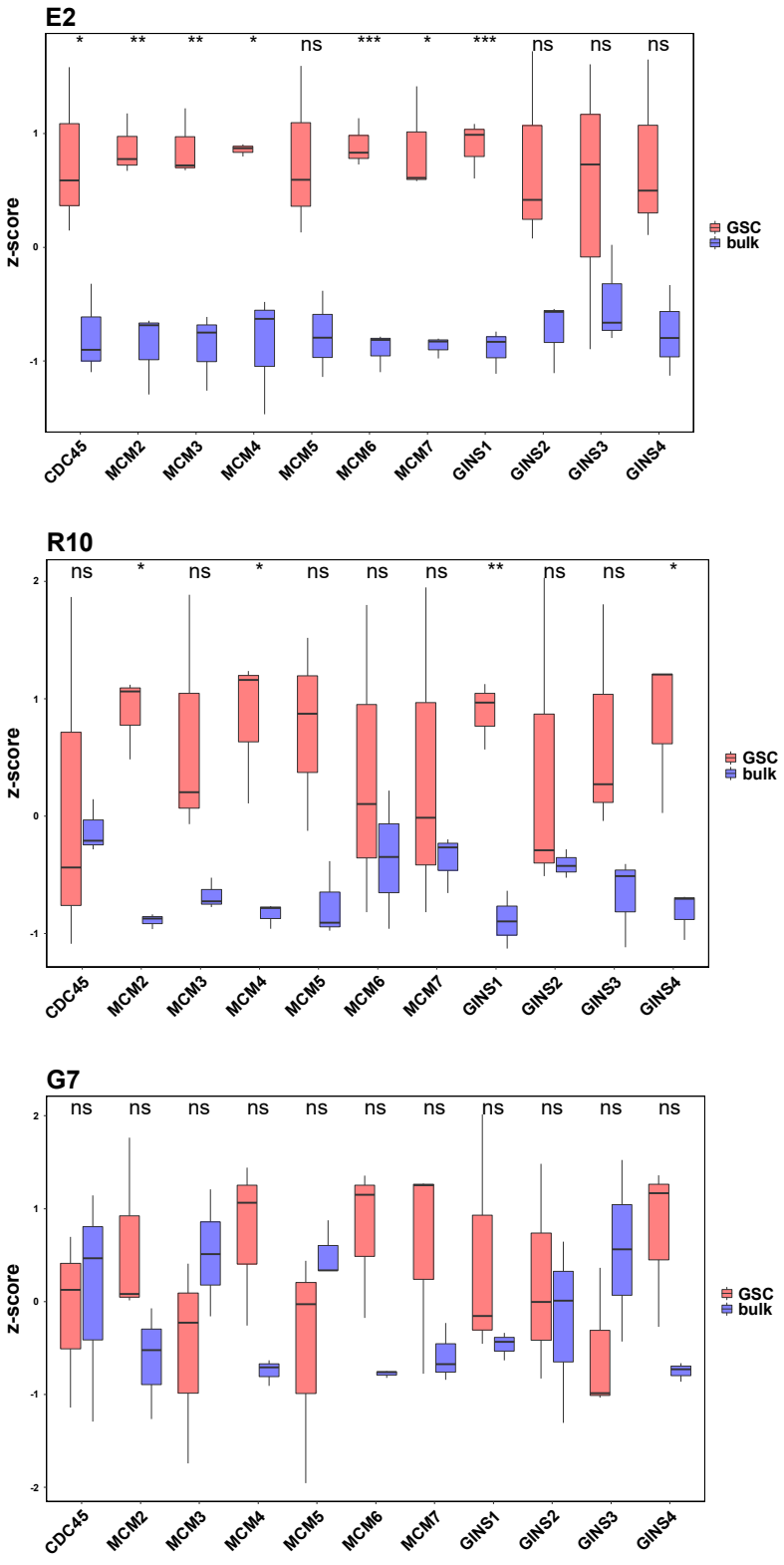

Figure 8.2. Transcriptional alterations between GSC and bulk cells of CMG complex origin firing factors. Baseline gene expression was analysed in E2, R10 and G7 paired GSC and bulk cells. RNA was extracted from cells before RNA sequencing and data processing. Count data was normalised using 'DeSeq2' and scaled to produce a z-score which was used to compare gene expression across the 11 gene CMG complex signature. Box plots represent data from 3 independent experiments, p-values calculated by T test using 'ggpubr' package in R (*p<0.05, **p<0.01, ***p<0.001, ns=not significant).

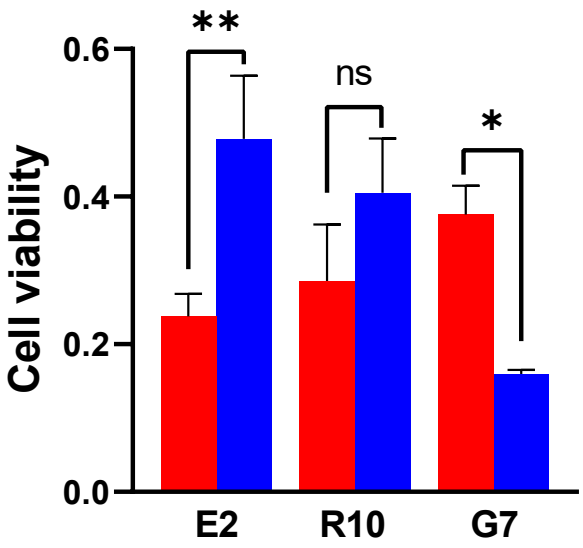

Figure 8.3. E2, R10 and G7 GSC and bulk CAiPi sensitivity. Summary of cell viability results from Chapter 4. Average cell viability in E2, R10 and G7 primary GSC and bulk cell lines was analysed using CellTiter-Glo® after six-day exposure to combined VE821 (5μM) and olaparib (1μM), relative to DMSO vehicle control. Cell viability in E2 and R10 was carried out previously by K. Strathdee. Bar charts represent mean and SEM of ≥3 independent experiments, adjusted p-values calculated by one-way ANOVA with post-hoc Sidak test (*p<0.05, **p<0.01, ns=not significant).

8.3 Upregulated re-replication factors in CAiPi-sensitive GSCs

Next, to investigate the underlying mechanism of GSC-associated re-replication in E2, the re-replication transcriptomic machinery was analysed in E2, R10 and G7 GSCs and bulk cells. Studies have shown that geminin is crucial for preventing relicensing and CDT1-induced re-replication (Vaziri et al., 2003). Additionally, they found that overexpression of CDC6, which cooperates with CDT1, induced subtle re-replication. Overexpression of both CDT1 and CDC6 increased re-replicating cells further. Subsequently, CDT1 and/or CDC6 overexpression is widely used to induce exogenous re-replication.

Overexpression of CDT1 or CDC6 was not investigated in this thesis, however baseline expression levels of both these re-replication factors were analysed from RNAseq data of GSC and bulk pairs in Figure 8.4, and LFC listed in Table 8.1. Baseline expression levels of these genes were analysed in E2, for which it is known that GSCs undergo more re-replication than bulk after CAiPi. Their expression was also assessed in R10 and G7. CDC6 was significantly increased in E2 GSCs compared to bulk, and neared significance for CDT1 (p=0.06). Both

genes exhibited the largest LFC increase in GSCs compared to paired bulk in E2, in comparison to R10 and G7. In R10, only CDC6 was significantly upregulated in GSCs compared to bulk. CDT1 had a LFC of 0.38 but did not reach significance. Furthermore, in G7, which is the most resistant of the three GSCs and the only cell line pair where GSC were more resistant to targeting of the RS response than its paired bulk counterpart, there was no significant differences between GSCs and bulk cells, and LFC were only 0.25 for CDC6 and -0.03 for CDT1. Additionally, comparison of CDT1 expression in all three GSC lines in Figure 8.5 found that E2 GSCs had higher expression than R10 and G7, therefore CDT1 expression correlated with sensitivity.

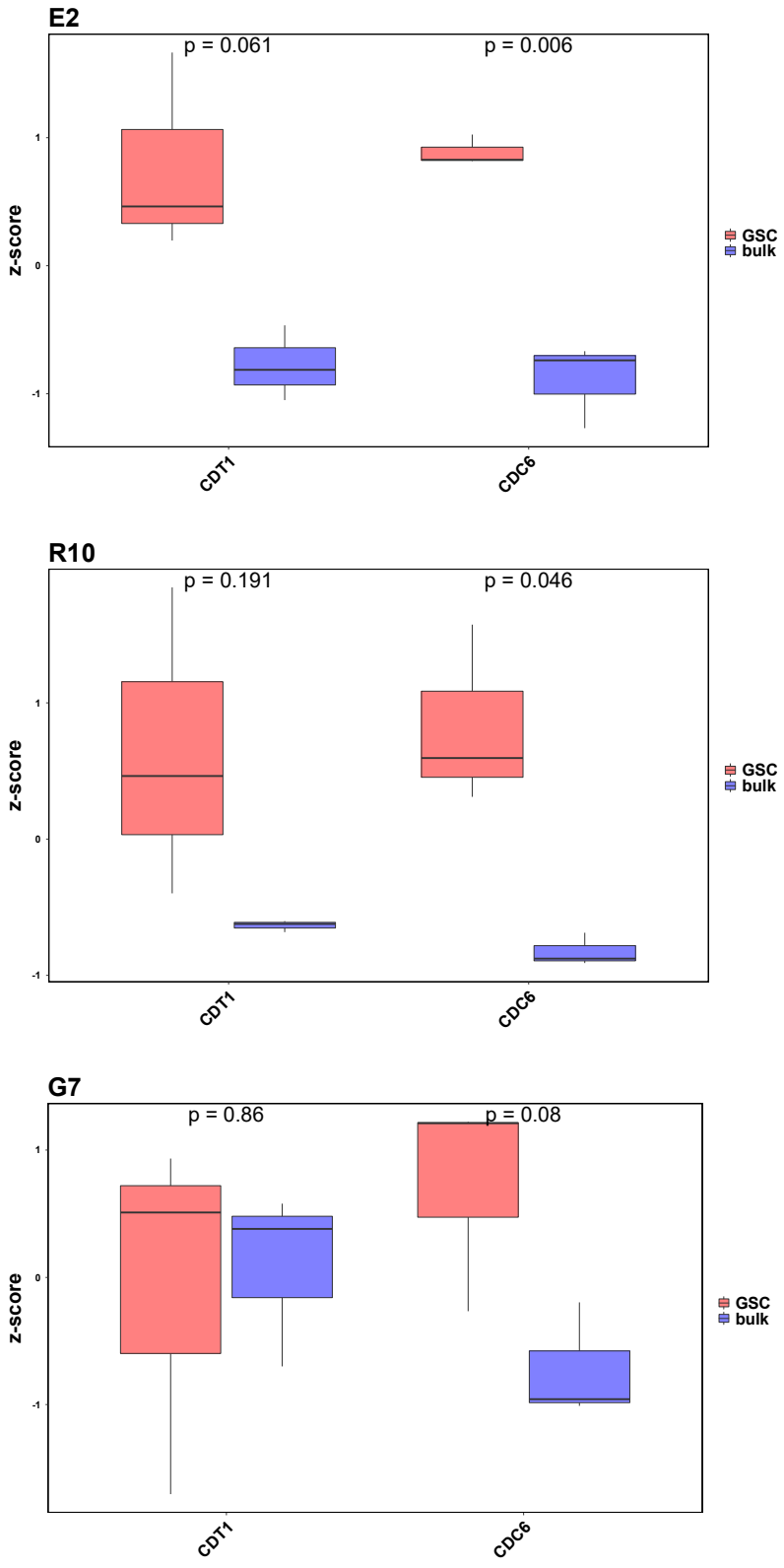

Figure 8.4. Increased replication factor expression in E2 GSCs. Baseline gene expression for CDT1 and CDC6 was analysed in E2, R10 and G7 paired GSC and bulk cells. RNA was extracted from cells before RNA sequencing and data processing. Count data was normalised using 'DeSeq2' and scaled to produce a z-score which was used to compare gene expression. Box plots represent data from three independent experiments, p-values calculated by T-test using 'ggpubr' package in R.

Table 8.1. Differential re-replication factor expression measured by LFC in GSC versus bulk.

	CDT1	CDC6
E2	0.60	0.60
R10	0.38	0.45
G7	-0.03	0.25

LFC for CDT1 and CDC6 gene expression between GSC and bulk cells was quantified by 'DeSeq2' package in R, comparing normalised count data.

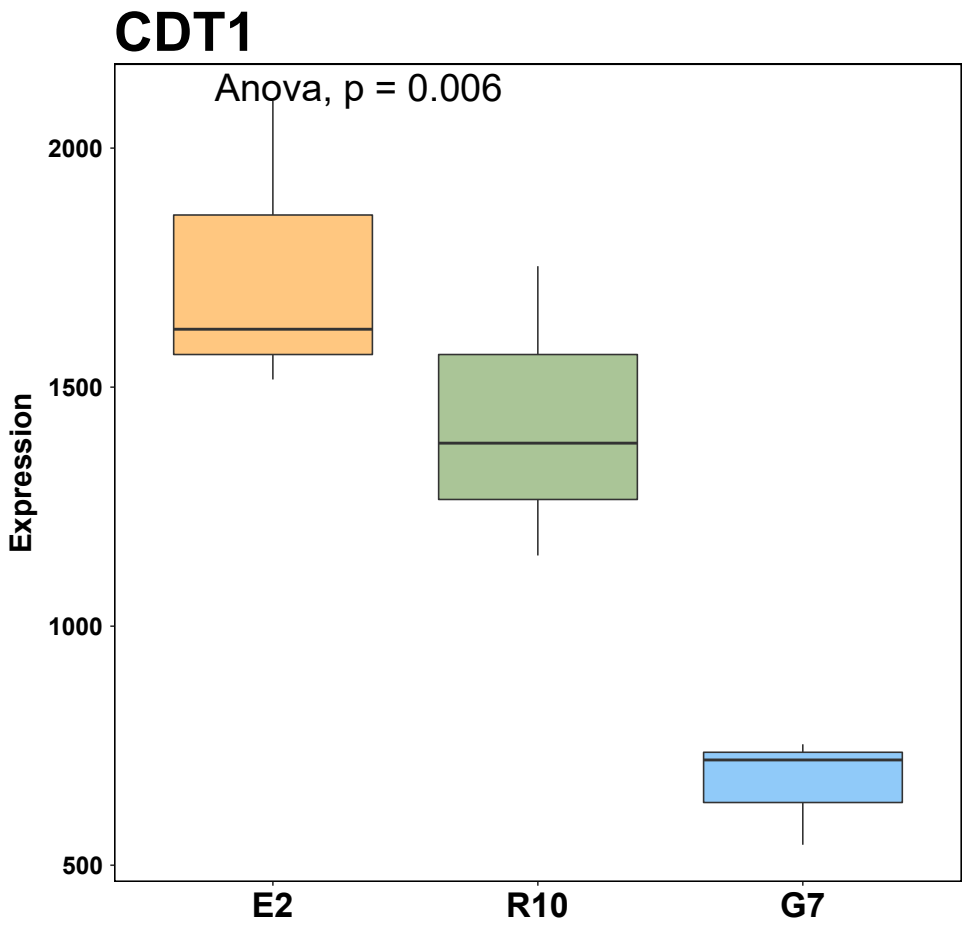

Figure 8.5. CDT1 expression in GSCs. Baseline gene expression for CDT1 was analysed in E2, R10 and G7 GSCs. RNA was extracted from cells before RNA sequencing and data processing. Count data was normalised using 'DeSeq2' to produce a median of ratios. Box plots represent data from three independent experiments, p-value calculated by one-way ANOVA, using the 'ggpubr' package in R.

8.4 Under-replication factors upregulated in CAiPi-sensitive GSCs

Lastly, investigations of CAiPi mechanisms of sensitivity in Chapter 7 found that CAiPi-sensitive GSCs were experiencing under-replication of DNA, a likely cause of observed chromosomal instability and mis-segregation via chromatin bridges and micronuclei. Underlying many investigations of UR-DNA is its localisation at

CFS and its resolution by MiDAS. Studies have shown that treatment with low dose aphidicolin to induce RS leads to mitotic chromosome breaks and also nascent MiDAS (Minocherhomji et al., 2015). These sites of MiDAS have been found to colocalise with FANCD2 foci and BLM-associated FS-UFB, marking CFS within the chromosome (Minocherhomji et al., 2015, Chan et al., 2009).

Since GSCs experience increased endogenous RS, and CAiPi-sensitive GSCs had increased chromatin bridging, micronuclei and 53BP1NB, it was hypothesised that this response to RS-associated UR-DNA at CFS was underpinning CAiPi-sensitivity. Therefore, investigations into gene expression of several key MiDAS and FS-UFB factors were carried out to predict sensitivity to RS-targeting therapies, which were discussed in detail in Chapter 1 and summarised in Figure 1.6.

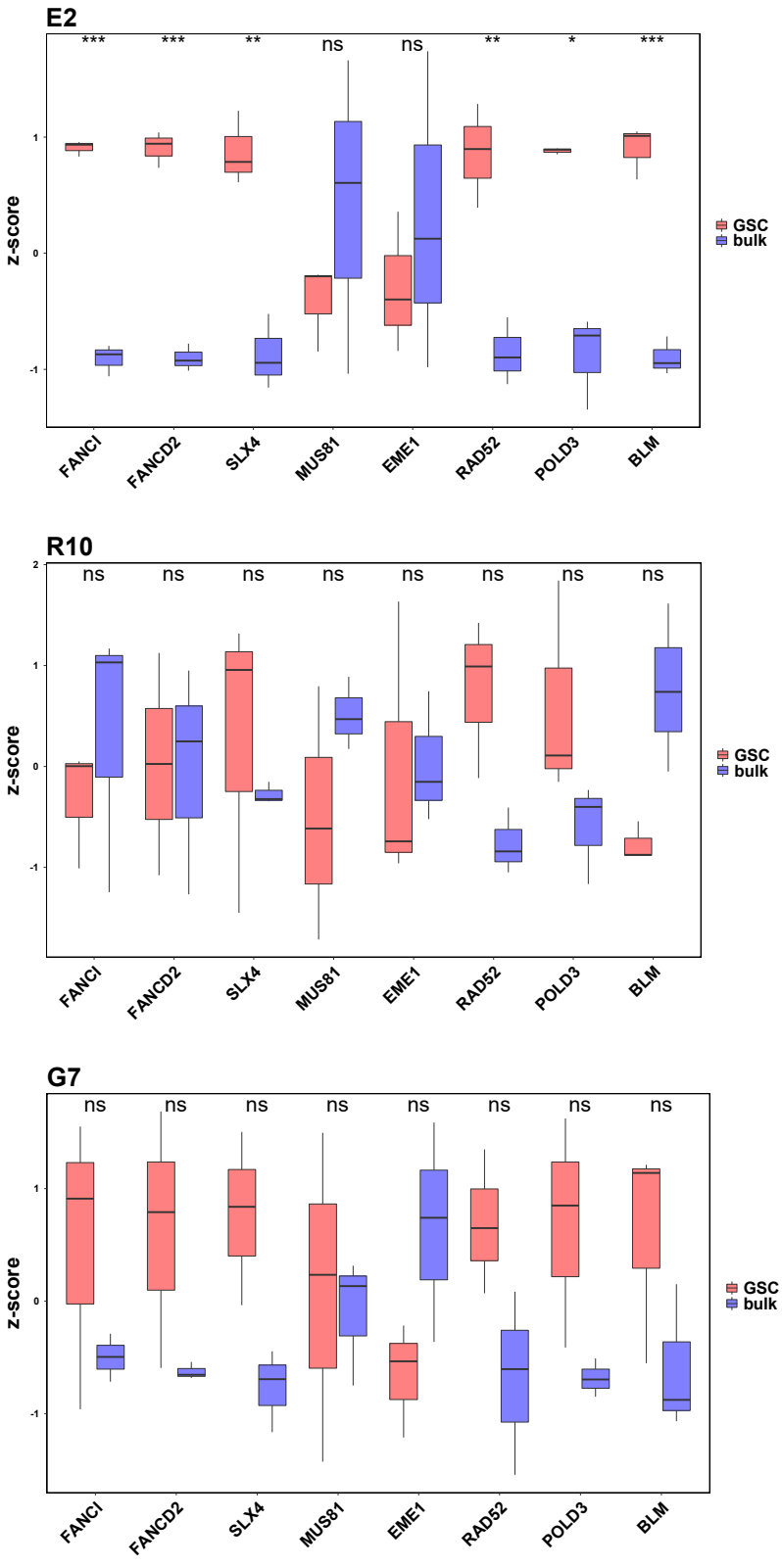

Figure 8.6. Differential expression of UR-DNA resolution-associated factors in GSC and bulk cells. Baseline gene expression was analysed in E2, R10 and G7 paired GSC and bulk cells. RNA was extracted from cells before RNA sequencing and data processing. Count data was normalised using 'DeSeq2' and scaled to produce a z-score which was used to compare gene expression across the eight gene signature. Box plots represent data from three independent experiments, p-values calculated by T test using 'ggpubr' package in R (*p<0.05, **p<0.01, ***p<0.001, ns=not significant).

Gene transcription was analysed in E2, R10 and G7 GSC and bulk pairs, after RNA extraction, sequencing and processing. Transcription of FANCI, FANCD2, SLX4, MUS81, EME1, RAD52, POLD3 and BLM was analysed and comparisons of scaled gene expression between GSC and bulk pairs are shown in Figure 8.6. All genes had a statistically significant increase in CAiPi-sensitive E2 GSC scaled expression over E2 bulk, except MUS81 and EME1. There was no significant difference between GSC and bulk pairs for R10 and G7 for expression of any of the eight genes.

8.5 CAiPi transcriptional signature of response

This chapter has discovered a general trend towards larger differences in gene expression between GSC and bulk cells in cell lines displaying increased sensitivity to targeting the RS response, for curated gene sets based on *in vitro* discoveries. These gene sets, based on origin firing, re-replication and responses to under-replication were therefore combined to create a 21 gene set, to assess their combined ability to predict CAiPi sensitivity. LFC between GSC and bulk pairs was quantified from normalised gene expression data, and hierarchical clustering of the 21 genes and cell lines was analysed (Figure 8.7). As expected from individual gene expression analysis, E2 had the greatest overall increase in candidate gene expression in GSCs versus bulk, only two genes had a negative LFC. R10 displayed a general trend towards increased expression in GSCs, but smaller LFCs were observed between GSC and bulk and more genes with a negative LFC were observed compared to E2. G7 showed the smallest LFC generally across the 21 candidate genes, both positive and negative. This was in keeping with E2 GSCs being more sensitive than E2 bulk, R10 GSCs and bulk having no significant differences and G7 GSCs being more resistant than their paired GSCs, as summarised in Figure 8.3.

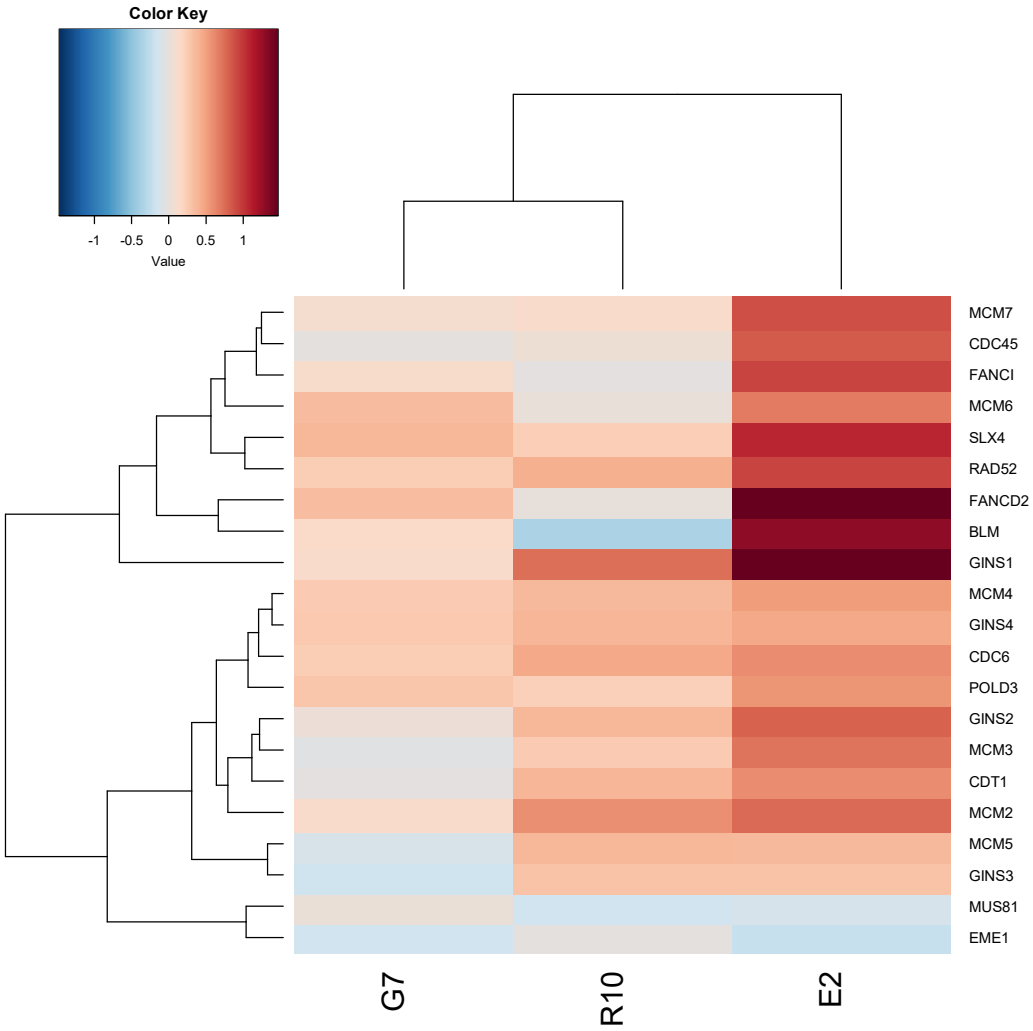

Figure 8.7. Heatmap of LFC between GSC and bulk expression across the 21 gene set. LFC for the 21 genes in the curated signature between GSC and bulk cells was quantified by 'DeSeq2' package in R, comparing differences in normalised count data. LFC was displayed in a heatmap, using the 'heatmap.2' package in R, to show hierarchical clustering between both genes and cell lines.

Since differences between GSC and bulk gene expression in a tumour cannot be readily assessed when stratifying patients by a proposed biomarker, a signature score was quantified by ssGSEA using the 'GSVA' package in R, which implements a single-sample gene-set enrichment method. Figure 8.8 shows the signature score for E2, R10 and G7 paired GSC and bulk cell lines. E2 displayed a statistically significant increase in signature score for GSC versus bulk, and also had the largest difference between the two cell types out of the three cell lines. R10 also had a statistically significant increase in signature score for GSC versus bulk, but no difference was observed for G7. The signature score was similar between E2 and R10 GSCs, in keeping with similar sensitivities between the two GSCs. However, both E2 and R10 GSCs had a statistically significant increase in

signature score compared to G7 GSC, in keeping with G7 GSC being relatively more resistant to CAiPi.

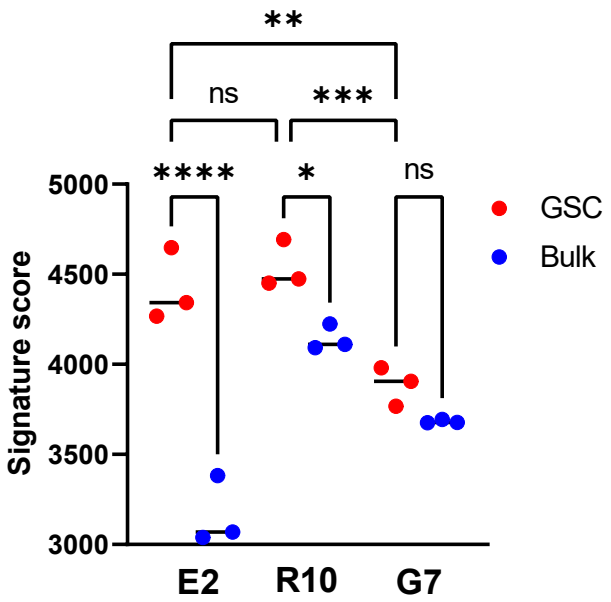

Figure 8.8. Signature score for gene set enrichment across GSC and bulk pairs. Signature score was quantified using ssGSEA in the 'GSVA' package in R, to assess enrichment of the curated 21 gene signature within each cell line. Adjusted p-values calculated by one-way ANOVA with post-hoc Sidak test (*p<0.05, **p<0.01, ***p<0.001,****p<0.0001, ns=not significant).

8.6 Transcriptional signature predicts survival in clinical patients

This chapter has shown that a curated 21 gene signature based on mechanistic studies can predict cell sensitivity to targeting the RS response. To investigate the clinical relevance of this signature and determine if it could identify a subset of GBM patients that may benefit from CAiPi treatment, survival analysis was carried out using the CGGA (Chinese Glioma Genome Atlas) database (Zhao et al., 2021). The CGGA database includes RNAseq data for 374 primary GBM patients with associated clinical data.

To analyse the effect of individual gene expression on patient survival, hazard ratios were calculated for all genes in the RS response signature. Analysis of the risk of individual candidate gene expression on survival of CGGA patients was assessed using the 'survivalAnalysis' package. Figure 8.9 shows the forest plot of candidate genes with associated hazard ratios. Only expression of GINS3 and CDC6 produced a statistically significant hazard ratio of 0.81 and 1.40

respectively. All other genes had non-significant hazard ratios that trended closer to one, suggestive of little to no effect on patient survival alone.

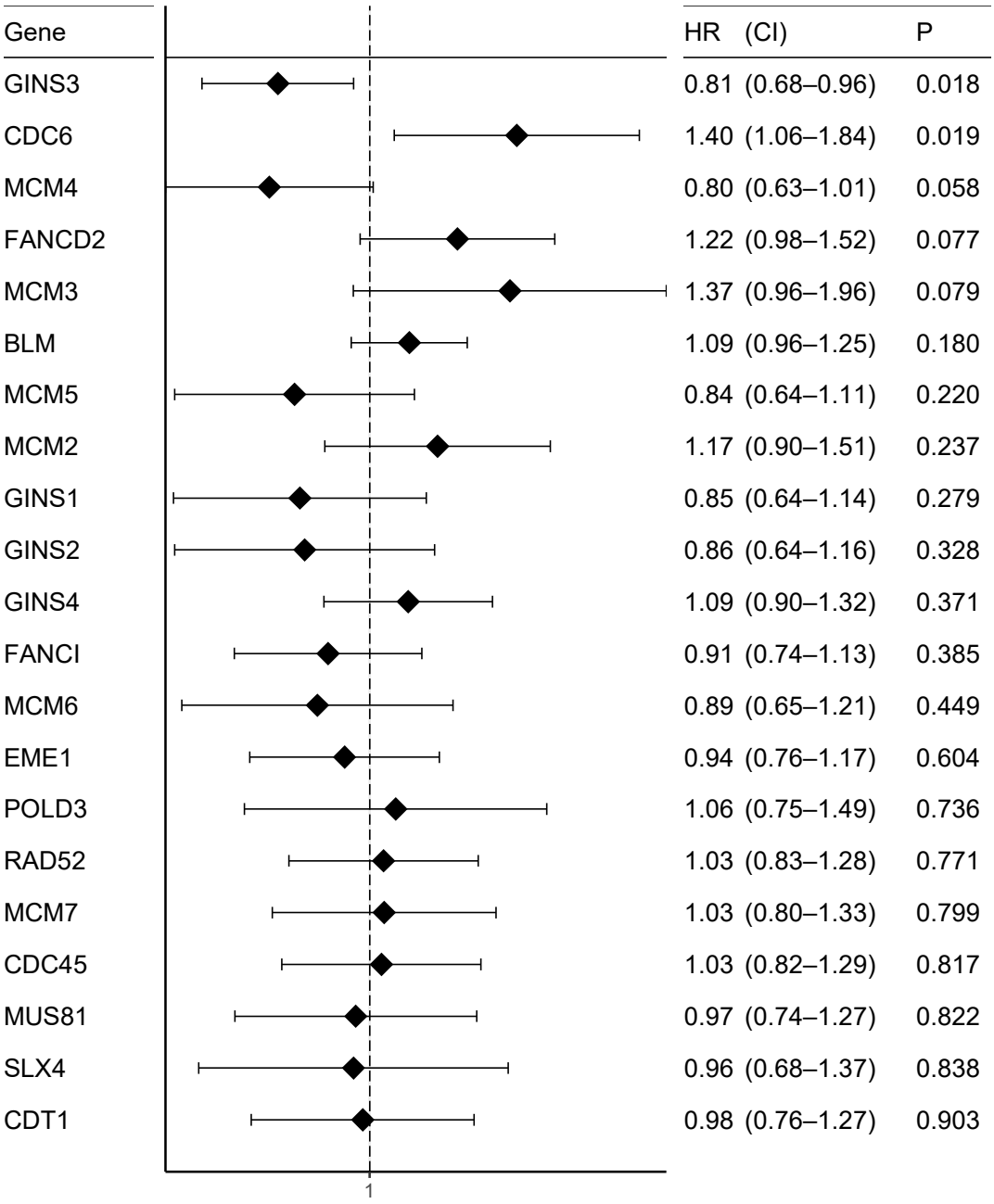

Figure 8.9. Forest plot of RS response signature genes in CGGA dataset. Hazard ratios for CGGA patient survival and associated p-values for each gene in the RS response signature were quantified by multivariate analysis and plotted using the 'survivalAnalysis' package in R. Genes were ranked by p-value.

Figure 8.10 visualises the correlation between RS response signature genes. Gene expression data from CGGA patients was used to assess gene correlation and 'corrplot' package in R used to analyse and plot the results. All genes in the signature had a significant positive correlation with each other, with the

exception of MUS81 with both GINS4 and MCM4 which were not statistically significant relationships.

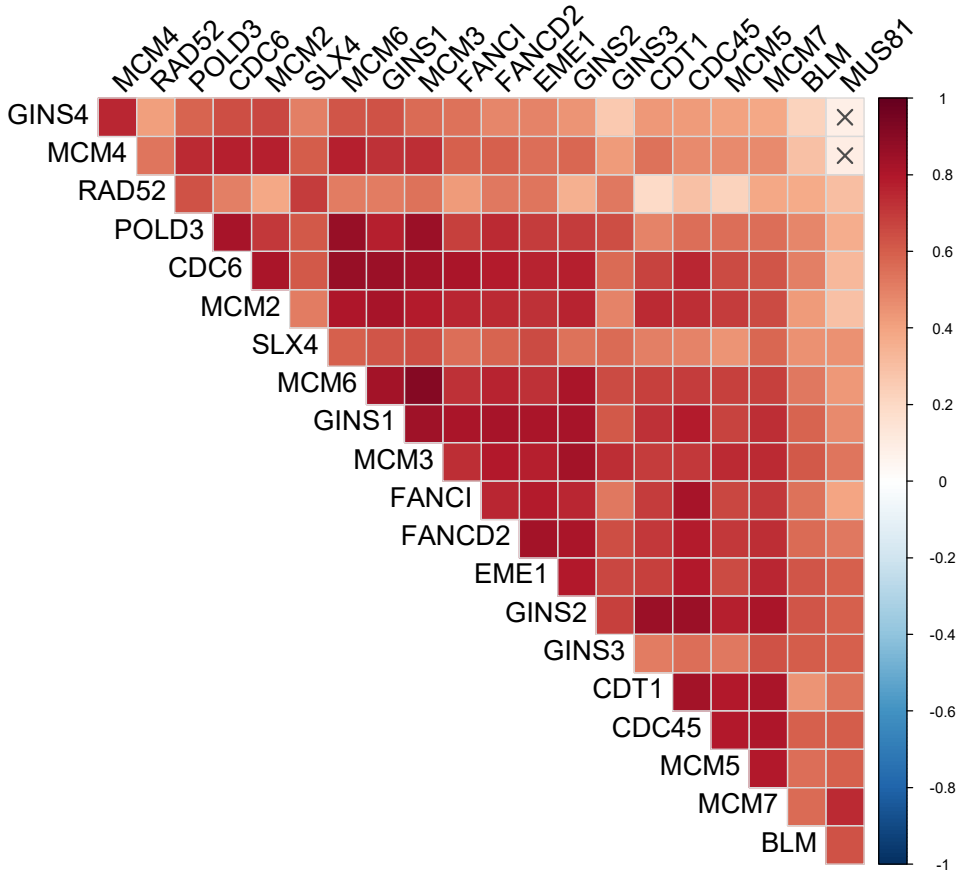

Figure 8.10. Correlation plot of RS response signature genes. Gene expression correlation was analysed in the CGGA dataset for the 21 genes in the RS response signature, using the 'corrplot' package in R. Colour corresponds to correlation coefficient and cross marks gene pairs that did not reach the significance cut off ($p<0.05$).

To assess the gene signature on CGGA patient survival, a Cox proportional hazards regression model was fitted, using the 'survival' package in R. A higher signature score correlated with worse survival, with a hazard ratio of 1.98 [95% CI: 1.12, 3.50] (n=374) and an associated p-value of 0.02. To visualise the effect of the gene signature on patient survival, the CGGA patients were ranked by signature score, and the top quarter categorised as "high" and the bottom quarter as "low". Survival analysis of high and low RS response signature score was carried out using the 'survminer' R package and the Kaplan Meier curve shown in Figure 8.11. A high gene signature score corresponded to a worse survival probability, with a log-rank p-value of 0.01. This gene signature was validated in other publicly available GBM RNAseq datasets and also predicted survival in the LeeY dataset (hazard ratio of 2.97 [95% CI: 1.29, 6.81], n=191,

p=0.01) (Lee et al., 2008) and the Phillips dataset (hazard ratio of 8.78 [95% CI: 2.29, 33.7], n=56, p=0.002) (Phillips et al., 2006). However, the signature did not predict survival in TCGA (The Cancer Genome Atlas) or Freije datasets.

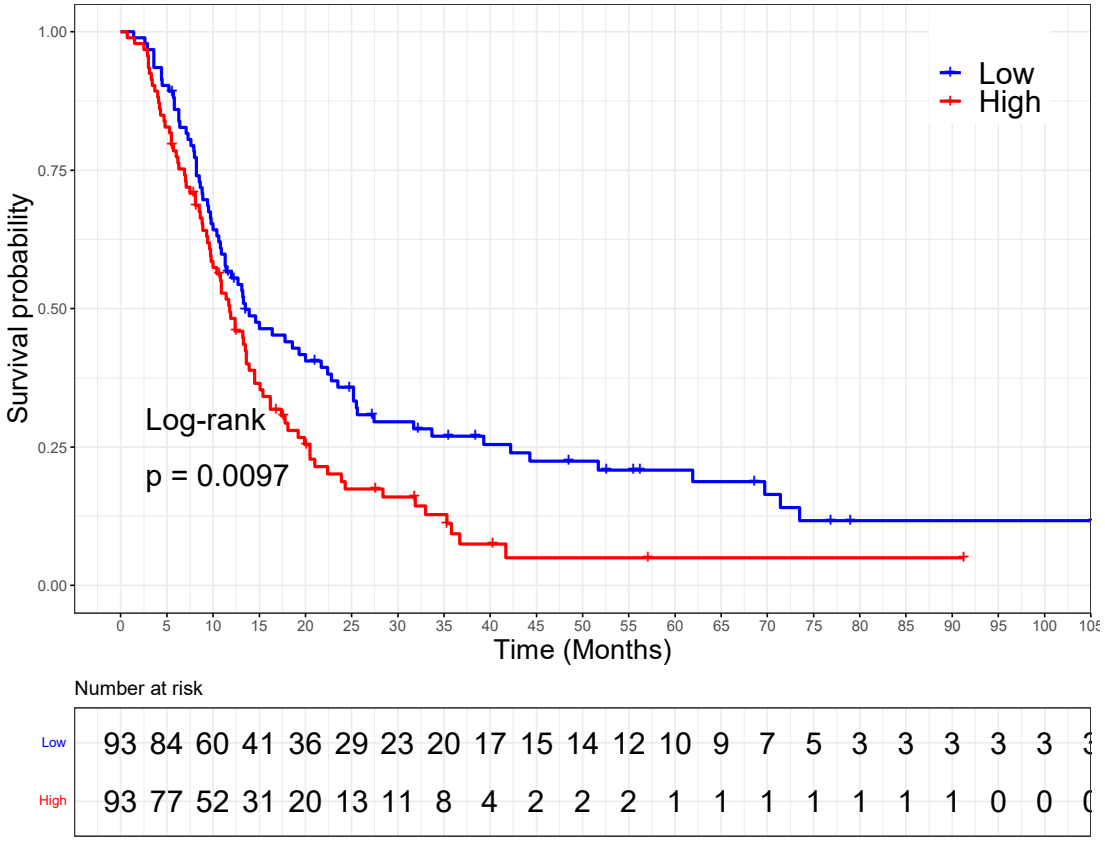

Figure 8.11. RS response gene signature score predicts patient survival. CGGA RNAseq dataset was analysed for RS response signature score by ssGSEA in 'GSVA' R package. The top quarter ranked were classed as "high" and the bottom quarter classed as "low" scoring. Survival analysis was carried out between the two groupings by 'survminer' R package and a Kaplan Meier curve plotted, with associated p-value from log-rank test.

Lastly, to investigate the proportion of patients that show evidence of the curated gene signature, a heatmap was plotted of all CGGA patients and associated signature scores (Figure 8.12). Hierarchical clustering identified two populations, one of which appeared to identify the proportion of patients within a population which were associated with this signature. This population represented 41.9% of the total patient group.

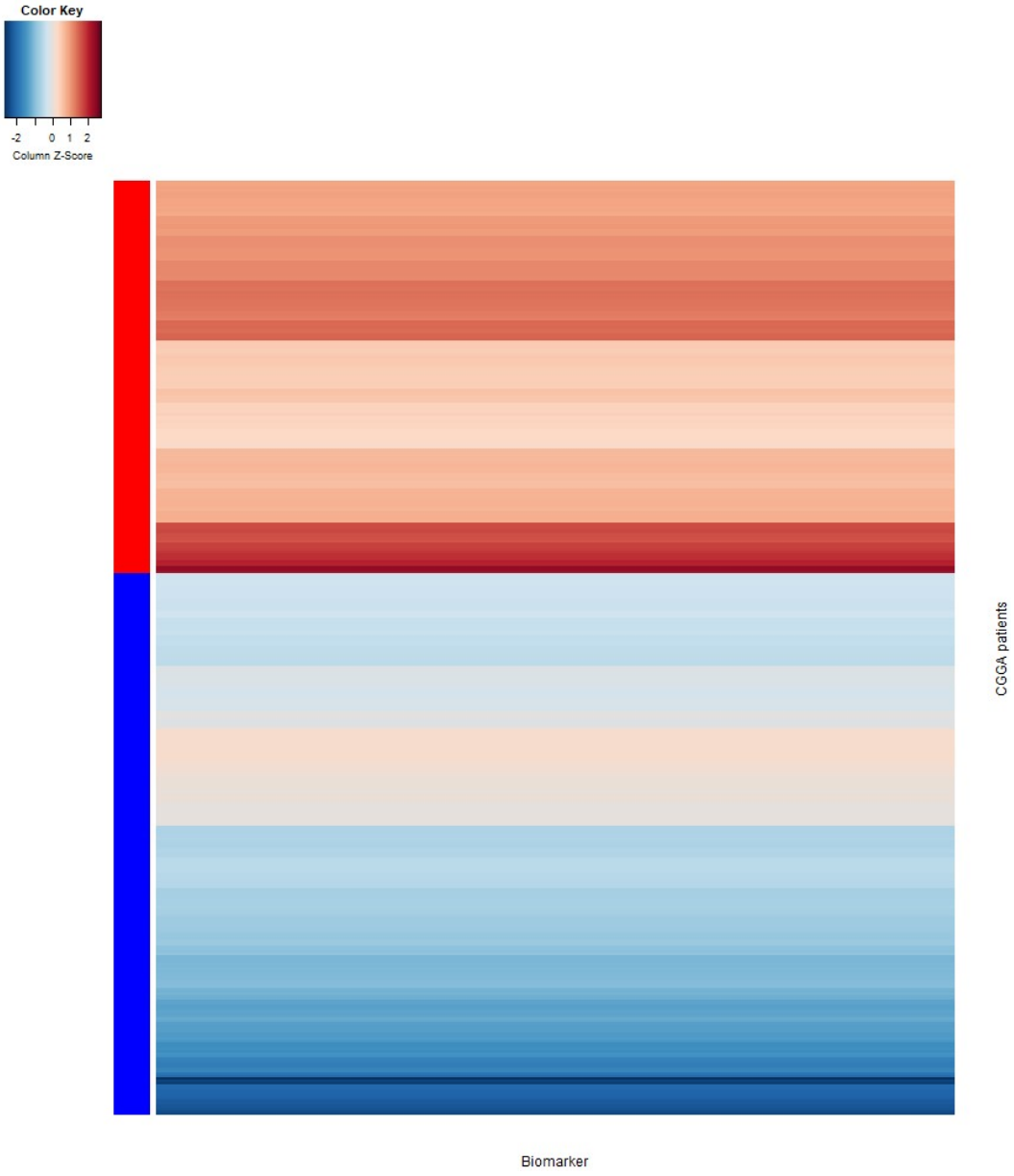

Figure 8.12. Heatmap of CGGA patients and RS response signature score. Signature score was quantified by ssGSEA using the 'GSVA' package in R for patients in the CGGA dataset and visualised by a heatmap using the 'heatmap.2' package in R.

8.7 Conclusions

This chapter has characterised transcriptomic aberrations in genes relevant to cellular mechanistic responses to CAiPi. Mechanistic *in vitro* studies found CAiPi-sensitive GSCs were undergoing increased origin firing, re-replication and UR-DNA which directed transcriptomic interrogations. A collated 21 gene signature predicted sensitivity to targeting the RS response in GSCs and predicted worse survival in several populations of GBM patients.

The CMG complex was identified as a gene set critical to origin firing, so gene expression of all 11 genes in the complex was investigated. Seven CMG complex genes were increased in E2 GSCs versus E2 bulk, only four were increased in R10 GSCs and no CMG complex genes were increased in G7 GSCs versus G7 bulk. Since E2 is the only cell line out of three that had significantly more sensitive GSCs than bulk cells, an increase in origin firing gene expression at baseline appears to predict GSC-bulk sensitivity relationships. Next, overexpression of CDT1 and/or CDC6 are frequently used to induce exogenous re-replication. Analysis of their baseline expression again found the greatest increase in GSCs over bulk in E2, followed by R10 and G7. Additionally, expression of the more critical re-replication factor, CDT1, correlated with relative GSC sensitivity. CDT1 and CDC6 were both identified in two of the top dysregulated GO terms in E2 GSCs in response to CAiPi, visualised in a cnetplot in Figure 5.11. Although these results are not akin to overexpression studies, they do indicate a potential predisposition for more CAiPi-sensitive GSCs to relicense origins.

Lastly, transcriptomic investigations focused on response to UR-DNA. Substantial evidence suggests that UR-DNA at CFS in response to RS is resolved by MiDAS to complete genome duplication and maintain chromosomal stability. Since this thesis has observed significant increases in UR-DNA in CAiPi-sensitive GSCs, with corresponding chromosomal instability via micronuclei and chromatin bridges, factors involved in MiDAS were investigated. In E2 GSCs, which exhibited increased micronuclei and chromatin bridges in response to CAiPi, six of the eight MiDAS factors were upregulated versus bulk, whereas none were upregulated in R10 or G7. In G7 micronuclei and chromatin bridges were increased in bulk versus GSCs after CAiPi. They were not investigated in R10. This work suggests that CAiPi-sensitive E2 GSCs may be experiencing more UR-DNA at CFS in response to endogenous RS compared to E2 bulk, requiring resolution by MiDAS. No differences were observed between GSCs and bulk in R10 and G7, in keeping with reduced or no increase in GSC sensitivity to targeting the RS response in these cell lines respectively. Future work should include analysis of MiDAS *in vitro* at baseline and after CAiPi.

These three gene sets were combined into one gene signature to investigate it as a predictive marker of sensitivity. In keeping with individual gene analysis, LFC

between GSC and bulk cells of the signature was greatest in E2, followed by R10 then G7. Overall, this suggests that this signature is a good marker of the GSC-bulk relationship within each cell line.

To further develop the translational potential of this approach, a signature score was calculated for each cell line. Again, this identified the largest difference between GSC and bulk in E2. Additionally, E2 and R10 GSCs exhibited similar scores, and both were significantly greater than G7 GSC. This was in keeping with patterns of GSC sensitivity, since E2 and R10 GSCs were comparatively more sensitive than G7. Future work aims to assess this signature in a validation dataset to predict CAiPi sensitivity. One issue with the clinical translation of this gene signature is it was developed in GSCs, which represents a tumour cell subpopulation which is not readily identifiable in clinical practice. However, we believe it could be reflective of CAiPi sensitivity in some tumours and therefore be of much wider clinical utility.

The RS response gene signature predicted survival in a population of GBM patients. High expression of the 21 gene set correlated with worse prognosis, with a hazard ratio of 1.99. Comparisons of patients with the highest expression versus the lowest highlighted this observation, with a log rank of 0.02 between the two groups. This signature identified a potentially targetable population of patients, with high signature expression correlating with worse survival, who may benefit from CAiPi treatment. This was validated in two further publicly available GBM datasets, however it did not predict survival in TCGA (Cancer Genome Atlas Research, 2008) or Freije (Freije et al., 2004) datasets.

Characteristics of these datasets were explored to investigate any explanations for differing predictive capacities. TCGA and Freije datasets were much smaller than the CGGA dataset but were comparable to LeeY and Phillips datasets, so sample size is unlikely to be the reason behind differing significance of hazard ratios between datasets. Interestingly, the LeeY dataset was an amalgamation of ten publicly available datasets (Lee et al., 2008), which included both the Phillips and Freije datasets for which the signature predicted survival in one but not the other. This potentially highlights an issue with utilising single datasets for survival analysis, which may be biased in how they are selected i.e. race, age. The LeeY dataset has the advantage of being a heterogenous population of

GBM patients. TCGA and CGGA datasets were created using RNA seq and Freije, LeeY and Phillips were all created by microarray. All datasets were produced from snap frozen resections and confirmed as GBM by neuropathologists. Therefore, these methodologies are unlikely to explain differing predictive capacities across this panel. The Freije and Phillips datasets were a single centre study whereas CGGA was curated by six centres, however all working to the same approved protocols (Zhao et al., 2021). TCGA was a retrospective study from 17 biospecimen repositories, so may be more varied in specimen collection protocols, however all specimens were reviewed by the same body for approval for the study. In regard to tissue approval, CGGA and Phillips required tumour cell percentage of 80% and 90% respectively, whereas TCGA required only 60% and the Freije study did not state a cut off. It may be that tumour cell content could be influencing the quality of the dataset and the subsequent ability to predict survival. Further validation of this signature is likely required in more datasets to fully understand its clinical utility, but generally this analysis suggests that dysregulated DNA replication is associated with poor prognosis in GBM. In conclusion, the curated 21 gene signature appeared to be best suited for predicting sensitivity in GSCs and can identify a potentially CAiPi-targetable population of patients.

Chapter 9 *In vivo* investigations into the clinical applicability of CAiPi

9.1 Introduction

To investigate CAiPi in a preclinical model, a tolerability and PK *in vivo* study was carried out. Since starting work on this thesis, the novel inhibitors BAY1895344 and pamiparib were described as potent and selective inhibitors of ATR and PARP respectively (Wengner et al., 2020, Xiong et al., 2020). Pamiparib was of particular translational interest in glioma due to reports of high brain penetrance. Many PARP inhibitors have shown unsuccessful brain penetration, due to them being targets of the efflux pumps P-glycoprotein (P-gp) and breast cancer resistance protein (BCRP) (Lawlor et al., 2014, Parrish et al., 2015, Kizilbash et al., 2017, Durmus et al., 2015). However, Xiong et al presented data supporting pamiparib as a brain penetrant PARPi due to it not being a P-gp or BCRP substrate (Xiong et al., 2020). They found a brain/plasma (B/P) ratio of ~19% four hours after dosing with pamiparib, which was greater than talazoparib (3%), olaparib (2%) and niraparib (14%), suggesting stronger BBB penetrance by pamiparib in a non brain tumour bearing model. They also showed that pamiparib was more potent than olaparib, despite comparable PARP trapping capacities, in a breast cancer xenograft model. PARylation inhibition lasted longer with pamiparib and pamiparib had a 16-fold higher efficacy than olaparib, likely due to higher and longer exposure (Xiong et al., 2020). This study highlighted the clinical potential, both in terms of anti-tumour effects and BBB penetration, of pamiparib. No *in vivo* studies have been published investigating the brain or brain tumour penetrant capacities of BAY1895344, but it has been described as a brain penetrant ATR inhibitor (discussions with manufacturer).

Since both BAY1895344 and pamiparib have been described as brain penetrant and with promising potency, but no studies have investigated brain tumour penetration, both inhibitors were investigated in an *in vivo* PDX model. Initial investigations focused on the tolerability and scheduling in an intracranial GBM mouse model. Secondly, PK analyses of blood, brain and tumour tissue samples were carried out to assess both the brain and tumour penetrance capacities of both inhibitors. This chapter also aimed to investigate the use of iRFP-tagged GSCs for detection of intracranial tumours.

9.2 Feasibility study of combined BAY1895344 and pamiparib

To investigate the tolerability of combined BAY1895344 and pamiparib in this study, two different doses of BAY1895344 were used, given alone or combined with pamiparib at 6mg/kg. Pamiparib at 6mg/kg was previously studied within the group and determined to be tolerable in this mouse model (data not published). Non-tumour bearing cohorts (n=3) of CD-1 nude mice were given BAY1895344 alone or combined with pamiparib twice daily, 5 on/2 off by oral gavage. Tolerability of the dosing schedule was assessed by changes in body weight, haemoglobin and WCC, as shown in Figure 9.1. End point was 31 days from initial dosing. Mice were monitored throughout the study and humanely sacrificed when they showed any signs of distress or neurological symptoms. Dosing and monitoring was carried out with assistance from D. Athineos and K. Blyth.

BAY1895344 at 10mg/kg alone was tolerated for the full study period, with no weight loss observed. WCC remained stable after an initial decline and haemoglobin decreased to 93.7% of starting value at day 31. BAY1895344 at 20mg/kg alone was not well tolerated, with unstable weights and decreases in haemoglobin and WCC resulting in one mouse being humanely sacrificed early on day 19. The addition of pamiparib at 6mg/kg to BAY1895344 exacerbated toxicity. All mice receiving BAY1895344 at 10mg/kg and pamiparib were humanely sacrificed early on day 18 or 19 due to weight loss of 16-19% of starting weight, with corresponding reductions in haemoglobin and WCC levels. BAY1895344 at 20mg/kg plus pamiparib was ended on day 13 because of weight loss observed from this combination with 10mg/kg BAY1895344 which was initiated first. In conclusion, BAY1895344 was not well tolerated at 20mg/kg or when combined with pamiparib.

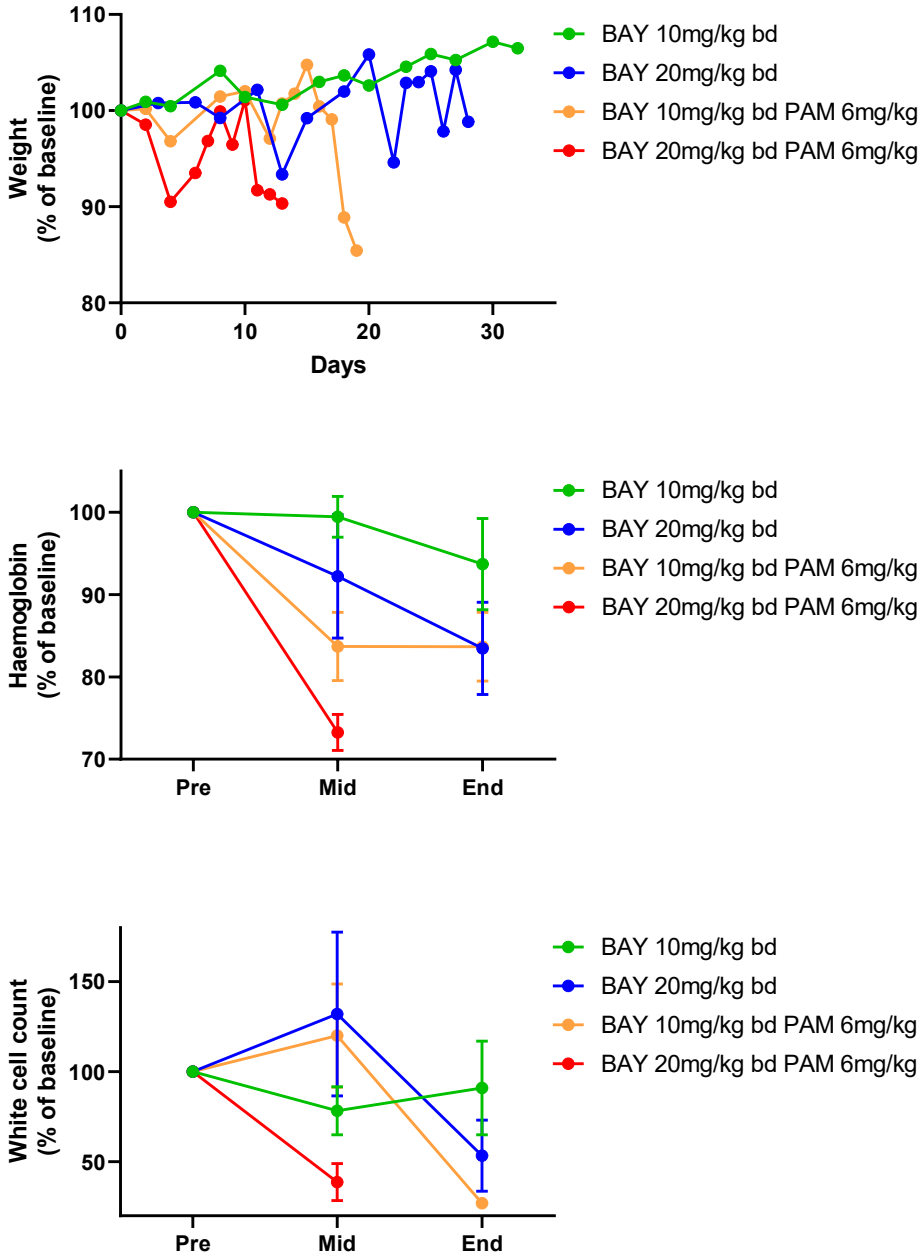

Figure 9.1. Tolerability metrics of BAY1895344 and pamiparib. Mouse weight, haemoglobin and WCC metrics were taken as a measure of tolerability. Starting weights and blood measurements were taken before initial dosing, and weights taken every day or second day throughout the study, and haemoglobin and WCC counts taken after day 15 and day 31, or on day of culling if study ended before planned endpoint. Results show mean and SD from three mice and are calculated as change from start point. BAY = BAY1895344, PAM = pamiparib.

9.3 Tolerability of BAY1895344 and pamiparib combined with irradiation

IR following debulking surgery remains the most effective treatment for GBM. Studies of RS-targeting therapies in a clinic will likely be given in combination with IR, however they could be given alone in a recurrent setting. An *in vivo*

study of the tolerability of CAiPi with IR was carried out, to investigate the feasibility of this treatment schedule. Importantly, an *in vitro* study by Carruthers et al found that CAiPi had potent radiosensitising capacity in GSCs, meaning this triple combination may have significant clinical benefit (Carruthers et al., 2018). A study was therefore carried out to investigate the longer-term tolerability of CAiPi and IR *in vivo*, utilising the lower dose of 10mg/kg for BAY1895344 and half the dose of pamiparib that was studied in section 9.2, given only once daily three times a week instead of twice daily every weekday.

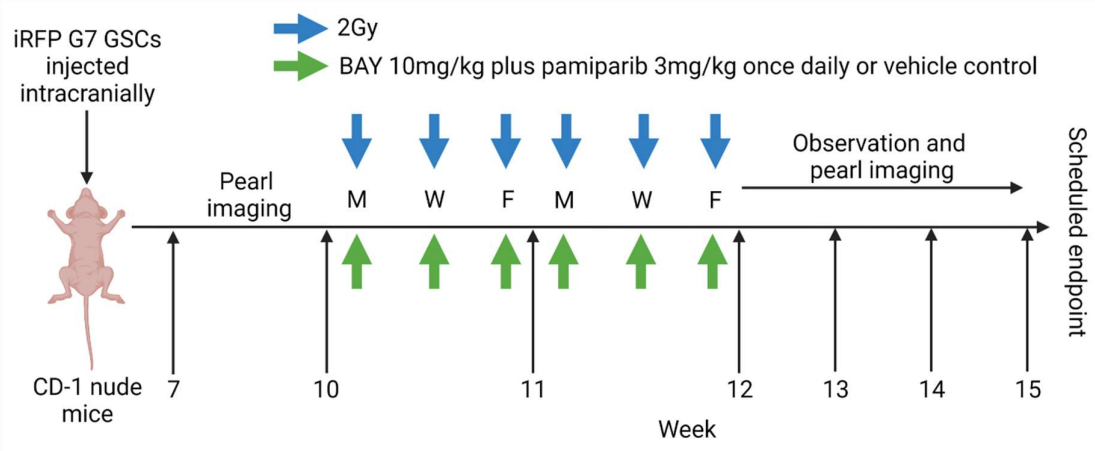

Figure 9.2. Schematic of *in vivo* pilot study of combined BAY1895344 and pamiparib with irradiation. G7 GSCs labelled with iRFP were injected intracranially into female CD-1 nude mice. Pearl® imaging began on week seven, and was carried out periodically throughout the study, avoiding the two weeks of dosing due to the requirement for isofluorane anaesthesia for both Pearl® imaging and IR. Dosing with BAY1895344 (10mg/kg) and pamiparib (3mg/kg) or vehicle control was carried out on Monday, Wednesday and Friday on week 10 and week 11 once daily by oral gavage, 30-60 minutes before 2Gy IR. After dosing schedule was complete, mice were continuously monitored until a scheduled endpoint at week 15. Created using BioRender.

A summary of the study and dosing schedule is shown in Figure 9.2. G7 GSCs labelled with iRFP were injected intracranially into CD-1 nude mice. Labelling of G7 GSCs with iRFP was carried out and cells made available by A Koessinger, as described previously (Koessinger et al., 2020). Mice were dosed with BAY1895344 and pamiparib or vehicle control (n=4) for two weeks on Monday, Wednesday and Friday, 30 to 60 minutes prior to 2Gy whole brain IR, which was carried out by K. Stevenson. Mice were monitored throughout the study and humanely sacrificed when they showed any symptoms or distress. To assess growth of intracranial tumours harbouring iRFP-positive cells, mice were monitored periodically by bioluminescence Pearl® imaging. Results from Pearl® imaging are summarised in Figure 9.3.

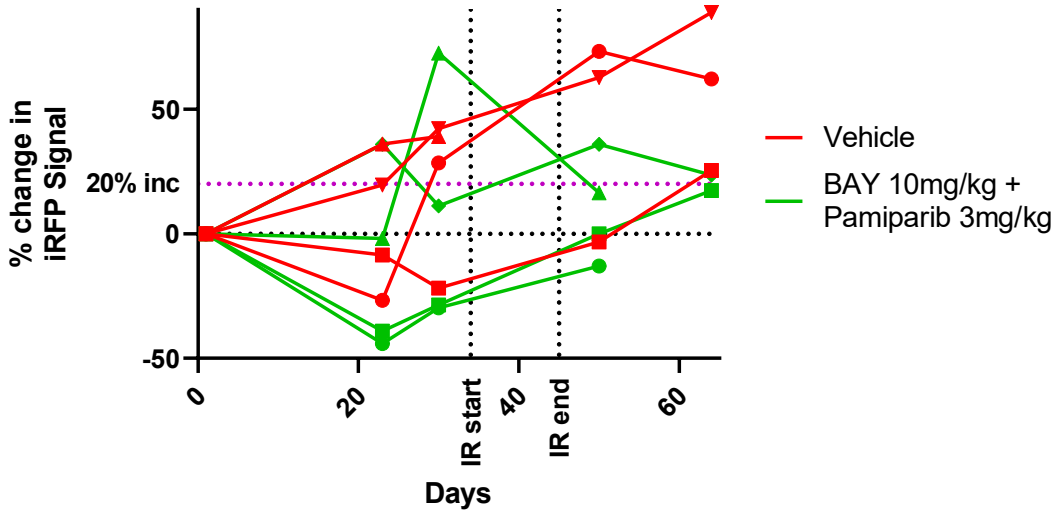

Figure 9.3. Change in iRFP signal throughout tolerability study. Bioluminescence Pearl® imaging (Li-Cor®) was used to assess intracranial tumours harbouring iRFP-positive cells. iRFP signal was quantified using ImageStudio™ software (Li-Cor®) and represented as a change in signal from initial baseline image. Start and end of IR and dosing is indicated, as well as an arbitrary 20% increase in signal cut off. Four mice received BAY1895344 (10mg/kg) plus pamiparib (3mg/kg) (green) and four mice received vehicle control (red).

One control mouse was culled in week 12, post IR, due to tumour-related symptoms, and two mice that received BAY1895344 plus pamiparib were culled in week 13, also due to tumour-related symptoms. All mice tolerated the two weeks of dosing plus IR. The three mice remaining in the vehicle cohort were above 20% increase in iRFP signal at the end of the experiment, however one had not reached that cut off by the start of dosing and IR. The mouse in the control cohort that was humanely sacrificed early with neurological symptoms had reached the 20% increase in iRFP signal. The two mice remaining in the BAY1895344 plus pamiparib cohort both had ~20% increase in signal at the end of the experiment, however both mice that were humanely sacrificed early due to neurological symptoms and weight loss had not reached the 20% cut off at their last scan. One of these mice (green triangle) had reached 72.5% increase in signal before initiation of treatment but this decreased post treatment to 16.5%.

9.4 Pharmacokinetic study of BAY1895344 and pamiparib

A PK study was carried out to investigate the brain and tumour penetrance of pamiparib and BAY1895344. BAY1895344 was assessed for tumour penetrance at both 10mg/kg and 20mg/kg since previous studies investigating BAY1895344 *in vivo* had used 20mg/kg and 50mg/kg to see anti-tumour effects (Wengner et al.,

2020). A summary of the study is shown in Figure 9.4. G7 GSCs labelled with iRFP were injected intracranially into female CD-1 nude mice. Growth of intracranial tumours harbouring iRFP-positive cells were assessed periodically by Pearl® imaging (Li-Cor®). A baseline scan was performed at week seven and any subsequent scans represented as a percentage change from baseline. At week 10, nine mice per cohort were dosed with BAY1895344 at 10mg/kg or 20mg/kg and pamiparib. Two mice were dosed with vehicle control for calibration. Mice were humanely sacrificed at 1 hour, 6 hours and 24 hours after dosing, with three mice per time point. Blood, brain and tumour specimens were collected. Quantitative MS analysis of both BAY1895344 and pamiparib for each of the tissue types was carried out by Pharmidex.

Change in iRFP signal throughout the study is shown in Figure 9.5. Results were variable between mice and between scans, however 15 of the 20 mice reached the 20% increase in iRFP signal at the point of dosing. Of the five mice that were below the 20% signal cut off, one reached 19.6%, three were around 0% so no change in signal was observed over 37 days (-1.7%, -0.9% and 3.3%) and one had a reduction in signal of 19.8% from baseline. All mice were randomly allocated to different dosing cohorts.

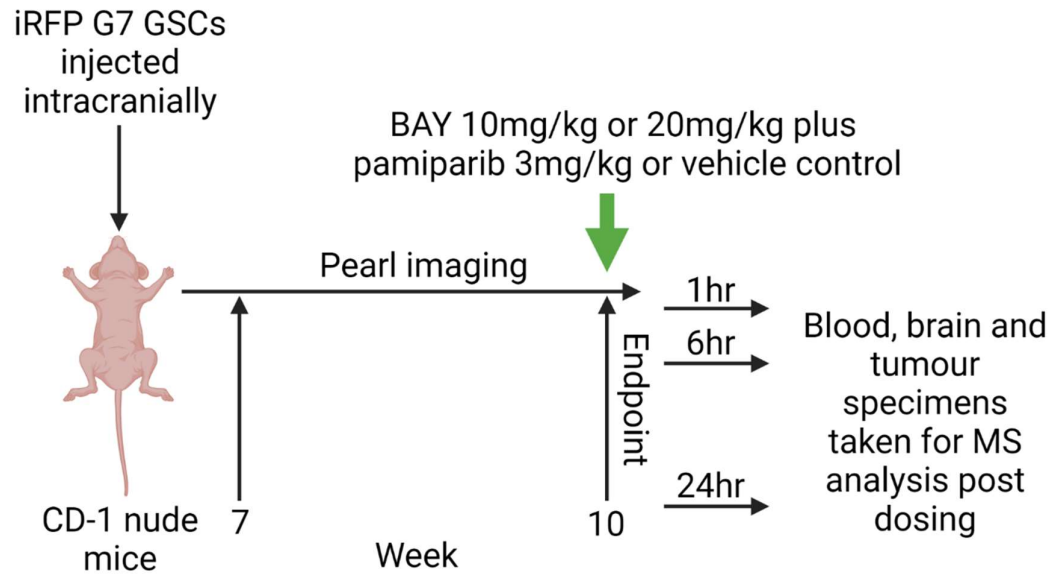

Figure 9.4. Schematic of pharmacokinetic *in vivo* study of BAY1895344 and pamiparib. G7 GSCs labelled with iRFP were injected intracranially into female CD-1 nude mice. Pearl® imaging began on week seven and was carried out periodically throughout the study. Dosing with BAY1895344 (10mg/kg or 20mg/kg) and pamiparib (3mg/kg) or vehicle control was carried out at week 10 by oral gavage. Mice were humanely sacrificed at 1, 6 and 24 hours after dosing and blood, brain and tumour samples collected for MS analysis of drugs. Created using BioRender.

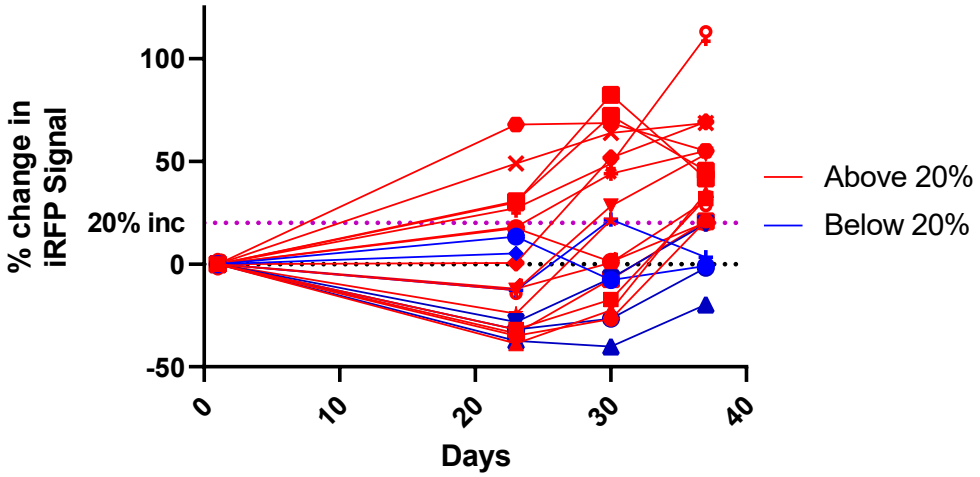

Figure 9.5. Change in iRFP signal throughout PK study. Bioluminescence Pearl® imaging (Li-Cor®) was used to assess intracranial tumours harbouring iRFP-positive cells. iRFP signal was quantified using Image-Studio™ software (Li-Cor®) and represented as a change in signal from initial baseline image. Arbitrary 20% increase in signal cut off is indicated on the graph. Red indicates a 20% increase in iRFP signal by the end of the study and blue indicates below 20%.

To investigate the clinical relevance of the concentrations that were reached within different tissue types, both PARylation levels and pChk1 levels were assessed with increasing concentrations of pamiparib and BAY1895344 respectively. Figure 9.6 shows the effect of increasing concentrations of pamiparib on PAR levels, as an indicator of its ability to inhibit PARP activity, carried out by K Strathdee. Pamiparib ablated H_2O_2-induced PARylation at all concentrations. Effective inhibition of PARP1 was observed even at 0.01μM. Phosphorylation of Chk1 was used as a marker of activated ATR, as its downstream effector, and a Western blot of pChk1 was used to assess the effectiveness of BAY1895344 to inhibit ATR (Figure 9.7). This study was carried out by R Carruthers. pChk1 was induced by HU and increasing concentrations of BAY1895344 analysed. The lowest concentration at 0.01μM reduced the levels of pChk1 induced by HU, which was ablated by 0.1μM. 0.03μM showed a reduction in pChk1 levels compared to HU alone.

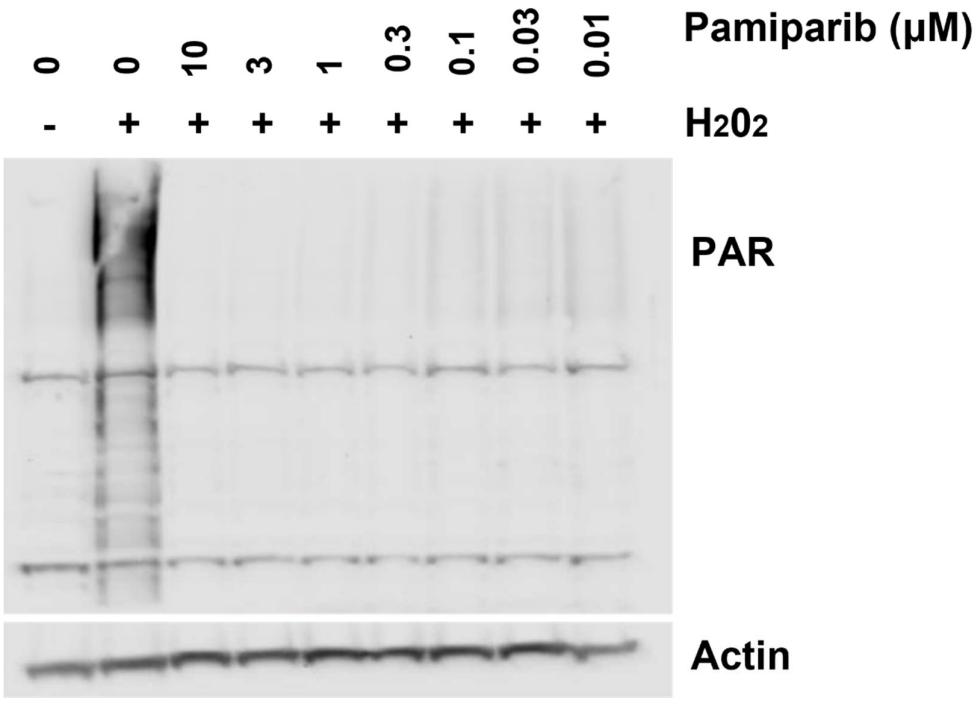

Figure 9.6. Inhibition of PARylation by pamiparib. Investigation of expression of PAR in G7 GSCs by Western blot after one hour incubation with increasing concentrations of pamiparib, followed by 20 minute incubation with 20mM H_2O_2. Actin was analysed as a loading control. Western blot carried out by K Strathdee.

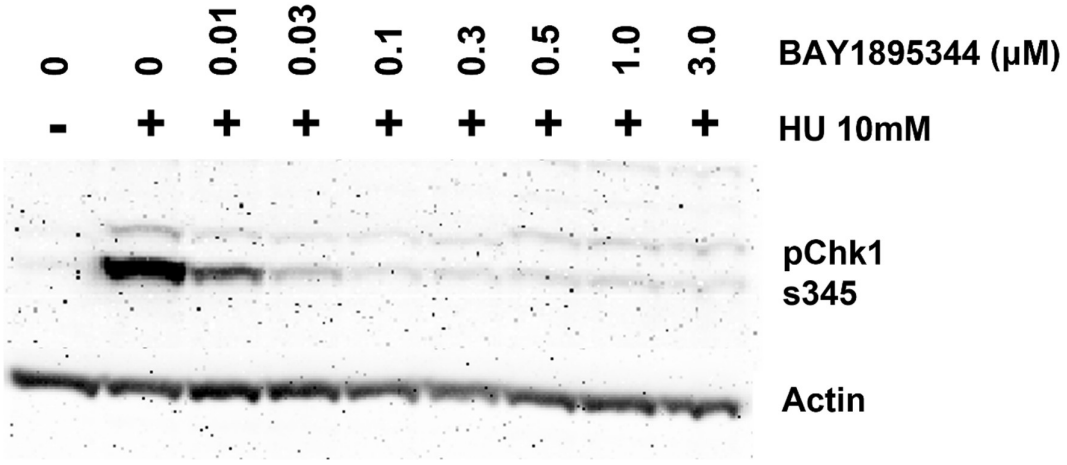

Figure 9.7. Inhibition of pChk1 by BAY1895344. Investigation of expression of pChk1 in G7 GSC by Western blot one hour after incubation with increasing concentrations of BAY1895344 for two hours, with and without HU (10mM). Actin was analysed as a loading control. Western blot carried out by R Carruthers.

MS results for the concentrations of BAY1895344 reached in blood, brain and tumour specimens are shown in Figure 9.8. The concentration of BAY1895344 reached in all tissue types was higher with 20mg/kg compared to 10mg/kg at all time points except 24 hours where both doses had undetectable drug concentrations. At one hour post dosing, BAY1895344 reached clinically relevant

concentrations in all tissue types for 10mg/kg and 20mg/kg. The red line on each graph indicates the clinically relevant concentration of 30nM, which was identified as being sufficient to inhibit pChk1 in Figure 9.7. At 10mg/kg and six hours, no drugs were detected in brain or tumour samples, and blood concentrations only ranged from 11.3nM to 40.5nM. 20mg/kg samples similarly reduced drastically at 6 hours but was still above the 30nM concentration in blood, brain and tumour, except one brain sample which had no detectable drug present. Overall, BAY1895344 showed both brain and tumour penetrance even at 10mg/kg and reached concentrations which inhibited pChk1 *in vitro*, however after six hours concentrations were reduced and by 24 hours no drug was present in any tissue type.

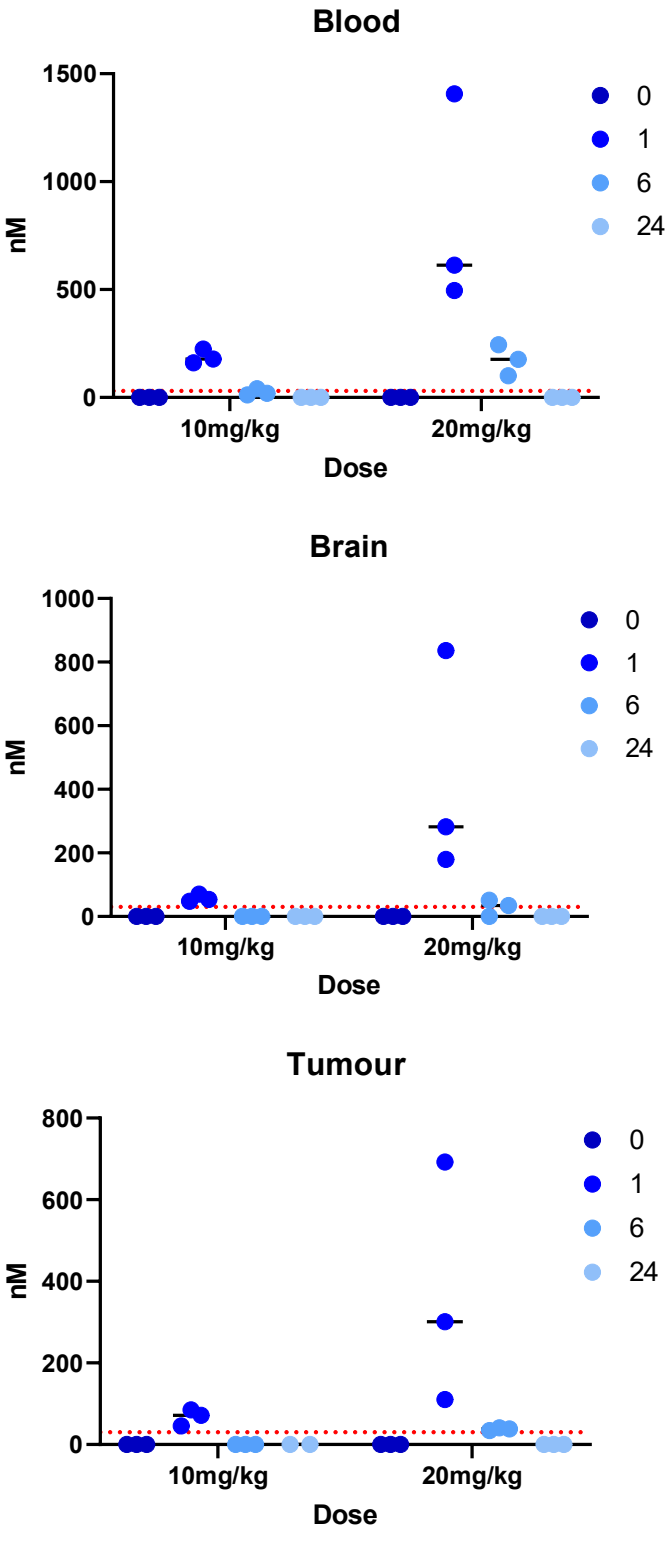

Figure 9.8. BAY1895344 concentration in blood, brain and tumour. CD-1 nude mice were injected intracranially with iRFP-tagged G7 GSCs 10 weeks prior to PK study. BAY1895344 concentrations in blood, brain and tumour murine samples were analysed by MS after dosing with 10mg/kg or 20mg/kg. Tissue samples were taken at 1, 6 and 24 hours post dosing, and analysis included a vehicle control at 0 hours.

Pamiparib concentrations in blood, brain and tumour specimens, analysed by MS, are shown in Figure 9.9. The red line on each graph marks 10nM, which was identified as being sufficient to inhibit PAR levels *in vitro* in Figure 9.6. At both one hour and six hours post dosing, pamiparib levels were high in all tissue types, reaching concentrations which inhibited PARylation *in vitro*. Concentrations of pamiparib were reduced at six hours compared to one hour but remained at clinically relevant levels. However, at 24 hours pamiparib was undetectable in blood, brain and tumour.

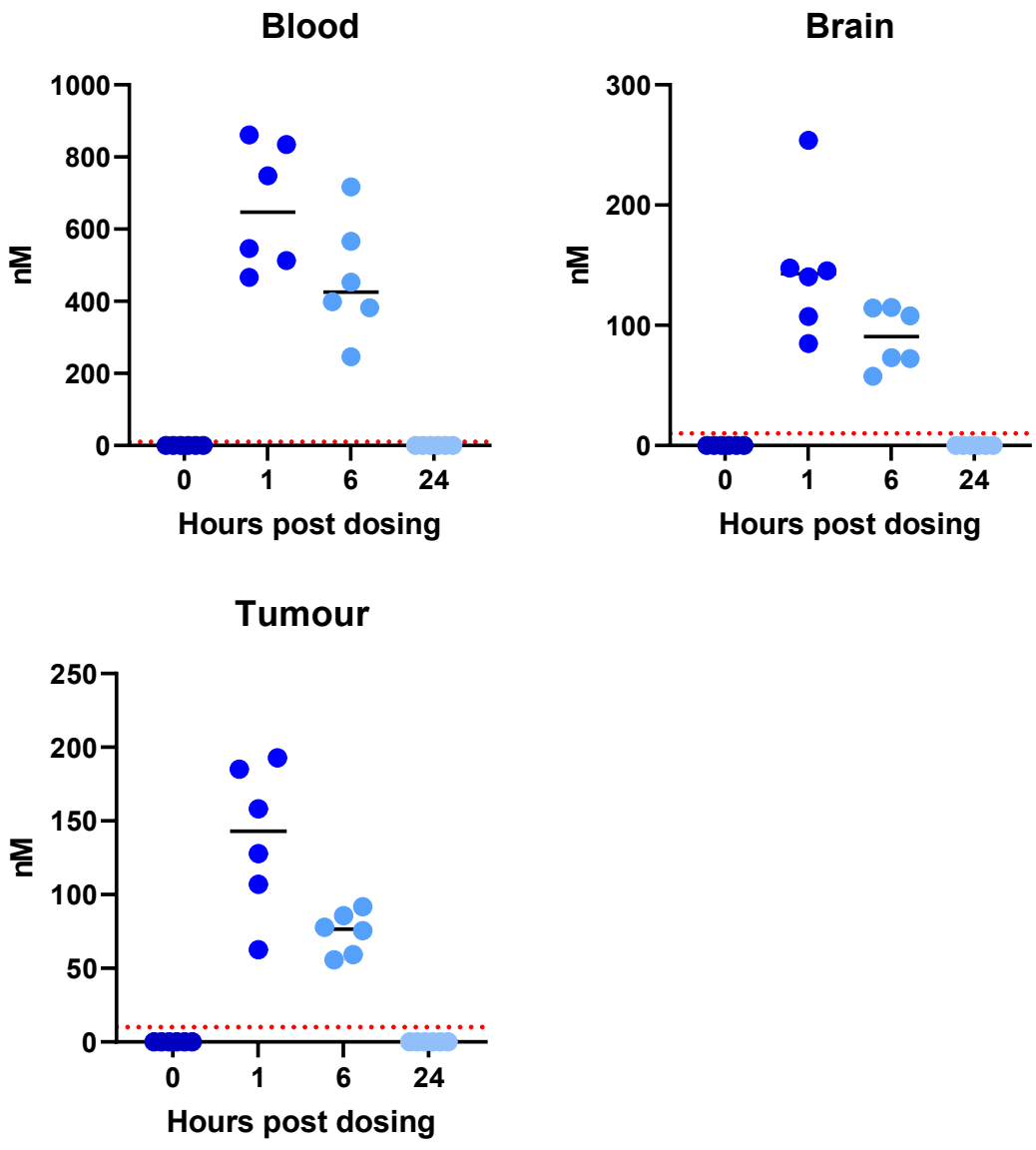

Figure 9.9. Pamiparib concentrations in murine blood, brain and tumour. CD-1 nude mice were injected intracranially with iRFP-tagged G7 GSCs 10 weeks prior to PK study. Pamiparib concentrations in blood, brain and tumour murine samples were analysed by MS after dosing with 3mg/kg. Tissue samples were taken at 1, 6 and 24 hours post dosing, and analysis included a vehicle control at 0 hours.

B/P and tumour-to-plasma (T/P) ratios were calculated at one and six hours after dosing and shown in Table 9.1. Pamiparib had comparable B/P and T/P at both one and six hours, remaining around 18-22%. BAY1895344 had high B/P and even higher T/P after one hour but dropped significantly after six hours, and was undetectable in brain and tumour with 10mg/kg and reducing to 19-21% with 20mg/kg. Overall, both drugs show promising BBB penetration, but evidence suggests BAY1895344 was not retained in brain or tumour as long as pamiparib.

Table 9.1. Brain- and tumour- plasma ratios for pamiparib and BAY1895344

	1hr		6hr	
	B/P	T/P	B/P	T/P
Pamiparib	22.1%	22.1%	21.2%	18.0%
BAY1895344 (10mg/kg)	30.3%	40.1%	0%	0%
BAY1895344 (20mg/kg)	46.1%	49.1%	19.4%	21.8%

Median concentrations for pamiparib and BAY1895344 are shown as a percentage of median blood concentration to give a B/P ratio and a T/P ratio, one and six hours after dosing. 24 hours not included as inhibitors were undetectable in blood.

9.5 Conclusions

This chapter has investigated the preclinical feasibility of CAiPi in a murine GBM PDX model. Initial investigations focused on the tolerability of combined BAY1895344 and pamiparib in CD-1 nude female mice, followed by analysis of brain and tumour penetrance. This chapter also investigated the utility of bioluminescent GSCs for detection of growth of intracranial tumours before initiation of treatment.

The aim and proposed benefit of iRFP-tagged GSCs for a GBM PDX mouse model is it can provide cost-effective, repeatable and non-invasive imaging of tumour-bearing mice, can be used to define treatment start dates based on a threshold and could be used to stratify cohorts based on tumour burden (Koessinger et al., 2020). Treatment was initiated at 10 weeks for the PK and the tolerability study, since previously tumours were detected at 10-12 weeks. At 10 weeks, Pearl® imaging produced variable results. Despite a general trend towards a >20% increase from baseline, these images could not be reliably used for determining tumour burden at 10 weeks. Koessinger et al also saw only a small increase in signal at 10 weeks, with a greater increase observed after 14 weeks (Koessinger et al., 2020). Unfortunately, by 14 weeks, an increase in mice displaying tumour-related symptoms occurs so ideally treatment would start before this

point. Variable signal could be due to large differences in tumour burden and therefore is an argument for treatment stratification, but factors such as tumour depth can also affect signal. An earlier baseline scan and more scans throughout the study may be beneficial to reduce the variation observed.

Previously, Wengner et al had described an MTD for BAY1895344 of 50mg/kg (twice daily, 3 on/4 off, orally) in their two PDX models, a PARPi-sensitive breast cancer NOD/SCID model and a PARPi-resistant prostate SCID model (Wengner et al., 2020). Both models also tolerated combined BAY1895344 at a sub-MDT of 20mg/kg with olaparib, either at its MTD (50mg/kg, once daily, intraperitoneally) in the breast cancer model or at a sub-MTD in the prostate model (20mg/kg, once daily, intraperitoneally). Maximum weight loss was <10% in their studies. All groups were sacrificed 83 days after tumour inoculation, with treatment ongoing once tumours reached 30-35mm^2. It was therefore surprising that 20mg/kg (twice daily, 5 on/2 off, orally) was not tolerated in this non-tumour bearing CD-1 nude model, which was further exacerbated by the addition of pamiparib at 6mg/kg with weight loss and haematological toxicity. Both NOD/SCID and SCID models are more immunodeficient than CD-1 nude mice, lacking both B and T cells and NOD/SCID also having defective dendritic and macrophages, whereas CD-1 nude mice are only lacking T cells (Charles River). Additionally, their model was tumour-bearing when given a higher dose, so differences in model utilised seems unlikely to explain differences in tolerability. Differences in scheduling may be a factor, as Wengner et al dosed with BAY1895344 twice daily, 3on/4off (Wengner et al., 2020) whereas this study dosed twice daily 5on/2off, so optimising scheduling could be explored in the future.

For further studies of tolerability of BAY1895344 and pamiparib in the GBM PDX model combined with IR, the lower dose for BAY1895344 of 10mg/kg was used, along with a reduction in pamiparib dose to 3mg/kg, which has previously been shown to abrogate PARylation in a brain tumour mouse model (Xiong et al., 2020). This dose was also given Monday, Wednesday, Friday for two weeks as opposed to 5on/2off. This schedule and dose was generally well tolerated for the whole two weeks, even combined with 2Gy IR. Three mice were humanely sacrificed during the study, one from the vehicle control cohort and two from

the treatment cohort, but all were displaying tumour-associated symptoms rather than treatment-specific toxicity. Finding an optimal scheduling and dose will always be a challenge, especially when there is such intra- and inter-study variability in tolerability. However, a first-in-human trial of BAY1895344 with a dose-escalation arm found a MTD of 40mg twice daily, 3on/4off, with the most common adverse haematologic toxicities being manageable and reversible (Yap et al., 2021), suggesting that despite challenges with pre-clinical models, BAY1895344 still has clinical applicability. Challenges remain when combining therapies with overlapping haematologic toxicities such as TMZ.

PK analysis of both BAY1895344 at 10mg/kg and 20mg/kg and pamiparib at 3mg/kg found successful brain and tumour penetrance after one hour at concentrations that inhibited both pChk1 and PARylation respectively. At one hour, BAY1895344 T/P ratio with 20mg/kg was high at 49.1% and was still relatively high at 40.1% with 10mg/kg. However, BAY1895344 did not remain in brain or tumour samples for long and by six hours there was no drug detectable with 10mg/kg, and with 20mg/kg it only just reached the concentration required for partial pChk1 inhibition. After six hours the T/P ratio had dropped to 21.8% for BAY1895344 (20mg/kg) from 49.1%. The early time point T/P ratio was promising for BAY1895344, but the actual concentration of drug present in tumour will largely be limited by tolerability.

Pamiparib was present in brain and tumour at one and six hours post dosing at concentrations that inhibited PARylation but was not detectable by 24 hours. Pamiparib B/P and T/P ratios remained around 20% at one hour and six hours. This was similar to work by Xiong et al who observed a B/P ratio of 19% at four hours, and supportive of pamiparib being a potent BBB penetrant PARPi in comparison to others (Xiong et al., 2020). They also similarly observed a minimum intra-tumour concentration after 24 hours.

Careful consideration is required for tolerability of this therapeutic strategy, however the first clinical trial of BAY1895344 showed that the drug is potentially better tolerated in humans than in mice. Ongoing clinical trials for both pamiparib and BAY1895344 separately will be informative of toxicities in humans.

Chapter 10 Discussion

10.1 Introduction

GBM is a cancer of extreme unmet need, associated with almost universal recurrence, few treatment options and very poor survival. Research into new therapeutic options for patients to improve clinical outcomes is therefore essential. CSCs in GBM drive treatment resistance and tumour recurrence, so targeting this subpopulation of cancer cells is pertinent. Carruthers et al were the first to demonstrate elevated RS in GSCs and describe RS as a targetable vulnerability, since CAiPi induced potent GSC-specific cytotoxicity (Carruthers et al., 2018). Understanding of this GSC-specific cytotoxicity is limited and there is a relative lack of studies analysing CAiPi in GBM, with further understanding and characterisation required before this strategy could progress into clinical trials. Therefore, this thesis firstly aimed to further characterise the response to targeting RS via CAiPi in a larger panel of GSCs and paired differentiated bulk cells by clonogenic, cell viability and neurosphere assays and to characterise the genomic and transcriptomic profiles of this panel utilising WGS and RNAseq. The secondary aim was to use CAiPi-induced transcriptional aberrations to direct mechanistic studies. Any novel mechanistic understanding was used to investigate a transcriptomic biomarker of CAiPi-sensitivity. Lastly, this thesis aimed to investigate the feasibility of novel ATR and PARP inhibitors in a preclinical model.

10.2 Model characterisation and CAiPi responses

This thesis utilised a model of paired GSC and differentiated tumour bulk cultures derived from single parental primary GBM cell lines. Through culturing under different, previously defined conditions, these cells can be maintained as either GSC-enriched or bulk-enriched cultures. This GSC model does not rely on cell sorting by a GSC marker, which overcomes the lack of a universally applicable marker problem. It also allows for greater heterogeneity in the GSC population and reduces variability between replicates due to re-equilibration of GSC and differentiated populations after cell sorting. However, there are limitations to this model, including the use of different medium which could be a confounding factor to any observations throughout this thesis. To validate the

cell viability findings in the enriched GSC model, E2 GSCs were sorted by CD133, which utilises the same media for both $CD133^+$ and $CD133^-$ cells so overcomes any confounding factors differing medium introduces. Another limitation is that these are enriched cultures as opposed to pure GSC and bulk populations. However, isolating and maintaining a "pure" GSC population is likely impossible as many GSC markers have been found in differentiated GBM cells. Additionally, GSCs have been identified that are not positive for GSC markers, meaning cell sorting may only be selecting for a sub-population of GSCs. Utilising this GSC-enriched model with an isogenic differentiated bulk cell line pair for internal comparisons, and validation in a sorted population addressed some of these issues.

The panel of seven GSCs was a relatively accurate representation of classical mutations and characteristics found in GBM patients. MGMT methylated and unmethylated promoters, TP53 mutations, EGFR SNPs, PTEN mutations, TERT promoter mutations and CDKN2A homozygous deletions were all identified in the panel of cells. However, no GSC line displayed evidence of EGFR amplification, despite being prevalent in GBM patients. Interestingly, Pandita et al reported that at the time of publication only one GBM cell line in the literature exhibited an EGFR amplification despite its prevalence in GBM patients, and they concluded that *in vitro* environments select against this gene alteration (Pandita et al., 2004). Further characterisation of EGFR amplification *in vitro* by William et al found that EGFR amplification can be maintained in serum-free medium, however higher doses (30ng/ml) of supplemented EGF showed the same rapid loss of EGFR amplification by passage 10 as FCS control (William et al., 2017). The cell lines utilised throughout this thesis were maintained in 20ng/ml supplemented EGF, and although no GSCs were used past 10 passages they have been passaged historically to maintain stocks. Therefore, it was not unexpected that these GSC lines have not maintained an EGFR amplification. This appears to be a limitation of *in vitro* GBM models as they are unlikely to fully recapitulate the EGFR landscape of clinical GBM. However, a more recent study found EGFR amplification, including up to 40 copies, in 11 out of 27 analysed GSCs which were maintained in similar medium utilised in this thesis (Wu et al., 2020). They noted that GSCs were passaged fewer than 15 times but did not discuss how they had been passaged historically.

Attempts to subtype GSC and bulk cells by a transcriptomic signature found that GSCs were enriched for the proneural and classical subtypes and bulk cells were enriched for the mesenchymal subtype. This was largely in keeping with work by Patel et al, who curated a GSC signature which correlated with proneural and classical subtypes but not mesenchymal (Patel et al., 2014). Contrary to these observations however, other studies have linked GSCs solely to proneural and mesenchymal subtypes, and additionally the mesenchymal subtype to more aggressive GBM and treatment resistance (Colman et al., 2010, Mao et al., 2013). Upon further inspection however, these studies curated their own signatures (Lottaz et al., 2010), utilised an older signature that only categorised GBM as proneural, mesenchymal or proliferative (Phillips et al., 2006), or only analysed proneural and mesenchymal subtypes (Mao et al., 2013, Narayanan et al., 2019), which may explain differing results. Due to differing methods of subtype classification, further analysis may be warranted to validate the categorisation of GBM cell lines utilised in this thesis using other signatures and analysis of genetic indicators of subtypes. Although valuable for complete GBM cell line characterisation, it is unlikely that subtypes will predict CAiPi sensitivity as they are not routinely used for treatment stratification and therefore the clinical implications are limited.

Since increased RS in GSCs had already been identified by Carruthers et al via decreased fork velocity in three primary, paired GBM cell lines (Carruthers et al., 2018), this thesis investigated transcriptional indicators of RS. Two previously described RS signatures were utilised, which used either RS-associated GO terms (Dreyer et al., 2021) or oncogenes known to induce RS (Guerrero Llobet et al., 2022). Both signatures indicated higher RS in GSCs compared to their paired bulk cell line, with the exception of the oncogenic RS signature in the S2 cell line. DNA fibre analysis of fork velocity is ongoing in further cell lines and ideally all cell lines would be investigated by a DNA fibre assay to characterise RS. However, it is a very time-consuming assay so characterisation of RS in a cell line panel by transcriptomic analysis represents a higher throughput analysis alternative. RS transcriptome analysis also represents a clinically accessible assay, unlike a DNA fibre assay.

Due to the work by Carruthers et al that identified RS-associated GSC-specific cytotoxicity by CAiPi (Carruthers et al., 2018) and transcriptional signatures indicating increased RS across a panel of GSCs, we hypothesised that these GSCs would all be selectively targeted by CAiPi. However, analysis of CAiPi-sensitivity by clonogenic assay in two cell lines identified G7 as having relatively more sensitive bulk cells to targeting of the RS response. High throughput cell viability assay identified highly heterogenous responses across a panel of seven paired cell lines, with some differentiated bulk cells more sensitive than their paired GSC line. Therefore, increased RS was not solely predicting sensitivity in this panel of cells. Additionally, characterisation of previously discussed biomarkers, including MYC and MYCN amplification, ATM deficiency and SLFN expression did not predict sensitivity. Therefore, further analyses of CAiPi mechanisms of sensitivity were required.

10.3 CAiPi-induced transcriptional dysregulation

To direct mechanistic studies, transcriptional dysregulation post CAiPi treatment was investigated in two cell lines with differing sensitivities. Despite CAiPi inducing the fewest DEGs in CAiPi-sensitive E2 GSCs, they were enriched for GO terms and pathways that were associated with previously described activities of CAiPi. DNA replication and cell cycle terms were highly dysregulated, which can be linked to CAiPi-activities in the RS response and ATRi effects on cell cycle progression. Additionally, the DNA secondary structure binding GO term, which was identified as a functional module in the E2 GSC emapplot in Figure 5.10, related to binding to a four-way junction, loop, Y-form DNA or a double-strand/single-strand junction and therefore may be indicative of increased RS via hard-to-replicate secondary structures. KEGG pathways in E2 GSCs were also of interest to CAiPi-response, despite only 14 being significantly dysregulated. DNA replication was the most dysregulated pathway, followed by cell cycle, and the top ten included many DNA damage pathways including mismatch repair, Fanconi Anaemia signalling and HR. Further analysis of specific DNA replication GO terms found limited dysregulation in other cell lines, and it was only significantly downregulated in E2 GSC. Interestingly, in CAiPi-sensitive E2 GSCs, clustering of the top dysregulated gene sets identified only four functional modules, whereas the relatively more resistant G7 GSCs had twelve. RNAseq analysis has its limitations, as it is only quantifying mRNA levels and not

necessarily protein levels. However, transcriptional investigations can give a general overview and it appeared as if E2 GSCs had a highly specific transcriptional response to CAiPi treatment that warranted further investigations.

Despite the other cell lines not appearing to have a highly specific transcriptomic response, there were some interesting pathways arising which may warrant investigations in the future. Gene sets associated with axon guidance/development and cell motility were highly dysregulated across several cell lines. Axon processes have been implicated in tumorigenicity in brain cancers associated with vascularisation and regulation of cell migration and apoptosis (Chedotal et al., 2005). Dysregulated gene sets also related to cell motility across G7 GSC and bulk cells included cell-substrate adhesion, cell-junction adhesion, focal adhesion and actin cytoskeleton. Additionally, nucleosome- and chromatin remodelling-associated gene sets were frequently dysregulated. Many DNA processes are regulated by chromatin structure, including replication and DNA repair (MacAlpine and Almouzni, 2013, Stadler and Richly, 2017). Current work is ongoing within the group investigating both the role of ATR in GSC motility and investigating chromatin accessibility in GSCs and bulk cells by ATACseq, in keeping with many enriched GO terms and KEGG pathways in GSCs but outwith the scope of this thesis.

10.4 Replication dynamics

Mechanistic investigations to understand CAiPi sensitivity were directed by transcriptomic discoveries, therefore DNA replication dynamics were characterised since it was highly dysregulated in CAiPi-sensitive E2 GSCs. Initial investigations of DNA replication used a DNA fibre assay to study fork velocity, new origins and stalled forks. CAiPi reduced fork velocity in E2 GSCs compared to ATRi alone but in G7 GSCs CAiPi sped up fork velocity compared to ATRi alone. If G7 GSCs can maintain fork velocity in the face of CAiPi this could partially explain why they were relatively less sensitive as they are better prepared for completion of replication. It has previously been shown that GSCs and bulk cells have comparable proliferative rates (Ahmed et al., 2015), so it would be interesting to investigate if that is still the case upon CAiPi treatment and if so differing replication rates will likely have more impact.

Total reduction in fork velocity for CAiPi versus control was greater in both bulk cell lines. However, both bulk cell lines had greater fork velocity at baseline associated with less RS and the resultant velocity of replication forks induced by CAiPi was comparable across all cell lines. It could be argued that there is a lower limit of fork velocity which all four cell lines trend towards with CAiPi. No literature appears to discuss a limit to replication fork velocity, however it seems feasible that there would be a fork speed below which does not support successful and timely replication and cell survival. If this is the case, the more modest reduction in replication fork speed in GSCs may be due to their baseline fork velocities being closer to the 'speed limit'.

Despite varying reports on PARPi effects on replication velocity, the most in-depth analysis was carried out by Maya-Mendoza et al, who found that PARPi increased fork velocity leading to RS and DDR activation (Maya-Mendoza et al., 2018). Through increasing PARPi concentration and length of exposure, they also found an increase of fork speed above 40% or a decrease of 20% lead to DNA damage, but within these limits the cell would be able to compensate for any alterations in fork speed. When comparing median fork velocity induced by PARPi, the largest increase was with CldU incorporation in E2 GSC, representing a 21.6% increase in fork speed over vehicle control. This result suggested that in our CAiPi-sensitive GSC, PARPi was inducing fork acceleration but did not reach a threshold proposed by Maya-Mendoza et al to activate DDR. In the relatively more resistant G7 GSC, fork speed increases via PARPi were 18.6% and 20.0% with IdU and CldU respectively so not dissimilar to E2 GSC. Conversely, G7 bulk, which were more sensitive to targeting of the RS response than G7 GSCs displayed significantly decreased fork velocities with PARPi, reaching the 20% decrease cut off proposed by Maya-Mendoza et al (46.7% for IdU and 36.7% for CldU). Since we observed highly heterogenous aberrations of fork velocity, it was unlikely that the GSC-specific PARPi-induced increase in fork speed was solely driving mechanism of sensitivity.

The most striking result from replication structure analysis was an increase in new origin firing with PARPi in E2 GSCs, which correlated with PARP trapping. This increase in origin firing in E2 GSCs was also observed with CAiPi, where it corresponded to decreased replication fork velocity. This data correlates with

reports that an increase in origin firing inversely affects fork speed (Zhong et al., 2013). Zhong et al hypothesised that this inverse relationship is due to competition for limiting replication factors after increased origin firing. Interestingly, with PARPi alone both increased origin firing and increased replication velocity were observed in E2 GSCs. Gonzalez-Besteiro et al found that in Chk1-deficient cells, replication fork velocity and origin firing were independent variables (Gonzalez Besteiro et al., 2019). The data explored in this thesis also suggests that under PARPi, these replication dynamics were occurring independently. Their study found that it was an increase in origin firing that drove DNA damage accumulation, not a decrease in fork speed, measured by γH2AX accumulation after separately restoring these replication aberrations. The data explored in this thesis supported this theory, since the more resistant bulk cells displayed greater reductions in fork speed, but a greater increase in origin firing was observed in CAiPi sensitive E2 GSCs.

The induction of new origins by the more potent PARP trapper olaparib also correlated with increased cytotoxicity compared to veliparib at a range of concentrations, and when combined with an ATRi. This correlation between a PARPi's trapping potential and single agent potency has been well characterised (Hopkins et al., 2019). It would therefore be reasonable to propose talazoparib as the optimal PARPi for cytotoxic effects to cancer cells, however studies have shown that trapping potential is inversely correlated with tolerability *in vivo* and as a result most PARPis induce comparable efficacies at MTD (Hopkins et al., 2015). Utilisation of the clinically well-characterised PARPi olaparib, which still ranks highly among PARPis for trapping potency, provides an optimal balance of PARP-trapping to induce new origins and tolerability.

10.5 Dysregulated S phase in CAiPi-sensitive GSCs led to genomic instability

Genomic stability is crucial to ensure cell survival and relies on tightly coordinated DNA replication processes and checkpoints. Disruption of these cell-protective mechanisms induces DNA damage and chromosomal and genomic instability which are consequently frequently observed in cancers. One crucial process to ensure genomic stability is the timely, successful and accurate completion of DNA replication during S phase. Following on from the

identification of loss of origin firing coordination via PARP inhibition in CAiPi-sensitive E2 GSCs, the causal effects on successful completion of replication were investigated. It was discovered that CAiPi-sensitive GSCs were undergoing both under-replication of DNA, quantified by 53BP1NB, and re-replication in response to CAiPi. This dual replication disorganisation was not observed in either their paired bulk cells or in relatively more resistant GSCs. This also corresponded to increased chromosomal instability and damage, assessed via an accumulation of chromatin bridges and micronuclei. Accordingly, the largest dysregulated functional module in E2 GSCs, identified by an emapplot in Figure 5.10, related to regulation of chromosome segregation and separation and metaphase/anaphase transition. All of these processes were downregulated in E2 GSCs, suggesting a loss of transcriptional coordination of chromosome segregation, which subsequently was observed *in vitro* via increased chromatin bridges and micronuclei.

53BP1NB were first identified by two corresponding studies in 2011 (Lukas et al., 2011, Harrigan et al., 2011). Both studies found that incomplete DNA synthesis in S phase resulted in the formation of nuclear sub-compartments in the subsequent G1 phase, marked by 53BP1. 53BP1NB were induced by exogenous RS and associated with CFS through ChIP techniques. RS-induced UR-DNA can be a result of increased stalled forks. Double fork stalling (DFS) has been hypothesised to be causal in increased UR-DNA, whereby two converging forks stall irreversibly with no compensatory licensed fork between them, as illustrated in Figure 10.1 (Bertolin et al., 2020, Newman et al., 2013). Origins are licensed redundantly to allow successful completion of replication under RS (Ibarra et al., 2008, Ge et al., 2007, Blow and Ge, 2009, Woodward et al., 2006). However, with an increase in cells under RS with CAiPi, it is reasonable to assume there is an associated increase in DFS events. Through mathematical modelling and validation *in vitro*, Moreno et al showed an inverse correlation between origin firing and DFS (Moreno et al., 2016). They also observed a strong link between DFS events and 53BP1NB, as expected. However, in contrast to this, CAiPi in GSCs resulted in an increase in both origin firing and 53BP1NB, and therefore presumably no origin firing-associated decrease in DFS events. It may be that in our model the increase in origin firing is insufficient to mitigate increased DFS events resulting in UR-DNA.

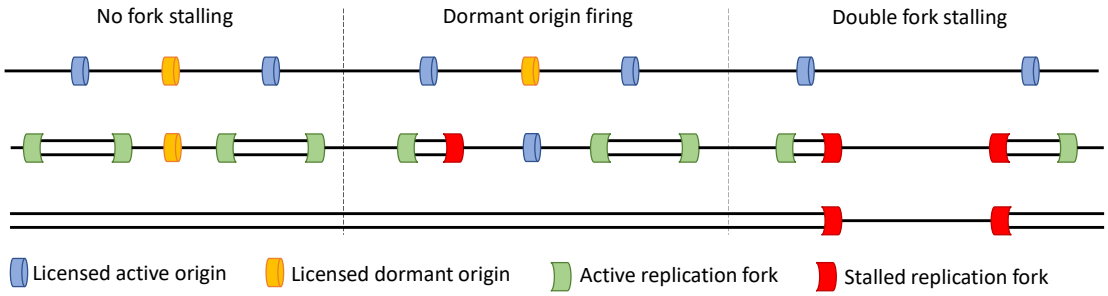

Figure 10.1. Under-replicated DNA from increased stalled forks. In an unperturbed cell cycle, limited fork stalling and an excess of licensed dormant origins leads to successful DNA duplication once active replication forks converge. If a replication fork stalls, a dormant origin that has been licensed in G1 phase can fire to compensate and cover affected regions of the genome, for successful replication to occur. Double fork stalling can occur when adjacent replication forks both stall and there are no compensatory licensed dormant forks. This is a source of under-replication of the genome.

UR-DNA appears to go relatively undetected by cell cycle checkpoint controls, with 53BP1NB present even in unperturbed cells (Moreno et al., 2016, Torres-Rosell et al., 2007). It has been hypothesised that UR-DNA bypasses checkpoints either by ssDNA in UR-DNA being insufficient to elicit an ATR/CHK1 response or UR-DNA actively preventing any cell cycle arrest, however the reason why remains to be elucidated (Bertolin et al., 2020). A recent model for cell cycle progression proposed that active DNA replication prevents mitotic entry by restricting CDK1 and PLK1 (polo-like kinase 1) activation, and therefore the checkpoint is detecting lack of ongoing DNA replication as opposed to successful completion, which would explain UR-DNA progression through mitosis (Lemmens et al., 2018). Despite these reports of no checkpoint activation in response to UR-DNA, ATR has been linked to minimising UR-DNA entering mitosis. Loss of ATR resulted in early entry into mitosis, with associated genomic instability in the form of chromatin bridges, failed cytokinesis and cell death (Eykelenboom et al., 2013). Cell death was however rescued by prolongation of mitosis by Cdk1 inhibition. ATR therefore has a critical role in mediating mitotic entry. It can be hypothesised that loss of ATR with CAiPi is driving premature exit out of S phase and therefore increasing UR-DNA.

Although 53BP1NB are routinely utilised as markers of UR-DNA, the consequences and fate of 53BP1NBs are relatively uncharacterised. Spies et al showed that 53BP1NB colocalised with PCNA and EdU before complete resolution in late S phase, suggesting that active replication in the subsequent cell cycle is required for repair (Spies et al., 2019), which may explain why UR-DNA bypasses mitotic

entry checkpoints. They found that cells with 53BP1NB have a second chance at resolving UR-DNA, by recruiting Replication Timing Regulatory Factor 1 (RIF1) which imposed late S phase replication timing on UR-DNA sites in the subsequent cell cycle, to allow for a replication-coupled RAD52-mediated repair earlier in S phase. 53BP1NB are found in unperturbed cells where genomic stability is maintained, which suggests they can be accurately resolved. Since we observed 53BP1NB increasing at such a rate with CAiPi, which was also associated with chromosomal instability, we hypothesised that there is a limit to how much UR-DNA a cell can handle before subsequent genomic instability and cell death, despite these active repair mechanisms.

As discussed in Chapter 1, a recently discovered post-replicative response to UR-DNA is MiDAS. Inhibition of MiDAS increased 53BP1NB (Bertolin et al., 2020, Minocherhomji et al., 2015) and it has been hypothesised that increased UR-DNA past a threshold could saturate MiDAS capabilities and require the activities and resolution of UR-DNA through 53BP1NB (Bertolin et al., 2020). Due to the close link of MiDAS to 53BP1NB and UR-DNA resolution, it would be interesting to investigate the relevance to CAiPi mechanism of response, especially to see if MiDAS reaches a saturation under CAiPi that results in increased reliance on 53BP1NB for UR-DNA response. Interestingly, GSCs have higher RS at baseline but this was not associated with an increase in endogenous chromatin bridges. It would be of value to investigate if an increase in MiDAS in GSCs is utilised to resolve their RS problems.

MiDAS and 53BP1NBs association with CFS is interesting. The link between UR-DNA and CFS is quite profound. 53BP1NB colocalised with CFS loci FRA16D and FRA3B via ChIP-qPCR (Lukas et al., 2011), and four of the top eight 53BP1NB-associated loci identified by ChIP-seq corresponded to known CFS (Harrigan et al., 2011). Furthermore, Harrigan et al found that 53BP1NB were only increased by RS-induction via aphidicolin but not HU, despite similar effects on DNA synthesis (Harrigan et al., 2011). CFS lesions are induced by aphidicolin, whereas HU is less CFS-specific, therefore the induction of 53BP1NB appear to represent UR-DNA at CFS. Additionally, DFS, which is a source of UR-DNA, correlates with 53BP1, CFS and late-replicating DNA (Moreno et al., 2016). ATR has been implicated in CFS stability upon reduced fork speed after an induction of breaks

at FRA3B following ATR depletion was identified, and furthermore CFS colocalise with ssDNA upon ATR loss (Koundrioukoff et al., 2013). In GBM, Carruthers et al have shown a significant increase in expression of very large genes (VLG) in GSCs compared to bulk, within which CFS are enriched (Carruthers et al., 2018). Higher expression of VLG in GSCs could be a source of increased UR-DNA in sensitive cell lines.

Conversely to an increase in UR-DNA, CAiPi-sensitive GSCs also exhibited re-replication after CAiPi treatment, which was not observed in the relatively more resistant paired bulk line. It is known that RS can induce the firing of licensed dormant origins to overcome increases in stalled forks to ensure full genome coverage, which may explain some of the increase in origin firing with PARPi and CAiPi. However, because replication is terminated when two forks converge this increased origin firing due to RS would not explain an increase in re-replication. Alternatively, origin re-licensing of already fired origins could explain this phenomenon, as described in Chapter 1.

Studies have shown that re-replication is promoted by overexpression of CDT1 and CDC6 in cancer cells with inactive p53, but not with intact, WT p53 (Vaziri et al., 2003). Additionally, the activities of p53 in preventing re-replication relies on activation of ATR (Vaziri et al., 2003). Characterisation of TP53 mutations in Chapter 3 identified SNPs or frameshift deletions in all seven GSC lines analysed, suggesting that these cells might be primed for re-replication due to loss of p53 and ATR activities via CAiPi. It has been hypothesised that re-replication is a rare occurrence in normal cells, since re-replication is so tightly regulated by temporal uncoupling of replication origin licensing and firing and any re-replication activates cell cycle checkpoints (Hook et al., 2007, Bertolin et al., 2020). However, E2 GSCs have displayed significant loss of replication coordination in response to CAiPi which may be driving re-replication.

It seems counterintuitive that E2 GSCs are undergoing both under-replication and re-replication. However, we propose that these occurrences are temporally and spatially separated. It has previously been discussed that UR-DNA is enriched at CFS, which replicate late in S phase. Conversely, studies have shown that re-replication is enriched at genomic regions replicated early in S phase. Regions of re-replication were enriched at euchromatin, corresponding to open and

generally early replicating genome, whereas heterochromatin which tends to replicate late were underrepresented for re-replication, with re-licensing occurring preferentially at origins fired early in S phase (Fu et al., 2021). Additionally, re-replication has been found at early S phase origins only 2-4 hours after an initial S phase firing (Vaziri et al., 2003). Not only were early replicating regions enriched for re-replication, copy number analysis suggested that some of these regions can undergo multiple initiations, and subsequently deplete replication in late-replicating regions, which the authors proposed was due to an enrichment of euchromatin at early replicating regions which represents readily accessible origins (Fu et al., 2021).

A model for dysregulated replication dynamics under CAiPi emerges, as shown in Figure 10.2. As discussed, re-replication occurs early in S phase at open euchromatin, and UR-DNA is enriched late in S phase at CFS and heterochromatic regions. Additionally, there is evidence that an increase in re-replication by relicensing depletes firing late in S phase (Fu et al., 2021). It could be hypothesised that this is due to a reduction in available replication factors, such as dNTPs or RPA, later in S phase through over-utilisation earlier in the cell cycle. Moreover, ATR has been shown to stimulate dNTP biosynthesis, with ATRi depleting dNTP supplies (Buisson et al., 2015, Le et al., 2017).

Unexpectedly, a reduction in origin firing with roscovitine reduced UR-DNA, quantified by 53BP1NB. This is also an opposite response suggested under the DFS model whereby origin firing reduction would increase UR-DNA due to a reduction in licensed dormant origins. However, under this model which describes concurrent re- and under-replication, a decrease in origin firing focused earlier in S phase could prevent exhaustion of replication factors and therefore reduce UR-DNA later in S phase.

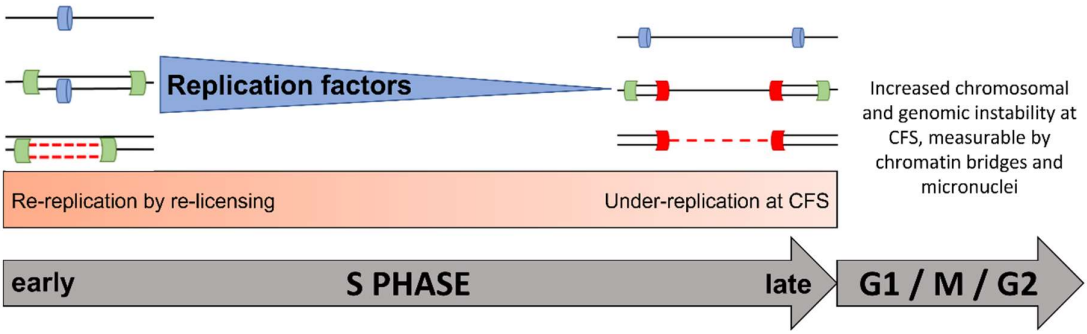

Figure 10.2. Proposed mechanism of under- and re-replicated DNA with CAiPi. Re-replication occurs early in S phase via re-licensing of origins. This increase in origin firing via re-licensing, combined with an increase in dormant origin firing via ATRi. leads to a decrease in replication factors as the cell moves through S phase. Therefore, UR-DNA occurs late in S phase, primarily at already hard to replicate CFSs. This results in chromosomal and genomic instability as the cell carries on through subsequent cell cycles. A reduction in origin firing via roscovitine reduces re-licensing and ATRi-induced dormant origin firing, reserving replication factors throughout the cell cycle and reducing UR-DNA.

Although there are associations between chromatin bridges and UR-DNA, a better analysis of error-prone chromosome segregation post RS may be quantification of UFBs. UFBs were first visualised in 2007, after identification of BLM-stained DNA bridges which did not stain for DAPI (Chan et al., 2007). Now known to contain uncondensed DNA, they are much more prevalent than chromatin bridges, existing in all cells in early anaphase before numbers begin to decline (Liu et al., 2014). FS-UFBs arise under RS conditions, and form between pairs of foci containing DNA repair proteins FANCD2 and FANCI (Chan et al., 2009, Naim and Rosselli, 2009). FS-UFBs are believed to arise at CFS due to UR-DNA, and UFBs correlate with 53BP1NB numbers (Moreno et al., 2016), so it may be useful to analyse their presence to further characterise the UR-DNA and CFS relationship. Additionally, inefficient resolution of FS-UFBs gave rise to micronuclei containing CFS DNA, so may explain CAiPi-associated increases in micronuclei (Chan et al., 2009).

10.6 Replication-associated transcriptional signature

Based on mechanistic investigations, a transcriptional signature of CAiPi sensitivity was curated. The signature included genes in the CMG complex which are critical for origin firing, the re-replication factors CDT1 and CDC6, and several factors involved in the resolution of UR-DNA including MiDAS factors. This signature was increased in E2 GSCs compared to E2 bulk cell lines. Additionally, as the difference between GSC and bulk sensitivity decreased or reversed in R10 and G7 respectively, the difference in signature score decreased. Although

promising, G7 GSC and bulk cells had comparable signature scores despite G7 bulk cell lines displaying increased sensitivity to targeting of the RS response. It may be that this signature was more predictive of GSC sensitivity, as opposed to GSC and bulk relationships. This signature is being explored in a validation cell line dataset, which should provide more insight into the utility of this as a predictive biomarker.

Interestingly, this signature predicted survival in several populations of GBM patients, including in the large CGGA dataset. Accordingly, the top-ranking patients for signature score had worse survival, suggesting that there is a population of patients with poor prognosis for which this DNA replication-associated signature is predictive. However, this signature was not predictive in several other datasets, including the commonly used TCGA dataset. Since CGGA was a larger dataset with longer survival results, differences in hazard ratios could be due to these differences in sample populations. However, the signature still predicted survival in some smaller datasets with shorter survival analysis. It may be that lack of heterogeneity within individual datasets may skew results. The LeeY GBM RNAseq dataset where the signature was predictive was curated from ten different studies, so likely represents a more diverse population of patients (Lee et al., 2008). Again, further validation datasets may be warranted to continue the investigation of the feasibility of this DNA replication signature.

10.7 CAiPi in a preclinical GBM model

A challenge that needs addressed for any studies into proposed GBM therapies is their ability to cross the BBB. The studies of the novel ATR and PARP inhibitors, BAY1895344 and pamiparib, in a GBM PDX murine model identified successful brain and tumour penetration suggesting that these inhibitors cross the BBB to some extent. At one hour, 20mg/kg BAY1895344 T/P ratio was as high as 49.1%, however this dropped to 21.8% after six hours. Conversely, pamiparib T/P ratio only reached ~20% but remained at those levels after six hours. However, despite pamiparib having lower T/P and B/P ratios at earlier time points, the concentrations of pamiparib reached in the tumour and brain were still clinically relevant and higher than those required to inhibit PARylation *in vitro*. Whereas by six hours the concentration of BAY1895344 in brain and tumour were borderline those required to inhibit phosphorylation of Chk1. By 24 hours both

pamiparib and BAY1895344 were not present in blood, brain or tumour, which raises an important question on optimal dosage and scheduling. A potential confounding factor for earlier time points was that with a highly vascular tumour such as GBM, inhibitors inside the vascularisation are likely also being measured, however it would be difficult to differentiate them. Since BAY1895344 was not retained in the brain as efficiently as pamiparib, future characterisation of BAY1895344 as a target of P-gp and BCRP efflux pumps may be useful, as the ATRi VX970 was found to have limited BBB penetration due to these transporters (Elmquist, 2019). The authors found that a P-gp and BCRP knockout model had a 22-fold increase in B/P ratio for VX970 versus a WT model. Pamiparib appears to be a promising brain and tumour penetrant PARPi. However, olaparib did not show brain penetrance in pre-clinical models but was present in every sample at pharmacodynamically significant levels as investigated by the OPARATIC trial (Hanna et al., 2020), which highlighted discrepancies between preclinical models and the clinic and the requirement for validation of any findings in GBM patients.

Activities of both ATR and PARP inhibitors are S phase dependent, and therefore it could be postulated that optimal efficacy *in vivo* may be reliant on prolonged exposure. The dose regimens investigated by this thesis provided only short exposures and more work is required to study the optimal schedule and dose for clinical translation. A twice daily regimen will likely prove most beneficial to ensure prolonged exposure to both inhibitors. Additionally, investigations are required for scheduling with IR. The study in this thesis dosed with CAiPi and then irradiated within one hour, however it is now known that the presence of the inhibitors in the brain and tumour was reduced between one and six hours. We therefore propose that irradiating one hour before dosing with CAiPi would provide maximal efficacy of this combination, as the concentrations of the inhibitors will peak as the cancer cells are responding to IR-induced damage and stress. Optimising scheduling requires further investigations and validation.

10.8 Concluding remarks

Highly heterogenous responses to CAiPi, genomics and transcriptomics within this GSC panel presented a challenge in mechanistic *in vitro* investigations and biomarker discovery, but also represents the highly heterogenous nature of GBM.

Despite the discovery that increased RS in GSCs was not solely predictive of CAiPi-sensitivity, the studies within this thesis identified dysregulated replication and associated genomic instability in CAiPi-sensitive GSCs. We propose that CAiPi-sensitivity is driven by this loss of replication coordination leading to chromosomal damage as cells move through S phase, as summarised in Figure 10.2. Accordingly, a transcriptomic signature which was curated based on these mechanistic investigations appears to have promising applicability in predicting CAiPi-sensitivity *in vitro* and in identifying a population of GBM patients with poor survival that may benefit from CAiPi.

Further work is required to fully validate this proposed mechanism. Since we propose that re-replication early in S phase is resulting in UR-DNA at genomic regions replicating later in S phase, inducing exogenous re-replication using overexpression of CDT1 to assess the effect on 53BP1NB numbers would be useful. It would also be of interest to investigate if a reduction in origin firing affects re-replication, to challenge the hypothesis that origin relicensing is driving re-replication. Lastly, for validation of this mechanism the effects of exogenous dNTPs or other exhaustive replicative factors could be analysed for their effects on 53BP1NB and CAiPi sensitivity. Investigating MiDAS both at baseline as a potential mechanism for GSCs to withstand increased RS and after CAiPi to investigate its role in maintaining chromosomal stability would be valuable, since it has been implicated in the transcriptomic data.

These data highlight that CAiPi is potently cytotoxic to a population of GSCs which can be selectively identified by a curated transcriptomic signature. This thesis would argue that targeting RS and the RS response represents a promising therapeutic strategy for selectively targeting this population of treatment resistant, recurrence-driving cancer cells to improve disease control, alleviate symptoms and improve clinical outcomes in GBM.

List of References

AASLAND, D., GOTZINGER, L., HAUCK, L., BERTE, N., MEYER, J., EFFENBERGER, M., SCHNEIDER, S., REUBER, E. E., ROOS, W. P., TOMICIC, M. T., KAINA, B. & CHRISTMANN, M. 2019. Temozolomide Induces Senescence and Repression of DNA Repair Pathways in Glioblastoma Cells via Activation of ATR-CHK1, p21, and NF-kappaB. *Cancer Res,* 79**,** 99-113.

AGUILERA, A. & GOMEZ-GONZALEZ, B. 2008. Genome instability: a mechanistic view of its causes and consequences. *Nat Rev Genet,* 9**,** 204-17.

AHMED, S. U., CARRUTHERS, R., GILMOUR, L., YILDIRIM, S., WATTS, C. & CHALMERS, A. J. 2015. Selective Inhibition of Parallel DNA Damage Response Pathways Optimizes Radiosensitization of Glioblastoma Stem-like Cells. *Cancer Res,* 75**,** 4416-28.

ALCANTARA LLAGUNO, S. R., WANG, Z., SUN, D., CHEN, J., XU, J., KIM, E., HATANPAA, K. J., RAISANEN, J. M., BURNS, D. K., JOHNSON, J. E. & PARADA, L. F. 2015. Adult Lineage-Restricted CNS Progenitors Specify Distinct Glioblastoma Subtypes. *Cancer Cell,* 28**,** 429-440.

ALTMEYER, M., NEELSEN, K. J., TELONI, F., POZDNYAKOVA, I., PELLEGRINO, S., GROFTE, M., RASK, M. D., STREICHER, W., JUNGMICHEL, S., NIELSEN, M. L. & LUKAS, J. 2015. Liquid demixing of intrinsically disordered proteins is seeded by poly(ADP-ribose). *Nat Commun,* 6**,** 8088.

ANACHKOVA, B., RUSSEV, G. & POIRIER, G. G. 1989. DNA replication and poly(ADP-ribosyl)ation of chromatin. *Cytobios,* 58**,** 19-28.

ANDERS, S., PYL, P. T. & HUBER, W. 2015. HTSeq--a Python framework to work with high-throughput sequencing data. *Bioinformatics,* 31**,** 166-9.

ANDREWS, S. 2010. *FastQC A Quality Control tool for High Throughput Sequence Data* [Online]. Available: http://www.bioinformatics.babraham.ac.uk/projects/fastqc/ [Accessed].

ANGLANA, M., APIOU, F., BENSIMON, A. & DEBATISSE, M. 2003. Dynamics of DNA replication in mammalian somatic cells: nucleotide pool modulates origin choice and interorigin spacing. *Cell,* 114**,** 385-94.

ANOOSHA, P., HUANG, L. T., SAKTHIVEL, R., KARUNAGARAN, D. & GROMIHA, M. M. 2015. Discrimination of driver and passenger mutations in epidermal growth factor receptor in cancer. *Mutat Res,* 780**,** 24-34.

APARICIO, T., GUILLOU, E., COLOMA, J., MONTOYA, G. & MENDEZ, J. 2009. The human GINS complex associates with Cdc45 and MCM and is essential for DNA replication. *Nucleic Acids Res,* 37**,** 2087-95.

ARCHAMBAULT, V., IKUI, A. E., DRAPKIN, B. J. & CROSS, F. R. 2005. Disruption of mechanisms that prevent rereplication triggers a DNA damage response. *Mol Cell Biol,* 25**,** 6707-21.

ARENTSON, E., FALOON, P., SEO, J., MOON, E., STUDTS, J. M., FREMONT, D. H. & CHOI, K. 2002. Oncogenic potential of the DNA replication licensing protein CDT1. *Oncogene,* 21**,** 1150-8.

AZVOLINSKY, A., GIRESI, P. G., LIEB, J. D. & ZAKIAN, V. A. 2009. Highly transcribed RNA polymerase II genes are impediments to replication fork progression in Saccharomyces cerevisiae. *Mol Cell,* 34**,** 722-34.

BACH, S., KNOCKAERT, M., REINHARDT, J., LOZACH, O., SCHMITT, S., BARATTE, B., KOKEN, M., COBURN, S. P., TANG, L., JIANG, T., LIANG, D. C., GALONS, H., DIERICK, J. F., PINNA, L. A., MEGGIO, F., TOTZKE, F., SCHACHTELE, C., LERMAN, A. S., CARNERO, A., WAN, Y., GRAY, N. & MEIJER, L. 2005. Roscovitine targets, protein kinases and pyridoxal kinase. *J Biol Chem,* 280**,** 31208-19.

BAILEY, L. J., BIANCHI, J. & DOHERTY, A. J. 2019. PrimPol is required for the maintenance of efficient nuclear and mitochondrial DNA replication in human cells. *Nucleic Acids Res,* 47**,** 4026-4038.

BALMUS, G., PILGER, D., COATES, J., DEMIR, M., SCZANIECKA-CLIFT, M., BARROS, A. C., WOODS, M., FU, B., YANG, F., CHEN, E., OSTERMAIER, M., STANKOVIC, T., PONSTINGL, H., HERZOG, M., YUSA, K., MARTINEZ, F. M., DURANT, S. T., GALANTY, Y., BELI, P., ADAMS, D. J., BRADLEY, A., METZAKOPIAN, E., FORMENT, J. V. & JACKSON, S. P. 2019. ATM orchestrates the DNA-damage response to counter toxic non-homologous end-joining at broken replication forks. *Nat Commun,* 10**,** 87.

BAO, S., WU, Q., MCLENDON, R. E., HAO, Y., SHI, Q., HJELMELAND, A. B., DEWHIRST, M. W., BIGNER, D. D. & RICH, J. N. 2006. Glioma stem cells promote radioresistance by preferential activation of the DNA damage response. *Nature,* 444**,** 756-60.

BARAZZUOL, L., JENA, R., BURNET, N. G., MEIRA, L. B., JEYNES, J. C., KIRKBY, K. J. & KIRKBY, N. F. 2013. Evaluation of poly (ADP-ribose) polymerase inhibitor ABT-888 combined with radiotherapy and temozolomide in glioblastoma. *Radiat Oncol,* 8**,** 65.

BARBIE, D. A., TAMAYO, P., BOEHM, J. S., KIM, S. Y., MOODY, S. E., DUNN, I. F., SCHINZEL, A. C., SANDY, P., MEYLAN, E., SCHOLL, C., FROHLING, S., CHAN, E. M., SOS, M. L., MICHEL, K., MERMEL, C., SILVER, S. J., WEIR, B. A., REILING, J. H., SHENG, Q., GUPTA, P. B., WADLOW, R. C., LE, H., HOERSCH, S., WITTNER, B. S., RAMASWAMY, S., LIVINGSTON, D. M., SABATINI, D. M., MEYERSON, M., THOMAS, R. K., LANDER, E. S., MESIROV, J. P., ROOT, D. E., GILLILAND, D. G., JACKS, T. & HAHN, W. C. 2009. Systematic RNA interference reveals that oncogenic KRAS-driven cancers require TBK1. *Nature,* 462**,** 108-12.

BARTKOVA, J., HOREJSI, Z., KOED, K., KRAMER, A., TORT, F., ZIEGER, K., GULDBERG, P., SEHESTED, M., NESLAND, J. M., LUKAS, C., ORNTOFT, T., LUKAS, J. & BARTEK, J. 2005. DNA damage response as a candidate anti-cancer barrier in early human tumorigenesis. *Nature,* 434**,** 864-70.

BARTKOVA, J., REZAEI, N., LIONTOS, M., KARAKAIDOS, P., KLETSAS, D., ISSAEVA, N., VASSILIOU, L. V., KOLETTAS, E., NIFOROU, K., ZOUMPOURLIS, V. C., TAKAOKA, M., NAKAGAWA, H., TORT, F., FUGGER, K., JOHANSSON, F., SEHESTED, M., ANDERSEN, C. L., DYRSKJOT, L., ORNTOFT, T., LUKAS, J., KITTAS, C., HELLEDAY, T., HALAZONETIS, T. D., BARTEK, J. & GORGOULIS, V. G. 2006. Oncogene-induced senescence is part of the tumorigenesis barrier imposed by DNA damage checkpoints. *Nature,* 444**,** 633-7.

BASCHNAGEL, A. M., ELNAGGAR, J. H., VANBEEK, H. J., KROMKE, A. C., SKIBA, J. H., KAUSHIK, S., ABEL, L., CLARK, P. A., LONGHURST, C. A., NICKEL, K. P., LEAL, T. A., ZHAO, S. G. & KIMPLE, R. J. 2021. ATR Inhibitor M6620 (VX-970) Enhances the Effect of Radiation in Non-Small Cell Lung Cancer Brain Metastasis Patient-Derived Xenografts. *Mol Cancer Ther,* 20**,** 2129-2139.

BECK, C., ROBERT, I., REINA-SAN-MARTIN, B., SCHREIBER, V. & DANTZER, F. 2014. Poly(ADP-ribose) polymerases in double-strand break repair: focus on PARP1, PARP2 and PARP3. *Exp Cell Res,* 329**,** 18-25.

BECK, H., NAHSE-KUMPF, V., LARSEN, M. S., O'HANLON, K. A., PATZKE, S., HOLMBERG, C., MEJLVANG, J., GROTH, A., NIELSEN, O., SYLJUASEN, R. G. & SORENSEN, C. S. 2012. Cyclin-dependent kinase suppression by WEE1 kinase protects the genome through control of replication initiation and nucleotide consumption. *Mol Cell Biol,* 32**,** 4226-36.

BEIER, D., HAU, P., PROESCHOLDT, M., LOHMEIER, A., WISCHHUSEN, J., OEFNER, P. J., AIGNER, L., BRAWANSKI, A., BOGDAHN, U. & BEIER, C. P. 2007. CD133(+) and CD133(-) glioblastoma-derived cancer stem cells show differential growth characteristics and molecular profiles. *Cancer Res,* 67**,** 4010-5.

BEN-PORATH, I., THOMSON, M. W., CAREY, V. J., GE, R., BELL, G. W., REGEV, A. & WEINBERG, R. A. 2008. An embryonic stem cell-like gene expression signature in poorly differentiated aggressive human tumors. *Nat Genet,* 40**,** 499-507.

BERTI, M., RAY CHAUDHURI, A., THANGAVEL, S., GOMATHINAYAGAM, S., KENIG, S., VUJANOVIC, M., ODREMAN, F., GLATTER, T., GRAZIANO, S., MENDOZA-MALDONADO, R., MARINO, F., LUCIC, B., BIASIN, V., GSTAIGER, M., AEBERSOLD, R., SIDOROVA, J. M., MONNAT, R. J., JR., LOPES, M. & VINDIGNI, A. 2013. Human RECQ1 promotes restart of replication forks reversed by DNA topoisomerase I inhibition. *Nat Struct Mol Biol,* 20**,** 347-54.

BERTOLIN, A. P., HOFFMANN, J. S. & GOTTIFREDI, V. 2020. Under-Replicated DNA: The Byproduct of Large Genomes? *Cancers (Basel),* 12.

BESTER, A. C., RONIGER, M., OREN, Y. S., IM, M. M., SARNI, D., CHAOAT, M., BENSIMON, A., ZAMIR, G., SHEWACH, D. S. & KEREM, B. 2011. Nucleotide deficiency promotes genomic instability in early stages of cancer development. *Cell,* 145**,** 435-46.

BETOUS, R., MASON, A. C., RAMBO, R. P., BANSBACH, C. E., BADU-NKANSAH, A., SIRBU, B. M., EICHMAN, B. F. & CORTEZ, D. 2012. SMARCAL1 catalyzes fork regression and Holliday junction migration to maintain genome stability during DNA replication. *Genes Dev,* 26**,** 151-62.

BHOWMICK, R., MINOCHERHOMJI, S. & HICKSON, I. D. 2016. RAD52 Facilitates Mitotic DNA Synthesis Following Replication Stress. *Mol Cell,* 64**,** 1117-1126.

BLOW, J. J. & GE, X. Q. 2009. A model for DNA replication showing how dormant origins safeguard against replication fork failure. *EMBO Rep,* 10**,** 406-12.

BOLGER, A. M., LOHSE, M. & USADEL, B. 2014. Trimmomatic: a flexible trimmer for Illumina sequence data. *Bioinformatics,* 30**,** 2114-20.

BONNET, D. & DICK, J. E. 1997. Human acute myeloid leukemia is organized as a hierarchy that originates from a primitive hematopoietic cell. *Nat Med,* 3**,** 730-7.

BOOS, D. & FERREIRA, P. 2019. Origin Firing Regulations to Control Genome Replication Timing. *Genes (Basel),* 10.

BOUKERROUCHA, M., JOSSE, C., SEGERS, K., EL-GUENDI, S., FRERES, P., JERUSALEM, G. & BOURS, V. 2015. BRCA1 germline mutation and glioblastoma development: report of cases. *BMC Cancer,* 15**,** 181.

BOWMAN, R. L., WANG, Q., CARRO, A., VERHAAK, R. G. & SQUATRITO, M. 2017. GlioVis data portal for visualization and analysis of brain tumor expression datasets. *Neuro Oncol,* 19**,** 139-141.

BRENNAN, C. W., VERHAAK, R. G., MCKENNA, A., CAMPOS, B., NOUSHMEHR, H., SALAMA, S. R., ZHENG, S., CHAKRAVARTY, D., SANBORN, J. Z., BERMAN, S. H., BEROUKHIM, R., BERNARD, B., WU, C. J., GENOVESE, G., SHMULEVICH, I., BARNHOLTZ-SLOAN, J., ZOU, L., VEGESNA, R., SHUKLA, S. A., CIRIELLO, G., YUNG, W. K., ZHANG, W., SOUGNEZ, C., MIKKELSEN, T., ALDAPE, K., BIGNER, D. D., VAN MEIR, E. G., PRADOS, M., SLOAN, A., BLACK, K. L., ESCHBACHER, J., FINOCCHIARO, G., FRIEDMAN, W., ANDREWS, D. W., GUHA, A., IACOCCA, M., O'NEILL, B. P., FOLTZ, G., MYERS, J., WEISENBERGER, D. J., PENNY, R., KUCHERLAPATI, R., PEROU,

C. M., HAYES, D. N., GIBBS, R., MARRA, M., MILLS, G. B., LANDER, E., SPELLMAN, P., WILSON, R., SANDER, C., WEINSTEIN, J., MEYERSON, M., GABRIEL, S., LAIRD, P. W., HAUSSLER, D., GETZ, G., CHIN, L. & NETWORK, T. R. 2013. The somatic genomic landscape of glioblastoma. *Cell,* 155**,** 462-77.

BRESCIA, P., ORTENSI, B., FORNASARI, L., LEVI, D., BROGGI, G. & PELICCI, G. 2013. CD133 is essential for glioblastoma stem cell maintenance. *Stem Cells,* 31**,** 857-69.

BROWN, E. J. & BALTIMORE, D. 2000. ATR disruption leads to chromosomal fragmentation and early embryonic lethality. *Genes Dev,* 14**,** 397-402.

BRYANT, H. E., PETERMANN, E., SCHULTZ, N., JEMTH, A. S., LOSEVA, O., ISSAEVA, N., JOHANSSON, F., FERNANDEZ, S., MCGLYNN, P. & HELLEDAY, T. 2009. PARP is activated at stalled forks to mediate Mre11-dependent replication restart and recombination. *EMBO J,* 28**,** 2601-15.

BRYANT, H. E., SCHULTZ, N., THOMAS, H. D., PARKER, K. M., FLOWER, D., LOPEZ, E., KYLE, S., MEUTH, M., CURTIN, N. J. & HELLEDAY, T. 2005. Specific killing of BRCA2-deficient tumours with inhibitors of poly(ADP-ribose) polymerase. *Nature,* 434**,** 913-7.

BUISSON, R., BOISVERT, J. L., BENES, C. H. & ZOU, L. 2015. Distinct but Concerted Roles of ATR, DNA-PK, and Chk1 in Countering Replication Stress during S Phase. *Mol Cell,* 59**,** 1011-24.

BYERS, L. A., WANG, J., NILSSON, M. B., FUJIMOTO, J., SAINTIGNY, P., YORDY, J., GIRI, U., PEYTON, M., FAN, Y. H., DIAO, L., MASRORPOUR, F., SHEN, L., LIU, W., DUCHEMANN, B., TUMULA, P., BHARDWAJ, V., WELSH, J., WEBER, S., GLISSON, B. S., KALHOR, N., WISTUBA, II, GIRARD, L., LIPPMAN, S. M., MILLS, G. B., COOMBES, K. R., WEINSTEIN, J. N., MINNA, J. D. & HEYMACH, J. V. 2012. Proteomic profiling identifies dysregulated pathways in small cell lung cancer and novel therapeutic targets including PARP1. *Cancer Discov,* 2**,** 798-811.

CANCER GENOME ATLAS RESEARCH, N. 2008. Comprehensive genomic characterization defines human glioblastoma genes and core pathways. *Nature,* 455**,** 1061-8.

CARRUTHERS, R. 2015. *Response to ionising radiation of glioblastoma stem-like cells.*, University of Glasgow.

CARRUTHERS, R. D., AHMED, S. U., RAMACHANDRAN, S., STRATHDEE, K., KURIAN, K. M., HEDLEY, A., GOMEZ-ROMAN, N., KALNA, G., NEILSON, M., GILMOUR, L., STEVENSON, K. H., HAMMOND, E. M. & CHALMERS, A. J. 2018. Replication Stress Drives Constitutive Activation of the DNA Damage Response and Radioresistance in Glioblastoma Stem-like Cells. *Cancer Res,* 78**,** 5060-5071.

CASPER, A. M., NGHIEM, P., ARLT, M. F. & GLOVER, T. W. 2002. ATR regulates fragile site stability. *Cell,* 111**,** 779-89.

CAYROU, C., COULOMBE, P., VIGNERON, A., STANOJCIC, S., GANIER, O., PEIFFER, I., RIVALS, E., PUY, A., LAURENT-CHABALIER, S., DESPRAT, R. & MECHALI, M. 2011. Genome-scale analysis of metazoan replication origins reveals their organization in specific but flexible sites defined by conserved features. *Genome Res,* 21**,** 1438-49.

CERAMI, E., GAO, J., DOGRUSOZ, U., GROSS, B. E., SUMER, S. O., AKSOY, B. A., JACOBSEN, A., BYRNE, C. J., HEUER, M. L., LARSSON, E., ANTIPIN, Y., REVA, B., GOLDBERG, A. P., SANDER, C. & SCHULTZ, N. 2012. The cBio cancer genomics portal: an open platform for exploring multidimensional cancer genomics data. *Cancer Discov,* 2**,** 401-4.

CHAN, K. L., NORTH, P. S. & HICKSON, I. D. 2007. BLM is required for faithful chromosome segregation and its localization defines a class of ultrafine anaphase bridges. *EMBO J,* 26, 3397-409.

CHAN, K. L., PALMAI-PALLAG, T., YING, S. & HICKSON, I. D. 2009. Replication stress induces sister-chromatid bridging at fragile site loci in mitosis. *Nat Cell Biol,* 11, 753-60.

CHARRIER, J. D., DURRANT, S. J., GOLEC, J. M., KAY, D. P., KNEGTEL, R. M., MACCORMICK, S., MORTIMORE, M., O'DONNELL, M. E., PINDER, J. L., REAPER, P. M., RUTHERFORD, A. P., WANG, P. S., YOUNG, S. C. & POLLARD, J. R. 2011. Discovery of potent and selective inhibitors of ataxia telangiectasia mutated and Rad3 related (ATR) protein kinase as potential anticancer agents. *J Med Chem,* 54, 2320-30.

CHEDOTAL, A., KERJAN, G. & MOREAU-FAUVARQUE, C. 2005. The brain within the tumor: new roles for axon guidance molecules in cancers. *Cell Death Differ,* 12, 1044-56.

CIMINO, P. J., BREDEMEYER, A., ABEL, H. J. & DUNCAVAGE, E. J. 2015. A wide spectrum of EGFR mutations in glioblastoma is detected by a single clinical oncology targeted next-generation sequencing panel. *Exp Mol Pathol,* 98, 568-73.

COLEMAN, R. L., FLEMING, G. F., BRADY, M. F., SWISHER, E. M., STEFFENSEN, K. D., FRIEDLANDER, M., OKAMOTO, A., MOORE, K. N., EFRAT BEN-BARUCH, N., WERNER, T. L., CLOVEN, N. G., OAKNIN, A., DISILVESTRO, P. A., MORGAN, M. A., NAM, J. H., LEATH, C. A., 3RD, NICUM, S., HAGEMANN, A. R., LITTELL, R. D., CELLA, D., BARON-HAY, S., GARCIA-DONAS, J., MIZUNO, M., BELL-MCGUINN, K., SULLIVAN, D. M., BACH, B. A., BHATTACHARYA, S., RATAJCZAK, C. K., ANSELL, P. J., DINH, M. H., AGHAJANIAN, C. & BOOKMAN, M. A. 2019. Veliparib with First-Line Chemotherapy and as Maintenance Therapy in Ovarian Cancer. *N Engl J Med,* 381, 2403-2415.

COLEMAN, R. L., SILL, M. W., BELL-MCGUINN, K., AGHAJANIAN, C., GRAY, H. J., TEWARI, K. S., RUBIN, S. C., RUTHERFORD, T. J., CHAN, J. K., CHEN, A. & SWISHER, E. M. 2015. A phase II evaluation of the potent, highly selective PARP inhibitor veliparib in the treatment of persistent or recurrent epithelial ovarian, fallopian tube, or primary peritoneal cancer in patients who carry a germline BRCA1 or BRCA2 mutation - An NRG Oncology/Gynecologic Oncology Group study. *Gynecol Oncol,* 137, 386-91.

COLICCHIA, V., PETRONI, M., GUARGUAGLINI, G., SARDINA, F., SAHUN-RONCERO, M., CARBONARI, M., RICCI, B., HEIL, C., CAPALBO, C., BELARDINILLI, F., COPPA, A., PERUZZI, G., SCREPANTI, I., LAVIA, P., GULINO, A. & GIANNINI, G. 2017. PARP inhibitors enhance replication stress and cause mitotic catastrophe in MYCN-dependent neuroblastoma. *Oncogene,* 36, 4682-4691.

COLMAN, H., ZHANG, L., SULMAN, E. P., MCDONALD, J. M., SHOOSHTARI, N. L., RIVERA, A., POPOFF, S., NUTT, C. L., LOUIS, D. N., CAIRNCROSS, J. G., GILBERT, M. R., PHILLIPS, H. S., MEHTA, M. P., CHAKRAVARTI, A., PELLOSKI, C. E., BHAT, K., FEUERSTEIN, B. G., JENKINS, R. B. & ALDAPE, K. 2010. A multigene predictor of outcome in glioblastoma. *Neuro Oncol,* 12, 49-57.

CONTI, C., SACCA, B., HERRICK, J., LALOU, C., POMMIER, Y. & BENSIMON, A. 2007. Replication fork velocities at adjacent replication origins are coordinately modified during DNA replication in human cells. *Mol Biol Cell,* 18, 3059-67.

CORTEZ, D., GLICK, G. & ELLEDGE, S. J. 2004. Minichromosome maintenance proteins are direct targets of the ATM and ATR checkpoint kinases. *Proc Natl Acad Sci U S A,* 101**,** 10078-83.

COSTELLO, J. F., FUTSCHER, B. W., TANO, K., GRAUNKE, D. M. & PIEPER, R. O. 1994. Graded methylation in the promoter and body of the O6-methylguanine DNA methyltransferase (MGMT) gene correlates with MGMT expression in human glioma cells. *J Biol Chem,* 269**,** 17228-37.

COUCH, F. B., BANSBACH, C. E., DRISCOLL, R., LUZWICK, J. W., GLICK, G. G., BETOUS, R., CARROLL, C. M., JUNG, S. Y., QIN, J., CIMPRICH, K. A. & CORTEZ, D. 2013. ATR phosphorylates SMARCAL1 to prevent replication fork collapse. *Genes Dev,* 27**,** 1610-23.

CRINIERE, E., KALOSHI, G., LAIGLE-DONADEY, F., LEJEUNE, J., AUGER, N., BENOUAICH-AMIEL, A., EVERHARD, S., MOKHTARI, K., POLIVKA, M., DELATTRE, J. Y., HOANG-XUAN, K., THILLET, J. & SANSON, M. 2007. MGMT prognostic impact on glioblastoma is dependent on therapeutic modalities. *J Neurooncol,* 83**,** 173-9.

DAS, S. P., BORRMAN, T., LIU, V. W., YANG, S. C., BECHHOEFER, J. & RHIND, N. 2015. Replication timing is regulated by the number of MCMs loaded at origins. *Genome Res,* 25**,** 1886-92.

DAS, S. P. & RHIND, N. 2016. How and why multiple MCMs are loaded at origins of DNA replication. *Bioessays,* 38**,** 613-7.

DAVIDSON, I. F., LI, A. & BLOW, J. J. 2006. Deregulated replication licensing causes DNA fragmentation consistent with head-to-tail fork collision. *Mol Cell,* 24**,** 433-43.

DE BONO, J., RAMANATHAN, R. K., MINA, L., CHUGH, R., GLASPY, J., RAFII, S., KAYE, S., SACHDEV, J., HEYMACH, J., SMITH, D. C., HENSHAW, J. W., HERRIOTT, A., PATTERSON, M., CURTIN, N. J., BYERS, L. A. & WAINBERG, Z. A. 2017. Phase I, Dose-Escalation, Two-Part Trial of the PARP Inhibitor Talazoparib in Patients with Advanced Germline BRCA1/2 Mutations and Selected Sporadic Cancers. *Cancer Discov,* 7**,** 620-629.

DE KLEIN, A., MUIJTJENS, M., VAN OS, R., VERHOEVEN, Y., SMIT, B., CARR, A. M., LEHMANN, A. R. & HOEIJMAKERS, J. H. 2000. Targeted disruption of the cell-cycle checkpoint gene ATR leads to early embryonic lethality in mice. *Curr Biol,* 10**,** 479-82.

DI MICCO, R., FUMAGALLI, M., CICALESE, A., PICCININ, S., GASPARINI, P., LUISE, C., SCHURRA, C., GARRE, M., NUCIFORO, P. G., BENSIMON, A., MAESTRO, R., PELICCI, P. G. & D'ADDA DI FAGAGNA, F. 2006. Oncogene-induced senescence is a DNA damage response triggered by DNA hyper-replication. *Nature,* 444**,** 638-42.

DIBITETTO, D., SIMS, J. R., ASCENCAO, C. F. R., FENG, K., KIM, D., OBERLY, S., FREIRE, R. & SMOLKA, M. B. 2020. Intrinsic ATR signaling shapes DNA end resection and suppresses toxic DNA-PKcs signaling. *NAR Cancer,* 2**,** zcaa006.

DIRKSE, A., GOLEBIEWSKA, A., BUDER, T., NAZAROV, P. V., MULLER, A., POOVATHINGAL, S., BRONS, N. H. C., LEITE, S., SAUVAGEOT, N., SARKISJAN, D., SEYFRID, M., FRITAH, S., STIEBER, D., MICHELUCCI, A., HERTEL, F., HEROLD-MENDE, C., AZUAJE, F., SKUPIN, A., BJERKVIG, R., DEUTSCH, A., VOSS-BOHME, A. & NICLOU, S. P. 2019. Stem cell-associated heterogeneity in Glioblastoma results from intrinsic tumor plasticity shaped by the microenvironment. *Nat Commun,* 10**,** 1787.

DOETSCH, F., PETREANU, L., CAILLE, I., GARCIA-VERDUGO, J. M. & ALVAREZ-BUYLLA, A. 2002. EGF converts transit-amplifying neurogenic precursors in the adult brain into multipotent stem cells. *Neuron,* 36**,** 1021-34.

DOMINGUEZ-SOLA, D., YING, C. Y., GRANDORI, C., RUGGIERO, L., CHEN, B., LI, M., GALLOWAY, D. A., GU, W., GAUTIER, J. & DALLA-FAVERA, R. 2007. Non-transcriptional control of DNA replication by c-Myc. *Nature,* 448**,** 445-51.

DONAWHO, C. K., LUO, Y., LUO, Y., PENNING, T. D., BAUCH, J. L., BOUSKA, J. J., BONTCHEVA-DIAZ, V. D., COX, B. F., DEWEESE, T. L., DILLEHAY, L. E., FERGUSON, D. C., GHOREISHI-HAACK, N. S., GRIMM, D. R., GUAN, R., HAN, E. K., HOLLEY-SHANKS, R. R., HRISTOV, B., IDLER, K. B., JARVIS, K., JOHNSON, E. F., KLEINBERG, L. R., KLINGHOFER, V., LASKO, L. M., LIU, X., MARSH, K. C., MCGONIGAL, T. P., MEULBROEK, J. A., OLSON, A. M., PALMA, J. P., RODRIGUEZ, L. E., SHI, Y., STAVROPOULOS, J. A., TSURUTANI, A. C., ZHU, G. D., ROSENBERG, S. H., GIRANDA, V. L. & FROST, D. J. 2007. ABT-888, an orally active poly(ADP-ribose) polymerase inhibitor that potentiates DNA-damaging agents in preclinical tumor models. *Clin Cancer Res,* 13**,** 2728-37.

DREYER, S. B., UPSTILL-GODDARD, R., PAULUS-HOCK, V., PARIS, C., LAMPRAKI, E. M., DRAY, E., SERRELS, B., CALIGIURI, G., REBUS, S., PLENKER, D., GALLUZZO, Z., BRUNTON, H., CUNNINGHAM, R., TESSON, M., NOURSE, C., BAILEY, U. M., JONES, M., MORAN-JONES, K., WRIGHT, D. W., DUTHIE, F., OIEN, K., EVERS, L., MCKAY, C. J., MCGREGOR, G. A., GULATI, A., BROUGH, R., BAJRAMI, I., PETTITT, S., DZIUBINSKI, M. L., CANDIDO, J., BALKWILL, F., BARRY, S. T., GRUTZMANN, R., RAHIB, L., GLASGOW PRECISION ONCOLOGY, L., AUSTRALIAN PANCREATIC CANCER GENOME, I., JOHNS, A., PAJIC, M., FROELING, F. E. M., BEER, P., MUSGROVE, E. A., PETERSEN, G. M., ASHWORTH, A., FRAME, M. C., CRAWFORD, H. C., SIMEONE, D. M., LORD, C., MUKHOPADHYAY, D., PILARSKY, C., TUVESON, D. A., COOKE, S. L., JAMIESON, N. B., MORTON, J. P., SANSOM, O. J., BAILEY, P. J., BIANKIN, A. V. & CHANG, D. K. 2021. Targeting DNA Damage Response and Replication Stress in Pancreatic Cancer. *Gastroenterology,* 160**,** 362-377 e13.

DUFOUR, C., CADUSSEAU, J., VARLET, P., SURENA, A. L., DE FARIA, G. P., DIAS-MORAIS, A., AUGER, N., LEONARD, N., DAUDIGEOS, E., DANTAS-BARBOSA, C., GRILL, J., LAZAR, V., DESSEN, P., VASSAL, G., PREVOT, V., SHARIF, A., CHNEIWEISS, H. & JUNIER, M. P. 2009. Astrocytes reverted to a neural progenitor-like state with transforming growth factor alpha are sensitized to cancerous transformation. *Stem Cells,* 27**,** 2373-82.

DUKAJ, L. & RHIND, N. 2021. The capacity of origins to load MCM establishes replication timing patterns. *PLoS Genet,* 17**,** e1009467.

DUNGEY, F. A., LOSER, D. A. & CHALMERS, A. J. 2008. Replication-dependent radiosensitization of human glioma cells by inhibition of poly(ADP-Ribose) polymerase: mechanisms and therapeutic potential. *Int J Radiat Oncol Biol Phys,* 72**,** 1188-97.

DUNGRAWALA, H., ROSE, K. L., BHAT, K. P., MOHNI, K. N., GLICK, G. G., COUCH, F. B. & CORTEZ, D. 2015. The Replication Checkpoint Prevents Two Types of Fork Collapse without Regulating Replisome Stability. *Mol Cell,* 59**,** 998-1010.

DURMUS, S., SPARIDANS, R. W., VAN ESCH, A., WAGENAAR, E., BEIJNEN, J. H. & SCHINKEL, A. H. 2015. Breast cancer resistance protein (BCRP/ABCG2) and P-glycoprotein (P-GP/ABCB1) restrict oral availability and brain accumulation of the PARP inhibitor rucaparib (AG-014699). *Pharm Res,* 32**,** 37-46.

DZIADKOWIEC, K. N., GASIOROWSKA, E., NOWAK-MARKWITZ, E. & JANKOWSKA, A. 2016. PARP inhibitors: review of mechanisms of action and BRCA1/2 mutation targeting. *Prz Menopauzalny,* 15, 215-219.

EICH, M., ROOS, W. P., NIKOLOVA, T. & KAINA, B. 2013. Contribution of ATM and ATR to the resistance of glioblastoma and malignant melanoma cells to the methylating anticancer drug temozolomide. *Mol Cancer Ther,* 12, 2529-40.

ELMQUIST, S. T. A. M. M. K. D. B. A. C. M. T. J. N. S. W. F. 2019. CNS delivery of VX-970: A selective ATR inhibitor for radiosensitization in GBM [abstract]. *American Association for Cancer Research,* 79.

ELVERS, I., JOHANSSON, F., GROTH, P., ERIXON, K. & HELLEDAY, T. 2011. UV stalled replication forks restart by re-priming in human fibroblasts. *Nucleic Acids Res,* 39, 7049-57.

ERAMO, A., RICCI-VITIANI, L., ZEUNER, A., PALLINI, R., LOTTI, F., SETTE, G., PILOZZI, E., LAROCCA, L. M., PESCHLE, C. & DE MARIA, R. 2006. Chemotherapy resistance of glioblastoma stem cells. *Cell Death Differ,* 13, 1238-41.

ERICE, O., SMITH, M. P., WHITE, R., GOICOECHEA, I., BARRIUSO, J., JONES, C., MARGISON, G. P., ACOSTA, J. C., WELLBROCK, C. & AROZARENA, I. 2015. MGMT Expression Predicts PARP-Mediated Resistance to Temozolomide. *Mol Cancer Ther,* 14, 1236-46.

EYKELENBOOM, J. K., HARTE, E. C., CANAVAN, L., PASTOR-PEIDRO, A., CALVO-ASENSIO, I., LLORENS-AGOST, M. & LOWNDES, N. F. 2013. ATR activates the S-M checkpoint during unperturbed growth to ensure sufficient replication prior to mitotic onset. *Cell Rep,* 5, 1095-107.

FAEL AL-MAYHANI, T. M., BALL, S. L., ZHAO, J. W., FAWCETT, J., ICHIMURA, K., COLLINS, P. V. & WATTS, C. 2009. An efficient method for derivation and propagation of glioblastoma cell lines that conserves the molecular profile of their original tumours. *J Neurosci Methods,* 176, 192-9.

FARMER, H., MCCABE, N., LORD, C. J., TUTT, A. N., JOHNSON, D. A., RICHARDSON, T. B., SANTAROSA, M., DILLON, K. J., HICKSON, I., KNIGHTS, C., MARTIN, N. M., JACKSON, S. P., SMITH, G. C. & ASHWORTH, A. 2005. Targeting the DNA repair defect in BRCA mutant cells as a therapeutic strategy. *Nature,* 434, 917-21.

FOKAS, E., PREVO, R., POLLARD, J. R., REAPER, P. M., CHARLTON, P. A., CORNELISSEN, B., VALLIS, K. A., HAMMOND, E. M., OLCINA, M. M., GILLIES MCKENNA, W., MUSCHEL, R. J. & BRUNNER, T. B. 2012. Targeting ATR in vivo using the novel inhibitor VE-822 results in selective sensitization of pancreatic tumors to radiation. *Cell Death Dis,* 3, e441.

FONG, P. C., YAP, T. A., BOSS, D. S., CARDEN, C. P., MERGUI-ROELVINK, M., GOURLEY, C., DE GREVE, J., LUBINSKI, J., SHANLEY, S., MESSIOU, C., A'HERN, R., TUTT, A., ASHWORTH, A., STONE, J., CARMICHAEL, J., SCHELLENS, J. H., DE BONO, J. S. & KAYE, S. B. 2010. Poly(ADP)-ribose polymerase inhibition: frequent durable responses in BRCA carrier ovarian cancer correlating with platinum-free interval. *J Clin Oncol,* 28, 2512-9.

FRAGKOS, M., GANIER, O., COULOMBE, P. & MECHALI, M. 2015. DNA replication origin activation in space and time. *Nat Rev Mol Cell Biol,* 16, 360-74.

FREIJE, W. A., CASTRO-VARGAS, F. E., FANG, Z., HORVATH, S., CLOUGHESY, T., LIAU, L. M., MISCHEL, P. S. & NELSON, S. F. 2004. Gene expression profiling of gliomas strongly predicts survival. *Cancer Res,* 64, 6503-10.

FU, H., REDON, C. E., THAKUR, B. L., UTANI, K., SEBASTIAN, R., JANG, S. M., GROSS, J. M., MOSAVARPOUR, S., MARKS, A. B., ZHUANG, S. Z., LAZAR, S. B., RAO, M., MENCER, S. T., BARIS, A. M., PONGOR, L. S. & ALADJEM, M. I.

2021. Dynamics of replication origin over-activation. *Nat Commun,* 12**,** 3448.

FULTON, B., SHORT, S. C., JAMES, A., NOWICKI, S., MCBAIN, C., JEFFERIES, S., KELLY, C., STOBO, J., MORRIS, A., WILLIAMSON, A. & CHALMERS, A. J. 2018. PARADIGM-2: Two parallel phase I studies of olaparib and radiotherapy or olaparib and radiotherapy plus temozolomide in patients with newly diagnosed glioblastoma, with treatment stratified by MGMT status. *Clin Transl Radiat Oncol,* 8**,** 12-16.

GALLI, R., BINDA, E., ORFANELLI, U., CIPELLETTI, B., GRITTI, A., DE VITIS, S., FIOCCO, R., FORONI, C., DIMECO, F. & VESCOVI, A. 2004. Isolation and characterization of tumorigenic, stem-like neural precursors from human glioblastoma. *Cancer Res,* 64**,** 7011-21.

GAN, W., GUAN, Z., LIU, J., GUI, T., SHEN, K., MANLEY, J. L. & LI, X. 2011. R-loop-mediated genomic instability is caused by impairment of replication fork progression. *Genes Dev,* 25**,** 2041-56.

GE, X. Q., JACKSON, D. A. & BLOW, J. J. 2007. Dormant origins licensed by excess Mcm2-7 are required for human cells to survive replicative stress. *Genes Dev,* 21**,** 3331-41.

GENOIS, M. M., GAGNE, J. P., YASUHARA, T., JACKSON, J., SAXENA, S., LANGELIER, M. F., AHEL, I., BEDFORD, M. T., PASCAL, J. M., VINDIGNI, A., POIRIER, G. G. & ZOU, L. 2021. CARM1 regulates replication fork speed and stress response by stimulating PARP1. *Mol Cell,* 81**,** 784-800 e8.

GILL, B. J., PISAPIA, D. J., MALONE, H. R., GOLDSTEIN, H., LEI, L., SONABEND, A., YUN, J., SAMANAMUD, J., SIMS, J. S., BANU, M., DOVAS, A., TEICH, A. F., SHETH, S. A., MCKHANN, G. M., SISTI, M. B., BRUCE, J. N., SIMS, P. A. & CANOLL, P. 2014. MRI-localized biopsies reveal subtype-specific differences in molecular and cellular composition at the margins of glioblastoma. *Proc Natl Acad Sci U S A,* 111**,** 12550-5.

GONZALEZ BESTEIRO, M. A., CALZETTA, N. L., LOUREIRO, S. M., HABIF, M., BETOUS, R., PILLAIRE, M. J., MAFFIA, A., SABBIONEDA, S., HOFFMANN, J. S. & GOTTIFREDI, V. 2019. Chk1 loss creates replication barriers that compromise cell survival independently of excess origin firing. *EMBO J,* 38**,** e101284.

GONZALEZ, S., KLATT, P., DELGADO, S., CONDE, E., LOPEZ-RIOS, F., SANCHEZ-CESPEDES, M., MENDEZ, J., ANTEQUERA, F. & SERRANO, M. 2006. Oncogenic activity of Cdc6 through repression of the INK4/ARF locus. *Nature,* 440**,** 702-6.

GORGOULIS, V. G., VASSILIOU, L. V., KARAKAIDOS, P., ZACHARATOS, P., KOTSINAS, A., LILOGLOU, T., VENERE, M., DITULLIO, R. A., JR., KASTRINAKIS, N. G., LEVY, B., KLETSAS, D., YONETA, A., HERLYN, M., KITTAS, C. & HALAZONETIS, T. D. 2005. Activation of the DNA damage checkpoint and genomic instability in human precancerous lesions. *Nature,* 434**,** 907-13.

GOUT, J., PERKHOFER, L., MORAWE, M., ARNOLD, F., IHLE, M., BIBER, S., LANGE, S., ROGER, E., KRAUS, J. M., STIFTER, K., HAHN, S. A., ZAMPERONE, A., ENGLEITNER, T., MULLER, M., WALTER, K., RODRIGUEZ-AZNAR, E., SAINZ, B., JR., HERMANN, P. C., HESSMANN, E., MULLER, S., AZOITEI, N., LECHEL, A., LIEBAU, S., WAGNER, M., SIMEONE, D. M., KESTLER, H. A., SEUFFERLEIN, T., WIESMULLER, L., RAD, R., FRAPPART, P. O. & KLEGER, A. 2021. Synergistic targeting and resistance to PARP inhibition in DNA damage repair-deficient pancreatic cancer. *Gut,* 70**,** 743-760.

GREEN, B. M. & LI, J. J. 2005. Loss of rereplication control in Saccharomyces cerevisiae results in extensive DNA damage. *Mol Biol Cell,* 16**,** 421-32.

GUERRERO LLOBET, S., BHATTACHARYA, A., EVERTS, M., KOK, K., VAN DER VEGT, B., FEHRMANN, R. S. N. & VAN VUGT, M. 2022. An mRNA expression-based signature for oncogene-induced replication-stress. *Oncogene,* 41**,** 1216-1224.

GUPTA, S. K., KIZILBASH, S. H., CARLSON, B. L., MLADEK, A. C., BOAKYE-AGYEMAN, F., BAKKEN, K. K., POKORNY, J. L., SCHROEDER, M. A., DECKER, P. A., CEN, L., ECKEL-PASSOW, J. E., SARKAR, G., BALLMAN, K. V., REID, J. M., JENKINS, R. B., VERHAAK, R. G., SULMAN, E. P., KITANGE, G. J. & SARKARIA, J. N. 2016. Delineation of MGMT Hypermethylation as a Biomarker for Veliparib-Mediated Temozolomide-Sensitizing Therapy of Glioblastoma. *J Natl Cancer Inst,* 108.

HANADA, K., BUDZOWSKA, M., DAVIES, S. L., VAN DRUNEN, E., ONIZAWA, H., BEVERLOO, H. B., MAAS, A., ESSERS, J., HICKSON, I. D. & KANAAR, R. 2007. The structure-specific endonuclease Mus81 contributes to replication restart by generating double-strand DNA breaks. *Nat Struct Mol Biol,* 14**,** 1096-104.

HANNA, C., KURIAN, K. M., WILLIAMS, K., WATTS, C., JACKSON, A., CARRUTHERS, R., STRATHDEE, K., CRUICKSHANK, G., DUNN, L., ERRIDGE, S., GODFREY, L., JEFFERIES, S., MCBAIN, C., SLEIGH, R., MCCORMICK, A., PITTMAN, M., HALFORD, S. & CHALMERS, A. J. 2020. Pharmacokinetics, safety, and tolerability of olaparib and temozolomide for recurrent glioblastoma: results of the phase I OPARATIC trial. *Neuro Oncol,* 22**,** 1840-1850.

HANSEL-HERTSCH, R., DI ANTONIO, M. & BALASUBRAMANIAN, S. 2017. DNA G-quadruplexes in the human genome: detection, functions and therapeutic potential. *Nat Rev Mol Cell Biol,* 18**,** 279-284.

HANZELMANN, S., CASTELO, R. & GUINNEY, J. 2013. GSVA: gene set variation analysis for microarray and RNA-seq data. *BMC Bioinformatics,* 14**,** 7.

HANZLIKOVA, H., GITTENS, W., KREJCIKOVA, K., ZENG, Z. & CALDECOTT, K. W. 2017. Overlapping roles for PARP1 and PARP2 in the recruitment of endogenous XRCC1 and PNKP into oxidized chromatin. *Nucleic Acids Res,* 45**,** 2546-2557.

HARRIGAN, J. A., BELOTSERKOVSKAYA, R., COATES, J., DIMITROVA, D. S., POLO, S. E., BRADSHAW, C. R., FRASER, P. & JACKSON, S. P. 2011. Replication stress induces 53BP1-containing OPT domains in G1 cells. *J Cell Biol,* 193**,** 97-108.

HEACOCK, M. L., STEFANICK, D. F., HORTON, J. K. & WILSON, S. H. 2010. Alkylation DNA damage in combination with PARP inhibition results in formation of S-phase-dependent double-strand breaks. *DNA Repair (Amst),* 9**,** 929-36.

HEGI, M. E., DISERENS, A.-C., GORLIA, T., HAMOU, M.-F., DE TRIBOLET, N., WELLER, M., KROS, J. M., HAINFELLNER, J. A., MASON, W., MARIANI, L., BROMBERG, J. E. C., HAU, P., MIRIMANOFF, R. O., CAIRNCROSS, J. G., JANZER, R. C. & STUPP, R. 2005. MGMT Gene Silencing and Benefit from Temozolomide in Glioblastoma. *New England Journal of Medicine,* 352**,** 997-1003.

HELMRICH, A., BALLARINO, M. & TORA, L. 2011. Collisions between replication and transcription complexes cause common fragile site instability at the longest human genes. *Mol Cell,* 44**,** 966-77.

HEMMATI, H. D., NAKANO, I., LAZAREFF, J. A., MASTERMAN-SMITH, M., GESCHWIND, D. H., BRONNER-FRASER, M. & KORNBLUM, H. I. 2003.

Cancerous stem cells can arise from pediatric brain tumors. *Proc Natl Acad Sci U S A,* 100, 15178-83.

HOFFELDER, D. R., LUO, L., BURKE, N. A., WATKINS, S. C., GOLLIN, S. M. & SAUNDERS, W. S. 2004. Resolution of anaphase bridges in cancer cells. *Chromosoma,* 112, 389-97.

HOOK, S. S., LIN, J. J. & DUTTA, A. 2007. Mechanisms to control rereplication and implications for cancer. *Curr Opin Cell Biol,* 19, 663-71.

HOPKINS, T. A., AINSWORTH, W. B., ELLIS, P. A., DONAWHO, C. K., DIGIAMMARINO, E. L., PANCHAL, S. C., ABRAHAM, V. C., ALGIRE, M. A., SHI, Y., OLSON, A. M., JOHNSON, E. F., WILSBACHER, J. L. & MAAG, D. 2019. PARP1 Trapping by PARP Inhibitors Drives Cytotoxicity in Both Cancer Cells and Healthy Bone Marrow. *Mol Cancer Res,* 17, 409-419.

HOPKINS, T. A., SHI, Y., RODRIGUEZ, L. E., SOLOMON, L. R., DONAWHO, C. K., DIGIAMMARINO, E. L., PANCHAL, S. C., WILSBACHER, J. L., GAO, W., OLSON, A. M., STOLARIK, D. F., OSTERLING, D. J., JOHNSON, E. F. & MAAG, D. 2015. Mechanistic Dissection of PARP1 Trapping and the Impact on In Vivo Tolerability and Efficacy of PARP Inhibitors. *Mol Cancer Res,* 13, 1465-77.

HU, Y. & SMYTH, G. K. 2009. ELDA: extreme limiting dilution analysis for comparing depleted and enriched populations in stem cell and other assays. *J Immunol Methods,* 347, 70-8.

IBARRA, A., SCHWOB, E. & MENDEZ, J. 2008. Excess MCM proteins protect human cells from replicative stress by licensing backup origins of replication. *Proc Natl Acad Sci U S A,* 105, 8956-61.

JACKSON, C. B., NOORBAKHSH, S. I., SUNDARAM, R. K., KALATHIL, A. N., GANESA, S., JIA, L., BRESLIN, H., BURGENSKE, D. M., GILAD, O., SARKARIA, J. N. & BINDRA, R. S. 2019. Temozolomide Sensitizes MGMT-Deficient Tumor Cells to ATR Inhibitors. *Cancer Res,* 79, 4331-4338.

JACKSON, D. A. & POMBO, A. 1998. Replicon clusters are stable units of chromosome structure: evidence that nuclear organization contributes to the efficient activation and propagation of S phase in human cells. *J Cell Biol,* 140, 1285-95.

JALILI, V., AFGAN, E., GU, Q., CLEMENTS, D., BLANKENBERG, D., GOECKS, J., TAYLOR, J. & NEKRUTENKO, A. 2020. The Galaxy platform for accessible, reproducible and collaborative biomedical analyses: 2020 update. *Nucleic Acids Res,* 48, W395-W402.

JETTE, N. R., RADHAMANI, S., ARTHUR, G., YE, R., GOUTAM, S., BOLYOS, A., PETERSEN, L. F., BOSE, P., BEBB, D. G. & LEES-MILLER, S. P. 2019. Combined poly-ADP ribose polymerase and ataxia-telangiectasia mutated/Rad3-related inhibition targets ataxia-telangiectasia mutated-deficient lung cancer cells. *Br J Cancer,* 121, 600-610.

JETTE, N. R., RADHAMANI, S., ARTHUR, G., YE, R., GOUTAM, S., BOLYOS, A., PETERSEN, L. F., BOSE, P., BEBB, D. G. & LEES-MILLER, S. P. 2020a. Correction: Combined poly-ADP ribose polymerase and ataxia-telangiectasia mutated/Rad3-related inhibition targets ataxia-telangiectasia mutated-deficient lung cancer cells. *Br J Cancer,* 122, 1872.

JETTE, N. R., RADHAMANI, S., YE, R., YU, Y., ARTHUR, G., GOUTAM, S., BISMAR, T. A., KUMAR, M., BOSE, P., YIP, S., KOLINSKY, M. & LEES-MILLER, S. P. 2020b. ATM-deficient lung, prostate and pancreatic cancer cells are acutely sensitive to the combination of olaparib and the ATR inhibitor AZD6738. *Genome Instability & Disease,* 1, 197-205.

JI, F., LIAO, H., PAN, S., OUYANG, L., JIA, F., FU, Z., ZHANG, F., GENG, X., WANG, X., LI, T., LIU, S., SYEDA, M. Z., CHEN, H., LI, W., CHEN, Z., SHEN, H. & YING, S. 2020. Genome-wide high-resolution mapping of mitotic DNA synthesis sites and common fragile sites by direct sequencing. *Cell Res,* 30**,** 1009-1023.

JIN, X., JIN, X., JUNG, J. E., BECK, S. & KIM, H. 2013. Cell surface Nestin is a biomarker for glioma stem cells. *Biochem Biophys Res Commun,* 433**,** 496-501.

JOHANNS, T. M., FU, Y., KOBAYASHI, D. K., MEI, Y., DUNN, I. F., MAO, D. D., KIM, A. H. & DUNN, G. P. 2016. High incidence of TERT mutation in brain tumor cell lines. *Brain Tumor Pathol,* 33**,** 222-7.

JONES, R. M., MORTUSEWICZ, O., AFZAL, I., LORVELLEC, M., GARCIA, P., HELLEDAY, T. & PETERMANN, E. 2013. Increased replication initiation and conflicts with transcription underlie Cyclin E-induced replication stress. *Oncogene,* 32**,** 3744-53.

JOO, K. M., KIM, S. Y., JIN, X., SONG, S. Y., KONG, D. S., LEE, J. I., JEON, J. W., KIM, M. H., KANG, B. G., JUNG, Y., JIN, J., HONG, S. C., PARK, W. Y., LEE, D. S., KIM, H. & NAM, D. H. 2008. Clinical and biological implications of CD133-positive and CD133-negative cells in glioblastomas. *Lab Invest,* 88**,** 808-15.

KASSAMBARA, A. 2020. ggpubr: 'ggplot2' Based Publication Ready Plots.

KASSAMBARA, A., KOSINSKI, M. & BIECEK, P. 2021. survminer: Drawing Survival Curves using 'ggplot2'.

KEDAR, P. S., STEFANICK, D. F., HORTON, J. K. & WILSON, S. H. 2012. Increased PARP-1 association with DNA in alkylation damaged, PARP-inhibited mouse fibroblasts. *Mol Cancer Res,* 10**,** 360-8.

KIM, D., LANGMEAD, B. & SALZBERG, S. L. 2015. HISAT: a fast spliced aligner with low memory requirements. *Nat Methods,* 12**,** 357-60.

KIM, D., LIU, Y., OBERLY, S., FREIRE, R. & SMOLKA, M. B. 2018. ATR-mediated proteome remodeling is a major determinant of homologous recombination capacity in cancer cells. *Nucleic Acids Res,* 46**,** 8311-8325.

KIM, H., GEORGE, E., RAGLAND, R., RAFAIL, S., ZHANG, R., KREPLER, C., MORGAN, M., HERLYN, M., BROWN, E. & SIMPKINS, F. 2017. Targeting the ATR/CHK1 Axis with PARP Inhibition Results in Tumor Regression in BRCA-Mutant Ovarian Cancer Models. *Clin Cancer Res,* 23**,** 3097-3108.

KIM, H., XU, H., GEORGE, E., HALLBERG, D., KUMAR, S., JAGANNATHAN, V., MEDVEDEV, S., KINOSE, Y., DEVINS, K., VERMA, P., LY, K., WANG, Y., GREENBERG, R. A., SCHWARTZ, L., JOHNSON, N., SCHARPF, R. B., MILLS, G. B., ZHANG, R., VELCULESCU, V. E., BROWN, E. J. & SIMPKINS, F. 2020. Combining PARP with ATR inhibition overcomes PARP inhibitor and platinum resistance in ovarian cancer models. *Nat Commun,* 11**,** 3726.

KING, D., SOUTHGATE, H. E. D., ROETSCHKE, S., GRAVELLS, P., FIELDS, L., WATSON, J. B., CHEN, L., CHAPMAN, D., HARRISON, D., YEOMANSON, D., CURTIN, N. J., TWEDDLE, D. A. & BRYANT, H. E. 2021. Increased Replication Stress Determines ATR Inhibitor Sensitivity in Neuroblastoma Cells. *Cancers (Basel),* 13.

KIZILBASH, S. H., GUPTA, S. K., CHANG, K., KAWASHIMA, R., PARRISH, K. E., CARLSON, B. L., BAKKEN, K. K., MLADEK, A. C., SCHROEDER, M. A., DECKER, P. A., KITANGE, G. J., SHEN, Y., FENG, Y., PROTTER, A. A., ELMQUIST, W. F. & SARKARIA, J. N. 2017. Restricted Delivery of Talazoparib Across the Blood-Brain Barrier Limits the Sensitizing Effects of PARP Inhibition on Temozolomide Therapy in Glioblastoma. *Mol Cancer Ther,* 16**,** 2735-2746.

KLEINBERG, L., SUPKO, J. G., MIKKELSEN, T., BLAKELEY, J. O. N., STEVENS, G., YE, X., DESIDERI, S., RYU, S., DESAI, B., GIRANDA, V. L. & GROSSMAN, S. A. 2013. ABSTRACT: Phase I adult brain tumor consortium (ABTC) trial of ABT-888 (veliparib), temozolomide (TMZ), and radiotherapy (RT) for newly diagnosed glioblastoma multiforme (GBM) including pharmacokinetic (PK) data. *Journal of Clinical Oncology,* 31**,** 2065-2065.

KNOTT, S. R., PEACE, J. M., OSTROW, A. Z., GAN, Y., REX, A. E., VIGGIANI, C. J., TAVARE, S. & APARICIO, O. M. 2012. Forkhead transcription factors establish origin timing and long-range clustering in S. cerevisiae. *Cell,* 148**,** 99-111.

KOESSINGER, A. L., KOESSINGER, D., STEVENSON, K., CLOIX, C., MITCHELL, L., NIXON, C., GOMEZ-ROMAN, N., CHALMERS, A. J., NORMAN, J. C. & TAIT, S. W. G. 2020. Quantitative in vivo bioluminescence imaging of orthotopic patient-derived glioblastoma xenografts. *Sci Rep,* 10**,** 15361.

KOHLER, C., KOALICK, D., FABRICIUS, A., PARPLYS, A. C., BORGMANN, K., POSPIECH, H. & GROSSE, F. 2016. Cdc45 is limiting for replication initiation in humans. *Cell Cycle,* 15**,** 974-85.

KOTSANTIS, P., PETERMANN, E. & BOULTON, S. J. 2018. Mechanisms of Oncogene-Induced Replication Stress: Jigsaw Falling into Place. *Cancer Discov,* 8**,** 537-555.

KOUNDRIOUKOFF, S., CARIGNON, S., TECHER, H., LETESSIER, A., BRISON, O. & DEBATISSE, M. 2013. Stepwise activation of the ATR signaling pathway upon increasing replication stress impacts fragile site integrity. *PLoS Genet,* 9**,** e1003643.

KUMAGAI, A., LEE, J., YOO, H. Y. & DUNPHY, W. G. 2006. TopBP1 activates the ATR-ATRIP complex. *Cell,* 124**,** 943-55.

KURZROCK, R., GALANIS, E., JOHNSON, D. R., KANSRA, V., WILCOXEN, K., MCCLURE, T., MARTELL, R. E. & AGARWAL, S. 2014. ABSTRACT: A phase I study of niraparib in combination with temozolomide (TMZ) in patients with advanced cancer. *Journal of Clinical Oncology,* 32**,** 2092-2092.

LAPIDOT, T., SIRARD, C., VORMOOR, J., MURDOCH, B., HOANG, T., CACERES-CORTES, J., MINDEN, M., PATERSON, B., CALIGIURI, M. A. & DICK, J. E. 1994. A cell initiating human acute myeloid leukaemia after transplantation into SCID mice. *Nature,* 367**,** 645-8.

LATHIA, J. D., MACK, S. C., MULKEARNS-HUBERT, E. E., VALENTIM, C. L. & RICH, J. N. 2015. Cancer stem cells in glioblastoma. *Genes Dev,* 29**,** 1203-17.

LAU, E., TSUJI, T., GUO, L., LU, S. H. & JIANG, W. 2007. The role of pre-replicative complex (pre-RC) components in oncogenesis. *FASEB J,* 21**,** 3786-94.

LAWLOR, D., MARTIN, P., BUSSCHOTS, S., THERY, J., O'LEARY, J. J., HENNESSY, B. T. & STORDAL, B. 2014. PARP Inhibitors as P-glyoprotein Substrates. *J Pharm Sci,* 103**,** 1913-20.

LE BEAU, M. M., RASSOOL, F. V., NEILLY, M. E., ESPINOSA, R., 3RD, GLOVER, T. W., SMITH, D. I. & MCKEITHAN, T. W. 1998. Replication of a common fragile site, FRA3B, occurs late in S phase and is delayed further upon induction: implications for the mechanism of fragile site induction. *Hum Mol Genet,* 7**,** 755-61.

LE, T. M., PODDAR, S., CAPRI, J. R., ABT, E. R., KIM, W., WEI, L., UONG, N. T., CHENG, C. M., BRAAS, D., NIKANJAM, M., RIX, P., MERKURJEV, D., ZARETSKY, J., KORNBLUM, H. I., RIBAS, A., HERSCHMAN, H. R., WHITELEGGE, J., FAULL, K. F., DONAHUE, T. R., CZERNIN, J. & RADU, C. G. 2017. ATR inhibition facilitates targeting of leukemia dependence on convergent nucleotide biosynthetic pathways. *Nat Commun,* 8**,** 241.

LEE, J., KOTLIAROVA, S., KOTLIAROV, Y., LI, A., SU, Q., DONIN, N. M., PASTORINO, S., PUROW, B. W., CHRISTOPHER, N., ZHANG, W., PARK, J. K. & FINE, H. A. 2006a. Tumor stem cells derived from glioblastomas cultured in bFGF and EGF more closely mirror the phenotype and genotype of primary tumors than do serum-cultured cell lines. *Cancer Cell,* 9**,** 391-403.

LEE, J., KUMAGAI, A. & DUNPHY, W. G. 2007. The Rad9-Hus1-Rad1 checkpoint clamp regulates interaction of TopBP1 with ATR. *J Biol Chem,* 282**,** 28036-44.

LEE, J. C., VIVANCO, I., BEROUKHIM, R., HUANG, J. H., FENG, W. L., DEBIASI, R. M., YOSHIMOTO, K., KING, J. C., NGHIEMPHU, P., YUZA, Y., XU, Q., GREULICH, H., THOMAS, R. K., PAEZ, J. G., PECK, T. C., LINHART, D. J., GLATT, K. A., GETZ, G., ONOFRIO, R., ZIAUGRA, L., LEVINE, R. L., GABRIEL, S., KAWAGUCHI, T., O'NEILL, K., KHAN, H., LIAU, L. M., NELSON, S. F., RAO, P. N., MISCHEL, P., PIEPER, R. O., CLOUGHESY, T., LEAHY, D. J., SELLERS, W. R., SAWYERS, C. L., MEYERSON, M. & MELLINGHOFF, I. K. 2006b. Epidermal growth factor receptor activation in glioblastoma through novel missense mutations in the extracellular domain. *PLoS Med,* 3**,** e485.

LEE, Y., SCHECK, A. C., CLOUGHESY, T. F., LAI, A., DONG, J., FAROOQI, H. K., LIAU, L. M., HORVATH, S., MISCHEL, P. S. & NELSON, S. F. 2008. Gene expression analysis of glioblastomas identifies the major molecular basis for the prognostic benefit of younger age. *BMC Med Genomics,* 1**,** 52.

LEIMBACHER, P. A., JONES, S. E., SHORROCKS, A. K., DE MARCO ZOMPIT, M., DAY, M., BLAAUWENDRAAD, J., BUNDSCHUH, D., BONHAM, S., FISCHER, R., FINK, D., KESSLER, B. M., OLIVER, A. W., PEARL, L. H., BLACKFORD, A. N. & STUCKI, M. 2019. MDC1 Interacts with TOPBP1 to Maintain Chromosomal Stability during Mitosis. *Mol Cell,* 74**,** 571-583 e8.

LEMMENS, B., HEGARAT, N., AKOPYAN, K., SALA-GASTON, J., BARTEK, J., HOCHEGGER, H. & LINDQVIST, A. 2018. DNA Replication Determines Timing of Mitosis by Restricting CDK1 and PLK1 Activation. *Mol Cell,* 71**,** 117-128 e3.

LESUEUR, P., LEQUESNE, J., GRELLARD, J. M., DUGUE, A., COQUAN, E., BRACHET, P. E., GEFFRELOT, J., KAO, W., EMERY, E., BERRO, D. H., CASTERA, L., GOARDON, N., LACROIX, J., LANGE, M., CAPEL, A., LECONTE, A., ANDRE, B., LEGER, A., LELAIDIER, A., CLARISSE, B. & STEFAN, D. 2019. Phase I/IIa study of concomitant radiotherapy with olaparib and temozolomide in unresectable or partially resectable glioblastoma: OLA-TMZ-RTE-01 trial protocol. *BMC Cancer,* 19**,** 198.

LETESSIER, A., MILLOT, G. A., KOUNDRIOUKOFF, S., LACHAGES, A. M., VOGT, N., HANSEN, R. S., MALFOY, B., BRISON, O. & DEBATISSE, M. 2011. Cell-type-specific replication initiation programs set fragility of the FRA3B fragile site. *Nature,* 470**,** 120-3.

LIGON, K. L., HUILLARD, E., MEHTA, S., KESARI, S., LIU, H., ALBERTA, J. A., BACHOO, R. M., KANE, M., LOUIS, D. N., DEPINHO, R. A., ANDERSON, D. J., STILES, C. D. & ROWITCH, D. H. 2007. Olig2-regulated lineage-restricted pathway controls replication competence in neural stem cells and malignant glioma. *Neuron,* 53**,** 503-17.

LIU, C., SAGE, J. C., MILLER, M. R., VERHAAK, R. G., HIPPENMEYER, S., VOGEL, H., FOREMAN, O., BRONSON, R. T., NISHIYAMA, A., LUO, L. & ZONG, H. 2011. Mosaic analysis with double markers reveals tumor cell of origin in glioma. *Cell,* 146**,** 209-21.

LIU, E., LEE, A. Y., CHIBA, T., OLSON, E., SUN, P. & WU, X. 2007. The ATR-mediated S phase checkpoint prevents rereplication in mammalian cells when licensing control is disrupted. *J Cell Biol,* 179**,** 643-57.

LIU, G., YUAN, X., ZENG, Z., TUNICI, P., NG, H., ABDULKADIR, I. R., LU, L., IRVIN, D., BLACK, K. L. & YU, J. S. 2006. Analysis of gene expression and chemoresistance of CD133+ cancer stem cells in glioblastoma. *Mol Cancer,* 5**,** 67.

LIU, H., TAKEDA, S., KUMAR, R., WESTERGARD, T. D., BROWN, E. J., PANDITA, T. K., CHENG, E. H. & HSIEH, J. J. 2010. Phosphorylation of MLL by ATR is required for execution of mammalian S-phase checkpoint. *Nature,* 467**,** 343-6.

LIU, J. J., CHAO, J. R., JIANG, M. C., NG, S. Y., YEN, J. J. & YANG-YEN, H. F. 1995. Ras transformation results in an elevated level of cyclin D1 and acceleration of G1 progression in NIH 3T3 cells. *Mol Cell Biol,* 15**,** 3654-63.

LIU, Q., GUNTUKU, S., CUI, X. S., MATSUOKA, S., CORTEZ, D., TAMAI, K., LUO, G., CARATTINI-RIVERA, S., DEMAYO, F., BRADLEY, A., DONEHOWER, L. A. & ELLEDGE, S. J. 2000. Chk1 is an essential kinase that is regulated by Atr and required for the G(2)/M DNA damage checkpoint. *Genes Dev,* 14**,** 1448-59.

LIU, Y., NIELSEN, C. F., YAO, Q. & HICKSON, I. D. 2014. The origins and processing of ultra fine anaphase DNA bridges. *Curr Opin Genet Dev,* 26**,** 1-5.

LLOYD, R. L., WIJNHOVEN, P. W. G., RAMOS-MONTOYA, A., WILSON, Z., ILLUZZI, G., FALENTA, K., JONES, G. N., JAMES, N., CHABBERT, C. D., STOTT, J., DEAN, E., LAU, A. & YOUNG, L. A. 2020. Combined PARP and ATR inhibition potentiates genome instability and cell death in ATM-deficient cancer cells. *Oncogene,* 39**,** 4869-4883.

LOPES, M., FOIANI, M. & SOGO, J. M. 2006. Multiple mechanisms control chromosome integrity after replication fork uncoupling and restart at irreparable UV lesions. *Mol Cell,* 21**,** 15-27.

LOTTAZ, C., BEIER, D., MEYER, K., KUMAR, P., HERMANN, A., SCHWARZ, J., JUNKER, M., OEFNER, P. J., BOGDAHN, U., WISCHHUSEN, J., SPANG, R., STORCH, A. & BEIER, C. P. 2010. Transcriptional profiles of CD133+ and CD133- glioblastoma-derived cancer stem cell lines suggest different cells of origin. *Cancer Res,* 70**,** 2030-40.

LOUIS, D. N., PERRY, A., WESSELING, P., BRAT, D. J., CREE, I. A., FIGARELLA-BRANGER, D., HAWKINS, C., NG, H. K., PFISTER, S. M., REIFENBERGER, G., SOFFIETTI, R., VON DEIMLING, A. & ELLISON, D. W. 2021. The 2021 WHO Classification of Tumors of the Central Nervous System: a summary. *Neuro Oncol,* 23**,** 1231-1251.

LOVE, M. I., HUBER, W. & ANDERS, S. 2014. Moderated estimation of fold change and dispersion for RNA-seq data with DESeq2. *Genome Biol,* 15**,** 550.

LU, W. J., LAN, F., HE, Q., LEE, A., TANG, C. Z., DONG, L., LAN, B., MA, X., WU, J. C. & SHEN, L. 2011. Inducible expression of stem cell associated intermediate filament nestin reveals an important role in glioblastoma carcinogenesis. *Int J Cancer,* 128**,** 343-51.

LUKAS, C., SAVIC, V., BEKKER-JENSEN, S., DOIL, C., NEUMANN, B., PEDERSEN, R. S., GROFTE, M., CHAN, K. L., HICKSON, I. D., BARTEK, J. & LUKAS, J. 2011. 53BP1 nuclear bodies form around DNA lesions generated by mitotic transmission of chromosomes under replication stress. *Nat Cell Biol,* 13**,** 243-53.

LUNDIN, C., ERIXON, K., ARNAUDEAU, C., SCHULTZ, N., JENSSEN, D., MEUTH, M. & HELLEDAY, T. 2002. Different roles for nonhomologous end joining and homologous recombination following replication arrest in mammalian cells. *Mol Cell Biol,* 22**,** 5869-78.

M. DILLON, J. G., K. MOHAMMED, S.A. SMITH, E. DEAN, L. MCLELLAN, Z. BOYLAN, J. SPICER, M.D. FORSTER, K.J. HARRINGTON 2019. ABSTRACT: A phase I study of ATR inhibitor, AZD6738, as monotherapy in advanced solid tumours (PATRIOT part A, B). *Annals of Oncology,* Volume 30**,** Pages v165-v166.

MA, S., RUDRA, S., CAMPIAN, J. L., DAHIYA, S., DUNN, G. P., JOHANNS, T., GOLDSTEIN, M., KIM, A. H. & HUANG, J. 2020. Prognostic impact of CDKN2A/B deletion, TERT mutation, and EGFR amplification on histological and molecular IDH-wildtype glioblastoma. *Neurooncol Adv,* 2**,** vdaa126.

MACALPINE, D. M. & ALMOUZNI, G. 2013. Chromatin and DNA replication. *Cold Spring Harb Perspect Biol,* 5**,** a010207.

MACDOUGALL, C. A., BYUN, T. S., VAN, C., YEE, M. C. & CIMPRICH, K. A. 2007. The structural determinants of checkpoint activation. *Genes Dev,* 21**,** 898-903.

MACHERET, M., BHOWMICK, R., SOBKOWIAK, K., PADAYACHY, L., MAILLER, J., HICKSON, I. D. & HALAZONETIS, T. D. 2020. High-resolution mapping of mitotic DNA synthesis regions and common fragile sites in the human genome through direct sequencing. *Cell Res,* 30**,** 997-1008.

MACHERET, M. & HALAZONETIS, T. D. 2015. DNA replication stress as a hallmark of cancer. *Annu Rev Pathol,* 10**,** 425-48.

MAILAND, N., GIBBS-SEYMOUR, I. & BEKKER-JENSEN, S. 2013. Regulation of PCNA-protein interactions for genome stability. *Nat Rev Mol Cell Biol,* 14**,** 269-82.

MANTIERO, D., MACKENZIE, A., DONALDSON, A. & ZEGERMAN, P. 2011. Limiting replication initiation factors execute the temporal programme of origin firing in budding yeast. *EMBO J,* 30**,** 4805-14.

MAO, P., JOSHI, K., LI, J., KIM, S. H., LI, P., SANTANA-SANTOS, L., LUTHRA, S., CHANDRAN, U. R., BENOS, P. V., SMITH, L., WANG, M., HU, B., CHENG, S. Y., SOBOL, R. W. & NAKANO, I. 2013. Mesenchymal glioma stem cells are maintained by activated glycolytic metabolism involving aldehyde dehydrogenase 1A3. *Proc Natl Acad Sci U S A,* 110**,** 8644-9.

MATSUDA, Y., ISHIWATA, T., YOSHIMURA, H., HAGIO, M. & ARAI, T. 2015. Inhibition of nestin suppresses stem cell phenotype of glioblastomas through the alteration of post-translational modification of heat shock protein HSPA8/HSC71. *Cancer Lett,* 357**,** 602-11.

MAYA-MENDOZA, A., MOUDRY, P., MERCHUT-MAYA, J. M., LEE, M., STRAUSS, R. & BARTEK, J. 2018. High speed of fork progression induces DNA replication stress and genomic instability. *Nature,* 559**,** 279-284.

MEHENNI, H., LIN-MARQ, N., BUCHET-POYAU, K., REYMOND, A., COLLART, M. A., PICARD, D. & ANTONARAKIS, S. E. 2005. LKB1 interacts with and phosphorylates PTEN: a functional link between two proteins involved in cancer predisposing syndromes. *Hum Mol Genet,* 14**,** 2209-19.

MENISSIER DE MURCIA, J., RICOUL, M., TARTIER, L., NIEDERGANG, C., HUBER, A., DANTZER, F., SCHREIBER, V., AME, J. C., DIERICH, A., LEMEUR, M., SABATIER, L., CHAMBON, P. & DE MURCIA, G. 2003. Functional interaction between PARP-1 and PARP-2 in chromosome stability and embryonic development in mouse. *EMBO J,* 22**,** 2255-63.

METELLUS, P., NANNI-METELLUS, I., DELFINO, C., COLIN, C., TCHOGANDJIAN, A., COULIBALY, B., FINA, F., LOUNDOU, A., BARRIE, M., CHINOT, O., OUAFIK, L. & FIGARELLA-BRANGER, D. 2011. Prognostic impact of CD133 mRNA expression in 48 glioblastoma patients treated with concomitant radiochemotherapy: a prospective patient cohort at a single institution. *Ann Surg Oncol,* 18**,** 2937-45.

MICHEL, B., EHRLICH, S. D. & UZEST, M. 1997. DNA double-strand breaks caused by replication arrest. *EMBO J,* 16**,** 430-8.

MINOCHERHOMJI, S., YING, S., BJERREGAARD, V. A., BURSOMANNO, S., ALELIUNAITE, A., WU, W., MANKOURI, H. W., SHEN, H., LIU, Y. & HICKSON, I. D. 2015. Replication stress activates DNA repair synthesis in mitosis. *Nature,* 528**,** 286-90.

MIRAGLIA, S., GODFREY, W., YIN, A. H., ATKINS, K., WARNKE, R., HOLDEN, J. T., BRAY, R. A., WALLER, E. K. & BUCK, D. W. 1997. A novel five-transmembrane hematopoietic stem cell antigen: isolation, characterization, and molecular cloning. *Blood,* 90**,** 5013-21.

MITTRA, A., COYNE, G. H. O. S., DO, K. T., PIHA-PAUL, S. A., KUMMAR, S., TAKEBE, N., BRUNS, A., JUWARA, L., RUBINSTEIN, L., HOGU, M., KINDERS, R. J., PARCHMENT, R. E., MILLER, B., WILSKER, D., B., M. C. M., KHAN, S. S., DOYLE, L. A., DOROSHOW, J. H. & CHEN, A. P. 2019. ABSTRACT: Safety and tolerability of veliparib, an oral PARP inhibitor, and M6620 (VX-970), an ATR inhibitor, in combination with cisplatin in patients with refractory solid tumors. *Journal of Clinical Oncology,* 37**,** 3067-3067.

MIYAZAWA-ONAMI, M., ARAKI, H. & TANAKA, S. 2017. Pre-initiation complex assembly functions as a molecular switch that splits the Mcm2-7 double hexamer. *EMBO Rep,* 18**,** 1752-1761.

MOHNI, K. N., THOMPSON, P. S., LUZWICK, J. W., GLICK, G. G., PENDLETON, C. S., LEHMANN, B. D., PIETENPOL, J. A. & CORTEZ, D. 2015. A Synthetic Lethal Screen Identifies DNA Repair Pathways that Sensitize Cancer Cells to Combined ATR Inhibition and Cisplatin Treatments. *PLoS One,* 10**,** e0125482.

MOISEEVA, T., HOOD, B., SCHAMUS, S., O'CONNOR, M. J., CONRADS, T. P. & BAKKENIST, C. J. 2017. ATR kinase inhibition induces unscheduled origin firing through a Cdc7-dependent association between GINS and And-1. *Nat Commun,* 8**,** 1392.

MOLENAAR, R. J., RADIVOYEVITCH, T., NAGATA, Y., KHURSHED, M., PRZYCHODZEN, B., MAKISHIMA, H., XU, M., BLEEKER, F. E., WILMINK, J. W., CARRAWAY, H. E., MUKHERJEE, S., SEKERES, M. A., VAN NOORDEN, C. J. F. & MACIEJEWSKI, J. P. 2018. IDH1/2 Mutations Sensitize Acute Myeloid Leukemia to PARP Inhibition and This Is Reversed by IDH1/2-Mutant Inhibitors. *Clin Cancer Res,* 24**,** 1705-1715.

MORENO, A., CARRINGTON, J. T., ALBERGANTE, L., AL MAMUN, M., HAAGENSEN, E. J., KOMSELI, E. S., GORGOULIS, V. G., NEWMAN, T. J. & BLOW, J. J. 2016. Unreplicated DNA remaining from unperturbed S phases passes through mitosis for resolution in daughter cells. *Proc Natl Acad Sci U S A,* 113**,** E5757-64.

MOSRATI, M. A., MALMSTROM, A., LYSIAK, M., KRYSZTOFIAK, A., HALLBECK, M., MILOS, P., HALLBECK, A. L., BRATTHALL, C., STRANDEUS, M., STENMARK-ASKMALM, M. & SODERKVIST, P. 2015. TERT promoter mutations and polymorphisms as prognostic factors in primary glioblastoma. *Oncotarget,* 6**,** 16663-73.

MOYER, S. E., LEWIS, P. W. & BOTCHAN, M. R. 2006. Isolation of the Cdc45/Mcm2-7/GINS (CMG) complex, a candidate for the eukaryotic DNA replication fork helicase. *Proc Natl Acad Sci U S A,* 103**,** 10236-10241.

MURAI, J., FENG, Y., YU, G. K., RU, Y., TANG, S. W., SHEN, Y. & POMMIER, Y. 2016. Resistance to PARP inhibitors by SLFN11 inactivation can be overcome by ATR inhibition. *Oncotarget,* 7**,** 76534-76550.

MURAI, J., HUANG, S. Y., DAS, B. B., RENAUD, A., ZHANG, Y., DOROSHOW, J. H., JI, J., TAKEDA, S. & POMMIER, Y. 2012. Trapping of PARP1 and PARP2 by Clinical PARP Inhibitors. *Cancer Res,* 72**,** 5588-99.

MURAI, J., HUANG, S. Y., RENAUD, A., ZHANG, Y., JI, J., TAKEDA, S., MORRIS, J., TEICHER, B., DOROSHOW, J. H. & POMMIER, Y. 2014. Stereospecific PARP trapping by BMN 673 and comparison with olaparib and rucaparib. *Mol Cancer Ther,* 13**,** 433-43.

MURGA, M., BUNTING, S., MONTANA, M. F., SORIA, R., MULERO, F., CANAMERO, M., LEE, Y., MCKINNON, P. J., NUSSENZWEIG, A. & FERNANDEZ-CAPETILLO, O. 2009. A mouse model of ATR-Seckel shows embryonic replicative stress and accelerated aging. *Nat Genet,* 41**,** 891-8.

NAIM, V. & ROSSELLI, F. 2009. The FANC pathway and BLM collaborate during mitosis to prevent micro-nucleation and chromosome abnormalities. *Nat Cell Biol,* 11**,** 761-8.

NAIM, V., WILHELM, T., DEBATISSE, M. & ROSSELLI, F. 2013. ERCC1 and MUS81-EME1 promote sister chromatid separation by processing late replication intermediates at common fragile sites during mitosis. *Nat Cell Biol,* 15**,** 1008-15.

NARAYANAN, A., GAGLIARDI, F., GALLOTTI, A. L., MAZZOLENI, S., COMINELLI, M., FAGNOCCHI, L., PALA, M., PIRAS, I. S., ZORDAN, P., MORETTA, N., TRATTA, E., BRUGNARA, G., ALTABELLA, L., BOZZUTO, G., GOROMBEI, P., MOLINARI, A., PADUA, R. A., BULFONE, A., POLITI, L. S., FALINI, A., CASTELLANO, A., MORTINI, P., ZIPPO, A., POLIANI, P. L. & GALLI, R. 2019. The proneural gene ASCL1 governs the transcriptional subgroup affiliation in glioblastoma stem cells by directly repressing the mesenchymal gene NDRG1. *Cell Death Differ,* 26**,** 1813-1831.

NEEB, A., HERRANZ, N., ARCE-GALLEGO, S., MIRANDA, S., BURONI, L., YUAN, W., ATHIE, A., CASALS, T., CARMICHAEL, J., RODRIGUES, D. N., GUREL, B., RESCIGNO, P., REKOWSKI, J., WELTI, J., RIISNAES, R., GIL, V., NING, J., WAGNER, V., CASANOVA-SALAS, I., CORDOBA, S., CASTRO, N., FENOR DE LA MAZA, M. D., SEED, G., CHANDRAN, K., FERREIRA, A., FIGUEIREDO, I., BERTAN, C., BIANCHINI, D., AVERSA, C., PASCHALIS, A., GONZALEZ, M., MORALES-BARRERA, R., SUAREZ, C., CARLES, J., SWAIN, A., SHARP, A., GIL, J., SERRA, V., LORD, C., CARREIRA, S., MATEO, J. & DE BONO, J. S. 2021. Advanced Prostate Cancer with ATM Loss: PARP and ATR Inhibitors. *Eur Urol,* 79**,** 200-211.

NEILSEN, B. K., SLEIGHTHOLM, R., MCCOMB, R., RAMKISSOON, S. H., ROSS, J. S., CORONA, R. J., MILLER, V. A., COOKE, M. & AIZENBERG, M. R. 2019. Comprehensive genetic alteration profiling in primary and recurrent glioblastoma. *J Neurooncol,* 142**,** 111-118.

NEWMAN, T. J., MAMUN, M. A., NIEDUSZYNSKI, C. A. & BLOW, J. J. 2013. Replisome stall events have shaped the distribution of replication origins in the genomes of yeasts. *Nucleic Acids Res,* 41**,** 9705-18.

NING, J. F., STANCIU, M., HUMPHREY, M. R., GORHAM, J., WAKIMOTO, H., NISHIHARA, R., LEES, J., ZOU, L., MARTUZA, R. L., WAKIMOTO, H. & RABKIN, S. D. 2019. Myc targeted CDK18 promotes ATR and homologous

recombination to mediate PARP inhibitor resistance in glioblastoma. *Nat Commun,* 10**,** 2910.

NIU, C. S., LI, D. X., LIU, Y. H., FU, X. M., TANG, S. F. & LI, J. 2011. Expression of NANOG in human gliomas and its relationship with undifferentiated glioma cells. *Oncol Rep,* 26**,** 593-601.

NOBUSAWA, S., WATANABE, T., KLEIHUES, P. & OHGAKI, H. 2009. IDH1 mutations as molecular signature and predictive factor of secondary glioblastomas. *Clin Cancer Res,* 15**,** 6002-7.

NONOGUCHI, N., OHTA, T., OH, J. E., KIM, Y. H., KLEIHUES, P. & OHGAKI, H. 2013. TERT promoter mutations in primary and secondary glioblastomas. *Acta Neuropathol,* 126**,** 931-7.

O'BRIEN, C. A., KRESO, A. & JAMIESON, C. H. 2010. Cancer stem cells and self-renewal. *Clin Cancer Res,* 16**,** 3113-20.

OGDEN, A. T., WAZIRI, A. E., LOCHHEAD, R. A., FUSCO, D., LOPEZ, K., ELLIS, J. A., KANG, J., ASSANAH, M., MCKHANN, G. M., SISTI, M. B., MCCORMICK, P. C., CANOLL, P. & BRUCE, J. N. 2008. Identification of A2B5+CD133-tumor-initiating cells in adult human gliomas. *Neurosurgery,* 62**,** 505-14; discussion 514-5.

OHTSUBO, M., THEODORAS, A. M., SCHUMACHER, J., ROBERTS, J. M. & PAGANO, M. 1995. Human cyclin E, a nuclear protein essential for the G1-to-S phase transition. *Mol Cell Biol,* 15**,** 2612-24.

OLIVIER, M., HOLLSTEIN, M. & HAINAUT, P. 2010. TP53 mutations in human cancers: origins, consequences, and clinical use. *Cold Spring Harb Perspect Biol,* 2**,** a001008.

PALLINI, R., RICCI-VITIANI, L., BANNA, G. L., SIGNORE, M., LOMBARDI, D., TODARO, M., STASSI, G., MARTINI, M., MAIRA, G., LAROCCA, L. M. & DE MARIA, R. 2008. Cancer stem cell analysis and clinical outcome in patients with glioblastoma multiforme. *Clin Cancer Res,* 14**,** 8205-12.

PANDITA, A., ALDAPE, K. D., ZADEH, G., GUHA, A. & JAMES, C. D. 2004. Contrasting in vivo and in vitro fates of glioblastoma cell subpopulations with amplified EGFR. *Genes Chromosomes Cancer,* 39**,** 29-36.

PARK, A. K., KIM, P., BALLESTER, L. Y., ESQUENAZI, Y. & ZHAO, Z. 2019. Subtype-specific signaling pathways and genomic aberrations associated with prognosis of glioblastoma. *Neuro Oncol,* 21**,** 59-70.

PARK, D., XIANG, A. P., MAO, F. F., ZHANG, L., DI, C. G., LIU, X. M., SHAO, Y., MA, B. F., LEE, J. H., HA, K. S., WALTON, N. & LAHN, B. T. 2010. Nestin is required for the proper self-renewal of neural stem cells. *Stem Cells,* 28**,** 2162-71.

PARRISH, K. E., CEN, L., MURRAY, J., CALLIGARIS, D., KIZILBASH, S., MITTAPALLI, R. K., CARLSON, B. L., SCHROEDER, M. A., SLUDDEN, J., BODDY, A. V., AGAR, N. Y., CURTIN, N. J., ELMQUIST, W. F. & SARKARIA, J. N. 2015. Efficacy of PARP Inhibitor Rucaparib in Orthotopic Glioblastoma Xenografts Is Limited by Ineffective Drug Penetration into the Central Nervous System. *Mol Cancer Ther,* 14**,** 2735-43.

PARSONS, D. W., JONES, S., ZHANG, X., LIN, J. C., LEARY, R. J., ANGENENDT, P., MANKOO, P., CARTER, H., SIU, I. M., GALLIA, G. L., OLIVI, A., MCLENDON, R., RASHEED, B. A., KEIR, S., NIKOLSKAYA, T., NIKOLSKY, Y., BUSAM, D. A., TEKLEAB, H., DIAZ, L. A., JR., HARTIGAN, J., SMITH, D. R., STRAUSBERG, R. L., MARIE, S. K., SHINJO, S. M., YAN, H., RIGGINS, G. J., BIGNER, D. D., KARCHIN, R., PAPADOPOULOS, N., PARMIGIANI, G., VOGELSTEIN, B., VELCULESCU, V. E. & KINZLER, K. W. 2008. An integrated genomic analysis of human glioblastoma multiforme. *Science,* 321**,** 1807-12.

PASTRANA, E., CHENG, L. C. & DOETSCH, F. 2009. Simultaneous prospective purification of adult subventricular zone neural stem cells and their progeny. *Proc Natl Acad Sci U S A,* 106, 6387-92.

PASTRANA, E., SILVA-VARGAS, V. & DOETSCH, F. 2011. Eyes wide open: a critical review of sphere-formation as an assay for stem cells. *Cell Stem Cell,* 8, 486-98.

PATEL, A. P., TIROSH, I., TROMBETTA, J. J., SHALEK, A. K., GILLESPIE, S. M., WAKIMOTO, H., CAHILL, D. P., NAHED, B. V., CURRY, W. T., MARTUZA, R. L., LOUIS, D. N., ROZENBLATT-ROSEN, O., SUVA, M. L., REGEV, A. & BERNSTEIN, B. E. 2014. Single-cell RNA-seq highlights intratumoral heterogeneity in primary glioblastoma. *Science,* 344, 1396-401.

PETERMANN, E. & HELLEDAY, T. 2010. Pathways of mammalian replication fork restart. *Nat Rev Mol Cell Biol,* 11, 683-7.

PETERMANN, E., WOODCOCK, M. & HELLEDAY, T. 2010. Chk1 promotes replication fork progression by controlling replication initiation. *Proc Natl Acad Sci U S A,* 107, 16090-5.

PHILLIPS, H. S., KHARBANDA, S., CHEN, R., FORREST, W. F., SORIANO, R. H., WU, T. D., MISRA, A., NIGRO, J. M., COLMAN, H., SOROCEANU, L., WILLIAMS, P. M., MODRUSAN, Z., FEUERSTEIN, B. G. & ALDAPE, K. 2006. Molecular subclasses of high-grade glioma predict prognosis, delineate a pattern of disease progression, and resemble stages in neurogenesis. *Cancer Cell,* 9, 157-73.

PIOTROWSKI A, P. V., WEN P, CAMPIAN J, COLMAN H, PEARLMAN M, BUTOWSKI N, BATTISTE J, GLASS J, CLOUGHESY T, SCHIFF D, VAN DEN BENT M, WALBERT T, AHLUWALIA M, BADRUDDOJA M, KALRA A, AREGAWI D, WELLER M, RAMAKRISHNAN V, ZHANG K, WOOD K, MELLINGHOFF I, SHIH K. 2019. ABSTRACT: PAMIPARIB IN COMBINATION WITH RADIATION THERAPY (RT) AND/OR TEMOZOLOMIDE (TMZ) IN PATIENTS WITH NEWLY DIAGNOSED OR RECURRENT/REFRACTORY (R/R) GLIOBLASTOMA (GBM); PHASE 1B/2 STUDY UPDATE. *Neuro Oncol,* (Suppl 6):vi21–2.

PLADEVALL-MORERA, D., MUNK, S., INGHAM, A., GARRIBBA, L., ALBERS, E., LIU, Y., OLSEN, J. V. & LOPEZ-CONTRERAS, A. J. 2019. Proteomic characterization of chromosomal common fragile site (CFS)-associated proteins uncovers ATRX as a regulator of CFS stability. *Nucleic Acids Res,* 47, 8332.

PLUMMER, R., LORIGAN, P., STEVEN, N., SCOTT, L., MIDDLETON, M. R., WILSON, R. H., MULLIGAN, E., CURTIN, N., WANG, D., DEWJI, R., ABBATTISTA, A., GALLO, J. & CALVERT, H. 2013. A phase II study of the potent PARP inhibitor, Rucaparib (PF-01367338, AG014699), with temozolomide in patients with metastatic melanoma demonstrating evidence of chemopotentiation. *Cancer Chemother Pharmacol,* 71, 1191-9.

POLLARD, S. M., YOSHIKAWA, K., CLARKE, I. D., DANOVI, D., STRICKER, S., RUSSELL, R., BAYANI, J., HEAD, R., LEE, M., BERNSTEIN, M., SQUIRE, J. A., SMITH, A. & DIRKS, P. 2009. Glioma stem cell lines expanded in adherent culture have tumor-specific phenotypes and are suitable for chemical and genetic screens. *Cell Stem Cell,* 4, 568-80.

PRESTEGARDEN, L., SVENDSEN, A., WANG, J., SLEIRE, L., SKAFTNESMO, K. O., BJERKVIG, R., YAN, T., ASKLAND, L., PERSSON, A., SAKARIASSEN, P. O. & ENGER, P. O. 2010. Glioma cell populations grouped by different cell type markers drive brain tumor growth. *Cancer Res,* 70, 4274-9.

QUINET, A., CARVAJAL-MALDONADO, D., LEMACON, D. & VINDIGNI, A. 2017. DNA Fiber Analysis: Mind the Gap! *Methods Enzymol,* 591, 55-82.

RAFIEI, S., FITZPATRICK, K., LIU, D., CAI, M. Y., ELMARAKEBY, H. A., PARK, J., RICKER, C., KOCHUPURAKKAL, B. S., CHOUDHURY, A. D., HAHN, W. C., BALK, S. P., HWANG, J. H., VAN ALLEN, E. M. & MOUW, K. W. 2020. ATM Loss Confers Greater Sensitivity to ATR Inhibition Than PARP Inhibition in Prostate Cancer. *Cancer Res,* 80**,** 2094-2100.

RATTNER, J. B., RAO, A., FRITZLER, M. J., VALENCIA, D. W. & YEN, T. J. 1993. CENP-F is a .ca 400 kDa kinetochore protein that exhibits a cell-cycle dependent localization. *Cell Motil Cytoskeleton,* 26**,** 214-26.

RAY CHAUDHURI, A., HASHIMOTO, Y., HERRADOR, R., NEELSEN, K. J., FACHINETTI, D., BERMEJO, R., COCITO, A., COSTANZO, V. & LOPES, M. 2012. Topoisomerase I poisoning results in PARP-mediated replication fork reversal. *Nat Struct Mol Biol,* 19**,** 417-23.

RAY CHAUDHURI, A. & NUSSENZWEIG, A. 2017. The multifaceted roles of PARP1 in DNA repair and chromatin remodelling. *Nat Rev Mol Cell Biol,* 18**,** 610-621.

REAPER, P. M., GRIFFITHS, M. R., LONG, J. M., CHARRIER, J. D., MACCORMICK, S., CHARLTON, P. A., GOLEC, J. M. & POLLARD, J. R. 2011. Selective killing of ATM- or p53-deficient cancer cells through inhibition of ATR. *Nat Chem Biol,* 7**,** 428-30.

REYNOLDS, B. A. & WEISS, S. 1992. Generation of neurons and astrocytes from isolated cells of the adult mammalian central nervous system. *Science,* 255**,** 1707-10.

RICH, J. N. 2016. Cancer stem cells: understanding tumor hierarchy and heterogeneity. *Medicine (Baltimore),* 95**,** S2-S7.

RICH, J. N., HANS, C., JONES, B., IVERSEN, E. S., MCLENDON, R. E., RASHEED, B. K., DOBRA, A., DRESSMAN, H. K., BIGNER, D. D., NEVINS, J. R. & WEST, M. 2005. Gene expression profiling and genetic markers in glioblastoma survival. *Cancer Res,* 65**,** 4051-8.

RIVERA, A. L., PELLOSKI, C. E., GILBERT, M. R., COLMAN, H., DE LA CRUZ, C., SULMAN, E. P., BEKELE, B. N. & ALDAPE, K. D. 2010. MGMT promoter methylation is predictive of response to radiotherapy and prognostic in the absence of adjuvant alkylating chemotherapy for glioblastoma. *Neuro Oncol,* 12**,** 116-21.

RODRIGUEZ-ESCUDERO, I., OLIVER, M. D., ANDRES-PONS, A., MOLINA, M., CID, V. J. & PULIDO, R. 2011. A comprehensive functional analysis of PTEN mutations: implications in tumor- and autism-related syndromes. *Hum Mol Genet,* 20**,** 4132-42.

SAKTHIKUMAR, S., ROY, A., HASEEB, L., PETTERSSON, M. E., SUNDSTROM, E., MARINESCU, V. D., LINDBLAD-TOH, K. & FORSBERG-NILSSON, K. 2020. Whole-genome sequencing of glioblastoma reveals enrichment of non-coding constraint mutations in known and novel genes. *Genome Biol,* 21**,** 127.

SALDIVAR, J. C., CORTEZ, D. & CIMPRICH, K. A. 2017. The essential kinase ATR: ensuring faithful duplication of a challenging genome. *Nat Rev Mol Cell Biol,* 18**,** 622-636.

SANDHU, S. K., SCHELMAN, W. R., WILDING, G., MORENO, V., BAIRD, R. D., MIRANDA, S., HYLANDS, L., RIISNAES, R., FORSTER, M., OMLIN, A., KREISCHER, N., THWAY, K., GEVENSLEBEN, H., SUN, L., LOUGHNEY, J., CHATTERJEE, M., TONIATTI, C., CARPENTER, C. L., IANNONE, R., KAYE, S. B., DE BONO, J. S. & WENHAM, R. M. 2013. The poly(ADP-ribose) polymerase inhibitor niraparib (MK4827) in BRCA mutation carriers and patients with sporadic cancer: a phase 1 dose-escalation trial. *Lancet Oncol,* 14**,** 882-92.

SARKARIA, J. N., BALLMAN, K. V., KIZILBASH, S. H., SULMAN, E. P., GIANNINI, C., MASHRU, S. H., PICCIONI, D. E., FRIDAY, B. E. B., DIXON, J. G., KABAT, B., LAACK, N. N., HU, L., KUMTHEKAR, P., ELLINGSON, B. M., ANDERSON, S. K. & GALANIS, E. 2022. ABSTRACT: Randomized phase II/III trial of veliparib or placebo in combination with adjuvant temozolomide in newly diagnosed glioblastoma (GBM) patients with MGMT promoter hypermethylation (Alliance A071102). *Journal of Clinical Oncology,* 40**,** 2001-2001.

SARKARIA, J. N., BUSBY, E. C., TIBBETTS, R. S., ROOS, P., TAYA, Y., KARNITZ, L. M. & ABRAHAM, R. T. 1999. Inhibition of ATM and ATR kinase activities by the radiosensitizing agent, caffeine. *Cancer Res,* 59**,** 4375-82.

SATOH, M. S. & LINDAHL, T. 1992. Role of poly(ADP-ribose) formation in DNA repair. *Nature,* 356**,** 356-8.

SCHAFER, N., GIELEN, G. H., RAUSCHENBACH, L., KEBIR, S., TILL, A., REINARTZ, R., SIMON, M., NIEHUSMANN, P., KLEINSCHNITZ, C., HERRLINGER, U., PIETSCH, T., SCHEFFLER, B. & GLAS, M. 2019. Longitudinal heterogeneity in glioblastoma: moving targets in recurrent versus primary tumors. *J Transl Med,* 17**,** 96.

SCHOONEN, P. M., KOK, Y. P., WIERENGA, E., BAKKER, B., FOIJER, F., SPIERINGS, D. C. J. & VAN VUGT, M. 2019. Premature mitotic entry induced by ATR inhibition potentiates olaparib inhibition-mediated genomic instability, inflammatory signaling, and cytotoxicity in BRCA2-deficient cancer cells. *Mol Oncol,* 13**,** 2422-2440.

SHAPIRO, G. I., WESOLOWSKI, R., DEVOE, C., LORD, S., POLLARD, J., HENDRIKS, B. S., FALK, M., DIAZ-PADILLA, I., PLUMMER, R. & YAP, T. A. 2021. Phase 1 study of the ATR inhibitor berzosertib in combination with cisplatin in patients with advanced solid tumours. *Br J Cancer,* 125**,** 520-527.

SHIHAB, H. A., GOUGH, J., COOPER, D. N., DAY, I. N. & GAUNT, T. R. 2013. Predicting the functional consequences of cancer-associated amino acid substitutions. *Bioinformatics,* 29**,** 1504-10.

SHIHAB, H. A., ROGERS, M. F., GOUGH, J., MORT, M., COOPER, D. N., DAY, I. N., GAUNT, T. R. & CAMPBELL, C. 2015. An integrative approach to predicting the functional effects of non-coding and coding sequence variation. *Bioinformatics,* 31**,** 1536-43.

SHIMURA, T., TORRES, M. J., MARTIN, M. M., RAO, V. A., POMMIER, Y., KATSURA, M., MIYAGAWA, K. & ALADJEM, M. I. 2008. Bloom's syndrome helicase and Mus81 are required to induce transient double-strand DNA breaks in response to DNA replication stress. *J Mol Biol,* 375**,** 1152-64.

SHINOJIMA, N., TADA, K., SHIRAISHI, S., KAMIRYO, T., KOCHI, M., NAKAMURA, H., MAKINO, K., SAYA, H., HIRANO, H., KURATSU, J., OKA, K., ISHIMARU, Y. & USHIO, Y. 2003. Prognostic value of epidermal growth factor receptor in patients with glioblastoma multiforme. *Cancer Res,* 63**,** 6962-70.

SIM, H. W., MCDONALD, K. L., LWIN, Z., BARNES, E. H., ROSENTHAL, M., FOOTE, M. C., KOH, E. S., BACK, M., WHEELER, H., SULMAN, E. P., BUCKLAND, M. E., FISHER, L., LEONARD, R., HALL, M., ASHLEY, D. M., YIP, S., SIMES, J. & KHASRAW, M. 2021. A randomized phase II trial of veliparib, radiotherapy, and temozolomide in patients with unmethylated MGMT glioblastoma: the VERTU study. *Neuro Oncol,* 23**,** 1736-1749.

SIMBULAN-ROSENTHAL, C. M., ROSENTHAL, D. S., BOULARES, A. H., HICKEY, R. J., MALKAS, L. H., COLL, J. M. & SMULSON, M. E. 1998. Regulation of the expression or recruitment of components of the DNA synthesome by poly(ADP-ribose) polymerase. *Biochemistry,* 37**,** 9363-70.

SIMBULAN-ROSENTHAL, C. M., ROSENTHAL, D. S., HILZ, H., HICKEY, R., MALKAS, L., APPLEGREN, N., WU, Y., BERS, G. & SMULSON, M. E. 1996. The expression of poly(ADP-ribose) polymerase during differentiation-linked DNA replication reveals that it is a component of the multiprotein DNA replication complex. *Biochemistry,* 35**,** 11622-33.

SIMBULAN-ROSENTHAL, C. M., ROSENTHAL, D. S., IYER, S., BOULARES, H. & SMULSON, M. E. 1999. Involvement of PARP and poly(ADP-ribosyl)ation in the early stages of apoptosis and DNA replication. *Mol Cell Biochem,* 193**,** 137-48.

SIMON, M., HOSEN, I., GOUSIAS, K., RACHAKONDA, S., HEIDENREICH, B., GESSI, M., SCHRAMM, J., HEMMINKI, K., WAHA, A. & KUMAR, R. 2015. TERT promoter mutations: a novel independent prognostic factor in primary glioblastomas. *Neuro Oncol,* 17**,** 45-52.

SIMONEAU, A., XIONG, R. & ZOU, L. 2021. The trans cell cycle effects of PARP inhibitors underlie their selectivity toward BRCA1/2-deficient cells. *Genes Dev,* 35**,** 1271-1289.

SINGH, S. K., CLARKE, I. D., TERASAKI, M., BONN, V. E., HAWKINS, C., SQUIRE, J. & DIRKS, P. B. 2003. Identification of a cancer stem cell in human brain tumors. *Cancer Res,* 63**,** 5821-8.

SINGH, S. K., HAWKINS, C., CLARKE, I. D., SQUIRE, J. A., BAYANI, J., HIDE, T., HENKELMAN, R. M., CUSIMANO, M. D. & DIRKS, P. B. 2004. Identification of human brain tumour initiating cells. *Nature,* 432**,** 396-401.

SMITH, D. I., ZHU, Y., MCAVOY, S. & KUHN, R. 2006. Common fragile sites, extremely large genes, neural development and cancer. *Cancer Lett,* 232**,** 48-57.

SOMYAJIT, K., GUPTA, R., SEDLACKOVA, H., NEELSEN, K. J., OCHS, F., RASK, M. B., CHOUDHARY, C. & LUKAS, J. 2017. Redox-sensitive alteration of replisome architecture safeguards genome integrity. *Science,* 358**,** 797-802.

SON, M. J., WOOLARD, K., NAM, D. H., LEE, J. & FINE, H. A. 2009. SSEA-1 is an enrichment marker for tumor-initiating cells in human glioblastoma. *Cell Stem Cell,* 4**,** 440-52.

SONG, W. S., YANG, Y. P., HUANG, C. S., LU, K. H., LIU, W. H., WU, W. W., LEE, Y. Y., LO, W. L., LEE, S. D., CHEN, Y. W., HUANG, P. I. & CHEN, M. T. 2016. Sox2, a stemness gene, regulates tumor-initiating and drug-resistant properties in CD133-positive glioblastoma stem cells. *J Chin Med Assoc,* 79**,** 538-45.

SORIANO, I., MORAFRAILE, E. C., VAZQUEZ, E., ANTEQUERA, F. & SEGURADO, M. 2014. Different nucleosomal architectures at early and late replicating origins in Saccharomyces cerevisiae. *BMC Genomics,* 15**,** 791.

SOTTORIVA, A., SPITERI, I., PICCIRILLO, S. G., TOULOUMIS, A., COLLINS, V. P., MARIONI, J. C., CURTIS, C., WATTS, C. & TAVARE, S. 2013. Intratumor heterogeneity in human glioblastoma reflects cancer evolutionary dynamics. *Proc Natl Acad Sci U S A,* 110**,** 4009-14.

SPIES, J., LUKAS, C., SOMYAJIT, K., RASK, M. B., LUKAS, J. & NEELSEN, K. J. 2019. 53BP1 nuclear bodies enforce replication timing at under-replicated DNA to limit heritable DNA damage. *Nat Cell Biol,* 21**,** 487-497.

STADLER, J. & RICHLY, H. 2017. Regulation of DNA Repair Mechanisms: How the Chromatin Environment Regulates the DNA Damage Response. *Int J Mol Sci,* 18.

STROM, C. E., JOHANSSON, F., UHLEN, M., SZIGYARTO, C. A., ERIXON, K. & HELLEDAY, T. 2011. Poly (ADP-ribose) polymerase (PARP) is not involved

in base excision repair but PARP inhibition traps a single-strand intermediate. *Nucleic Acids Res,* 39**,** 3166-75.

STUPP, R., HEGI, M. E., MASON, W. P., VAN DEN BENT, M. J., TAPHOORN, M. J., JANZER, R. C., LUDWIN, S. K., ALLGEIER, A., FISHER, B., BELANGER, K., HAU, P., BRANDES, A. A., GIJTENBEEK, J., MAROSI, C., VECHT, C. J., MOKHTARI, K., WESSELING, P., VILLA, S., EISENHAUER, E., GORLIA, T., WELLER, M., LACOMBE, D., CAIRNCROSS, J. G., MIRIMANOFF, R. O., EUROPEAN ORGANISATION FOR, R., TREATMENT OF CANCER BRAIN, T., RADIATION ONCOLOGY, G. & NATIONAL CANCER INSTITUTE OF CANADA CLINICAL TRIALS, G. 2009. Effects of radiotherapy with concomitant and adjuvant temozolomide versus radiotherapy alone on survival in glioblastoma in a randomised phase III study: 5-year analysis of the EORTC-NCIC trial. *Lancet Oncol,* 10**,** 459-66.

STUPP, R., MASON, W. P., VAN DEN BENT, M. J., WELLER, M., FISHER, B., TAPHOORN, M. J., BELANGER, K., BRANDES, A. A., MAROSI, C., BOGDAHN, U., CURSCHMANN, J., JANZER, R. C., LUDWIN, S. K., GORLIA, T., ALLGEIER, A., LACOMBE, D., CAIRNCROSS, J. G., EISENHAUER, E., MIRIMANOFF, R. O., EUROPEAN ORGANISATION FOR, R., TREATMENT OF CANCER BRAIN, T., RADIOTHERAPY, G. & NATIONAL CANCER INSTITUTE OF CANADA CLINICAL TRIALS, G. 2005. Radiotherapy plus concomitant and adjuvant temozolomide for glioblastoma. *N Engl J Med,* 352**,** 987-96.

SUGIMURA, K., TAKEBAYASHI, S., TAGUCHI, H., TAKEDA, S. & OKUMURA, K. 2008. PARP-1 ensures regulation of replication fork progression by homologous recombination on damaged DNA. *J Cell Biol,* 183**,** 1203-12.

SULE, A., VAN DOORN, J., SUNDARAM, R. K., GANESA, S., VASQUEZ, J. C. & BINDRA, R. S. 2021. Targeting IDH1/2 mutant cancers with combinations of ATR and PARP inhibitors. *NAR Cancer,* 3**,** zcab018.

SULKOWSKI, P. L., CORSO, C. D., ROBINSON, N. D., SCANLON, S. E., PURSHOUSE, K. R., BAI, H., LIU, Y., SUNDARAM, R. K., HEGAN, D. C., FONS, N. R., BREUER, G. A., SONG, Y., MISHRA-GORUR, K., DE FEYTER, H. M., DE GRAAF, R. A., SUROVTSEVA, Y. V., KACHMAN, M., HALENE, S., GUNEL, M., GLAZER, P. M. & BINDRA, R. S. 2017. 2-Hydroxyglutarate produced by neomorphic IDH mutations suppresses homologous recombination and induces PARP inhibitor sensitivity. *Sci Transl Med,* 9.

SUN, K., MIKULE, K., WANG, Z., POON, G., VAIDYANATHAN, A., SMITH, G., ZHANG, Z. Y., HANKE, J., RAMASWAMY, S. & WANG, J. 2018. A comparative pharmacokinetic study of PARP inhibitors demonstrates favorable properties for niraparib efficacy in preclinical tumor models. *Oncotarget,* 9**,** 37080-37096.

TANAKA, S., NAKATO, R., KATOU, Y., SHIRAHIGE, K. & ARAKI, H. 2011. Origin association of Sld3, Sld7, and Cdc45 proteins is a key step for determination of origin-firing timing. *Curr Biol,* 21**,** 2055-63.

TANG, Y., QAZI, M. A., BROWN, K. R., MIKOLAJEWICZ, N., MOFFAT, J., SINGH, S. K. & MCNICHOLAS, P. D. 2021. Identification of five important genes to predict glioblastoma subtypes. *Neurooncol Adv,* 3**,** vdab144.

TENTORI, L., PORTARENA, I., TORINO, F., SCERRATI, M., NAVARRA, P. & GRAZIANI, G. 2002. Poly(ADP-ribose) polymerase inhibitor increases growth inhibition and reduces G(2)/M cell accumulation induced by temozolomide in malignant glioma cells. *Glia,* 40**,** 44-54.

TENTORI, L., RICCI-VITIANI, L., MUZI, A., CICCARONE, F., PELACCHI, F., CALABRESE, R., RUNCI, D., PALLINI, R., CAIAFA, P. & GRAZIANI, G. 2014. Pharmacological inhibition of poly(ADP-ribose) polymerase-1 modulates

resistance of human glioblastoma stem cells to temozolomide. *BMC Cancer,* 14**,** 151.
THERNEAU, T. M. 2022. A Package for Survival Analysis in R.
TOLEDO, L. I., MURGA, M., GUTIERREZ-MARTINEZ, P., SORIA, R. & FERNANDEZ-CAPETILLO, O. 2008. ATR signaling can drive cells into senescence in the absence of DNA breaks. *Genes Dev,* 22**,** 297-302.
TOLEDO, L. I., MURGA, M., ZUR, R., SORIA, R., RODRIGUEZ, A., MARTINEZ, S., OYARZABAL, J., PASTOR, J., BISCHOFF, J. R. & FERNANDEZ-CAPETILLO, O. 2011. A cell-based screen identifies ATR inhibitors with synthetic lethal properties for cancer-associated mutations. *Nat Struct Mol Biol,* 18**,** 721-7.
TORRES-ROSELL, J., DE PICCOLI, G., CORDON-PRECIADO, V., FARMER, S., JARMUZ, A., MACHIN, F., PASERO, P., LISBY, M., HABER, J. E. & ARAGON, L. 2007. Anaphase onset before complete DNA replication with intact checkpoint responses. *Science,* 315**,** 1411-5.
TSANTOULIS, P. K., KOTSINAS, A., SFIKAKIS, P. P., EVANGELOU, K., SIDERIDOU, M., LEVY, B., MO, L., KITTAS, C., WU, X. R., PAPAVASSILIOU, A. G. & GORGOULIS, V. G. 2008. Oncogene-induced replication stress preferentially targets common fragile sites in preneoplastic lesions. A genome-wide study. *Oncogene,* 27**,** 3256-64.
TUDURI, S., CRABBE, L., CONTI, C., TOURRIERE, H., HOLTGREVE-GREZ, H., JAUCH, A., PANTESCO, V., DE VOS, J., THOMAS, A., THEILLET, C., POMMIER, Y., TAZI, J., COQUELLE, A. & PASERO, P. 2009. Topoisomerase I suppresses genomic instability by preventing interference between replication and transcription. *Nat Cell Biol,* 11**,** 1315-24.
TUNICI, P., BISSOLA, L., LUALDI, E., POLLO, B., CAJOLA, L., BROGGI, G., SOZZI, G. & FINOCCHIARO, G. 2004. Genetic alterations and in vivo tumorigenicity of neurospheres derived from an adult glioblastoma. *Mol Cancer,* 3**,** 25.
TUTT, A., NOWECKI, Z., SZOSZKIEWICZ, R., IM, S. A., ARKENAU, H. T., ARMSTRONG, A. C., JACOT, W., KIM, J. H., WEBSTER, M., BALMANA, J., DELALOGE, S., LUKASHCHUK, N., ODEGBAMI, R., CASSON, E., LOEMBE, A. B., DRACHSLER, M. W., DEAN, E. J. & PUNIE, K. 2022. ABSTRACT: VIOLETTE: Randomised phase II study of olaparib (ola) plus ceralasertib (cer) or adavosertib (ada) vs ola alone in patients (pts) with metastatic triple-negative breast cancer (mTNBC).
UCHIDA, K., SUZUKI, H., MARUTA, H., ABE, H., AOKI, K., MIWA, M. & TANUMA, S. 1993. Preferential degradation of protein-bound (ADP-ribose)n by nuclear poly(ADP-ribose) glycohydrolase from human placenta. *J Biol Chem,* 268**,** 3194-200.
UCHIDA, N., BUCK, D. W., HE, D., REITSMA, M. J., MASEK, M., PHAN, T. V., TSUKAMOTO, A. S., GAGE, F. H. & WEISSMAN, I. L. 2000. Direct isolation of human central nervous system stem cells. *Proc Natl Acad Sci U S A,* 97**,** 14720-5.
VAITSIANKOVA, A., BURDOVA, K., SOBOL, M., GAUTAM, A., BENADA, O., HANZLIKOVA, H. & CALDECOTT, K. W. 2022. PARP inhibition impedes the maturation of nascent DNA strands during DNA replication. *Nat Struct Mol Biol,* 29**,** 329-338.
VAZIRI, C., SAXENA, S., JEON, Y., LEE, C., MURATA, K., MACHIDA, Y., WAGLE, N., HWANG, D. S. & DUTTA, A. 2003. A p53-dependent checkpoint pathway prevents rereplication. *Mol Cell,* 11**,** 997-1008.
VENDETTI, F. P., LAU, A., SCHAMUS, S., CONRADS, T. P., O'CONNOR, M. J. & BAKKENIST, C. J. 2015. The orally active and bioavailable ATR kinase

inhibitor AZD6738 potentiates the anti-tumor effects of cisplatin to resolve ATM-deficient non-small cell lung cancer in vivo. *Oncotarget,* 6**,** 44289-305.

VENERE, M., HAMERLIK, P., WU, Q., RASMUSSEN, R. D., SONG, L. A., VASANJI, A., TENLEY, N., FLAVAHAN, W. A., HJELMELAND, A. B., BARTEK, J. & RICH, J. N. 2014. Therapeutic targeting of constitutive PARP activation compromises stem cell phenotype and survival of glioblastoma-initiating cells. *Cell Death Differ,* 21**,** 258-69.

VERHAAK, R. G., HOADLEY, K. A., PURDOM, E., WANG, V., QI, Y., WILKERSON, M. D., MILLER, C. R., DING, L., GOLUB, T., MESIROV, J. P., ALEXE, G., LAWRENCE, M., O'KELLY, M., TAMAYO, P., WEIR, B. A., GABRIEL, S., WINCKLER, W., GUPTA, S., JAKKULA, L., FEILER, H. S., HODGSON, J. G., JAMES, C. D., SARKARIA, J. N., BRENNAN, C., KAHN, A., SPELLMAN, P. T., WILSON, R. K., SPEED, T. P., GRAY, J. W., MEYERSON, M., GETZ, G., PEROU, C. M., HAYES, D. N. & CANCER GENOME ATLAS RESEARCH, N. 2010. Integrated genomic analysis identifies clinically relevant subtypes of glioblastoma characterized by abnormalities in PDGFRA, IDH1, EGFR, and NF1. *Cancer Cell,* 17**,** 98-110.

VOGELAUER, M., RUBBI, L., LUCAS, I., BREWER, B. J. & GRUNSTEIN, M. 2002. Histone acetylation regulates the time of replication origin firing. *Mol Cell,* 10**,** 1223-33.

WANG, J., SAKARIASSEN, P. O., TSINKALOVSKY, O., IMMERVOLL, H., BOE, S. O., SVENDSEN, A., PRESTEGARDEN, L., ROSLAND, G., THORSEN, F., STUHR, L., MOLVEN, A., BJERKVIG, R. & ENGER, P. O. 2008. CD133 negative glioma cells form tumors in nude rats and give rise to CD133 positive cells. *Int J Cancer,* 122**,** 761-8.

WANG, K., LI, M. & HAKONARSON, H. 2010. ANNOVAR: functional annotation of genetic variants from high-throughput sequencing data. *Nucleic Acids Res,* 38**,** e164.

WANG, L., YANG, C., XIE, C., JIANG, J., GAO, M., FU, L., LI, Y., BAO, X., FU, H. & LOU, L. 2019. Pharmacologic characterization of fluzoparib, a novel poly(ADP-ribose) polymerase inhibitor undergoing clinical trials. *Cancer Sci,* 110**,** 1064-1075.

WANG, Q., HU, B., HU, X., KIM, H., SQUATRITO, M., SCARPACE, L., DECARVALHO, A. C., LYU, S., LI, P., LI, Y., BARTHEL, F., CHO, H. J., LIN, Y. H., SATANI, N., MARTINEZ-LEDESMA, E., ZHENG, S., CHANG, E., GABRIEL SAUVE, C. E., OLAR, A., LAN, Z. D., FINOCCHIARO, G., PHILLIPS, J. J., BERGER, M. S., GABRUSIEWICZ, K. R., WANG, G., ESKILSSON, E., HU, J., MIKKELSEN, T., DEPINHO, R. A., MULLER, F., HEIMBERGER, A. B., SULMAN, E. P., NAM, D. H. & VERHAAK, R. G. W. 2018. Tumor Evolution of Glioma-Intrinsic Gene Expression Subtypes Associates with Immunological Changes in the Microenvironment. *Cancer Cell,* 33**,** 152.

WANSINK, D. G., MANDERS, E. E., VAN DER KRAAN, I., ATEN, J. A., VAN DRIEL, R. & DE JONG, L. 1994. RNA polymerase II transcription is concentrated outside replication domains throughout S-phase. *J Cell Sci,* 107 (Pt 6)**,** 1449-56.

WARD, P. S., CROSS, J. R., LU, C., WEIGERT, O., ABEL-WAHAB, O., LEVINE, R. L., WEINSTOCK, D. M., SHARP, K. A. & THOMPSON, C. B. 2012. Identification of additional IDH mutations associated with oncometabolite R(-)-2-hydroxyglutarate production. *Oncogene,* 31**,** 2491-8.

WARNES, G. R., BOLKER, B., BONEBAKKER, L., GENTLEMAN, R., HUBER, W., LIAW, A., LUMLEY, T., MAECHLER, M., MAGNUSSON, A., MOELLER, S.,

SCHWARTZ, M. & VENABLES, B. 2022. gplots: Various R Programming Tools for Plotting Data.

WATKINS, S., ROBEL, S., KIMBROUGH, I. F., ROBERT, S. M., ELLIS-DAVIES, G. & SONTHEIMER, H. 2014. Disruption of astrocyte-vascular coupling and the blood-brain barrier by invading glioma cells. *Nat Commun,* 5**,** 4196.

WATTS, G. S., PIEPER, R. O., COSTELLO, J. F., PENG, Y. M., DALTON, W. S. & FUTSCHER, B. W. 1997. Methylation of discrete regions of the O6-methylguanine DNA methyltransferase (MGMT) CpG island is associated with heterochromatinization of the MGMT transcription start site and silencing of the gene. *Mol Cell Biol,* 17**,** 5612-9.

WEI, T. & SIMKO, V. 2021. R package 'corrplot': Visualization of a Correlation Matrix.

WENGNER, A. M., SIEMEISTER, G., LUCKING, U., LEFRANC, J., WORTMANN, L., LIENAU, P., BADER, B., BOMER, U., MOOSMAYER, D., EBERSPACHER, U., GOLFIER, S., SCHATZ, C. A., BAUMGART, S. J., HAENDLER, B., LEJEUNE, P., SCHLICKER, A., VON NUSSBAUM, F., BRANDS, M., ZIEGELBAUER, K. & MUMBERG, D. 2020. The Novel ATR Inhibitor BAY 1895344 Is Efficacious as Monotherapy and Combined with DNA Damage-Inducing or Repair-Compromising Therapies in Preclinical Cancer Models. *Mol Cancer Ther,* 19**,** 26-38.

WICKHAM, H. 2016. ggplot2: Elegant Graphics for Data Analysis. *Springer-Verlag New York*.

WIESWEG, M. 2022. survivalAnalysis: High-Level Interface for Survival Analysis and Associated Plots.

WILHELM, T., OLZIERSKY, A. M., HARRY, D., DE SOUSA, F., VASSAL, H., ESKAT, A. & MERALDI, P. 2019. Mild replication stress causes chromosome mis-segregation via premature centriole disengagement. *Nat Commun,* 10**,** 3585.

WILLIAM, D., MOKRI, P., LAMP, N., LINNEBACHER, M., CLASSEN, C. F., ERBERSDOBLER, A. & SCHNEIDER, B. 2017. Amplification of the EGFR gene can be maintained and modulated by variation of EGF concentrations in in vitro models of glioblastoma multiforme. *PLoS One,* 12**,** e0185208.

WILSON, T. E., ARLT, M. F., PARK, S. H., RAJENDRAN, S., PAULSEN, M., LJUNGMAN, M. & GLOVER, T. W. 2015. Large transcription units unify copy number variants and common fragile sites arising under replication stress. *Genome Res,* 25**,** 189-200.

WILSON, Z., ODEDRA, R., WALLEZ, Y., WIJNHOVEN, P. W. G., HUGHES, A. M., GERRARD, J., JONES, G. N., BARGH-DAWSON, H., BROWN, E., YOUNG, L. A., O'CONNOR, M. J. & LAU, A. 2022. ATR Inhibitor AZD6738 (Ceralasertib) Exerts Antitumor Activity as a Monotherapy and in Combination with Chemotherapy and the PARP Inhibitor Olaparib. *Cancer Res,* 82**,** 1140-1152.

WOODWARD, A. M., GOHLER, T., LUCIANI, M. G., OEHLMANN, M., GE, X., GARTNER, A., JACKSON, D. A. & BLOW, J. J. 2006. Excess Mcm2-7 license dormant origins of replication that can be used under conditions of replicative stress. *J Cell Biol,* 173**,** 673-83.

WU, S., GAO, F., ZHENG, S., ZHANG, C., MARTINEZ-LEDESMA, E., EZHILARASAN, R., DING, J., LI, X., FENG, N., MULTANI, A., SULMAN, E. P., VERHAAK, R. G., DE GROOT, J. F., HEFFERNAN, T. P., YUNG, W. K. A. & KOUL, D. 2020. EGFR Amplification Induces Increased DNA Damage Response and Renders Selective Sensitivity to Talazoparib (PARP Inhibitor) in Glioblastoma. *Clin Cancer Res,* 26**,** 1395-1407.

WU, T., HU, E., XU, S., CHEN, M., GUO, P., DAI, Z., FENG, T., ZHOU, L., TANG, W., ZHAN, L., FU, X., LIU, S., BO, X. & YU, G. 2021. clusterProfiler 4.0: A universal enrichment tool for interpreting omics data. *Innovation (Camb),* 2, 100141.

WYATT, H. D., SARBAJNA, S., MATOS, J. & WEST, S. C. 2013. Coordinated actions of SLX1-SLX4 and MUS81-EME1 for Holliday junction resolution in human cells. *Mol Cell,* 52, 234-47.

XIONG, Y., GUO, Y., LIU, Y., WANG, H., GONG, W., LIU, Y., WANG, X., GAO, Y., YU, F., SU, D., WANG, F., ZHU, Y., ZHAO, Y., WU, Y., QIN, Z., SUN, X., REN, B., JIANG, B., JIN, W., SHEN, Z., TANG, Z., SONG, X., WANG, L., LIU, X., ZHOU, C. & JIANG, B. 2020. Pamiparib is a potent and selective PARP inhibitor with unique potential for the treatment of brain tumor. *Neoplasia,* 22, 431-440.

XOURI, G., LYGEROU, Z., NISHITANI, H., PACHNIS, V., NURSE, P. & TARAVIRAS, S. 2004. Cdt1 and geminin are down-regulated upon cell cycle exit and are over-expressed in cancer-derived cell lines. *Eur J Biochem,* 271, 3368-78.

XU, B., SUN, Z., LIU, Z., GUO, H., LIU, Q., JIANG, H., ZOU, Y., GONG, Y., TISCHFIELD, J. A. & SHAO, C. 2011. Replication stress induces micronuclei comprising of aggregated DNA double-strand breaks. *PLoS One,* 6, e18618.

XU, H., ZONG, H., MA, C., MING, X., SHANG, M., LI, K., HE, X., DU, H. & CAO, L. 2017. Epidermal growth factor receptor in glioblastoma. *Oncol Lett,* 14, 512-516.

XU, S. P., SUN, G. P., SHEN, Y. X., PENG, W. R., WANG, H. & WEI, W. 2007. Synergistic effect of combining paeonol and cisplatin on apoptotic induction of human hepatoma cell lines. *Acta Pharmacol Sin,* 28, 869-78.

YAN, H., PARSONS, D. W., JIN, G., MCLENDON, R., RASHEED, B. A., YUAN, W., KOS, I., BATINIC-HABERLE, I., JONES, S., RIGGINS, G. J., FRIEDMAN, H., FRIEDMAN, A., REARDON, D., HERNDON, J., KINZLER, K. W., VELCULESCU, V. E., VOGELSTEIN, B. & BIGNER, D. D. 2009. IDH1 and IDH2 mutations in gliomas. *N Engl J Med,* 360, 765-73.

YANG, Y. G., CORTES, U., PATNAIK, S., JASIN, M. & WANG, Z. Q. 2004. Ablation of PARP-1 does not interfere with the repair of DNA double-strand breaks, but compromises the reactivation of stalled replication forks. *Oncogene,* 23, 3872-82.

YAP, T. A., O'CARRIGAN, B., PENNEY, M. S., LIM, J. S., BROWN, J. S., DE MIGUEL LUKEN, M. J., TUNARIU, N., PEREZ-LOPEZ, R., RODRIGUES, D. N., RIISNAES, R., FIGUEIREDO, I., CARREIRA, S., HARE, B., MCDERMOTT, K., KHALIQUE, S., WILLIAMSON, C. T., NATRAJAN, R., PETTITT, S. J., LORD, C. J., BANERJI, U., POLLARD, J., LOPEZ, J. & DE BONO, J. S. 2020. Phase I Trial of First-in-Class ATR Inhibitor M6620 (VX-970) as Monotherapy or in Combination With Carboplatin in Patients With Advanced Solid Tumors. *J Clin Oncol,* 38, 3195-3204.

YAP, T. A., TAN, D. S. P., TERBUCH, A., CALDWELL, R., GUO, C., GOH, B. C., HEONG, V., HARIS, N. R. M., BASHIR, S., DREW, Y., HONG, D. S., MERIC-BERNSTAM, F., WILKINSON, G., HREIKI, J., WENGNER, A. M., BLADT, F., SCHLICKER, A., LUDWIG, M., ZHOU, Y., LIU, L., BORDIA, S., PLUMMER, R., LAGKADINOU, E. & DE BONO, J. S. 2021. First-in-Human Trial of the Oral Ataxia Telangiectasia and RAD3-Related (ATR) Inhibitor BAY 1895344 in Patients with Advanced Solid Tumors. *Cancer Discov,* 11, 80-91.

YEELES, J. T., DEEGAN, T. D., JANSKA, A., EARLY, A. & DIFFLEY, J. F. 2015. Regulated eukaryotic DNA replication origin firing with purified proteins. *Nature,* 519, 431-5.

YEKEZARE, M., GOMEZ-GONZALEZ, B. & DIFFLEY, J. F. 2013. Controlling DNA replication origins in response to DNA damage - inhibit globally, activate locally. *J Cell Sci,* 126**,** 1297-306.

YING, S., MINOCHERHOMJI, S., CHAN, K. L., PALMAI-PALLAG, T., CHU, W. K., WASS, T., MANKOURI, H. W., LIU, Y. & HICKSON, I. D. 2013. MUS81 promotes common fragile site expression. *Nat Cell Biol,* 15**,** 1001-7.

YU, G., WANG, L. G., HAN, Y. & HE, Q. Y. 2012. clusterProfiler: an R package for comparing biological themes among gene clusters. *OMICS,* 16**,** 284-7.

YU, G., WANG, L. G., YAN, G. R. & HE, Q. Y. 2015. DOSE: an R/Bioconductor package for disease ontology semantic and enrichment analysis. *Bioinformatics,* 31**,** 608-9.

YUAN, X., CURTIN, J., XIONG, Y., LIU, G., WASCHSMANN-HOGIU, S., FARKAS, D. L., BLACK, K. L. & YU, J. S. 2004. Isolation of cancer stem cells from adult glioblastoma multiforme. *Oncogene,* 23**,** 9392-400.

ZAHRADKA, P. & EBISUZAKI, K. 1982. A shuttle mechanism for DNA-protein interactions. The regulation of poly(ADP-ribose) polymerase. *Eur J Biochem,* 127**,** 579-85.

ZELLWEGER, R., DALCHER, D., MUTREJA, K., BERTI, M., SCHMID, J. A., HERRADOR, R., VINDIGNI, A. & LOPES, M. 2015. Rad51-mediated replication fork reversal is a global response to genotoxic treatments in human cells. *J Cell Biol,* 208**,** 563-79.

ZEMAN, M. K. & CIMPRICH, K. A. 2014. Causes and consequences of replication stress. *Nat Cell Biol,* 16**,** 2-9.

ZEPPERNICK, F., AHMADI, R., CAMPOS, B., DICTUS, C., HELMKE, B. M., BECKER, N., LICHTER, P., UNTERBERG, A., RADLWIMMER, B. & HEROLD-MENDE, C. C. 2008. Stem cell marker CD133 affects clinical outcome in glioma patients. *Clin Cancer Res,* 14**,** 123-9.

ZHANG, L., YU, H., YUAN, Y., YU, J. S., LOU, Z., XUE, Y. & LIU, Y. 2020. The necessity for standardization of glioma stem cell culture: a systematic review. *Stem Cell Res Ther,* 11**,** 84.

ZHANG, Y., DUBE, C., GIBERT, M., JR., CRUICKSHANKS, N., WANG, B., COUGHLAN, M., YANG, Y., SETIADY, I., DEVEAU, C., SAOUD, K., GRELLO, C., OXFORD, M., YUAN, F. & ABOUNADER, R. 2018. The p53 Pathway in Glioblastoma. *Cancers (Basel),* 10.

ZHAO, Z., ZHANG, K. N., WANG, Q., LI, G., ZENG, F., ZHANG, Y., WU, F., CHAI, R., WANG, Z., ZHANG, C., ZHANG, W., BAO, Z. & JIANG, T. 2021. Chinese Glioma Genome Atlas (CGGA): A Comprehensive Resource with Functional Genomic Data from Chinese Glioma Patients. *Genomics Proteomics Bioinformatics,* 19**,** 1-12.

ZHONG, Y., NELLIMOOTTIL, T., PEACE, J. M., KNOTT, S. R., VILLWOCK, S. K., YEE, J. M., JANCUSKA, J. M., REGE, S., TECKLENBURG, M., SCLAFANI, R. A., TAVARE, S. & APARICIO, O. M. 2013. The level of origin firing inversely affects the rate of replication fork progression. *J Cell Biol,* 201**,** 373-83.

ZHU, W. & DUTTA, A. 2006. An ATR- and BRCA1-mediated Fanconi anemia pathway is required for activating the G2/M checkpoint and DNA damage repair upon rereplication. *Mol Cell Biol,* 26**,** 4601-11.

ZHU, Y., GUIGNARD, F., ZHAO, D., LIU, L., BURNS, D. K., MASON, R. P., MESSING, A. & PARADA, L. F. 2005. Early inactivation of p53 tumor suppressor gene cooperating with NF1 loss induces malignant astrocytoma. *Cancer Cell,* 8**,** 119-30.

ZOU, L. & ELLEDGE, S. J. 2003. Sensing DNA damage through ATRIP recognition of RPA-ssDNA complexes. *Science,* 300**,** 1542-8.